

1225-0767(ISSN Print)
2287-6715(ISSN Online)
한국연구재단 우수등재학술지

Journal of Ocean Engineering and Technology

Vol. 35, No. 1 (Serial Number 158)

February 2021

한국해양공학회지



www.joet.org



The Korean Society of Ocean Engineers

Editorial Board

■ Editor-in-Chief

Joonmo Choung Inha University, Korea

■ Manuscript Editors

Hyeongsik Choi Korea Maritime and Ocean University, Korea

Joon-Young Kim Korea Maritime and Ocean University, Korea

Seokhwan Ahn Jungwon University, Korea

Sungwon Shin Hanyang University, Korea

Woo Dong Lee Gyeongsang National University, Korea

■ Editorial Board Members

Ahmet Ergin Istanbul Technical University, Turkey

Atila Incecik University of Strathclyde, UK

Beom-Seon Jang Seoul National University, Korea

Bo Woo Nam Seoul National University, Korea

Chang Yong Song Mokpo National University, Korea

Chong Hyun Lee Jeju National University, Korea

Do Kyun Kim Newcastle University, UK

Dongho Jung Korea Research Institute of Ships & Ocean Engineering, Korea

Erkan Oterkus University of Strathclyde, UK

Geoffrey Lyons BPP-TECH, UK

Gökhan Tansel Tayyar Istanbul Technical University, Turkey

Gyungsoo Cho Tongmyong University, Korea

Hee Jin Kang Korea Research Institute of Ships & Ocean Engineering, Korea

Hooi-Siang Kang Universiti Teknologi Malaysia, Malaysia

Hyeon Kyu Yoon Changwon National University, Korea

Hyun-Sik Kim Tongmyong University, Korea

Jinwhan Kim Korea Advanced Institute of Science and Technology, Korea

Jong Chun Park Pusan National University, Korea

Kangsu Lee Korea Research Institute of Ships & Ocean Engineering, Korea

Kookhyun Kim Tongmyong University, Korea

Kwang-Jun Paik Inha University, Korea

Masashi Kashiwagi Osaka University, Japan

Moo Hyun Kim Texas A&M University, USA

Narakorn Srini Newcastle University, UK

Norimi Mizutani Nagoya University, Japan

Se-Min Jeong Chosun University, Korea

Seongim Choi Virginia Tech, USA

Seung Min Park Hyein Engineering & Construction, Co., Ltd., Korea

Soonchul Kwon Pusan National University, Korea

Sungnam Hong Gyeongsang National University, Korea

Sung-Woong Choi Gyeongsang National University, Korea

Taemin Ha Kangwon National University, Korea

TaeSeong Kim Loughborough University, UK

TaeSoon Kang GeoSystem Research Corp., Korea

Tak Kee Lee Gyeongsang National University, Korea

Weoncheol Koo Inha University, Korea

Yeon-Joong Kim Inje University, Korea

Yong Uk Ryu Chonnam National University, Korea

Younghun Kim Kyungnam University, Korea

Youngsub Lim Seoul National University, Korea

Research Ethics Board

■ Chief

Sung-Bu Suh Dongeui University, Korea

■ Research Ethics Board Members

Han Koo Jeong Kunsan National University, Korea

Jinwhan Kim Korea Advanced Institute of Science and Technology, Korea

Yong Uk Ryu Chonnam National University, Korea

Published on February 28, 2021

Published by The Korean Society of Ocean Engineers (KSOE)

Room 1302, 13, Jungang-daero 180beon-gil, Dong-gu, Busan, 48821, Korea

TEL: +82-51-759-0656 FAX: +82-51-759-0657 E-mail: ksoehj@ksoe.or.kr URL: http://www.ksoe.or.kr

Printed by Hanrimwon Co., Ltd., Seoul, Korea E-mail: hanrim@hanrimwon.co.kr

ISSN(print) 1225-0767 **ISSN(online)** 2287-6715

This journal was supported by the Korean Federation of Science and Technology Societies (KOFST) grant funded by the Korean government.

© 2021 by The Korean Society of Ocean Engineers (KSOE)

This is an open access article distributed under the terms of the creative commons attribution non-commercial license (<http://creativecommons.org/licenses/by-nc/4.0>) which permits unrestricted non-commercial use, distribution, and reproduction in any medium, provided the original work is properly cited.

Journal of Ocean Engineering and Technology

한국해양공학회지

CONTENTS

Volume 35, Number 1

February, 2021

<Original Research Articles>

- Study on a Fully Electrified Car Ferry Design Powered by Removable Battery Systems Considering Domestic Coastal Environment
Jang Pyo Hong, Young-Shik Kim, Hyung-Won Shim, Hee-Jin Kang, YunHo Kim, Gyu Bum Kim and Seongpil Cho 1
- Numerical Study to Evaluate Course-Keeping Ability in Regular Waves Using Weather Vaning Simulation
In-Tae Kim and Sang-Hyun Kim 13
- A Study on the Performance Variation of a Three-Dimensional Hydrofoil Using Jet Flow
Myeong-Jin Eom, Kwang-Jun Paik, Ju-Han Lee, Shin-Min Kang and Dong-Young Kim 24
- Numerical Study on Taylor Bubble Rising in Pipes
Seung Chul Shin, Gang Nam Lee, Kwang Hyo Jung, Hyun Jung Park, Il Ryong Park and Sung-bu Suh 38
- Parameter Study of Boiling Model for CFD Simulation of Multiphase-Thermal Flow in a Pipe
Soh-Myung Chung, Yong-Seok Seo, Gyu-Mok Jeon, Jae-Won Kim and Jong-Chun Park 50
- An Experimental Study on the H-Beam Under Fire Load in Open Space
Min Suk Ki, Beom Jin Park, Kangsu Lee, Byoungjae Park, Kyle Fernandez and In Sik Nho 59
- Application of the Artificial Coral Reef as a Coastal Erosion Prevention Method with Numerical-Physical Combined Analysis
(Case Study: Cheonjin-Bongpo Beach, Kangwon Province, South Korea)
Sunghoon Hong, Yeon Myeong Jeong, Taeyoon Kim, Van Men Huynh, Inho Kim, Jungmin Nam, Dong Soo Hur, Jooyong Lee and Soonchul Kwon 75
- Analysis of Wave Transmission Characteristics on the TTP Submerged Breakwater Using a Parabolic-Type Linear Wave Deformation Model
Jin-Hwan Jeong, Jin-Hoon Kim and Jung-Lyul Lee 82
- ### <Technical Article>
- Fundamental Research for Video-Integrated Collision Prediction and Fall Detection System to Support Navigation Safety of Vessels
Bae-Sung Kim, Yun-Tae Woo, Yung-Ho Yu and Hun-Gyu Hwang 91

GENERAL INFORMATION

“Journal of Ocean Engineering and Technology” is the official journal published by “The Korean Society of Ocean Engineers (KSOE)”. The ISO abbreviation is “J. Ocean Eng. Technol.” and acronym is “**JOET**”. It was launched in 1987. It is published bimonthly in February, April, June, August, October, and December each year. Supplement numbers are published at times.

Journal of Ocean Engineering and Technology (JOET) is a medium for the publication of original research and development work in the field of ocean engineering. JOET covers the entire range of issues and technologies related to the following topics:

Ships and offshore platforms: Design of marine structures; Resistance and propulsion; Seakeeping and maneuvering; Experimental and computational fluid dynamics; Ocean wave mechanics; Fatigue strength; Plasticity; Optimization and reliability; Arctic technology and extreme mechanics; Noise, vibration, and acoustics; Concrete engineering; Thermodynamics and heat transfer; Hydraulics and pneumatics;
Coastal civil engineering: Coastal structures; Port and harbor structures; Soil mechanics; Drilling and exploration; Hydraulics of estuary; Seismic engineering; Coastal disaster prevention engineering;
Ocean renewable energy platforms: Offshore wind turbines; Wave energy platforms; Tidal current energy platforms; Floating photovoltaic energy platforms;
Marine robots: Robot sensor system; Autonomous navigation; Robot equipments; Spatial information and communications; Underwater network; Design of underwater vehicles;
Multidisciplinary areas: Design for safety; IT-based design; IT-based production engineering; Welding mechanics; Control engineering; GPS and GIS; Inspection and sensor; Port and logistics; Leisure boat and deep sea water; Offshore process systems engineering; Marine metallic materials; Marine organic materials; Marine Composite materials; Materials properties; Corrosion and Anti-corrosion; Tribology;

It contains original research articles, case reports, brief communications and reviews on technical issues. Conference papers, research papers, diploma papers and academic articles can be submitted.

All of the manuscripts are peer-reviewed. **JOET** has a system where two or more peer reviewers must review each submitted paper and it is operated very strictly.

JOET is an open access journal distributed under the terms of the creative commons attribution non-commercial license (<http://creativecommons.org/licenses/by-nc/4.0>). Therefore, all ocean engineers and researchers around the world can easily access all journal articles via the journal homepage (<http://www.joet.org>) and download the PDF-based original texts or view the web-based XML texts for free.

JOET is being indexed in some prominent database such as Korean Citation Index (KCI), Google Scholar, Science Central, Korea Science and Directory of Open Access Journals (DOAJ).

For correspondences concerning business matters, author needs to contact KSOE Secretariat by email or phone (e-mail: ksoehj@ksoe.or.kr or Tel: +82 51 759 0656). Correspondences for publication matters can be asked via email to the Editor-in-Chief (email: heroeswise2@gmail.com).

Study on a Fully Electrified Car Ferry Design Powered by Removable Battery Systems Considering Domestic Coastal Environment

Jang Pyo Hong¹, Young-Shik Kim¹, Hyung-Won Shim¹, Hee-Jin Kang¹,
 YunHo Kim¹, Gyu Bum Kim¹ and Seongpil Cho¹

¹Alternative Fuels and Power System Research Center, Korea Research Institute of Ships and Ocean Engineering, Daejeon, Korea

KEY WORDS: Battery-powered car ferry, Removable power supply system, Roll-on/roll-off battery system, Fully electrified car ferry, Eco-friendly ship design

ABSTRACT: As increasing the international community's awareness of greenhouse gas reduction, the demand for eco-friendly ship fuel has accelerated recently. The fundamental aim of this study is to develop a new type of fully electrified ferry for passengers and cars considering Korean domestic coastal environmental conditions. Several technical difficulties are encountered in applying a fully electric propulsion system based on removable battery systems into a ship due to limitations imposed by the batteries' size and capacity. This paper reviews and analyzes marine environment regulations strengthened recently, technology trends related to fully electric propulsion vessels in each country, and Korean domestic coastal environments. We propose a new fully electrified car ferry design with a displacement of 400 t applied in Korea. It is powered by removable battery systems pre-charged in a safe inland charging station. The mobile battery system is developed to enable roll-on and roll-off using wheels. The characteristics of the ship motion are analyzed based on the weight and location of the battery systems. We expect our battery systems to be applicable to larger ships in the future.

1. Introduction

The temperature on Earth has been increased by 0.74 °C due to human activities over the past century. When the body temperature rises by 1 or 2 °C, a human feels the strangeness of health. Likewise, Earth temperature changes have resulted in various environmental abnormal phenomena, such as sea ice melting and desertification. Furthermore, temperature changes caused by global warming are causing extreme weather events, such as heat waves, large hurricanes, droughts, typhoons, heavy rains, and heavy snow in areas inhabited by humans. The main cause of global warming is carbon dioxide. Carbon dioxide is primarily emitted from fossil fuels used by humans. It is accumulated in the atmosphere and causes the greenhouse effect, thereby negatively affecting living organisms and humans' survival. The international community has recognized this problem, and members of the United Nations (UN) have agreed to the obligation of greenhouse gas (GHG) reduction at the 21st General Assembly of the Parties to the UN Framework Convention on Climate Change held in Paris in 2015. This UN obligation of GHG has been applied to all 195 UN member countries from January 2021. The convention presents the

long-term goal of maintaining the global average temperature increase below 2 °C.

Among anthropogenic GHG emissions, the shipping sector's contribution increased from 800 million tons in 2012 to 1 billion tons in 2018, constituting approximately 3% of the total global emissions. Hence, GHGs generated from the shipping industry must be reduced urgently. In April 2018, the International Maritime Organization (IMO) announced an early strategy to reduce GHGs emitted from ships by 50% compared with those emitted in 2008 and has continuously expressed the importance of reducing GHG emissions (Kim et al., 2018). To reduce GHGs in the shipping industry, the existing ships must be transformed into eco-friendly systems. To comply with environmental regulations, the global shipping industry changes ship fuels from heavy fuel oil (HFO) to liquefied natural gas (LNG) or marine diesel oil. And the additional emission reduction systems such as scrubber systems for SOx reduction and selective catalytic reduction systems for NOx reduction are installed on the ships (Lee, 2018). However, the solutions for GHG reduction in the shipping sector are still insufficient to achieve the IMO's GHG reduction goal. One of the well-known practical alternative solutions

Received 16 October 2020, revised 30 December 2020, accepted 30 December 2020

Corresponding author Young-Shik Kim: +82-42-866-3951, yskim@kriso.re.kr

© 2021, The Korean Society of Ocean Engineers

This is an open access article distributed under the terms of the creative commons attribution non-commercial license (<http://creativecommons.org/licenses/by-nc/4.0>) which permits unrestricted non-commercial use, distribution, and reproduction in any medium, provided the original work is properly cited.

for implementing the GHG reduction strategy during ships' operation is operating them at low speed, i.e., less than 50% of the specified ship speed, resulting in undesirable repercussions to the shipping industry. Hence, various alternative fuels applicable to ships must be developed. The stable fuel-supplying to automobiles and industrial machines in one country is not a big issue. However, owing to the nature of the shipping industry, which requires fuels worldwide, the fuel-supplying stability is critical for the development of alternative fuels for the shipping industry.

Electric energy with battery systems is strongly attracting attention as an alternative eco-friendly fuel for shipping. Electric energy guarantees fuel-supplying stability because it is produced in every country. And zero-emission is realized in the operation of the ships with electrical propulsion systems. However, it is difficult to apply the battery system to large ocean-crossing vessels due to the energy density problems concerning volume, weight, and cost. Hence, it would be desirable to promote battery usage as ship fuel by securing related technology development through their application to relatively small vessels operating near the seashore. Recently, performance evaluation techniques for electric propulsion systems have been investigated as an element technology for eco-friendly ships to reduce air pollutant emissions (Joung et al., 2013). Furthermore, a prototype of a 20 HP-class outboard electric motor drive system was developed, and its performance was evaluated (Moon et al., 2018). However, electric propulsion vessels using the battery system as the main power source have not been investigated.

In this study, recent technology issues relating to the fully electric propulsion system are investigated by analyzing technology

development and research projects in major countries for realizing IMO's GHG reduction strategies. And also, the developing status of fully electrified vessels over the world is analyzed. In addition, vessel types applicable to the current technology level of fully electric propulsion vessels that do not emit GHGs during the operation are analyzed. Based on the analysis results, a conceptual design of a fully electrified ferry for passengers and cars powered by removable power supply systems that is suitable for coastal environments with significant tidal differences and frequent typhoons such as Korea.

2. IMO's Initial Strategy for Reducing GHG Emissions and Characteristics of Alternative Fuels

2.1 IMO's Initial Strategy for Reducing GHG Emissions

South Korea's GHG emission in the shipping sector was approximately 800 million tons in 2012, greater than those of Germany, which ranked the sixth in the world. Therefore, efforts to reduce GHG emissions in the shipping sector are essential (Kim et al., 2018). The Marine Environment Protection Committee of the IMO adopted an initial strategy to implement GHG reduction in the shipping sector in the committee's 72nd session. The strategy's vision was to commit to reducing GHG emissions from international shipping and phase them the soonest possible.

To achieve the initial strategy goal, the IMO derived short-term, mid-term, and long-term measures to reduce GHG emissions in ships, as shown in Table 1. After reviewing (1) the geographic access and connectivity to key markets, (2) value and type of cargo, (3) dependence on transport, (4) transport costs, (5) food security, (6)

Table 1 IMO's strategic measures for reducing greenhouse gas emissions in ships

Period	Content
Short-term	<ul style="list-style-type: none"> - Additional improvements of energy efficiency systems focused on EEDI and SEEMP - Development of technical and operational measures based on a three-step approach with indexes for performance measurement and improvement of ship energy efficiency for new and existing ships - Program establishment for improvement of an existing ship - Review of speed optimization considering operational safety, market distortion, and maritime transport capacity - Strengthen measures for treatment of methane and volatile organic compounds (VOCs) - Development of policies and strategies for reduction of greenhouse gas emissions from international transport in according to IMO guidelines - Continuous technical cooperation with ITPC activities - Port developments for the power supply to onshore/offshore regions and ships through renewable energy, infrastructure for low or zero carbon emission fuel supplies, and the optimization of logistics networks and plans - Establishment of the International Maritime Research and Development Board (IMRB) to improve ship propulsion, alternative low or zero carbon emission fuel, and ship energy efficiency and to supervise R&D support - Incentive payments for developing and adopting new technologies - Guideline development of greenhouse gas/carbon intensity for all fuel types - Promotion of emission reduction efforts according to IMO-level to the international community - Investigation of additional GHG Study and policy establishment regarding regulations for zero carbon emission fuel
Mid-term	<ul style="list-style-type: none"> - Program development for ensuring alternative low carbon and zero emission fuel - Operational energy efficiency measures based on a three-step approach with indexes for new and existing ships - Emission reduction measures considering market-based measures (MBMs) - Continuous promotion of technical cooperation (e.g. ITCP) and capacity enhancement activities - Development of feedback measures for information exchange on best cases
Long-term	<ul style="list-style-type: none"> - Development of technologies for low carbon emission or decarbonation in the maritime transport sector - Promotion and utilization of new and innovative emission reduction measures

disaster response, (7) cost-effectiveness, and (8) socio-economic progress and development, the IMO urged every member country to analyze the effects and seek solutions if adverse effects to short-term approaches are identified.

If the ship fuel consumption can be reduced, then GHG emissions can be reduced. Shipping is a logistics industry that constitutes more than 90% of global cargo, and the amount of delivery and adherence to a set delivery time are key factors of the industry. Although the reduction in ship fuel consumption reduces GHGs, the economic logic of the industry is violated. Therefore, instead of reducing fuel consumption, alternative fuels should be developed. In the next section, we analyze the characteristics of alternative fuels for vessels.

2.2 Characteristics of Alternative Fuels

HFO has been used as a fuel for existing ships. The necessity for eco-friendly alternative fuels in vessels has recently increased due to efforts from the international community. In this study, the advantages and disadvantages of eco-friendly alternative fuels such as LNG, which is widely used in the shipping industry, bio-fuel, ammonia, and battery, were analyzed. The results are summarized in Table 2. Fuel for vessels must be eco-friendly; additionally, fuel supply, space utilization, and shipbuilding cost should be considered. Among the alternative fuels analyzed in this study, LNG garners attention as an eco-friendly fuel because it can be supplied stably, has infrastructures by continuous investments, and does not emit sulfides. However, LNG must be used strategically because its GHG reduction level is only 20%. Hydrogen and ammonia are carbon-free fuels that can satisfy the IMO's GHG reduction strategy. Hydrogen technology development is in the early stage. It is necessary to pre-emptively develop applied technologies, such as liquid hydrogen storage below absolute temperature and high-pressure gas utilization. Furthermore, ammonia offers advantages of low production cost, zero carbon dioxide

emission, and relatively low barrier to entry of liquefaction technology; however, its popularity as ship fuel depends on the corrosiveness resolution and toxicity problems.

Regarding the power source of vessels, conversion to an electric system is garnering attention in consideration of the scalability of operation efficiency and the use of eco-friendly alternative fuels. In particular, the battery is considered as the eco-friendliest fuel, with zero emissions in principle. However, due to the limitations of the current battery technology, the development of punctual short-distance vessels must be prioritized based on the constraint of vessel displacement and the resulting weight restriction. Technologies that accommodate large sizes should be developed after proving the effects.

3. Technology Development Trends

Many countries worldwide are developing various technologies and supporting policies to achieve GHG reduction goals via conversion to eco-friendly vessels. The policies and technology developments of various countries are summarized in Table 3.

The European Union is promoting “sea transportation strategies” to prepare for an eco-friendly competition from the shipping industry, including a reduction in GHG emissions, use of eco-friendly port facilities, and flagship projects for hydrogen ship development. Germany is developing new technologies under the “Maritime Agenda 2025” policy to develop alternative fuels for vessels. The United States is promoting a strong air pollutant regulation policy in ports separately from the IMO. South Korea enforced the Act on Promotion of the Development and Distribution of Environment-friendly Ships in January 2020 and is supporting the policy to propagate eco-friendly vessels. As a result of policy support and technology development in these countries, technology development for carbon-free ships is

Table 2 Characteristics of alternate fuels

Fuels	Relative characteristic of technology			Advantage and disadvantage
	TRL	Fuel supply	GHG reduction	
Petroleum	10	10	0	(A) Reliable fuel supply and usage of existing infrastructure (D) Dissatisfaction of various regulations
LNG	9	4	20	(A) Reliable fuel supply and usage of existing infrastructure (D) Unsatisfaction of GHG regulation and high investment costs
LPG	10	8	20	(A) Reliable fuel supply and usage of existing infrastructure (D) High possibility of fire due to relative high specific gravity
Electric powered	5	2	65	(A) Zero emission of greenhouse gases (D) Limited range due to battery size and capacity
Hydrogen	2	1	70	(A) High energy density, carbon-free fuel (D) Initial stage of technology development
Ammonia	10	6	50	(A) Zero emission of greenhouse gas, ease of liquidization (D) Corrosive and nitrogen oxide discharge
Methanol	-	-	50	(A) Low cost of bunkering (D) Unsatisfaction of GHG regulations
Bio-fuel	10	9	72	(A) High compatibility with existing fuel (D) Sediment generation and limited production while fuel usage

Table 3 Trends in the development of eco-friendly ship related policies and technologies in several countries

Section	Country	Content
R&D	Europe	Evaluation of existing technical methods for 11 future ships for reduction of greenhouse gases
	Norway	Construction of eco-friendly fuel supply facility, demonstration of next generation ship in sea
	South Korea	Eco-friendly technology development based on advanced shipbuilding technology
	Japan	Demonstration of 8,000 t liquefied hydrogen transport ship and the development of alternative fuel technology
	Singapore	Development of standards for advanced LNG bunkering technology with maritime transport Industries
Policy support	Europe	Provide loans of up to 50% of the cost of overheating eco-friendly shipping investment
	Norway	Financial support required for the construction and renovation of LNG-powered ships up to 80% of the overall costs
	South Korea	Legislation on support of tax and promotion of eco-friendly ships
	Japan	Support for the construction of shipping facilities and LNG bunkering vessels at Yokohama Port
	Singapore	Tax reduction and subsidy support for eco-friendly ships

actively performed. A carbon-free ship refers to a ship that is fully powered by electricity using a battery, i.e., without requiring an internal combustion engine.

Regarding fully electric propulsion vessels, the introduction of punctual short-distance coastal passenger ships is being promoted worldwide. Norway has been operating a fully electrified car ferry (MF Ampere), which operates 34 times per day for a distance of 5.6 km in fjords since May 2015. This vessel measures 80 m (length) × 20 m (width) and comprises two 450 kW propulsion systems. Furthermore, Norway has installed an electric charging facility, including an energy storage system (ESS) of approximately 400 kWh in a berth pier for ship batteries (Korea Energy Agency, 2017). Based on the achievement of MF Ampere, Norway has been operating the vessel “Future of the Fjords” for tourism in fjords since April 2018. Future of the Fjords can accommodate 400 passengers, consumes 1.8 MWh of power from batteries on board, and has an operating speed of approximately 29 km/h. Photographs of the Future of the Fjords are shown in Fig. 1.

In addition to the abovementioned vessels operating in constant-temperature waters, Norway has been developing a container cargo ship (YARA Birkeland) with fully electric propulsion and autonomous navigation features since 2017. This ship is expected to have an operating speed of 12–15 kn (6–8 m/s) and support approximately 100 containers. An image of the YARA Birkeland under development is shown in Fig. 2.



Fig. 1 Future of the Fjords in Norway, 2018



Fig. 2 Autonomous transport electric container cargo ship (YARA) in Norway



Fig. 3 Elektra in Finland (2017)

Finland has been operating a fully electrified car ferry that operates 25 times per day for a round trip distance of approximately 3 km in the Turku Islands since January 2017. The vessel is named Elektra (Fig. 3); it measures 97.92 m (length) × 15.2 m (width) and can transport approximately 370 passengers and 90 vehicles. Elektra comprises two propulsion systems with 900 kW capacity and 1 MWh power consumption from batteries. A 690 V charging facility was installed at a pier to charge this vessel.

Iceland and Canada are planning to introduce electric propulsion vessels that have been proven effective in Europe and Norway to their



Fig. 4 Pure electric propulsion ship in America

domestic coasts. These vessels are punctual coastal ferries for transporting vehicles and passengers. Furthermore, the U.S. has recognized the necessity for electric propulsion vessels and is currently developing an E-ferry that can transport over 150 passengers between Williamsburg and East Manhattan (Fig. 4).

As described above, Europe and North America are developing and supplying battery-powered fully electric propulsion vessels in calm waters (e.g., fjords, rivers, and lakes). This provides evidence that punctual vessels operating a short distance can solve problems associated with the battery system's weight and volume.

China, which has well-developed inland canals around the Yangtze and Yellow River, is developing technologies through demonstration for coastal vessels that do not need to satisfy international standards. One example is an electric propulsion container ship built in November 2017 (Fig. 5) that measures approximately 70 m (length) × 14 m (wide) with a battery consumption of approximately 2.4 MWh. This inland ship is operated on the Pearl River in Guangzhou and can operate for up to 80 km by charging for two hours at a time.

South Korea, a global shipbuilding industry leader, is primarily developing hybrid ships used in combination with diesel engines and

generators instead of using fully electric propulsion vessels. Examples include the icebreaker Araon and the LNG fuel vessel Econuri. The Araon was introduced in 2009 for polar research; it is driven by an electric propulsion system using a diesel generator. An electric propulsion system, which can actively respond to rapid output variations and be accurately controlled, is typically applied to offshore support vessels. An electric propulsion system for supplying materials, rescuing stranded fishing boats, and collecting polar samples has been applied to the Araon. The Econuri is a port guide ship that the Incheon Port Authority is operating; it generates electricity using an LNG/diesel dual-fuel generator. As the first LNG-powered vessel in Asia, the Econuri reduces the operation cost by approximately 100 million KRW per year compared with diesel vessels. The photographs of the Araon and the Econuri are shown in Fig. 6.

South Korea has more than 80,000 registered vessels and various types of small vessels (e.g., fishing boats and leisure yachts). To satisfy the eco-friendly policies of the global community, eco-friendly vessels using electric energy are being actively investigated, e.g., the application of a hybrid power generation system with wind and solar cells applied to a leisure boat (Oh et al., 2016) and a localization study pertaining to electric propulsion outboards for imported small ships (Moon et al., 2018).

Countries worldwide are competing with each other in developing technologies for eco-friendly vessels. Europe is leading the development of fully electric propulsion vessels for calm waters, whereas Asia uses technologies that apply a hybrid system with an existing ship engine to merchant ships. However, for the active management of pollutants generated on coasts in the future, technologies for fully electric propulsion vessels using batteries during ship operation should be developed for various ship types.



Fig. 5 Pure electric propulsion container ship in China



Fig. 6 Araon (left) and Econuri (right)

Table 4 Registered ship statistics of Korea

Tonne	Total (ship)	Passenger ship	Cargo ship	Oil tanker	Tug-boat	Barge	Etc.
Total	8,953	337	653	768	1,212	1,864	4,119
< 5 t	1,733	8	2	1	3	-	1,719
< 5-20 t	1,337	14	9	26	91	-	1,197
< 20-30 t	738	19	47	48	163	39	422
< 30-50 t	515	10	27	49	161	29	239
< 50-100 t	793	42	35	92	224	129	271
< 100-200 t	948	85	21	135	308	262	137
< 200-300 t	571	43	5	28	204	243	48
< 300-500 t	600	62	14	50	55	374	45
< 500-1,000 t	527	34	19	60	2	394	18
< 1,000-2,000 t	357	4	96	51	1	197	8
< 2,000-5,000 t	396	7	130	107	-	146	6
< 5,000-10,000 t	238	4	106	90	-	29	9
< 10,000-20,000 t	70	5	46	6	-	13	-
< 20,000-50,000 t	67	-	53	8	-	6	-
< 50,000-100,000 t	48	-	37	9	-	2	-
> 100,000 t	15	-	6	8	-	1	-

4. Conversion of Domestic Ships to Electric Propulsion Vessels

4.1 Current Status of Ships in South Korea

Approximately 8,900 registered ships exist in South Korea, and they are classified by use into 337 passenger ships (3.8%), 653 cargo ships (7.3%), 768 oil tankers (8.6%), and 1,212 tug boats (13.6%). The classifications of the registered ships in South Korea by use and tonne are summarized in Table 4. When barges without power are excluded, the sizes of cargo ships and oil tankers are primarily distributed in over 2,000 t, whereas passenger ships and tug boats are primarily distributed in less than 1,000 t (Ministry of Oceans and Fisheries, 2019).

Based on the previous section's analysis results, battery-powered pure electric propulsion vessels require batteries of greater volume and weight as the required power and energy increase. Therefore, it is inefficient to use batteries to operate the main propulsion engines of

vessels sailing the oceans or vessels operating on unspecified routes. However, fully electric propulsion vessels are the most useful eco-friendly solution for ships that do not emit pollutants. Hence, considering the decrease of the battery price and the increase of the energy density in volume and weight through the battery technology development, the possibility of commercialization and expansion of fully battery-powered ships are highly promising. Therefore, it is believed that car ferries interconnecting islands would yield significant eco-friendly effects if they are converted to fully electrified vessels as public transportation operating on designated routes in South Korea.

4.2. Areas Expected to introduce electric propulsion vessels

As stated in the previous section, the ship type for pure electric propulsion vessels should be a car ferry for passengers that periodically operate on a fixed route. South Korea has 162 coastal passenger ships operating in 100 sea routes. As a peninsula surrounded by seas on three sides, South Korea has many small islands, and

Table 5 Registered ship statistics of South Korea Current status of coastal passengers by region in Korea

Region	Busan	Incheon	Yeosu	Masan	Donghae	Gunsan	Mokpo	Pohang	Daesan	Jeju
Car ferry (open space)	-	11	11	16	-	4	59	-	6	-
Car ferry	1	-	2	-	-	-	3	-	-	2
High-speed car ferry	-	2	-	-	-	-	-	1	-	-
High-speed vessel	-	4	-	-	-	1	3	2	-	2
Ultra-high speed vessel	-	1	2	-	4	-	7	3	-	-
General vessel	-	-	5	8	-	-	-	-	3	4
Total	1	18	20	24	4	5	72	6	9	8

coastal passenger ships interconnecting the islands with the land are considered public transportation. Hence, it is believed that when pure electric propulsion vessels are introduced, the effect of technology diffusion will be evident. Considering the maximization of effects arising from fully electrified car ferries and the possibility of mounting battery systems, the introduction of car ferries as a coastal passenger ship is regarded as appropriate. The introduction of fully electrified car ferries in the Mokpo area, where more than 60% of domestic car ferries are operated, will clearly reveal their difference from existing ships and emphasize their eco-friendliness. The current status of coastal passenger ships by region in South Korea are shown in Table 5 (Korea Shipping Association, 2019).

4.3 Suggestion for introduction of removable power supply system for vessels

Fully electric propulsion vessels are one of the most useful eco-friendly vessels that do not emit pollutants during operation. However, due to the high price of batteries, the building cost of a battery-powered ship with the same specifications is approximately twice that of building an engine powered ship. Hence, the initial investment cost will increase significantly, and passenger fares will increase accordingly, owing to the significant burden on shipping companies. Moreover, when batteries are embedded in vessels, because of the difference between the battery replacement life (10 years) and ships' operating life (25 years), an unintended operation loss will most likely occur, causing economic losses to the shipping company.

Removable power supply systems (battery systems) must be developed and supplied to solve such durability and initial investment cost problems. Because removable power supply systems are not installed inside a ship permanently and are replaced every cruising, operation loss due to service life differences can be prevented. After the spread of removable power supply systems is completed, an industry that can effectively operate and maintain ship batteries will emerge. The battery cost can be shared, thereby reducing the initial investment cost. This is expected to provide an opportunity to increase the competitiveness of the Korean coastal shipping industry through the establishment of a new ship battery supply business, similar to

using affordable electricity on land. Furthermore, when this system is constructed, safe ports can be maintained because a high-voltage port infrastructure need not be installed. This can be a solution optimized for battery maintenance through the integrated management of ship batteries (Kim et al., 2019a; Kim et al., 2019b).

It is expected that the fuel cost of a car ferry, which can transport 300 passengers and 40 cars and operate round trips for two hours, will be reduced by approximately 200 million won per year when the removable power supply system instead of marine diesel (Kim. et al., 2019b). This concept is illustrated in Fig. 7.

5. Fully Electrified Car Ferry Design Powered by Removable Power Supply System

Vessels are built and operated based on rules stipulated by the classification society and maritime authorities. The removable power supply system proposed herein has not been applied to the rules of the classification society or maritime authority. This is because it is a new concept in this era of evolving ship fuels. It would be desirable to apply this concept to the rules after a more comprehensive review of safety is performed.

The car ferry was selected as the target vessel in this study because vehicles with a battery system can be easily loaded on the vessel as the removable power supply system. Moreover, the car ferry has not been applied to the international classification society's rules, which are severe to apply to the fully electrified vessel. A roll-on/roll-off type removable power supply system that can move by itself was applied to a fully electrified car ferry in order. This concept of a fully electrified car ferry with removable battery systems can give a technical advantage to overcome environmental weaknesses like big tidal differences and frequent typhoon occurrence to South Korea and other regions having similar coastal environments. Furthermore, this concept can achieve economic feasibility in the initial investment cost for fully electrified vessels. The principal dimensions of the vessel are outlined in Table 6. The designed fully electrified car ferry can transport approximately 100 passengers and more than 20 passenger cars, has a power capacity exceeding 1.6 MWh, and can operate for approximately 2 hr at the standard speed of 10 kn (5.144 m/s).

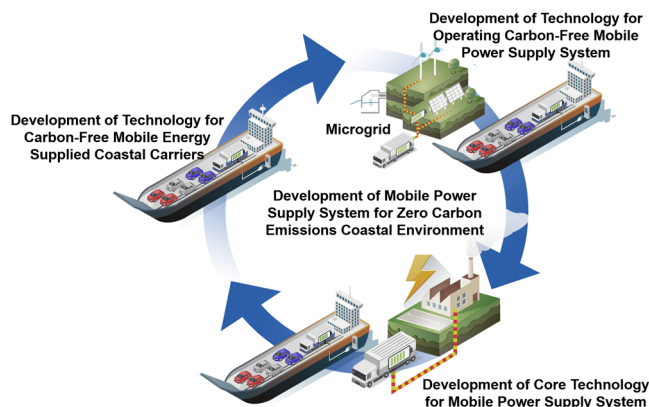


Fig. 7 Concept of fully electrified ferry for passengers and cars

Table 6 Principal dimensions of a fully electrified car ferry

Category	Unit	Specification
Length overall (LOA)	m	58.6
Length between perpendiculars (LBP)	m	49.0
Breadth	m	13.0
Depth	m	2.5
Draft	m	1.65
Design speed	km/h	29
Passengers	persons	120
Cars	units	20

Table 7 Design variables for removable power supply system

System	Category	Unit	Specification
Power supply system	Number	set	2
	Size	m	6.1 m container specification
	Weight	t	< 12
	Power capacity	kWh	800
	Output reference voltage	Vdc	780
	Output voltage range	Vdc	650-900
Power transportation vehicle	Reference /maximum voltage	A	350/450
	Length	m	< 10
	Load weight	t	12
	Fuel usage		Eco-friendly fuel (CNG)

The roll-on/roll-off type removable power supply system must be equipped with a secondary battery, and a technology that ensures stability during vessel movement must be applied. The removable power supply system is designed as a self-moving system equipped with various safety systems; battery management system (BMS), cell anomaly detection system, thermal management system through

air-conditioning, and battery thermal runaway limit system. Furthermore, the system will be designed based on the standardized ISO (the International Organization for Standardization) container size of 6 m to account for future scalability. The main design variables of the removable power supply system are outlined in Table 7.

The fully electrified car ferry was designed to locate and safely fasten the roll-on/roll-off-type removable power supply system in a specified space in the vessel. Its layout was designed so that a removable power supply system can be placed separately from the passenger zone to enhance passenger safety and prevent secondary fire damage by installing additional fire extinguishing equipment. The general arrangement of the fully electrified car ferry with a removable power supply system is shown in Fig. 8.

The general arrangement shows that, unlike existing vessels, two removable power supply systems are located on the deck of the vessel, causing a change in weight by approximately 30 t; this results in a change in the vessel's center of gravity.

The car ferry's seakeeping performance was analyzed to analyze the effects of such a change in the center of gravity on the vessel's behaviors. It was assumed that the removable power supply system was installed on the deck or at the bottom of the vessel. The resultant change in the center of gravity was assumed to be approximately 10 cm. The lines and wave spectrum used in the analysis of the seakeeping performance are shown in Figs. 9–10.

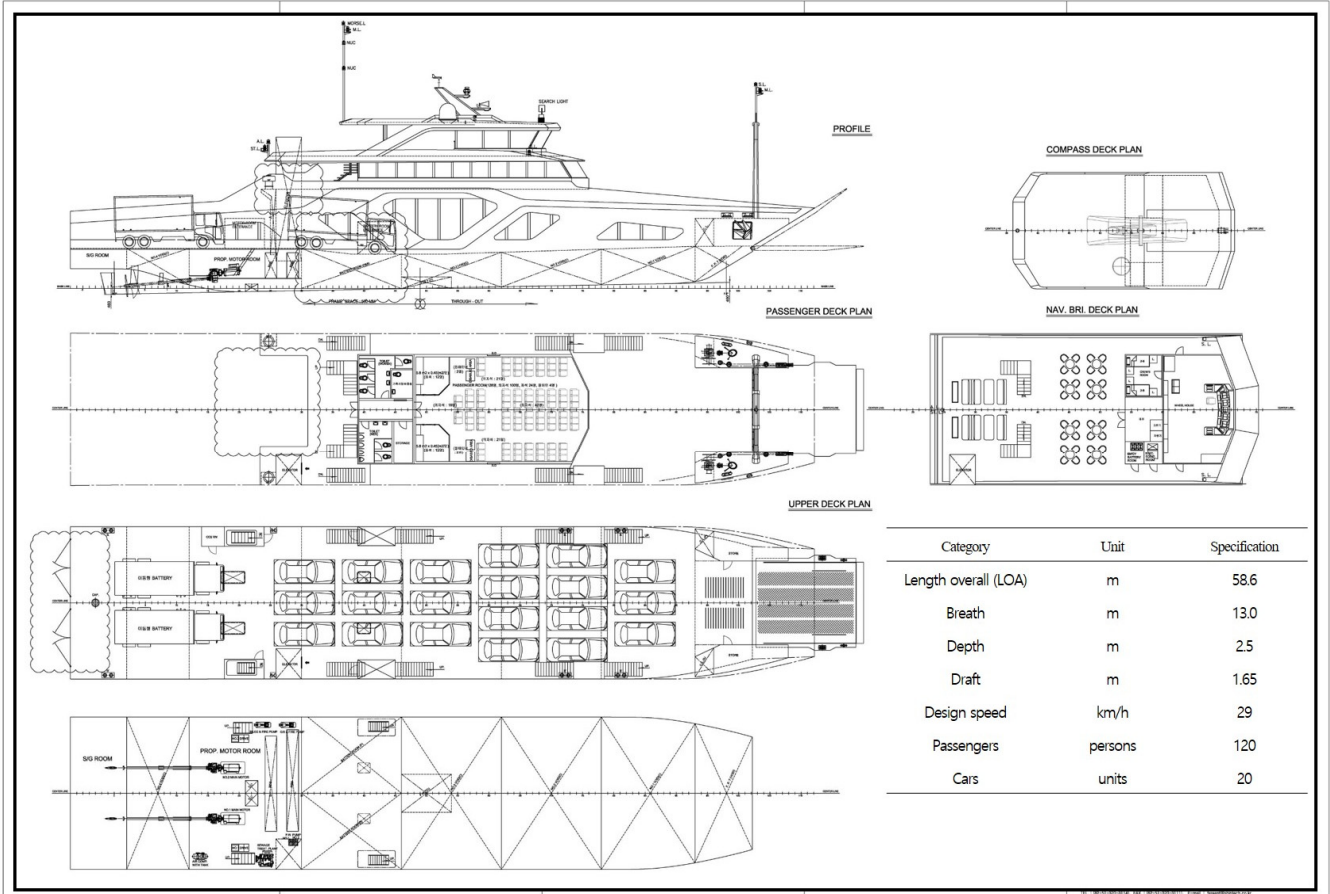


Fig. 8 General arrangement of a fully electrified car ferry

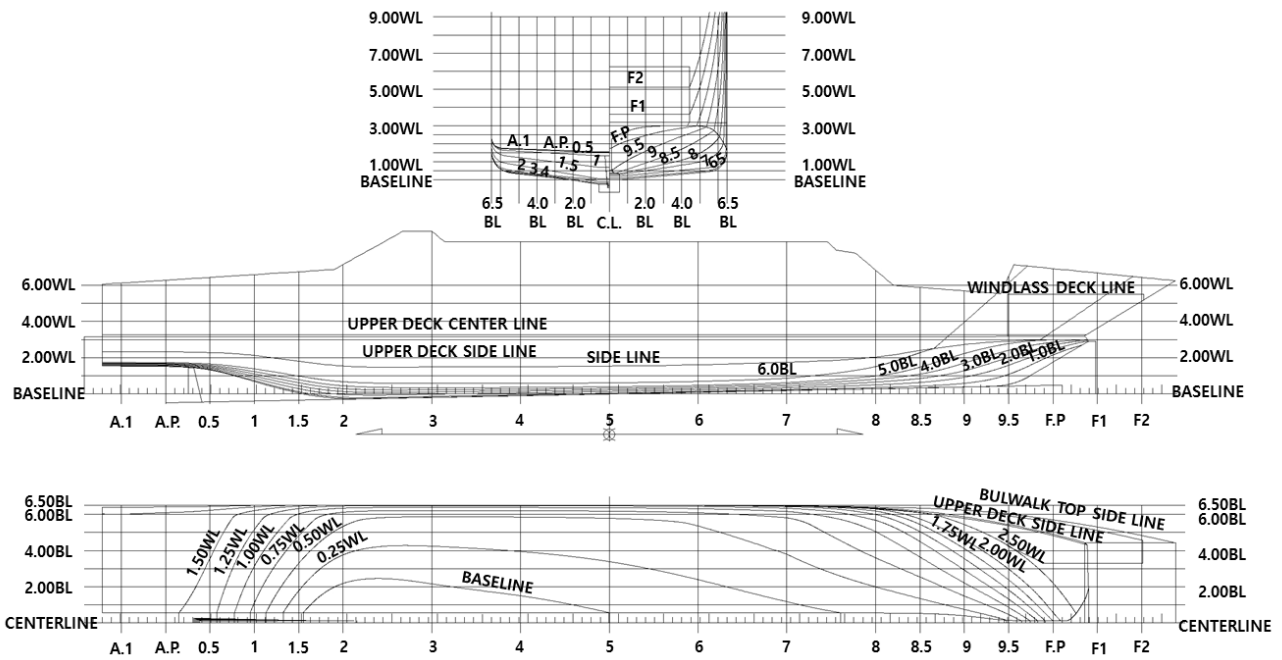


Fig. 9 Lines of a fully electrified car ferry

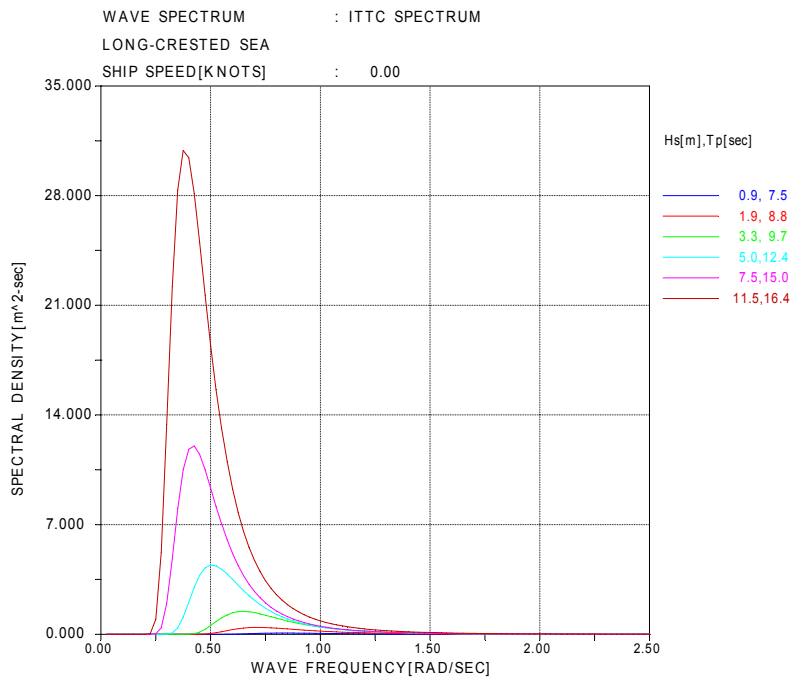


Fig. 10 Wave spectrum

An analysis of the change in behavior characteristics due to the change in the removable power supply system's position indicated that the behavioral changes due to the change in the center of gravity were insignificant. Furthermore, the behavior characteristics were determined by adding the ship speed to analyze the behavioral change characteristics at the ship's reference speed to be developed. The ship motion response amplitude operator (RAO) graphs based on the change in the center of gravity are shown in Fig. 11, and the changes in heave, pitch, and roll based on the ship speed are shown in Fig. 12.

The analysis result confirmed that the car ferry's behavior characteristics for guaranteeing the safety of passengers exhibited insignificant differences, based on the change in the location of the removable power supply system. Furthermore, ship safety is ensured if the removable power supply system is fastened appropriately.

The safety of the removable power supply system has not been proven because it is a new concept. Ships are characterized by relatively high safety standards and high entry barriers due to

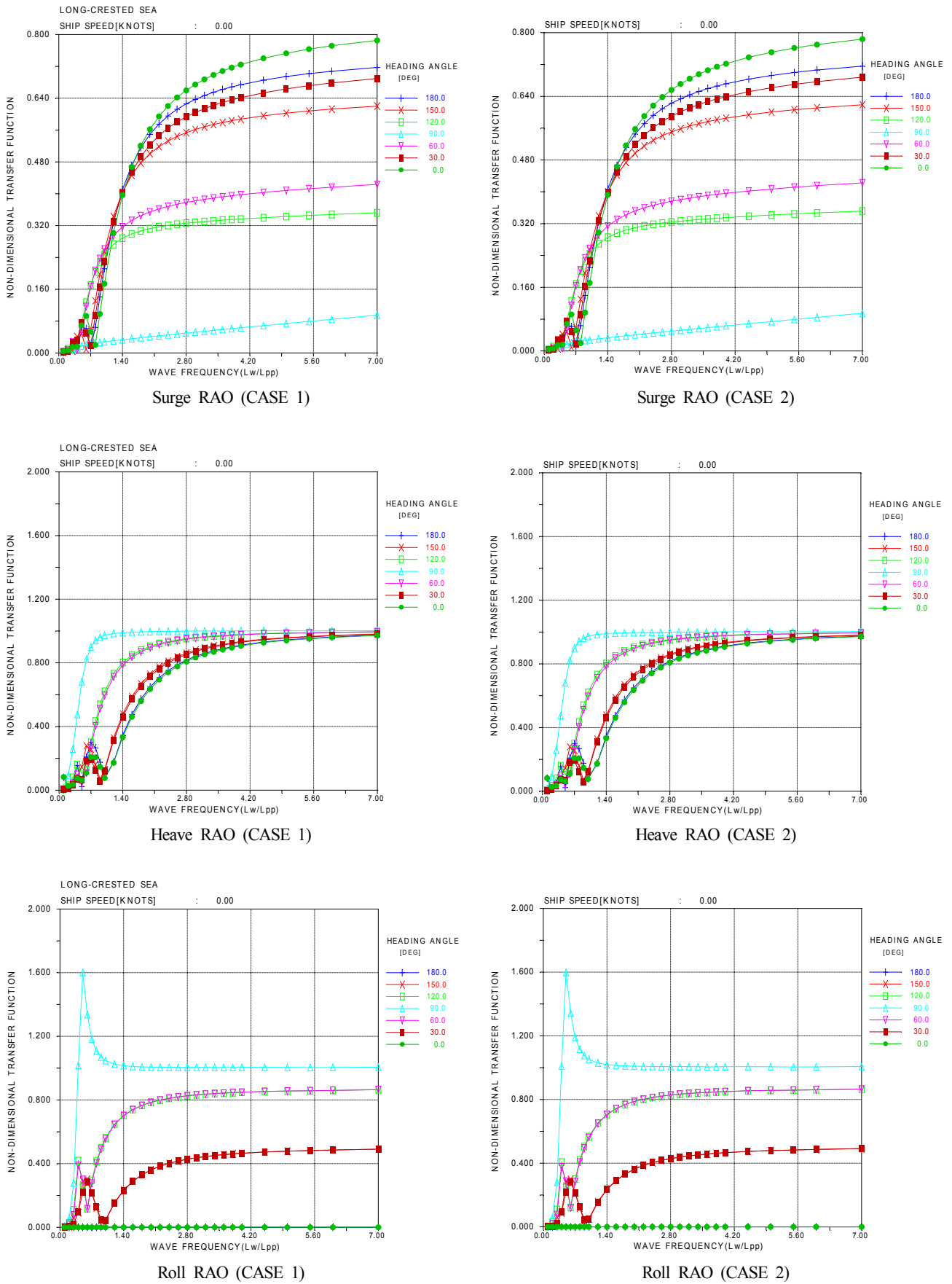


Fig. 11 Results of analysis of ship motion performance by conditions (change of center of gravity)

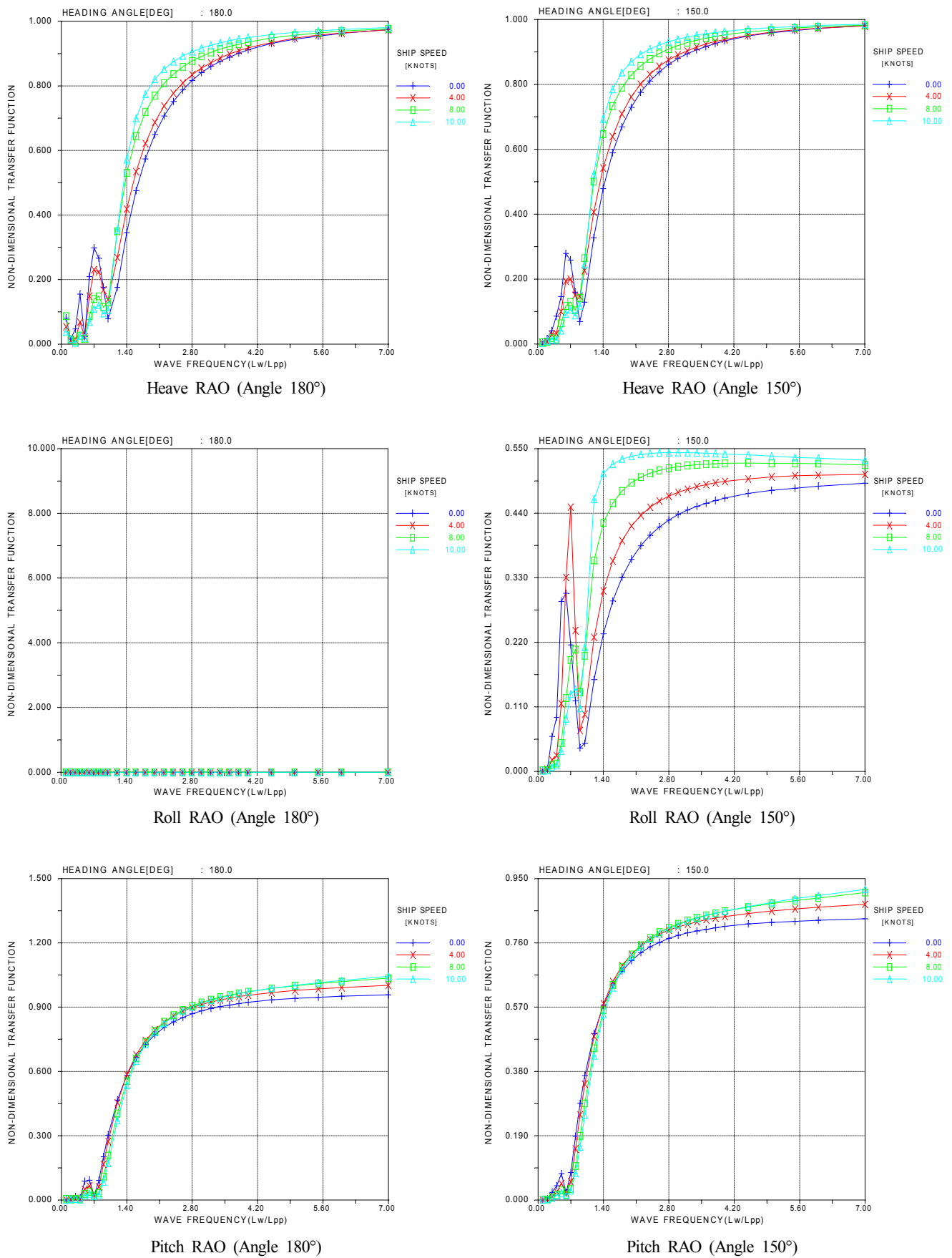


Fig. 12 Results of analysis of ship motion performance per speed (change of angle)

large-scale human damage and significant environmental effects due to accidents. The safety of the fully electrified car ferry developed in this study will be guaranteed through risk analysis. The best measures will be implemented, such as fire extinguishing and waterproofing systems for passenger safety.

6. Future Plans and Prospects

In the global trend of environmental protection and environmental preservation, fossil fuel has to be replaced by alternative fuels for shipping and shipbuilding industries according to GHG reduction strategy from IMO. In this study, the coastal shipping characteristics of South Korea were investigated, and the characteristics of emerging eco-friendly fuels were analyzed. Subsequently, a conceptual design of a fully electrified car ferry was presented for the conversion of coastal passenger ships to eco-friendly ships. The fully electrified car ferry to be developed in the future is the first of its kind. Hence, no relevant rules exist from the classification society, and hence appropriate preparations are required. To promote eco-friendliness in the shipping industry and encourage the introduction of new technologies, we plan to conduct further investigations such that safety will be secured and fully electrified car ferries can be developed and recognized by the classification society and the port authorities. An export model of this ship will be developed and is expected to be exported to neighboring countries with similar environments to activate the shipbuilding market for small and medium businesses in South Korea.

In the future, we plan to estimate the resistance of vessels through model tests based on concepts and basic designs as well as enable new-concept ships to operate safely in our country's territorial waters through risk analysis.

Funding

This study was conducted under the support of the "The development of a fully electrified car ferry and a removable power supply system (20200469-01, PMS4420)," which is a national R&D project of the Ministry of Oceans and Fisheries. Additionally, we would like to express our sincere gratitude for the research fund granted.

References

- Kim, J.H., Kim, J.H., & Lee, J.Y. (2018). IMO's Initial Strategies for Reducing Ship Greenhouse Gases(in KOREA). *International Journal of naval architecture and ocean engineering*, 55(2), 24–27. http://www.snak.or.kr/02_journal/journal01.htm
- Oh, K.G., Moon, B.Y., & Lee, K.Y. (2016). Performance Evaluation

and Technical Development of Eco-environmental Photovoltaic Leisure Ship with Sail-controlling Device With Respect to Solar-Hybrid Generating System. *Journal of Ocean Engineering and Technology*, 30(1), 57–67. <https://doi.org/10.5574/KSOE2016.30.1.057>

- Jeong, Y.-K., Lee, D.K., Jeong, U.-C., Ryu, C., Oh, D., & Shin, J.G. (2013). Study on Operating Performance Estimation Process of Electric Propulsion Systems for 2.5 Displacement Ton Class Catamaran. *Journal of Ocean Engineering and Technology*, 27(5), 1–9. <https://doi.org/10.5574/KSOE2013.27.5.001>
- Moon, B.Y., Shin, K.H., & Lee, K.Y. (2018). Performance Evaluating of 20 HP Outboard Motot in Consideration of Driving System Applied to Electric-Propulsion Boat. *Journal of Ocean Engineering and Technology*, 32(6), 518–526. <https://doi.org/10.26748/KSOE.2018.32.6.518>
- Kim, Y.-S., Shim, H.-W., & Jung, S.-J. (2019a). A Concept Study On and All Electrified Passenger Car Ferry and Its Removable Electric Power Supply System. *Proceedings of Fall Conference of Ocean Engineering and Technology*, Gimhae, Korea, 83–85.
- Kim, Y.-S., Shim, H.-W., Kang, H.-J., & Jung, S.-J. (2019b). A Concept Study of an All Electrified Passenger Car Ferry Based on Movable Power Supply System. *Proceedings of the Korean Society for Power System Engineering*, Jeju, Korea, 41–42.
- Ministry of Oceans and Fisheries. (2019). Registered Ship Statistics. Retrieved December 2019 from <http://www.mof.go.kr/statPortal/cate/partStat.do>
- Korea Energy Agency. (2017). Norway to Operate the World's First 100% Electric Ship. Retrieved July 2017 from https://blog.naver.com/kea_sese/221061203587
- Korea Shipping Association. (2019). *Statistical Year book of Coastal Shipping(2019)*. Seoul, Korea: Korea Shipping Association.
- Lee, I.-A. (2018). Lack of Response to Eco-friendly Facilities for Foreign Ships of Nationality. Retrieved June 2018 from <http://m.monthlymaritimekorea.com/news/articleView.html?id=xno22445>

Author ORCIDs

Author name	ORCID
Hong, Jang Pyo	0000-0002-5054-2110
Kim, Young-Shik	0000-0001-5673-6314
Shim, Hyung-Won	0000-0002-7314-2881
Kang, Hee-jin	0000-0002-8241-3751
Kim, Yun-Ho	0000-0003-1465-5844
Kim, Gyu Bum	0000-0001-9960-4960
Cho, Seongpil	0000-0002-6613-4592

Numerical Study to Evaluate Course-Keeping Ability in Regular Waves Using Weather Vaning Simulation

In-Tae Kim¹ and Sang-Hyun Kim²

¹Doctor's course, Department of Naval Architecture and Ocean Engineering, Inha University, Incheon, Korea

²Professor, Department of Naval Architecture and Ocean Engineering, Inha University, Incheon, Korea

KEY WORDS: Weather vaning, Manoeuvrability, Wave force, CFD, Regular wave

ABSTRACT: Since the introduction of the mandatory energy efficiency design index (EEDI), several studies have been conducted on the maneuverability of waves owing to the decrease in engine power. However, most studies have used the mean wave force during a single cycle to evaluate maneuverability and investigated the turning performance. In this study, we calculated the external force in accordance with the angle of incidence of the wave width and wavelengths encountered by KVLCC2 (KRISO very large crude-oil carrier) operating at low speeds in regular waves using computational fluid dynamics (CFD). We compare the model test results with those published in other papers. Based on the external force calculated using CFD, an external force that varies according to the phase of the wave that meets the hull was derived, and based on the derived external force and MMG control simulation, a maneuvering simulation model was constructed. Using this method, a weather vaning simulation was performed in regular waves to evaluate the course-keeping ability of KVLCC2 in waves. The results confirmed that there was a difference in the operating trajectory according to the wavelength and phase of the waves encountered.

1. Introduction

With increasing environmental concerns worldwide, the Maritime Environment Protection Committee (MEPC) of the International Maritime Organization (IMO) introduced the mandatory energy efficiency design index (EEDI) to regulate greenhouse gas emissions from ships. However, there have been cases where the EEDI is satisfied by reducing the engine power of the ship, which may result in insufficient thrust required to maintain maneuverability in adverse conditions (SHOPERA, 2016). Therefore, the MEPC introduced guidelines for the minimum horsepower required to maintain maneuverability in adverse conditions (MEPC, 2013); these guidelines are still under discussion. Since studying maneuverability in waves was selected as the main task of the 28th International Towing Tank Conference (ITTC) maneuvering committee, there has been an increased need for research on methods for analyzing maneuverability in waves. Accordingly, studies estimating the maneuverability in waves are being conducted internationally by the joint European projects SHOPERA (SHOPERA, 2016) and SIMMAN (SIMMAN, 2020).

Numerous related studies have been conducted on predicting maneuverability in waves. Not only is there additional resistance caused by the waves, but forces form swaying oscillations or yaw motions that act on a ship as external forces. Various studies have been conducted to reflect the influence of these external forces in a mathematical model of the maneuvering motion. Yasukawa and Faizul (2006) experimentally determined the average wave force on SR108 operating in oblique sea conditions. Xu et al. (2007) performed a pure sway test in waves and proposed a method of testing the planar motion mechanism (PMM) in waves by analyzing the results. Cura-Hochbaum and Uharek (2016) conducted a study to reflect the influence of waves by pre-calculating the wave forces from various angles, digitizing them, and reflecting them in a simulation.

Yasukawa et al. (2018) examined the effectiveness of the zero-speed three-dimensional panel method (3DPM) and the strip theory-based Kochin-function method (SKFM) in calculating the wave force by comparing the results with experimental ones. Moreover, the estimation of the turning motion in irregular waves was validated by comparing the simulation and model test results using the wave force in irregular waves obtained using the 3DPM and SKFM. Seo et al.

Received 23 June 2020, revised 10 December 2020, accepted 14 December 2020

Corresponding author Sang-Hyun Kim: +82-32-860-7344, kimsh@inha.ac.kr

© 2021, The Korean Society of Ocean Engineers

This is an open access article distributed under the terms of the creative commons attribution non-commercial license (<http://creativecommons.org/licenses/by-nc/4.0>) which permits unrestricted non-commercial use, distribution, and reproduction in any medium, provided the original work is properly cited.

(2018) used a method of substituting the wave drift force as the external force in the maneuvering equation of motion. To this end, the advancing speed, the direction of the incident wave, and the wave force according to the wave length were calculated in advance and converted into a database to extract values suitable for simulation. In addition, the effect of the wave drifting force on the turning trajectory and turning parameters was studied based on a sensitivity analysis of the wave drift force. Additionally, a study was conducted to confirm the change in the maneuvering characteristics in waves using a free running model test rather than the mathematical model of maneuvering motion. Sprenger et al. (2017) observed the difference in the additional resistance among waves according to the depth by changing the depth and wave length for a tanker line and a container ship and examined the changes in the wave drifting force acting on the hull according to the water depth in oblique sea conditions. A free running model test was performed in waves to examine the change in the trajectory during a turning test according to the direction of the incident wave. Kim et al. (2019) evaluated the turning characteristics of KVLCC2 (KRISO very large crude-oil carrier 2) by performing a free running model test in regular waves. The free running model test was performed by changing the wave incidence angle and wave length, and the results were compared with those showing the trajectory of the free running model test in calm water.

As described above, many studies have been conducted to estimate the maneuverability in waves by using the wave force in the mathematical model of maneuvering motion in waves. However, most studies have evaluated the influence of the wave force using an average value and have not considered the change in external force according to the phase of the wave encountered by the ship. Additionally, most studies have focused on the change in the turning trajectory; however, weather vaning must be investigated to maintain the maneuverability of the ship in adverse conditions. Weather vaning is a movement in which the bow faces the direction of an incident current, wave, etc., and it plays an important role in preventing overturning due to the rolling motions in waves.

This fundamental study focuses on how to evaluate ship-handling safety in adverse conditions, in which the course-keeping ability of the ship in regular waves has not been evaluated. For this, the external force of the wave for the forward velocity was calculated using computational fluid dynamics (CFD) for an incident angle of 15° to 45° from the bow wave. The calculated external wave force was compared with model test results published in other studies. In addition, a simulation of the maneuvering motion was performed using the calculated wave force and maneuvering hydrodynamic coefficients published in previous studies. At this time, the wave conditions of regular waves were determined by referring to the revised guidelines of the MEPC 71st draft (MEPC, 2017). Simulations for the course-keeping ability evaluation were also performed in head sea and oblique sea conditions at an angle of 30° in the forward direction as specified by the MEPC guidelines to examine the course-keeping ability through weather vaning and the heel angle during the simulation.

2. Maneuvering Equation of Motion

2.1 Coordinate Systems

The coordinate systems used in this study are the Earth-Centered-Earth-Fixed (ECEF) coordinate system and the body-fixed coordinate system, as shown in Fig. 1. The origin of the x - and y -axes of the body-fixed coordinate system is taken as the center of the hull, and the bow direction of the ship is defined as the x axis; the direction perpendicular to the starboard is defined as the y axis; and the direction toward the bottom of the ship is defined as the positive (+) direction of the z axis. The spatial coordinate system defined the initial travel direction of the ship as the x direction (Kim, et al., 2016).

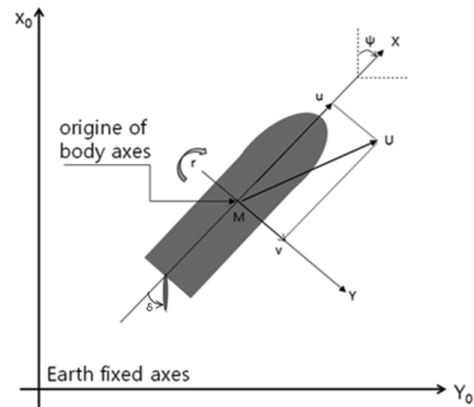


Fig. 1 Coordinate system

2.2 Mathematical Model for the Maneuvering Motion in Waves

In this study, as shown in Eq. (1), the influence of waves derived by numerical calculations was considered as an external force on the mathematical modeling group (MMG) type mathematical model used for the analysis of turning performance in calm water to build a simulation model of turning in regular waves. The left side represents the maneuvering equation of motion for the surge force, sway force, and yaw moment, in order, and the right side represents the hydrodynamic forces by the hull, rudder, propeller, and external forces. The m on the left side denotes the mass of the ship; I_z denotes the moment of inertia; u denotes the longitudinal velocity; v denotes the lateral velocity; r denotes the bow rotation angular velocity; and the point marked on each velocity denotes the acceleration. The X on the left side denotes the longitudinal force; Y denotes the lateral force; N denotes the yaw moment; and the point marked on each velocity denotes the acceleration; the subscripts H , R , and P denote the hull, rudder, and propeller, respectively, and the subscript W denotes the wave force. Here, the wave force is defined as the difference between the hydrodynamic force acting on the hull in waves and in calm water.

$$\begin{aligned}
 m'(\dot{u}' - v'r' - x_G'r'^2) &= X_H' + X_P' + X_R' + X_W' \\
 m'(\dot{v}' + u'r' + x_G'r'^2) &= Y_H' + Y_R' + Y_W' \\
 I_z'r' + m'x_G'(\dot{v}' + u'r') &= N_H' + N_R' + N_W'
 \end{aligned} \tag{1}$$

Table 1 Hydrodynamic force coefficients used in simulations

R'_0	0.022	Y'_v	-0.315	N'_v	-0.137
X'_{vv}	-0.040	Y'_r	0.083	N'_r	-0.049
X'_{vr}	0.002	Y'_{vvv}	-1.607	N'_{vvv}	-0.030
X'_{rr}	0.011	Y'_{vvr}	0.379	N'_{vvr}	-0.294
X'_{vvvv}	0.771	Y'_{vrr}	-0.391	N'_{vrr}	0.055
		Y'_{rrr}	0.008	N'_{rrr}	-0.013

The hydrodynamic force acting on the hull is expressed as Eq. (2), and it is nondimensionalized using the density, length between perpendiculars, draft, and advancing speed, as given in Eq. (3). Both the influence of plane motion and the influence of the moment acting on the hull according to the heel angle are considered in the hydrodynamic force acting on the hull. The hydrodynamic coefficients used to calculate the hydrodynamic force acting on the hull are shown in Table 1.

$$\begin{aligned}
 X'_H &= -R'_0 + X'_{vv}v'^2 + X'_{vr}v'r' + X'_{rr}r'^2 + X'_{vvvv}v'^4 \\
 Y'_H &= Y'_v v' + Y'_{vvv}v'^3 + Y'_r r' + Y'_{rrr}r'^3 + Y'_{vvr}v'r'^2 + Y'_{vrr}v'^2 r' \quad (2) \\
 N'_H &= N'_v v' + N'_{vvv}v'^3 + N'_r r' + N'_{rrr}r'^3 + N'_{vrr}v'r'^2 + N'_{vvr}v'^2 r' + N'_\phi \phi \\
 X' &= X/0.5\rho L_{pp} TU^2 \\
 Y' &= Y/0.5\rho L_{pp} TU^2 \\
 N' &= N/0.5\rho L_{pp}^2 TU^2
 \end{aligned} \quad (3)$$

The hydrodynamic force caused by the propeller was considered as in Eq. (4), and the hydrodynamic force caused by the rudder was reflected using Eqs. (5) and (6). The flow velocity flowing into the rudder in Eq. (6) is reflected by the difference between the flow velocities flowing into the rudder in waves and in calm water using the value obtained from the calculation of self-propulsion.

$$X_p = (1 - t_p) T \quad (4)$$

$$\begin{aligned}
 X_R &= -(1 - t_R) F_N \sin \delta \\
 Y_R &= -(1 + a_H) F_N \cos \delta
 \end{aligned} \quad (5)$$

$$N_R = -(x_R + a_H x_H) F_N \cos \delta$$

$$F_N = (1/2) \rho A_R (U_R^2 f_a \sin \alpha_R)$$

$$U_R = \sqrt{u_R^2 + v_R^2} \quad (6)$$

$$u_R = \sqrt{\frac{A_{RP}}{A_R} u_{RP}^2 + \frac{A_{R0}}{A_R} u_{R0}^2} = \sqrt{\eta u_{RPW}^2 + (1 - \eta) u_{R0}^2}$$

Eq. (7) is the equation of the rolling motion in waves. Each of the coefficients employed is expressed as Eq. (8) using the equation for estimating the roll damping coefficient published in a study by Seok et al. (2016).

$$K_{We} = (I_{44} + A_{44}) \ddot{\Phi} + B_{44} \dot{\Phi} + C_{44} \Phi \quad (7)$$

$$I_{44} = k_{xx}^2 \nabla \rho, \quad A_{44} = 0.3 I_{44}$$

$$B_{44} = \frac{\beta_{44}}{2\sqrt{C_{44}(I_{44} + A_{44})}}, \quad \beta_{44} = \frac{\ln(\text{Grad})}{2\pi} \quad (8)$$

$$C_{44} = GM \nabla \rho g$$

The meanings of the symbols used in the above Eqs. (4)–(8) are shown in Table 2 below.

Table 2 List of symbol

Symbols	Mean	Symbols	Mean
A_R	Profile area of movable part of mariner rudder	A_{RP}	Rudder area where propeller slip stream hits
A_{R0}	Rudder area where propeller slip stream do not hits	F_N	Rudder normal force
T	Propeller thrust	U_R	Rudder inflow velocity
u_R	longitudinal velocity component to rudder	u_{RPw}	Inflow velocity to rudder in waves
v_R	Lateral velocity component to rudder	t_p	Thrust deduction factor
t_R	Steering resistance deduction factor	η	Ratio of propeller diameter to rudder span
α_H	Rudder force increase factor	α_R	Effective inflow angle to rudder
x_H	Longitudinal coordinate of acting point of the additional lateral force	f_a	Rudder lift gradient coefficient
K_{We}	Roll moment	k_{xx}	Roll moment of inertia
β_{44}	Non-dimensional roll damping coefficient	Grad	Free roll decay damping ratio

3. Conditions for Wave Force Calculation

3.1 Target Ship

KVLCC2 (SIMMAN, 2008) was selected as the target ship, and numerical calculations were performed on a 1:58 scale. The main specifications of the model ship are shown in Table 3. The testing with the hull alone at the speed of $Fn = 0.037$ was based on the speed in adverse conditions proposed by the MEPC 65th interim guideline.

Table 3 Principal dimensions of KVLCC2 model ship

Item	Value
Scale ratio	1/58
Length between perpendiculars (L_{pp})	5.5172 m
Breadth	1 m
Draft	0.3586 m
Displacement (in fresh water)	1,599 kg
Froude number (Fn)	0.037

3.2 Conditions for Virtual Captive Model Test

This study used the commercial CFD software STAR-CCM+, which was proven to be useful in the study by Simonsen et al. (2012). The computational domain that was formed to perform numerical calculations is as shown in Fig. 2. From the midship, it was set as 1.5 times the length of the hull toward the inlet boundary, 2.5 times the length of the hull toward the outlet boundary, twice the length of the hull toward the side boundaries, the length of the hull toward the top boundary, and 1.5 times the length of the hull toward the bottom boundary.

To create the grid, the trimmed mesh and prism layer techniques provided by STAR-CCM+ were used. The size of the trimmer grid was set to be relatively small in the free water surface and around the hull, and it was relatively large in the simple flow region. The prism layer technique was used to accurately calculate the prism layer flow on the hull surface, and a total of four prism layers were created from the hull surface. The thickness of the first prism layer grid from the hull surface was defined with the value and was within the range of 40 to 70. Dynamic fluid body interaction (DFBI) and overset mesh techniques were used to consider the effect of changes in posture according to the

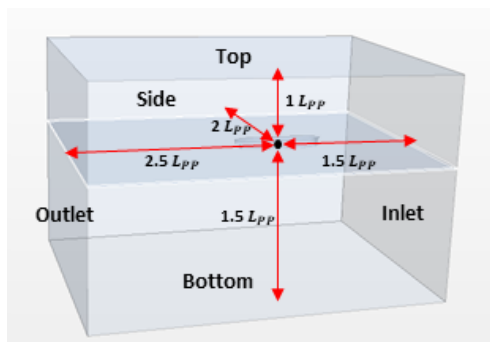


Fig. 2 Computational domain

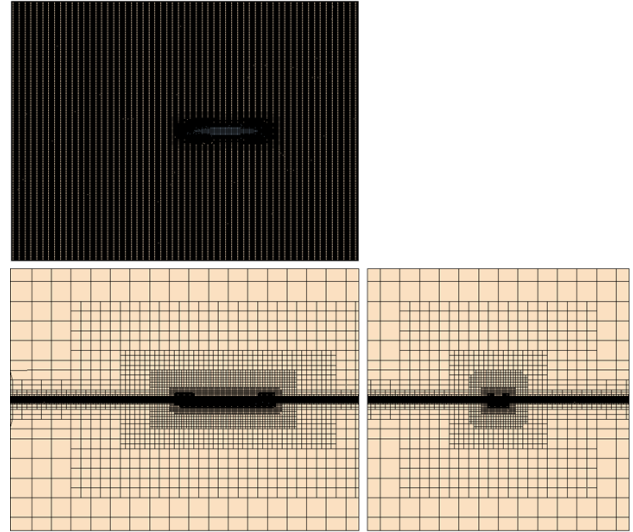


Fig. 3 Volume mesh

Table 4 Boundary condition

	Boundary condition
Inlet	Velocity inlet
Outlet	Velocity inlet
Side	Velocity inlet
Top	Pressure outlet
Ship	Wall
Bottom	Velocity inlet

wave, and as shown in Fig. 3 a total of approximately 4.3 to 5.2 million grids were generated.

Free water surface was considered by using the volume of fluid (VOF) technique, and the realizable $k-\epsilon$ (RKE) model was used as the turbulence model to ensure the stability and efficiency of numerical calculations. Unsteady condition analysis was performed for the dynamic analysis of the hull. A first-order implicit method was used for temporal discretization, and a second-order up-wind scheme was used for spatial discretization. The boundary conditions for the CFD calculation used in this study are shown in Table 4.

Infinite depth was configured by setting the inlet boundary of the computational domain as a velocity inlet, the top boundary as a pressure outlet, and the outlet, bottom, and side boundaries as velocity inlets. In addition, the wave forcing feature provided by STAR-CCM+ was applied to the section of one time of the length between perpendiculars from each of the inlet, outlet, left and right boundaries to minimize the influence of reflected waves.

3.3 Verification of Wave Generation

The wave conditions used in this study are shown in Table 5 below. For the regular waves used in this study, the wave height was determined by setting the wave slope to $H/\lambda = 0.02$ at $\lambda/L_{pp} = 0.5, 1.0$; and the wave condition was determined by setting the wave height was determined by setting the wave slope to

Table 5 Wave condition

	Boundary condition
Wave length	$\lambda/L_{PP} = 0.5, 1.0, 1.6$
Wave height	$\lambda/L_{PP} = 0.5, 1.0 - H/\lambda = 0.02$ $\lambda/L_{PP} = 1.6 - H/\lambda = 0.01$
Incident angle	180° (Head sea), 165°, 150°, 135°
Wave frequency	$\lambda/L_{PP} = 0.5 - 4.197\text{rad/s}$ $\lambda/L_{PP} = 1.0 - 2.967\text{rad/s}$ $\lambda/L_{PP} = 1.6 - 2.346\text{rad/s}$

$H/\lambda = 0.01$ at $\lambda/L_{PP} = 1.6$, according to the ITTC recommended procedure and guideline (ITTC, 2014). The wave incident angle to be used in the maneuver simulation in waves was determined by employing the weather vaning wave incident angle (30° from the bow wave) proposed in the 71st draft revised guidelines of MEPC.

In order to verify the waves generated using CFD, verification was performed using theoretical waves. The wave was created using the Stokes order wave theory, the wave length of the incident wave used for verification was $\lambda/L_{PP} = 1.0$ the wave height was $H/\lambda = 0.02$, and the period at this time was about 1.31 s for the model ship. The grid conditions used to generate waves were set based on the study by Kim. (2019), with 60 gratings per wave length in the x direction, 20 gratings per wave height in the z direction, and the aspect ratio of the grid in the x-direction to the grid in the y-direction is 1:4. Wave calculations were performed for a total of 10 cycles with 20 internal iterations. The time interval was designated to allow 500 calculations per wave cycle. Fig. 4 represents the difference from the theoretical waves generated by CFD for 10 cycles, and Table 6 shows the difference from the theoretical crest and trough values for five cycles. The generated waves showed an error of -4.33% from the theoretical waves at the wave crest, and -4.02% at the trough.

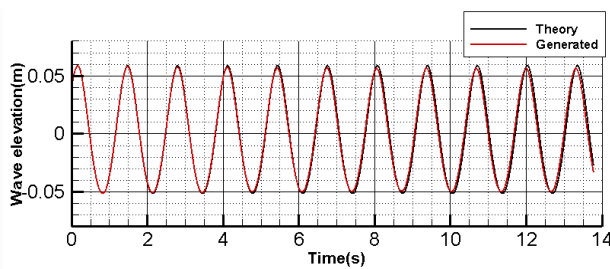

Fig. 4 Comparison of Stokes 5th order wave and generated wave ($\lambda/L_{PP} = 1.0, H/\lambda = 0.02$)

Table 6 Difference between generated wave and Stokes 5th order wave

	Stokes 5 th wave elevation (m)		
	Theory	Generated	
Crest	0.05862	0.056083	-4.33%
Trough	-0.05158	-0.04951	-4.02%

3.4 Review of Grid Convergence

Prior to calculating the wave force acting on the hull in regular waves, a convergence review was performed on the generated grid system. Grid convergence was reviewed with a grid strain of according to the ITTC recommended procedure and guideline (ITTC, 1999). The size of the grids corresponding to the fine, medium, and coarse grids is shown in Table 7 below. Surge, sway force and yaw moment, and convergence ratio for each grid are shown in Fig. 5 and Table 8.

Table 7 Information related to different types of grids for convergence test

Grid no.	Grid density	Base size	Number of cells	Number of grid / wave length	Number of grid / wave height
1	Coarse	0.020	3.18M	48	16
2	Medium	0.018	3.97M	53	18
3	Fine	0.016	5.01M	60	20

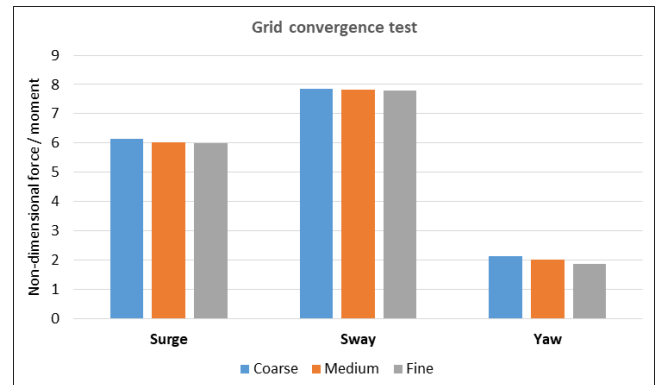

Fig. 5 Non-dimensional surge, sway force and yaw moment

Table 8 Predicted convergence ratio

	ϵ_{21}	ϵ_{32}	R_G
Surge force'	0.083	0.019	0.23
Sway force'	0.047	0.035	0.74
Yaw moment'	0.11	0.11	0.94

As a result of examining the grid convergence, the calculated result values converge as the number of grids increases. In this study, numerical calculations were performed on the forces and moment acting on the hull in regular waves based on the grid size applied to the densest grid system.

4. Results of Wave Force Calculation

Fig. 6 shows the average value of the wave force according to the angle of incidence for each wave length obtained by CFD calculation. Except for the resistance generated during operation in calm water, only the external force corresponding to the additional resistance was expressed as the surge force, and each of the forces and moment was

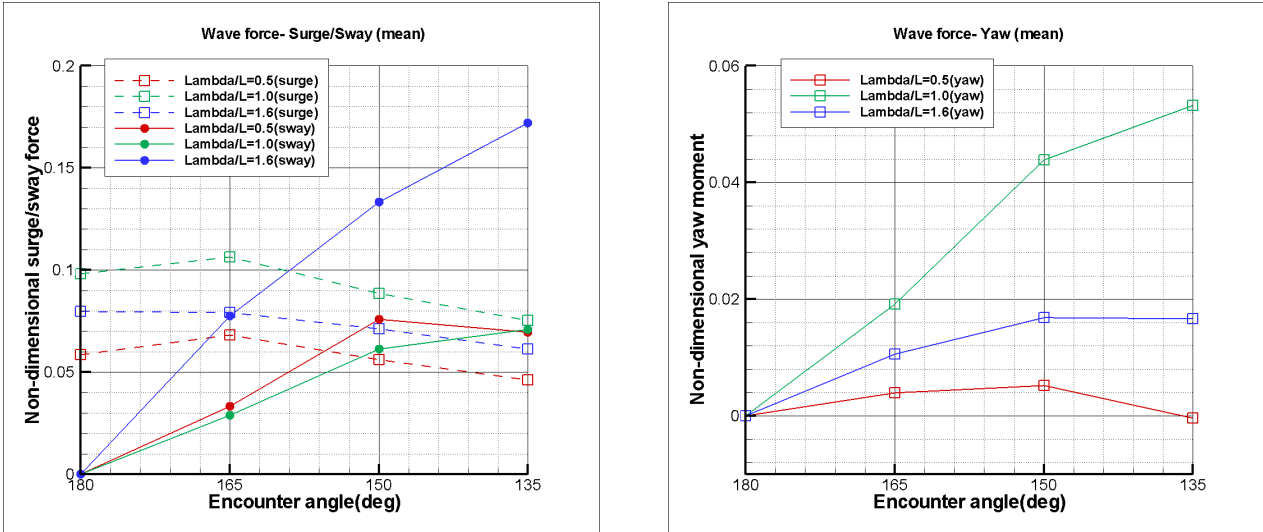


Fig. 6 Wave force according to wave length

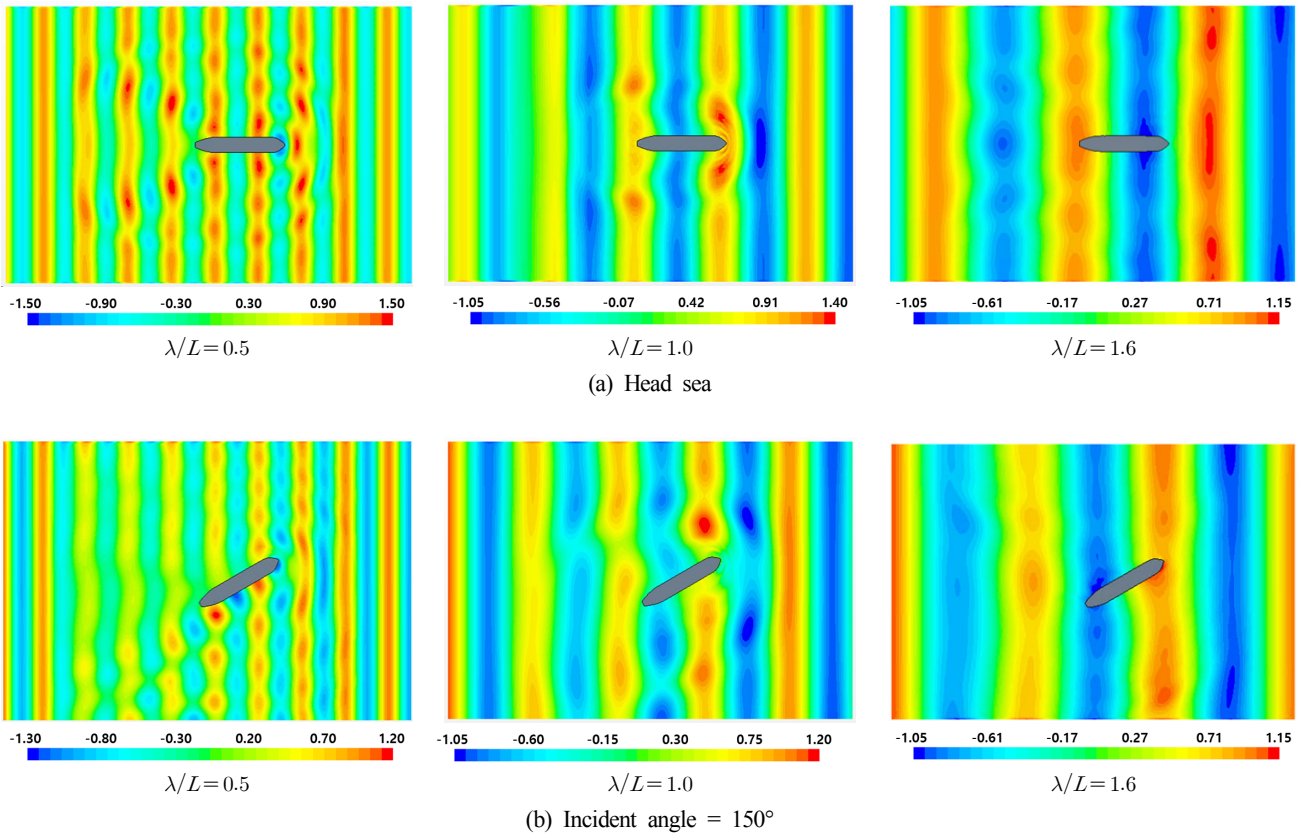


Fig. 7 Free surface distribution at head sea / incident angle 150°

made nondimensionalized using Eq. (3). The surge force was relatively low with a low wave height at $\lambda/L = 0.5$, the sway force was the highest with a long wave length, and the yaw moment was the greatest at $\lambda/L = 1.0$.

Fig. 7 shows the wave shape around the hull calculated at angles of incidence of 180° and 150°. The height of the free water surface was nondimensionalized using the wave amplitude. The wave shape around the hull appears more clearly at the short wave length than at the long wave length as it is easier for the wave to penetrate the hull

with the longer wave length.

Fig. 8 shows the results of the comparison with the S-Cb84 linear model test results reported by Yasukawa et al. (2018). Direct comparison with KVLCC2 was not possible because there was no published model test result performed at low speed. As the depot ship of S-CB84 is KVLCC1, the result of the wave force acting on the hull of S-CB84 was believed to be similar to that of KVLCC2; the comparison was performed under such an assumption. The black points in the figure are the additional resistance ΔR lateral force, the yaw moment acting on S-Cb84

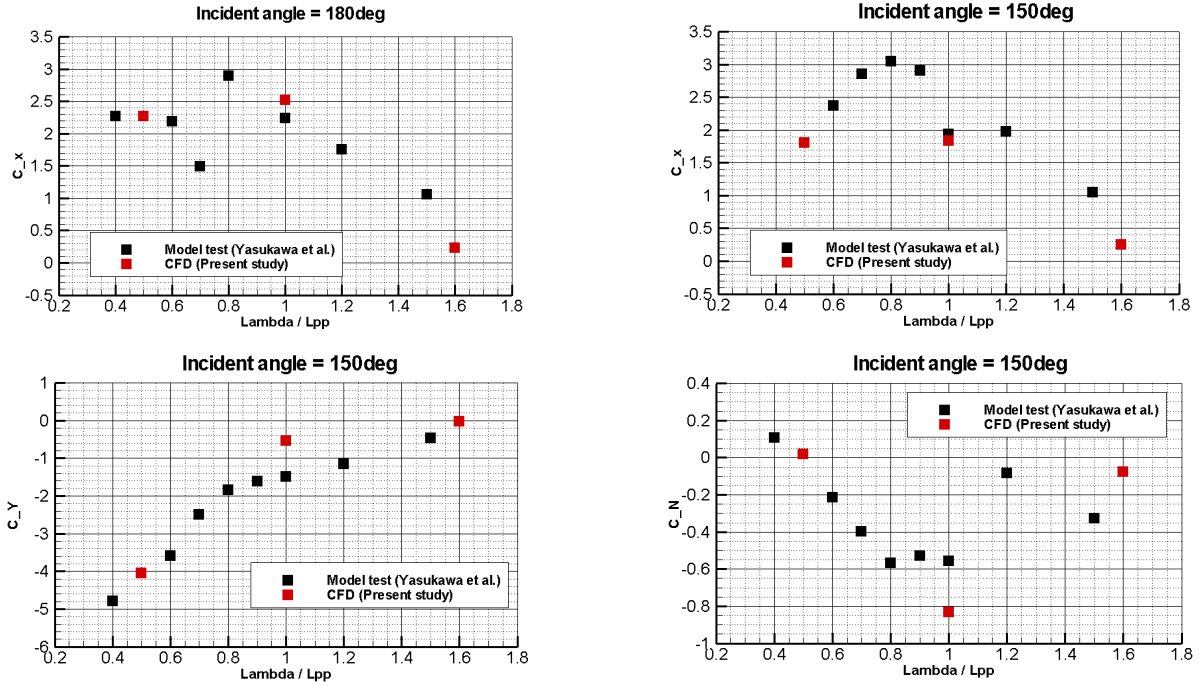


Fig. 8 Comparison of wave force based on CFD results and model test results

measured under the condition of $F_n = 0.049$ and wave height = 3.1 m (solid line), and the points indicate the results of the CFD calculation in this study. The forces and moment were nondimensionalized using the wave height, length of the hull, and width of the hull, as shown in Eq. (10). Similar trends appeared when comparing the forces and moment according to the wave length. The weather vaning simulation was performed using the calculated wave force.

$$\begin{aligned} C_X &= (R_0 - \overline{X_W}) / (\rho g (H/2)^2 B^2 / L_{pp}) \\ C_Y &= \overline{Y_W} / (\rho g (H/2)^2 B^2 / L_{pp}) \\ C_N &= \overline{N_W} / (\rho g (H/2)^2 B^2) \end{aligned} \quad (10)$$

5. Weather Vaning Simulation in Waves

5.1 Conditions for Weather Vaning Simulation

In this study, a weather vaning simulation considering the phase of waves encountered with the hull was proposed for the evaluation of the course-keeping ability in waves. The simulation was performed in

head sea and oblique sea conditions at an angle of 30° in the forward direction, according to the 71st draft revised guidelines of MEPC, in order to examine the course-keeping ability through weather vaning. The simulation conditions are as in Table 9, and the steering was performed from the moment when the wave was encountered at the midship after moving forward during the initial 5 s in calm water. The simulation was performed by dividing the phase of the wave encountered at the midship from the start of steering, as shown in Fig. 9. The results were compared with the simulation using the average wave force. When the heading angle reached the initial 30° , rudder angle control was performed to maintain the course. It was controlled by inverting the rudder to the maximum rudder angle based on the heading angle of 30° .

Table 9 Weather vaning simulation condition

Wave length	$\lambda / L_{pp} = 0.5, 1.0, 1.6$
Wave height	$\lambda / L_{pp} = 0.5, 1.0 - H/\lambda = 0.02$ $\lambda / L_{pp} = 1.6 - H/\lambda = 0.01$
F_n	0.037
Incident angle	150°

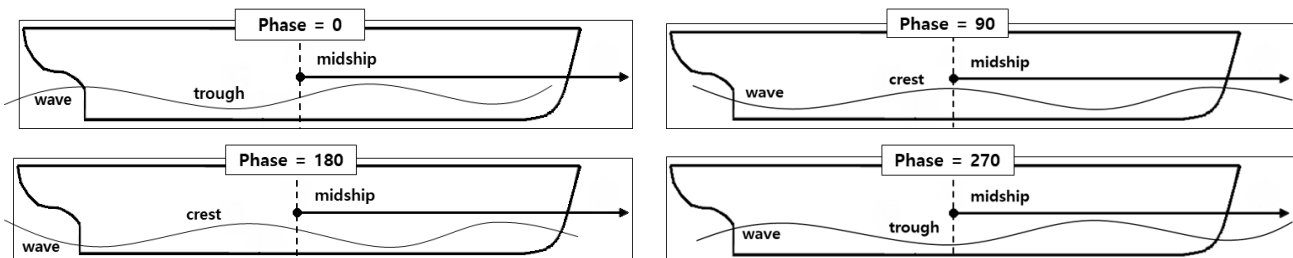


Fig. 9 Wave initial condition - encountered wave phase at midship

With respect to the external wave force used in the simulation, the previously calculated time series data showing the result of calculating the wave force at incident angle intervals of 15° were reflected in the simulation through Fourier transform. The values in calm water from the study by Yasukawa and Yoshimura (2015) were used for the maneuvering hydrodynamic coefficients, and factors used in the simulation pertained to the propeller and rudder.

5.2 Results of Weather Vaning Simulation

Weather vaning simulations were performed to evaluate the

course-keeping ability of KVLCC2 in waves. Figs. 10 to 13 show the results of the weather vaning simulation for 30° heading angle turning in calm water, and the 150° angle incident wave in waves showing the trajectory, heading angle, and heel angle according to the wave length. The heel angle from the motion was not considered for the simulation in calm water, and no result was obtained.

The solid black line shows the simulation result obtained using the average wave force, and the other colored lines are the results of simulation by dividing the phase encountered from the start of steering, as shown in Fig. 9. With respect to the trajectory in waves, the

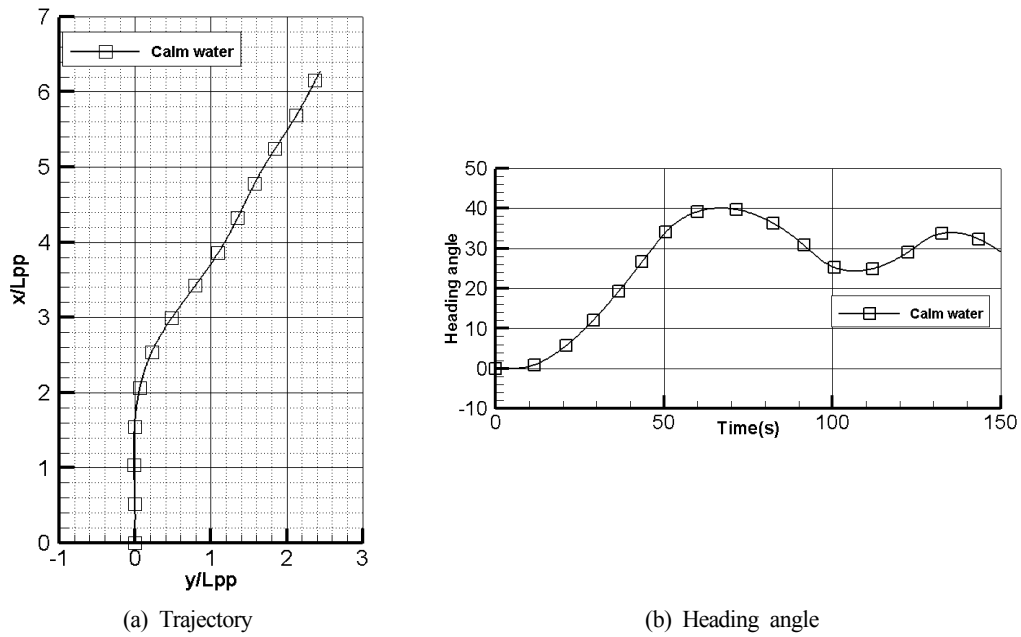


Fig. 10 Heading angle for 30° turning simulation result in calm water

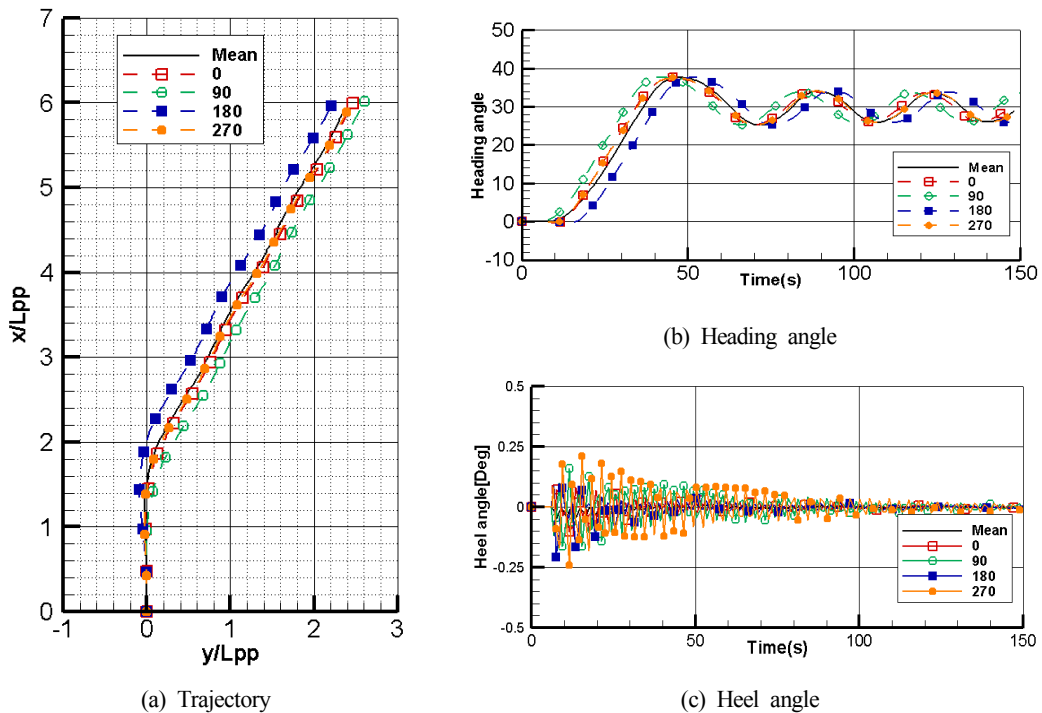


Fig. 11 Weather vaning simulation result at $\lambda/L=0.5$

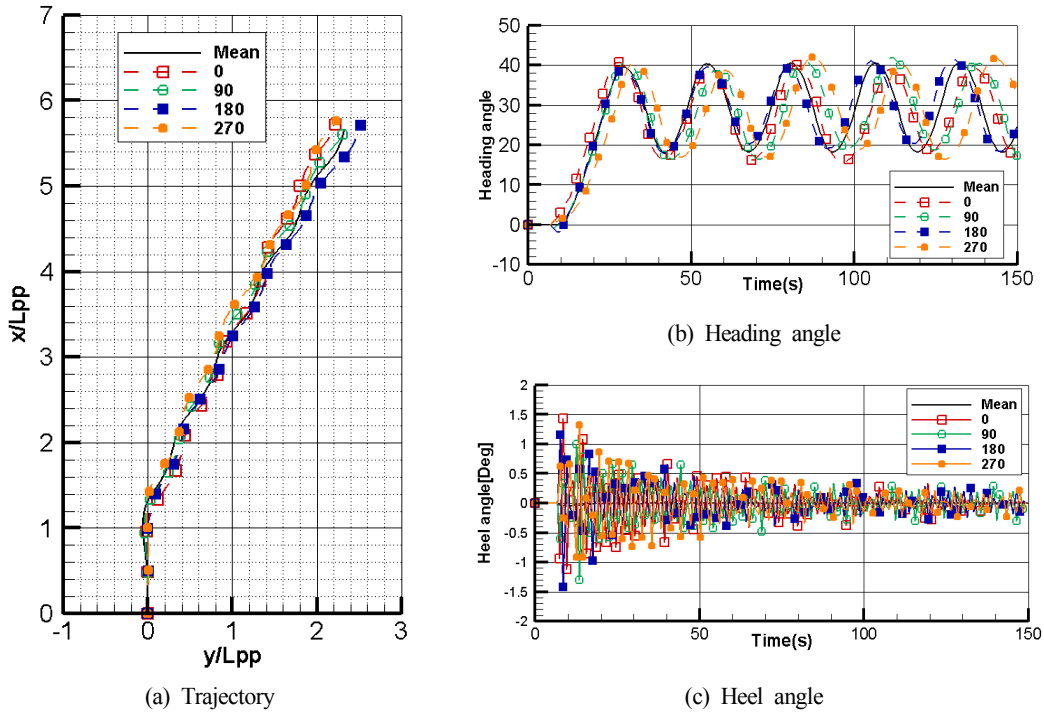


Fig. 12 Weather vaning simulation result at $\lambda/L=1.0$

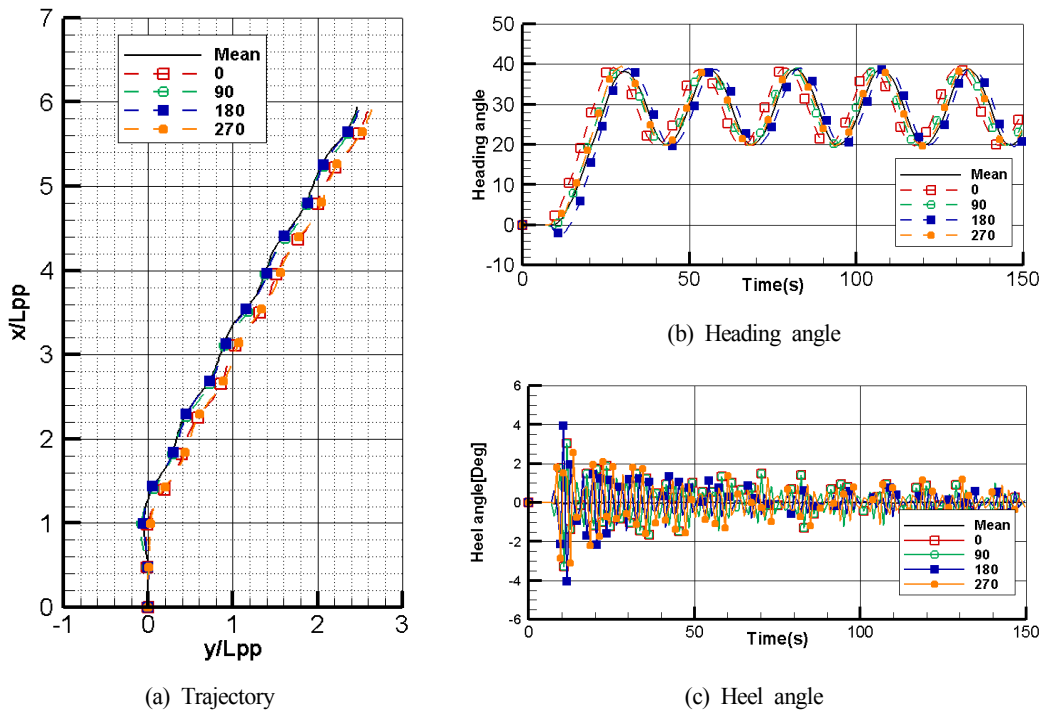


Fig. 13 Weather vaning simulation result at $\lambda/L=1.6$

moving distance varies depending on the wave length when it initially turns up to 30° , compared with the turn in calm water. In calm water, it was about $1.82L_{pp}$, but in waves, it was $1.42L_{pp}$ at $0.93L_{pp}$ at $\lambda/L = 1.0$, and $1.01L_{pp}$ at $\lambda/L = 1.6$. This may have been caused by the change in the number of propeller rotations according to the wave length to maintain the same advancing speed of 4 kn (1.85 km/h), and the rudder force increased with the increased number of propeller

rotations against the relatively high additional resistance at $\lambda/L = 1.0$ and $\lambda/L = 1.6$, resulting in the fast turning. The trajectory also varied depending on the phase of the wave encountered at the start of steering.

With respect to the change in heading angle, turning occurs faster at $\lambda/L = 1.0$ and $\lambda/L = 1.6$, compared to the simulation in calm water. In addition, the tendency of the overshoot angle of the heading angle

decreased in calm water and at $\lambda/L = 0.5$. Regular vibration is generated based as for 30° at $\lambda/L = 1.0$ and $\lambda/L = 1.6$. This appears to have been caused by the rudder control method to shift the rudder to the maximum rudder angle upon exceeding 0° from the heading angle, resulting in the overshoot angle at $\lambda/L = 1.0$ and $\lambda/L = 1.6$. The overshoot angle may be reduced by changing the controller, such as the proportional-integral-differential controller (PID) controller.

The maximum heel angle was about 3.71° greater at $\lambda/L = 1.6$ than at $\lambda/L = 0.5$, and about 2.48° greater than at $\lambda/L = 1.0$. The relative difference at each wave length was large, but the original absolute heel angle was not very large, which may have been because nature of the tanker did not cause much rolling motion.

When comparing the difference according to the phase encountered during initial steering, at $\lambda/L = 0.5$, there was a varying speed at which the heading angle changes according to the phase of the wave encountered during the initial steering, resulting in different initial trajectories. However, there was subsequently little influence during the steering to maintain the course. However, at $\lambda/L = 1.0$, the trajectory during steering to maintain the course varied depending on the phase of the wave encountered during turning as well as the initial steering. With respect to the phase = 270 simulation, an overshoot angle of up to 13.4° occurs from 30° . Even at $\lambda/L = 1.6$, there was a difference in the heading angle change depending on the phase of the encountered wave, and the maximum heel angle was greater than the result obtained from the simulation using the average wave force.

6. Conclusion

This study aimed to evaluate the course-keeping ability of KVLCC2 in regular waves by performing weather vaning simulations. Simulations were also performed in head sea and oblique sea conditions at an angle of 30° in the forward direction according to the MEPC 71st draft revised guidelines to examine the course-keeping ability through weather vaning against the incident waves.

To this end, the maneuvering equation of motion in waves using the wave force as the external force in the existing maneuvering equation of motion in calm water and the equation of the rolling motion in waves to calculate the heel angle in waves were configured. In addition, an equation was developed to consider the yaw motion according to the heel angle to the hydrodynamic force acting on the hull in order to determine the influence according to the heel angle in the maneuvering motion. The external force of the wave was calculated according to the incident angle using CFD, and external forces such as the surge force, sway force, and yaw moment were compared with the results of the similar ship model test. In order to reflect the influence of the phase of the waves encountered with the hull in addition to the average wave force, it was configured to change according to the phase using the Fourier transform.

The following conclusions were made by performing a simulation according to the phase change of the wave encountered with the hull using the simulation configured in this study.

(1) Based on the evaluation results of for the course-keeping ability of KVLCC2, weather vaning was possible despite the differences in the trajectory and heading angle according to the wave length. The heel angle did not exceed the generally known stability range.

(2) The results of the simulation obtained using the average wave forces was different from the results of the simulation considering the changes in external forces according to the phase of the waves encountered by the ship. The simulation results also differed according to the phase encountered initially.

(3) The differences according to the phase of the wave were more profound with a long wave length than with a short wave length, which may have been caused by the increased wave height owing to the increase in wave length.

For a further evaluation of the maneuverability and course-keeping ability in high waves, a study considering the influence of the hull and the encountered phase will be required. It may also be necessary to consider the motion with 4 degrees of freedom or 6 degrees of freedom in addition to the plane motion generally used in studies of maneuvering motions.

Funding

This study was carried out with the support of “Experimental Study on the Development of Large Control Algorithm for Multiple Unmanned Ships (project number: 2020R1F1A1071610),” a basic research project of the National Research Foundation of Korea (NRF), and “Development of Autonomous Navigation System with Intelligent Route Planning System (project number: 20200615),” an autonomous ship technology development project of the Ministry of Maritime Affairs and Fisheries, Republic of Korea.

References

- Cura-Hochbaum, A., & Uharek, S.(2016). Prediction of Ship Manoeuvrability in Waves Based on RANS Simulations. Proceedings of the 31st Symposium on Naval Hydrodynamics Monterey, California.
- International Towing Tank Conference (ITTC). (1999). ITTC - Recommended Procedures and Guidelines: CFD Verification (7.5-03-01-04). International Towing Tank Conference.
- International Towing Tank Conference (ITTC). (2014). ITTC - Recommended Procedures and Guidelines: Seakeeping Experiments (7.5-02-07-02). International Towing Tank Conference.
- Kim, D.J., Yun, K.H., Park, J.Y., Yeo, D.J., & Kim, Y.G. (2019). Experimental Investigation on Turning Characteristics of KVLCC2 Tanker in Regular Waves. *Ocean Engineering*, 175, 197-206. <https://doi.org/10.1016/j.oceaneng.2019.02.011>
- Kim, D.Y., Kim, I.T., Han, J.S., Kim, S.J., & Kim, S.H. (2016). A Study on the Hydrodynamic Derivatives Estimation of KVLCC2 using Virtual Captive Model Test. Proceedings of KAOSTS

- Academic Conference, Pusan, Korea, 510-513.
- Kim, J.H. (2019). A Study on the Turning Ability of the KVLCC2 in Regular Wave Using MMG Model (Master's thesis). Inha University, Korea.
- MEPC. (2013). Interim Guidelines for Determining Minimum Propulsion Power to Maintain the Manoeuvrability of Ships in Adverse Conditions. MEPC 65/22.
- MEPC. (2017). Draft Revised Guidelines for Determining Minimum Propulsion Power to Maintain the Manoeuvrability of Ships in Adverse Conditions. MEPC 71/INF.28.
- Seo, M.G., Nam, B.W., & Kim, Y.G. (2018). Numerical Analysis of Turning Performance in Waves by Considering Wave Drift Forces. *Journal of the Society of Naval Architects of Korea*, 55(2), 103-115. <https://doi.org/10.3744/SNAK.2018.55.2.103>
- Seok, J., Kim, S.Y., Yang, Y.J., Jin, S.H., & Park, J.C., (2016). A Study for Roll Damping Performance of a Platform Supply Vessel with or without Bilge Keel using CFD. *Journal of the Korean Society of Marine Engineering*, 40(9), 791-798. <https://doi.org/10.5916/jkosme.2016.40.9.791>
- SHOPERA. (2016). Presentation of Benchmark Results. SHOPERA (Energy Efficient Safe Ship Operation) Benchmark Workshop, London.
- SIMMAN. (2008). Preprints of Workshop Proceeding. SIMMAN 2008, Copenhagen, April 14-16.
- SIMMAN. (2020). SIMMAN 2020 Purpose. Retrieved Jun 2020 from <http://www.simman2019.kr/contents/Purpose.php>
- Simonsen, C.D., Otzen, J.F., Klimt, C., Larsen, N.L. & Stern, F. (2012). Maneuvering Predictions in the Early Design Phase using CFD Generated PMM Data. Proceedings of 29th Symposium of Naval Hydrodynamics, Gothenburg, Sweden, 1057-1074.
- Sprenger, F., Maron, A., Delefortrie, G., Zwijnsvoorde, T., Cura-Hochbaum, A., Lengwinat, A., & Papanikolaou, A. (2017). Experimental Studies on Seakeeping and Maneuverability of Ships in Adverse Weather Conditions. *Journal of Ship Research*, 61(3), 131-152.
- Xu, Y., Kinoshita, T., & Itakura, H. (2007). A PMM Experimental Research on Ship Manoeuvrability in Waves. Proceedings of the 26th International Conference on Offshore Mechanics and Arctic Engineering, San Diego, USA. <https://doi.org/10.1115/OMAE.2007-29521>
- Yasukawa, H., & Faizul, A.A. (2006). Experimental Study on Wave-Induced Motions and Steady Drift Forces of an Obliquely Moving Ship. *Journal of the Japan Society of Naval Architects and Ocean Engineers*, 3, 133-138. <https://doi.org/10.2534/jjasnaoe.3.133>
- Yasukawa, H., & Yoshimura, Y. (2015). Introduction of MMG Standard Method for Ship Maneuvering Predictions. *Journal of Marine Science and Technology*, 20(1), 37-52. <https://doi.org/10.1007/s00773-014-0293-y>
- Yasukawa, H., Hirata, H., Matsumoto, A., Kuroiwa, R., & Mizokami, S. (2018). Evaluations of Wave-Induced Steady Forces and Turning Motion of a Full Hull Ship in Waves. *Journal of Marine Science and Technology*, 24, 1-15. <https://doi.org/10.1007/s00773-018-0537-3>

Author ORCIDs

Author name	ORCID
Kim, In-Tae	0000-0003-1382-3471
Kim, Sang-Hyun	0000-0002-3625-2328

A Study on the Performance Variation of a Three-Dimensional Hydrofoil Using Jet Flow

Myeong-Jin Eom¹, Kwang-Jun Paik², Ju-Han Lee¹, Shin-Min Kang¹ and Dong-Young Kim¹

¹Graduate Student, Department of Naval Architecture and Ocean Engineering, Inha University, Incheon, Korea

²Professor, Department of Naval Architecture and Ocean Engineering, Inha University, Incheon, Korea

KEY WORDS: Hydrofoil, Coanda effect, Computational fluid dynamics, Experimental fluid dynamics, Jet flow

ABSTRACT: As one of the development directions of high-performance ships to reduce greenhouse gas emissions, there is research on high-performance propellers. However, in the case of conventional screw propellers, as they have been studied for a long time, there is a limit to improving efficiency only by depending on the conventional design and analysis methods. In this study, we tried to solve the problems using the Coanda effect by spraying a jet on the surface of the hydrofoil. The Coanda hydrofoil consists of a tunnel and jet slit to make jet flow. The computation was performed for each tunnel and slit position, and the efficiency according to the geometry of the hydrofoil was analyzed. In addition, a study on the 3D geometry change was conducted to analyze the performance according to the span direction spraying range and hydrofoil shape. As the height of the slit and the diameter of the tip were lower, when the slit is located in the center of the hydrofoil, the lift force increased and the drag force decreased. The increase rate of lift-to-drag ratio was different according to the shape of the hydrofoil, and the efficiency of the spraying condition of 0.1S-0.5S, which had the least effect on the vortex at the tip of the blade, was high for all 3D hydrofoils. When the geometry of the slit was optimized, and also the shape and spray range of the hydrofoil in 3D was considered, the efficiency of the jet sprayed hydrofoil was increased.

Nomenclature

C	Chord length of hydrofoil (m)
S	Span length of hydrofoil (m)
\dot{m}	Mass flow rate (kg/s)
V_{jet}	Spraying velocity at slit (m/s)
ρ	Density (kg/m ³)
S_j	Spraying jet area of the hydrofoil (m ²)
V_∞	Inflow velocity (m/s)
α	Angle of attack (°)
C_L	Lift coefficient, $C_L = \frac{L}{0.5\rho V_\infty^2 CS}$
C_D	Drag coefficient, $C_D = \frac{D}{0.5\rho V_\infty^2 CS}$

1. Introduction

The International Maritime Organization (IMO) established its Energy Efficiency Design Index standard in 2013 and has been

strengthening the regulations on air pollutants since 2020, such as lowering the baseline emissions of sulfur oxides (SOx) in ship fuel from 3.5% to 0.5%. As these regulations have been enforced, interest in improving the operational efficiency of ships for fuel savings has increased. To improve the propulsion efficiency of ships, attempts have been made to optimize the propeller designs and apply fuel-saving devices installed at the front and back of the propeller. However, the improved designs that maintain the existing framework have had a limitation in achieving dramatic fuel savings. In particular, screw propellers are propulsion machines using lift as a propulsion force, which is generated by the relative angle of attack created between the rotation of the propeller hydrofoils and the inflow, and have been used in ships for more than 150 years. Screw propellers have become currently the most efficient marine propulsion device through a long period of research and development, and for this reason, it is nearly impossible to improve the efficiency by more than 2% even if advanced optimization tools and analysis techniques are used. To dramatically improve the efficiency of conventional marine propulsion systems, beyond the concept of screw propellers, which have been in

Received 6 January 2021, revised 20 January 2021, accepted 25 January 2021

Corresponding author Kwang-Jun Paik: +82-32-860-7331, kwangjun.paik@inha.ac.kr

© 2021, The Korean Society of Ocean Engineers

This is an open access article distributed under the terms of the creative commons attribution non-commercial license (<http://creativecommons.org/licenses/by-nc/4.0>) which permits unrestricted non-commercial use, distribution, and reproduction in any medium, provided the original work is properly cited.

use since the 19th century, a new type of propulsion device should be developed. In this study, we focused on applying the Coanda effect to propeller hydrofoils for developing a high-efficiency propulsion system that can be differentiated from conventional screw propellers.

A performance improvement of the wings when using the Coanda effect has been mainly achieved in the aviation field by spraying the jet along the surface of the wings. For example, Pfingsten and Radespiel (2007) used jet blowing at the flap to delay a wing stall and obtain a high lift. Furthermore, they compared the pressure distribution based on the jet injection and angle of attack, thereby analyzing the effect of the jet on the pressure distribution of the wing. In addition, Yoon et al. (2012) used a main slit and a sub-slit to conduct a study on the Coanda effect according to the spraying strength of each slit and the material change in the cylinder shape, thereby experimentally and numerically investigating the change in flow according to the spraying strength of the two adjacent slits in the cylinder structure. Furthermore, Djojodihardjo (2013) conducted a study on the vortex occurring at the wing tip when a jet blows over the wing surface.

Furthermore, although studies have been conducted in a variety of ways in the aviation field, in comparison, very few studies have been conducted in the shipbuilding field, and representative studies include those conducted by Seo and Lee (2013) and Seo et al. (2016). Seo and Lee (2013) analyzed the performance of a Coanda hydrofoil by spraying type based on the changes in the lift and drag characteristics and the boundary layer for application to marine rudder systems. Seo et al. (2016), by contrast, conducted a study on the performance variation of a marine stabilizer fin based on the geometry and amount of spraying of the slit.

Because the physical properties of water and air are different, a basic study was conducted on applying the Coanda effect to the hydrofoils of vessels, and a previous study analyzed the changes and cavitation performance of lift and drag in a two-dimensional geometry (Eom et al., 2020). Based on this, the present study investigated the position, geometry, and scope of the jet slit and analyzed the three-dimensional effect of a Coanda hydrofoil.

2. Numerical Validation

2.1 Experimental Equipment

Because comparisons of the results between this study and the studies of other institutions have been limited, to validate the numerical analysis results, we conducted experiments by creating our own experimental equipment. The experiments were conducted in the towing tank of Inha University, and the overall geometry of the experimental equipment is as shown in Fig. 1. The towing tank of Inha University has a drivable distance of approximately 45 m. In addition, the capacity of the load cell used in the experiments was 100 N in the $\pm z$ -direction, and the capacity of the pump was 100W at maximum. The chord length of the hydrofoil was 200 mm and the length in the span direction was 300 mm. To increase the Reynolds number as much as possible, the towing speed was set to 2 m/s, which was the fastest

speed possible within the allowed ranges of the load cell and the towing carriage.

The experimental equipment consists of four main components: a hydrofoil, a tube that supplies water to the spray jets, a chamber that lets the water pass through the hydrofoil, and a frame for fixing the hydrofoil on the carriage. Fig. 2 illustrates the drawings used for fabrication of the experimental equipment. The hydrofoil was made of acrylic material, and the angle of attack could be adjusted by rotating the chamber fixed on both sides of the hydrofoil. Considering the manufacturing tolerance, the height of jet spraying slit (h_s) was set to 0.5% (1 mm) of the chord length, and the diameter of the tip (h_T)

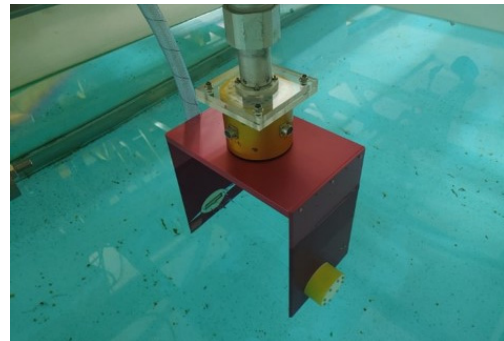


Fig. 1 Experimental setup for Coanda hydrofoil

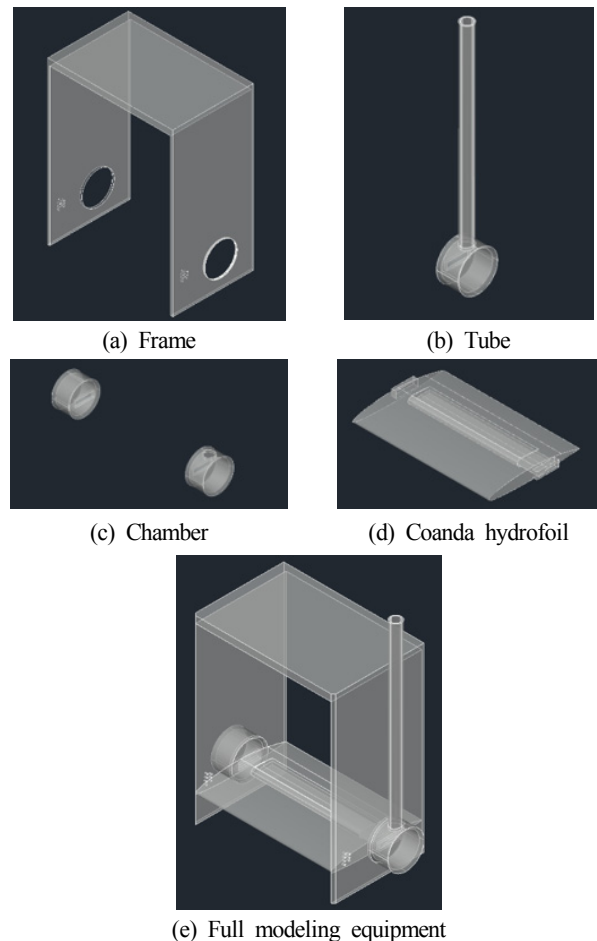
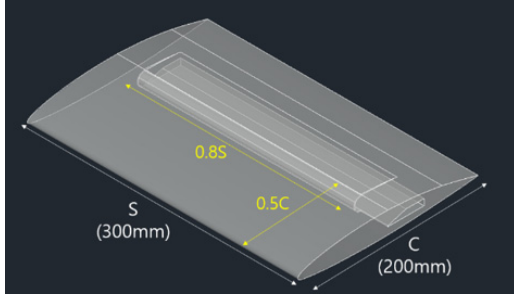
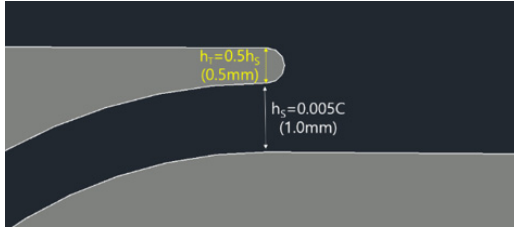


Fig. 2 Geometry of experimental equipment



(a) Dimension of Coanda hydrofoil and jet flow range



(b) Dimension of slit and tip height

Fig. 3 Geometry of Coanda hydrofoil for experiment and numerical simulation

where the slit and the suction side meet was set to 0.5 mm, which was 50% of the slit height. The jet spaying range was 80% of the span direction, and Fig. 3 illustrates the geometry of the hydrofoil. For the cross-section of the hydrofoil, the same dimensional specifications of a previous study (Eom et al., 2020) was used.

2.2 Numerical Analysis and Conditions

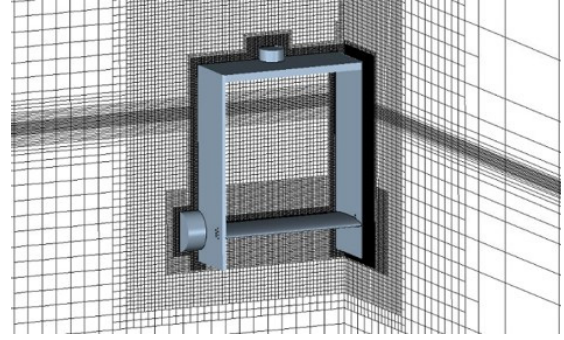
In this study, we used STAR-CCM+ v13.06, a commercial program, to conduct the numerical analysis. An unsteady incompressible turbulence flow was selected as the condition of the numerical analysis, and a continuous equation and Reynolds-averaged Navier-Stokes (RANS) equation were considered as governing factors, as shown in Eqs. (1)–(2) below, respectively:

$$\frac{d}{dt} \int_{\Omega} \rho d\Omega + \int_S \rho u_i n_i dS = 0 \quad (1)$$

$$\frac{d}{dt} \int_{\Omega} \rho u_i d\Omega + \int_S \rho u_i u_j n_j dS = \int_S (\tau_{ij} n_j - p n_i) dS + \int_{\Omega} \rho b_i d\Omega \quad (2)$$

SST $k-\omega$ was used for the turbulence model. The SST $k-\omega$ model is a hybrid that combines the $k-\epsilon$ model with the $k-\omega$ model according to the characteristics of the flow field, and this model is usually considered when analyzing the turbulent flow phenomenon such as a propeller wake.

To implement a free surface, we used the volume of fluid (VOF) method, which a typical method applied used to implement free surfaces. The VOF method belongs to the class of Eulerian methods, is capable of implementing a multi-phase flow, and is suitable for implementing flat free surfaces of wide range, such as a free surface around a vessel. The VOF method uses the phase volume fraction

**Fig. 4** Grid system around the experimental equipment

concept to define the proportion of fluid in a grid, thereby classifying the phase to track the interface between phases.

Because the experimental equipment has asymmetry, the experiment was repeated many times to accurately measure the lift and drag. In addition, a numerical analysis was conducted by including the experimental equipment for an accurate comparison of the resulting values. Because the pump had a fixed output, the flow rate of the spray was adjusted by opening the level of the middle valve, and the jet momentum coefficient was reverse-calculated by attaching a hydraulic system to the tube connected to the hydrofoil and measuring the fluid pressure. After analyzing the experimental results, a numerical analysis was conducted under the same conditions using a reverse-calculated jet momentum coefficient. Fig. 4 illustrates the grid system used during the numerical analysis. For a comparison with the experimental results, the numerical analysis included the free surface and other experimental equipment, thereby applying approximately 6.4 million grids. The volume of jet spray is determined using Eq. (3), which shows the jet momentum coefficient:

$$C_j = \frac{\dot{m} V_{jet}}{\frac{1}{2} \rho S V^2_{\infty}} \quad (3)$$

For a numerical validation, we conducted experiments and a numerical analysis using a normal hydrofoil, in which the internal geometry including the slit does not exist, and a Coanda hydrofoil, which facilitates the jet spray. The inflow rate was set to 2 m/s, and the experiment and numerical analyses were conducted by changing the angle of attack.

2.3 Results of Experiment and Numerical Analysis

Figs. 5 and 6 show the results of the experiment and numerical analysis. The experiment using the normal hydrofoil, in which a jet was not sprayed, was conducted after removing the tube that injects water. Fig. 5 shows the lift and drag coefficients by the angle of attack, and the experiment on the normal hydrofoil was conducted from zero to 6°. The resulting trend between the experiment and the numerical analysis was quite consistent, although the numerical analysis showed higher values in the lift and lower values in the drag. Thereafter, the same trend was shown in the results of the Coanda hydrofoil, in which

a jet was sprayed.

The experiment on a jet spray was conducted at angle of attack of zero, 2°, and 4°, and Fig. 6 shows the change in lift and drag forces based on the angle of attack and jet momentum coefficient. As

mentioned above, the flow rate was adjusted by opening the level of the middle valve because the output of the pump could not be controlled in the experimental equipment. Hence, the jet momentum coefficient by the angle of attack was not constant. Because the drag

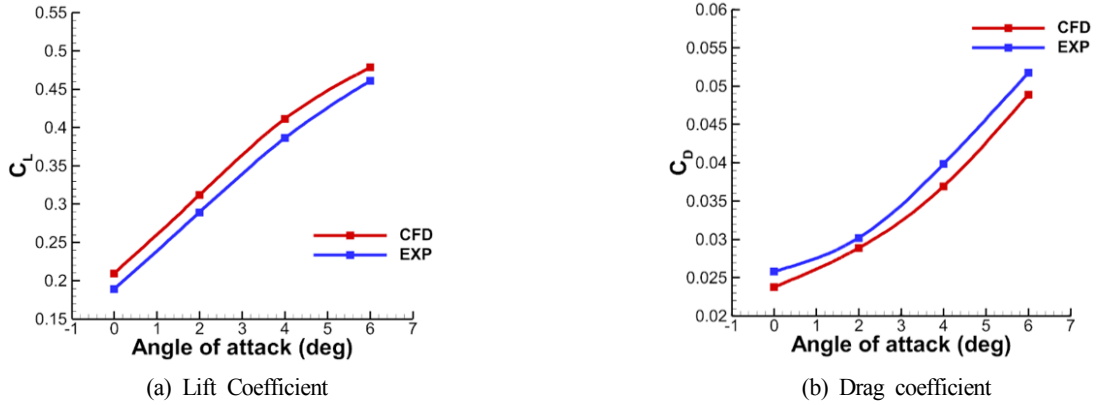


Fig. 5 Comparison of Normal hydrofoil performance between experiment and numerical simulation

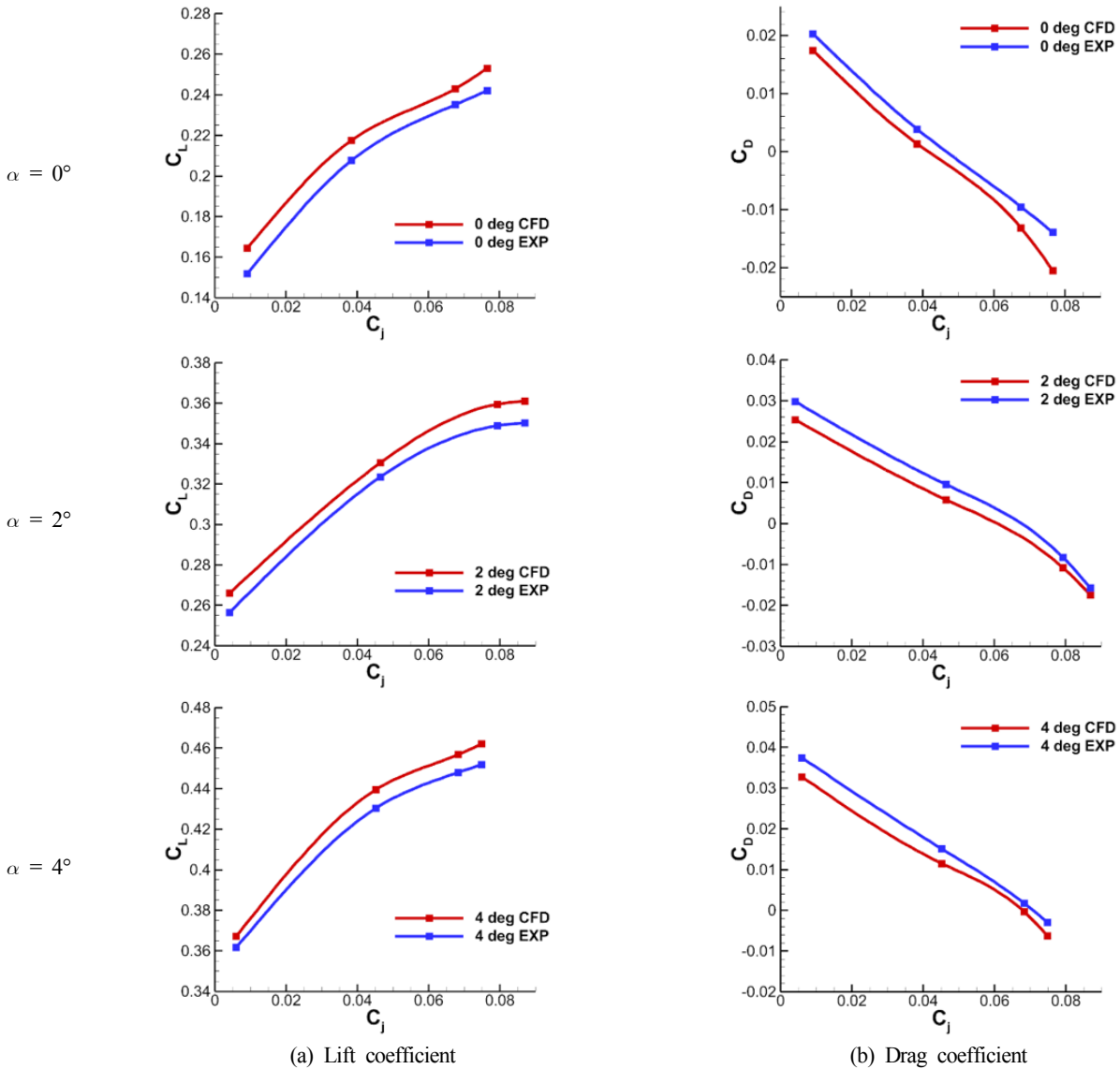


Fig. 6 Comparison of Coanda hydrofoil performance between experiment and numerical simulation

converged to zero owing to the propulsion by the jet spray, its error rate was difficult to show. In the case of lift, by contrast, the error rate was generally less than 5%.

The Reynolds number under the conditions of the present experiment and the calculation was approximately 4.5×10^5 , corresponding to a transition flow regime. However, the jet flow rate under the conditions of the experiment and numerical analysis was 7.3 m/s at maximum, at which the Reynolds number was 1.64×10^6 , corresponding to a turbulent flow regime. Therefore, the fully turbulence model was selected, and when the results were compared, a same trend was shown in the lift and drag, respectively, for all angles of attack and C_j .

The above results demonstrated that the Coanda effect induced changes in the lift and drag characteristics, which were analyzed using a numerical analysis and were found to be sufficiently reliable; based on this result, using an additional numerical analysis, a study was conducted on a variety of spraying conditions.

3. Optimization of Slit Geometry

The numerical analysis was used to analyze the performance variation of the Coanda hydrofoil based on the height of the spraying slit (h_s), the height of the tip (h_T), and the position of the slit. Fig. 7 shows the calculation domain and the grid system of the numerical analysis used for a performance comparison between the slit geometries.

The spraying range of the jet was 80% of the span direction as in the

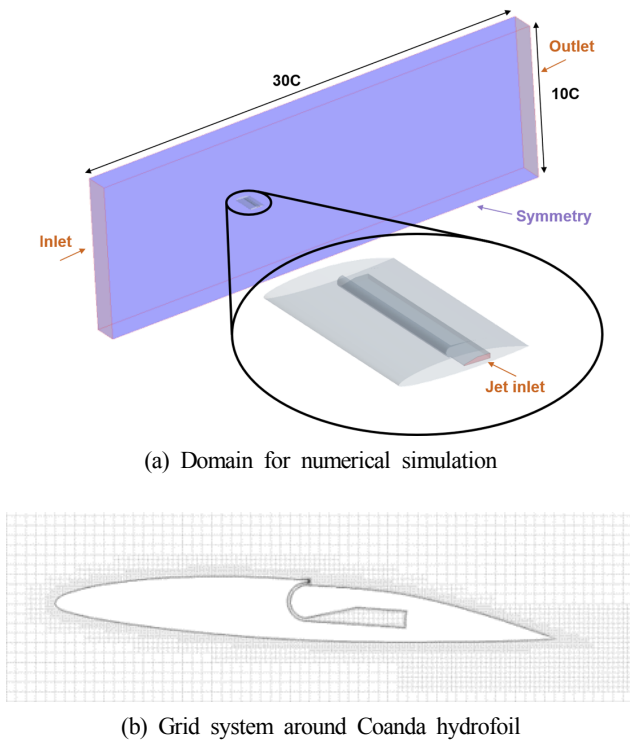


Fig. 7 Domain and grid system of numerical simulation for performance analysis according to the slit shape

experiment, and a two-dimensional calculation was conducted by assigning a symmetry boundary condition for both sides of the hydrofoil. However, considering that the water must flow in from one side when the jet is actually sprayed on the hydrofoil surface, we applied the inlet boundary condition to the left part of the hydrofoil. The basic geometry of the hydrofoil was identical to that of the experiment and based on the comparison between the numerical and experimental results, we created a grid system excluding the experimental equipment, in which approximately 2.9 million grids were used.

3.1 Performance Variation by Slit Height (h_s)

The geometry conditions considered to analyze the effect of the slit height were $h_s = 0.003 C$, $0.005 C$, and $0.007 C$, and the calculation condition was $C_j = 0.02-0.1$. Under all conditions, the angle of attack was 4° , the flow rate was 2 m/s, and the diameter of the tip was $0.5 h_s$. Fig. 8 shows the performance variation by the slit height. As the slit height decreases, the lift tends to increase overall, and in the case of drag, the slope changes according to the slit height. In general, C_L/C_D is usually considered when analyzing the performance of a hydrofoil, whereas in the case of a Coanda hydrofoil, it is inappropriate to use C_L/C_D for the analysis because the propulsion by jet spraying can be

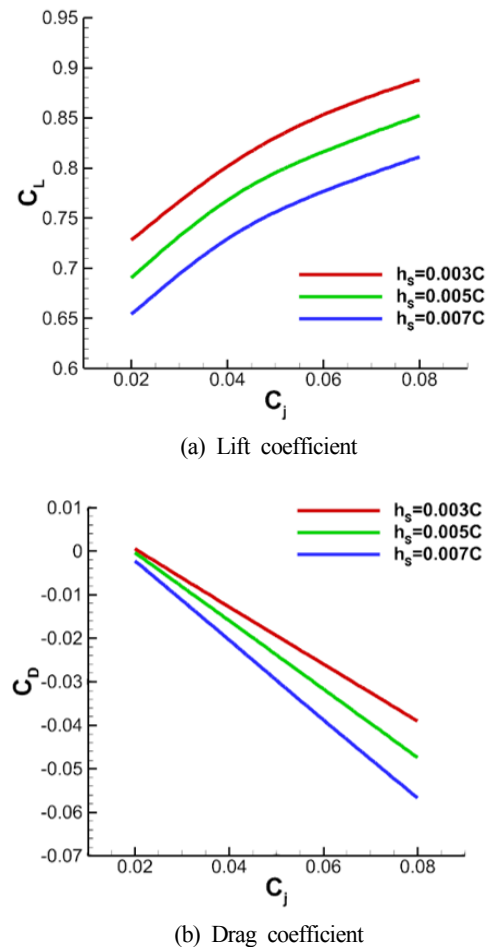


Fig. 8 Lift and drag performance according to slit height ($\alpha=4^\circ$)

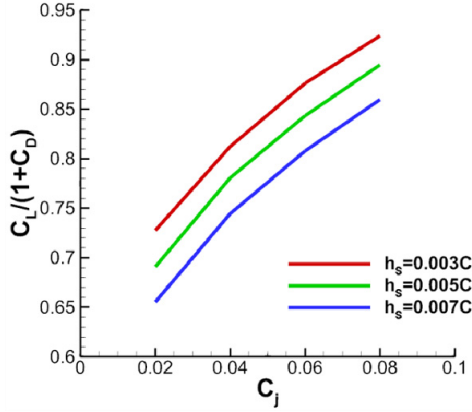


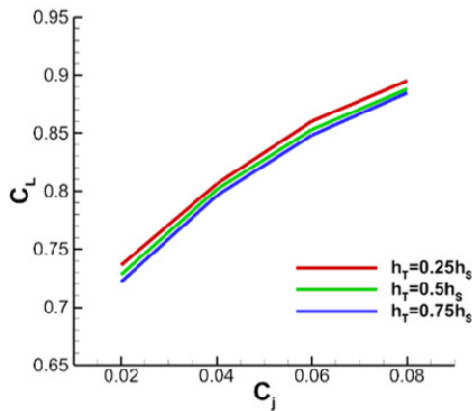
Fig. 9 Variation of lift and drag ratio according to slit height ($\alpha = 4^\circ$)

higher than the drag of the hydrofoil. Because the drag has a negative value in most of the above calculation conditions, $C_L/(1+C_D)$ was used to analyze the trend of the lift according to the drag. Although it does not have much physical meaning because a constant was introduced, the change in lift by the drag can be easily checked.

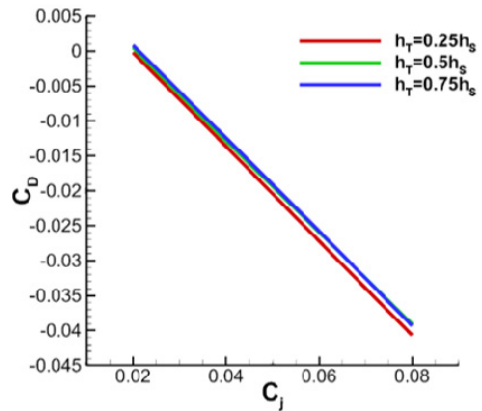
Fig. 9 shows the trend according to the jet momentum coefficient and $C_L/(1+C_D)$. It demonstrates that, as the slit height decreases, the performance of the hydrofoil increases according to the jet sprayed. Therefore, the slit height was fixed at $h_s = 0.003C$ in the numerical analysis hereafter.

3.2 Performance Variation by Tip Height (h_T)

In this study, $h_T = 0.25h_s$, $0.50h_s$, and $0.75h_s$ were used as the geometry conditions to analyze the performance variation by the height of the tip, and Fig. 10 illustrates the change in the hydrofoil performance according to the tip height. The variation in performance based on tip height was relatively simple: As the tip height decreased, the lift increased, and the drag decreased. The thickness of the tip may affect the Coanda effect of the jet sprayed from the slit (Yoon et al., 2012), and if the thickness of tip increases, a part of the jet, which should flow along the hydrofoil surface, may flow in the tip direction, thereby reducing the lift and drag performance from the Coanda effect.



(a) Lift coefficient



(b) Drag coefficient

Fig. 10 Lift and drag performance according to tip height ($\alpha = 4^\circ$)

Therefore, h_T was set to $0.25h_s$ in the rest of this study.

3.3 Performance Variation by Slit Position

Previous studies have shown that the performance increases as the slit height and the thickness of the tip decrease. However, considering the actual production problem, it is recommended to select as small of a slit height and tip thickness as possible. Following a study on the slit shape, this paragraph analyzes the trend based on the hydrofoil chord direction position of the slit. The geometry conditions considered included the position of the slit at $0.1C$, $0.3C$, and $0.5C$ on the front part of the hydrofoil, and the analysis was conducted at an angle of attack, 2° , 4° , and 6° . The results are illustrated in Fig. 11.

The results in Fig. 11 confirm that the lift is the largest and the drag is the smallest, thereby showing the best performance, when the slit is positioned at $0.5C$ on the front part of the hydrofoil. The condition of the slit position after $0.5C$ is not considered because the thickness of the hydrofoil decreases, and the cross-sectional internal geometry, which is the basis of this study, cannot be positioned. Because Eom et al. (2020) conducted a study on the hydrofoil geometry to improve the cavitation performance, the pressure distribution of the hydrofoil based on the slit position was analyzed. To compare the pressure distribution, Fig. 12 illustrates the pressure distribution on hydrofoil surface of each geometry under an angle of attack of 6° and $C_j = 0.08$.

In the pressure distribution of each hydrofoil, it was confirmed that the pressure decreases significantly at $x/C = 0.1$, 0.3 , and 0.5 owing to the jet flow at a high flow rate sprayed from the slit. Because the angle of attack and the jet spraying amount were identical, the pressure drop at the front part of the hydrofoil was similar in all three hydrofoils. In the case of $0.3C$ and $0.5C$ hydrofoils, the pressure drops occurring at the slit were similar, but in the case of the $0.1C$ hydrofoil, in which the slit was positioned right behind the front part of the hydrofoil, an extremely high pressure drop occurred at the slit. Based on this fact, it was determined that, in terms of the slit position, the most appropriate geometry for NACA66 (mod) hydrofoil is $0.5C$, which has a relatively uniform pressure distribution as well as a higher lift and lower drag than other slit positions, with respect to all values of C_j .

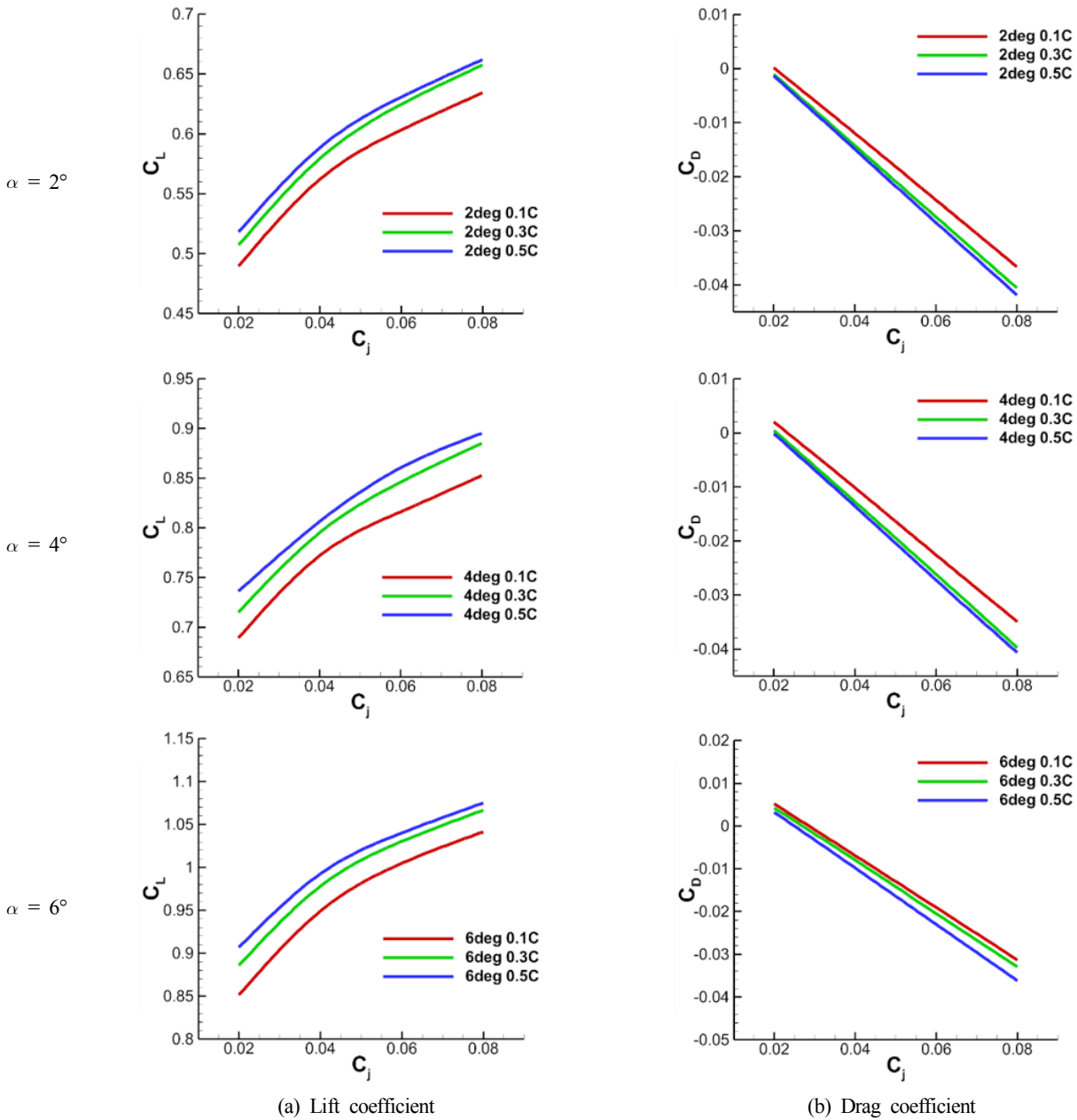


Fig. 11 Lift and drag performance according to slit position

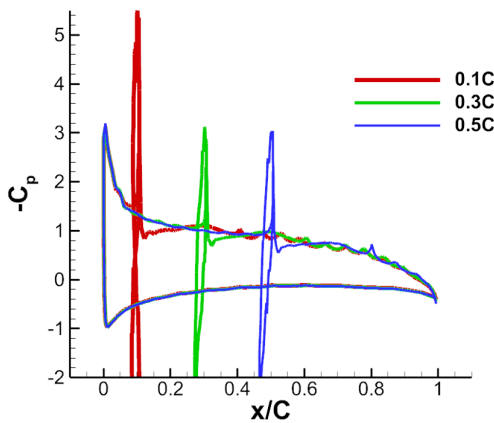
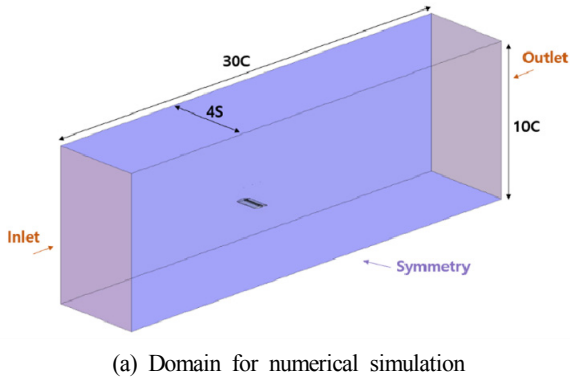


Fig. 12 Comparison of pressure distribution according to slit position ($\alpha = 6^\circ$, $C_j = 0.08$)

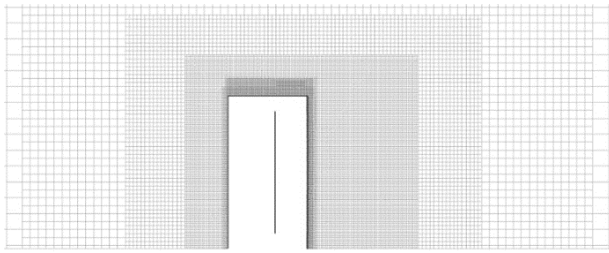
4. Performance Variation According to 3D Effect and Spraying Range

An appropriate geometry of the jet slit for NACA66 (mod) was derived based on the performance variation of the hydrofoil with respect to the slit height, tip thickness, and slit position derived above, and based on this, this variation in performance according to the three-dimensional (3D) effect and the range of the jet spraying of the hydrofoil when applying the Coanda effect are analyzed in this section.

Fig. 13 shows the calculation domain used in the 3D numerical simulation. Although basically the same as shown in Fig. 7, the 3D effect was considered by assigning a size of 4S in the span direction.



(a) Domain for numerical simulation



(b) Grid system around Coanda hydrofoil

Fig. 13 Domain and grid system of 3-dimensional numerical simulation

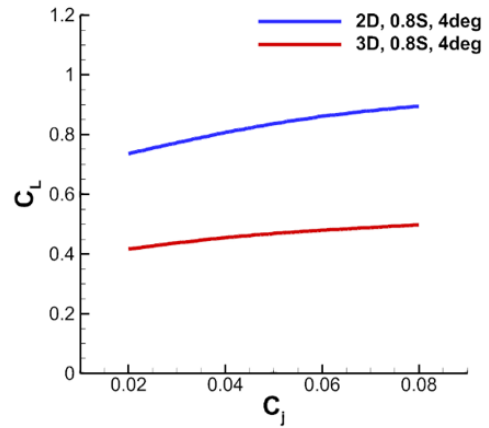
The geometry of the grid system is also mostly identical, but the total number of grids is approximately 3.4 million because some grids are added in the span direction.

4.1 Performance Variation According to 3D Effect

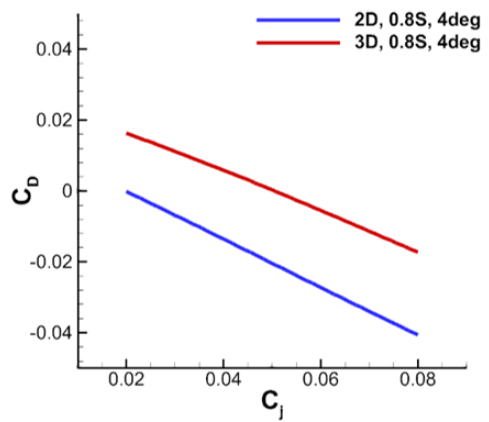
To analyze the 3D effect, a 3D analysis was conducted during which one side was opened in the aforementioned 2D calculation with an angle of attack of 4° . Fig. 14 illustrates the performance of the lift and drag according to the jet moment coefficient in the 2D and 3D geometries of the Coanda hydrofoil with an angle of attack of 4° and a slit range of $0.8S$.

Overall, as the jet momentum coefficient increased, the lift force decreased and the drag force increased, whereby the lift force decreased by as much as about 42%. Although the geometry and spraying conditions of the Coanda hydrofoils were identical, the performance changed owing to the 3D effect because one side was opened. To analyze the causes of changes in the lift and drag forces, Fig. 15 illustrates the pressure and velocity distribution of the Coanda hydrofoil.

Fig. 15 shows comparisons of the pressure distribution, x-direction velocity, and y-direction velocity distributions between 2D and 3D Coanda hydrofoils. First, the 2D hydrofoil shows that the pressure distribution is formed relatively high compared to the 3D hydrofoil. In the case of the 2D hydrofoil, as confirmed in the x-direction velocity distribution, the direction of all flows at the upper part of the hydrofoil changes owing to the hydrofoil. In the case of a 3D hydrofoil, by contrast, the flow is reduced owing to the hydrofoil because of the 3D



(a) Lift coefficient



(b) Drag coefficient

Fig. 14 Comparison of lift and drag performance between two and three dimensional ($\alpha = 4^\circ$)

effect in the lateral direction of the hydrofoil. Thus, the pressure distribution is different between the 2D and 3D hydrofoils.

In the case of a 2D hydrofoil, the x-direction velocity distribution is uniform on the front part of the hydrofoil because the flow coming in is constant. Furthermore, because the water flows in and is delivered in the y-direction in the tunnel inside the hydrofoil, the x-direction flow rate sprayed from the slit is pushed to the span direction, thereby producing a difference in velocity. In the 3D calculation, the velocity distribution in the x-direction shows that the inflow changes velocity in the span direction, and the jet at the tip of the hydrofoil shows that the pushing phenomenon of the span-direction increases, thereby producing a strong jet flow around a side of the hydrofoil. In the velocity distribution of the 3D calculation in the y-direction, a strong vortex occurs at the side of hydrofoil, inducing the velocity in this direction, and this effect affects the jet spray, which causes larger changes of in the x-direction velocity in the 3D calculation than the 2D calculation. Fig. 16 shows the turbulent kinetic energy distribution to visualize the vortex occurring at the side of the hydrofoil and confirms that a high turbulent kinetic energy distribution appears at the side of the hydrofoil.

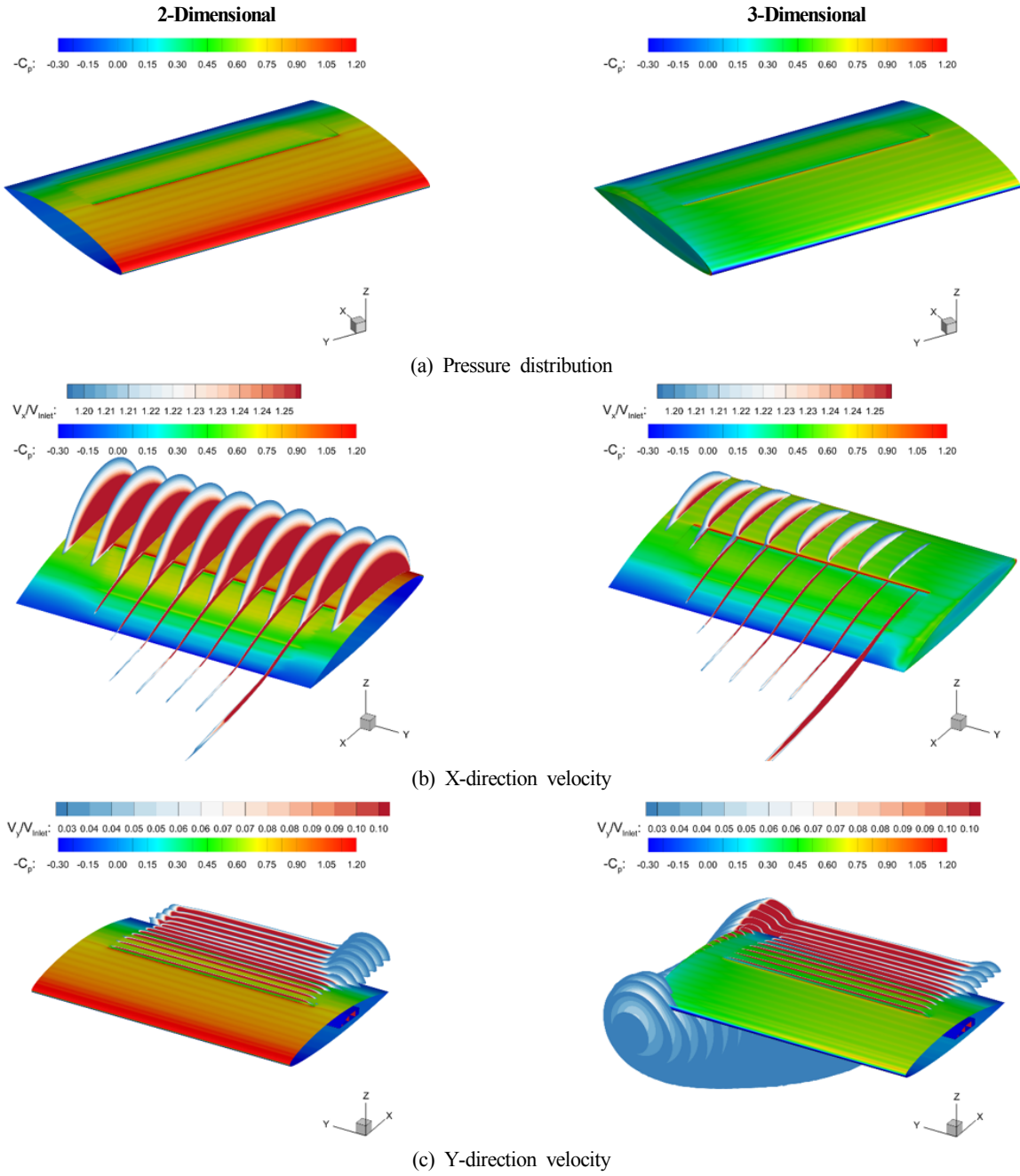


Fig. 15 Flow characteristics around the Coanda hydrofoil ($\alpha = 4^\circ$, $C_j = 0.06$)

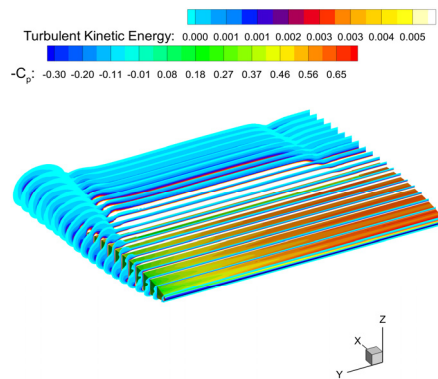


Fig. 16 Turbulent kinetic energy around the Coanda hydrofoil with 3D effect ($\alpha = 4^\circ$, $C_j = 0.06$)

4.2 Performance Variation According to Change of Scale in the Span Direction

As shown in Fig. 17, a study was conducted by selecting two geometry types to analyze the performance variation when the geometry of the hydrofoil is changed by changing the scale of the span direction of the Coanda hydrofoil. The two types were labeled W-type and V-type, respectively, based on their geometry when considering the symmetry of the boundary conditions. W-type has a geometry whereby the size of the span direction changes to $0.625C \rightarrow 0.875C \rightarrow 0.625C$, and the in the case of the V-type, it changes in the sequential order of $1.0C \rightarrow 0.5C$. The projection area of the two geometries is identical.

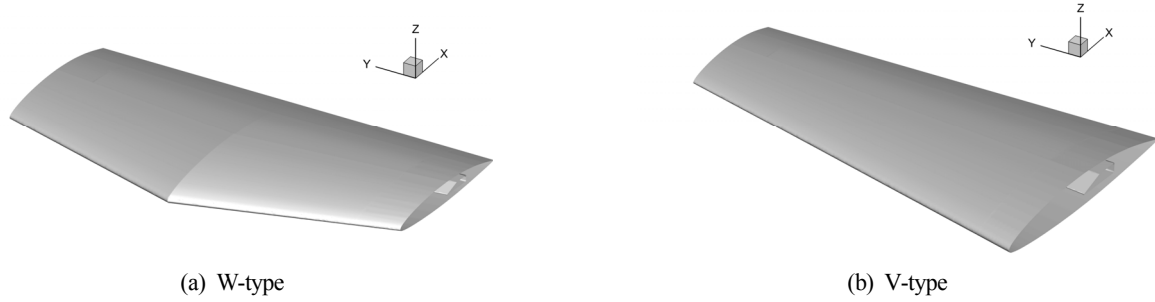


Fig. 17 Various geometry of Coanda hydrofoil

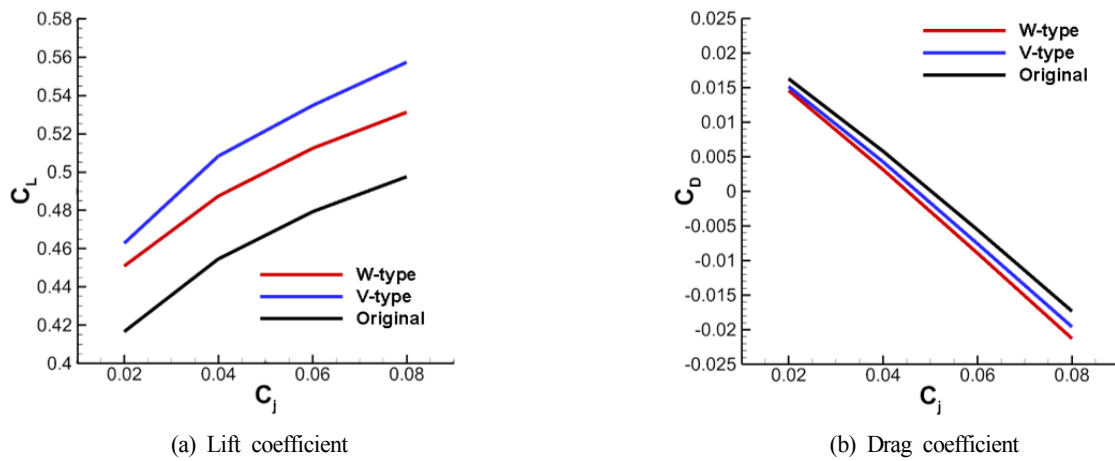


Fig. 18 Turbulent kinetic energy around the Coanda hydrofoil with 3D effect ($\alpha = 4^\circ$)

At an angle of attack of 4° , Fig. 18 compares the lift and drag performances between the W-type, V-type, and the hydrofoil (Original) with a fixed chord length in the span direction. When the size of the chord changes in the span direction, the performance is better than that of the hydrofoil with a fixed chord length, and among them, the V-type shows a relatively larger lift force, and the W-type shows a relatively smaller drag force. To analyze the cause of the performance variation according to the geometry and flow characteristics of the two geometry types, Fig. 19 illustrates the flow characteristics under the conditions of an attack angle of 4° and a jet momentum coefficient of $C_j = 0.06$.

When Fig. 19(d) and Fig. 16 are compared, it can be seen that the vortex at the sides of the W-type and V-type hydrofoils are significantly smaller than that of the Original, and for this reason, the lift and drag performances of the W-type and V-type are high. In the case of Original, the y-direction velocity component is induced only by the vortex at the tip of hydrofoil before the jet slit, as shown in Fig. 15(c). By contrast, in the case of the W-type or V-type, the y-direction velocity component is induced by the slope of the hydrofoil even before the jet slit owing to the angle of inclination of the hydrofoil. As a result, the fluid at the front of the hydrofoil, which is pushed toward the span direction, flows along the slope, thereby reducing the vortex.

In both the W-type and V-type, a large difference occurs in the flow characteristics. In the case of the W-type, the highest lift force occurs

around approximately $0.05S$ – $0.4S$ because the slopes are opposite each other based on the center of the span direction. This phenomenon occurs because the flow is gathered within the $0.1S$ – $0.4S$ area owing to the slope occurring in the shape of the W-type. At $0.5S$, the W-type has a chord length of $0.875C$, at which the slit height is the highest, and for this reason, the jet spraying is concentrated at approximately $0.5S$.

By contrast, in the case of the V-type, the slit height decreases gradually, and the jet is rarely sprayed after $0.6S$, at which the slit height is low, and the jet is concentrated within the area of $0.6S$ or less where the slit height is high. Furthermore, as the y-direction velocity component is generated from the front end of hydrofoil, this movement reduces the vortex at the side of hydrofoil, and owing to this tendency, the V-type has a relatively high lift force compared to the cross-sectional area.

4.3 Performance Variation According to Slit Range

To analyze the performance variation according to the slit range in the span direction, an analysis was conducted for an angle of attack of 4° by changing the slit range in the Original hydrofoil, which had a fixed chord length in the span direction. The slit range was $0.1S$ – $0.5S$, $0.3S$ – $0.7S$, and $0.5S$ – $0.9S$, respectively. The geometry of the hydrofoil is illustrated in Fig. 20, and the numerical analysis results are shown in Fig. 21.

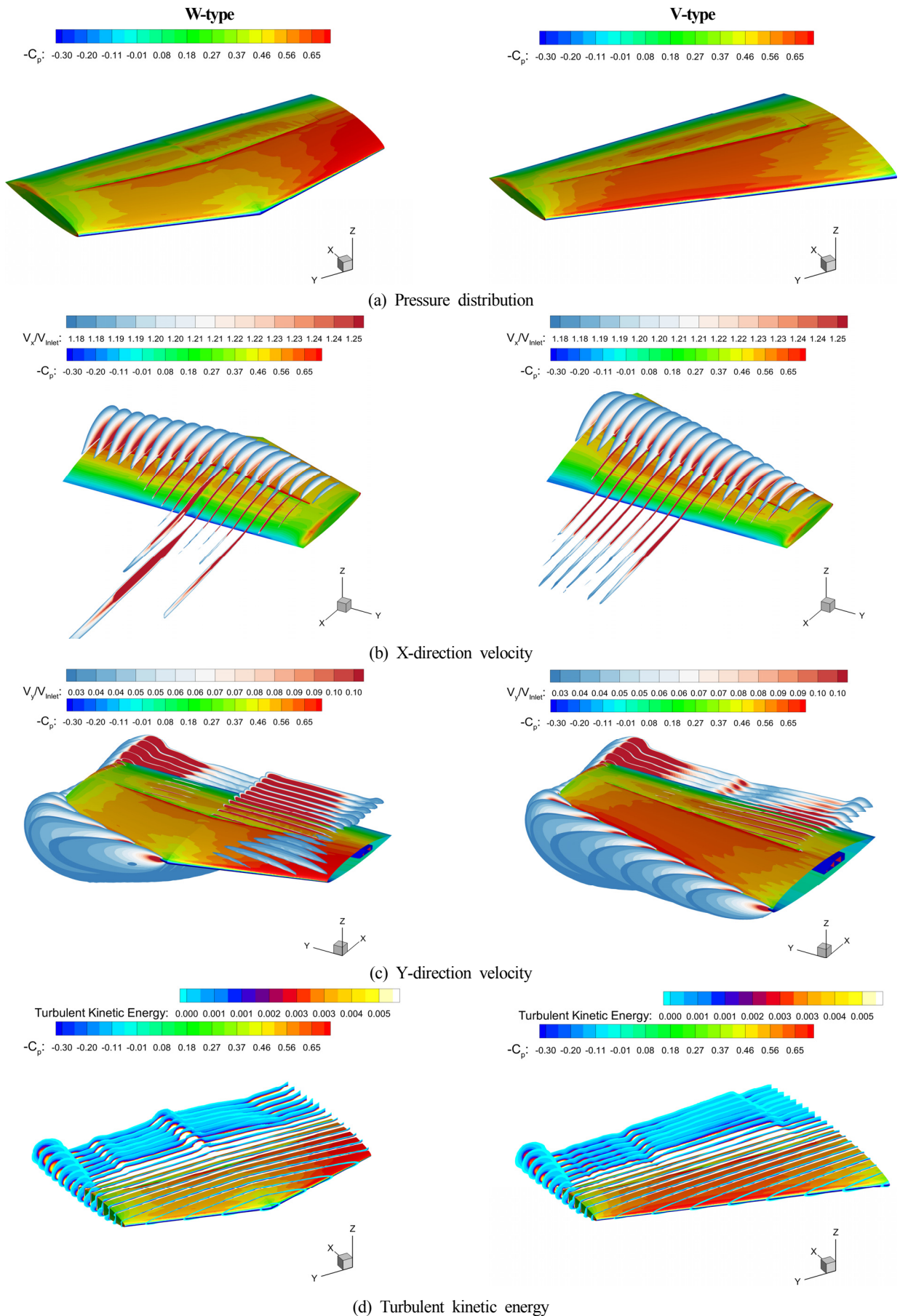


Fig. 19 Flow characteristics around the Coanda hydrofoil with 3D effect ($\alpha = 4^\circ$, $C_j = 0.06$)

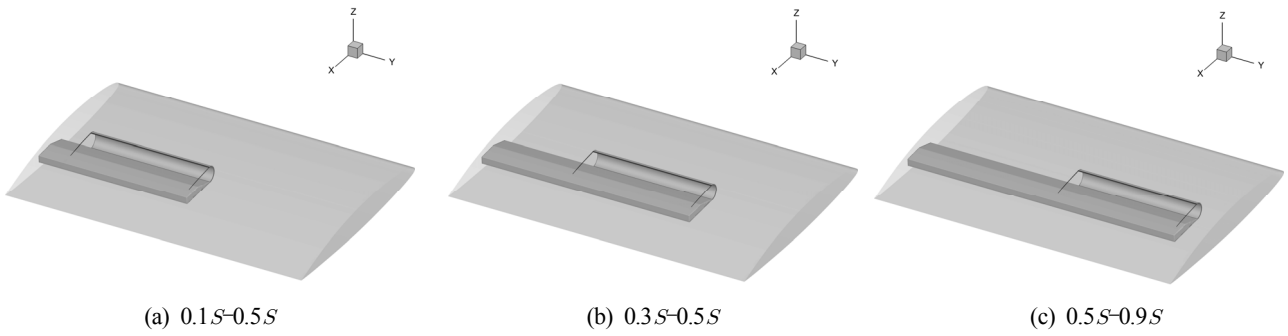


Fig. 20 Geometry of Coanda hydrofoil with various slit range

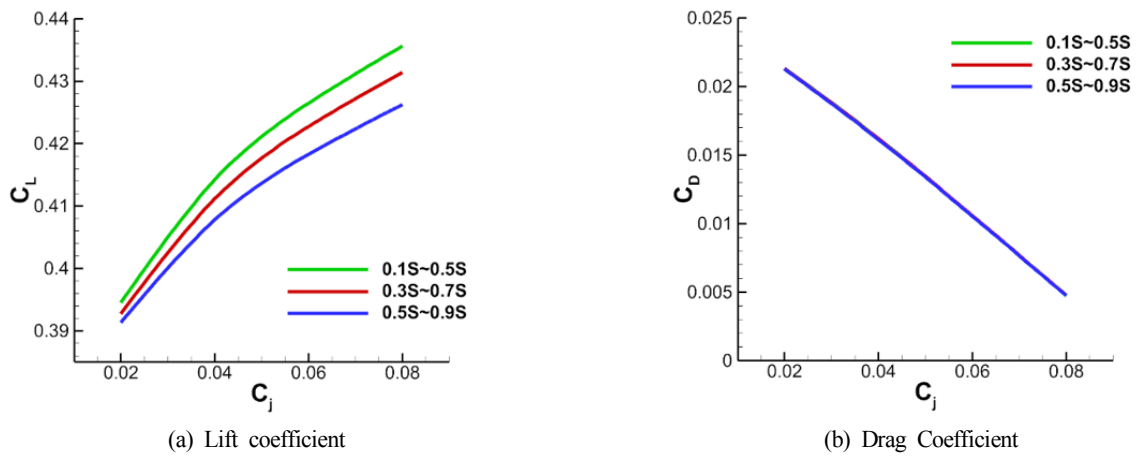


Fig. 21 Comparison of lift and drag performance with various slit range

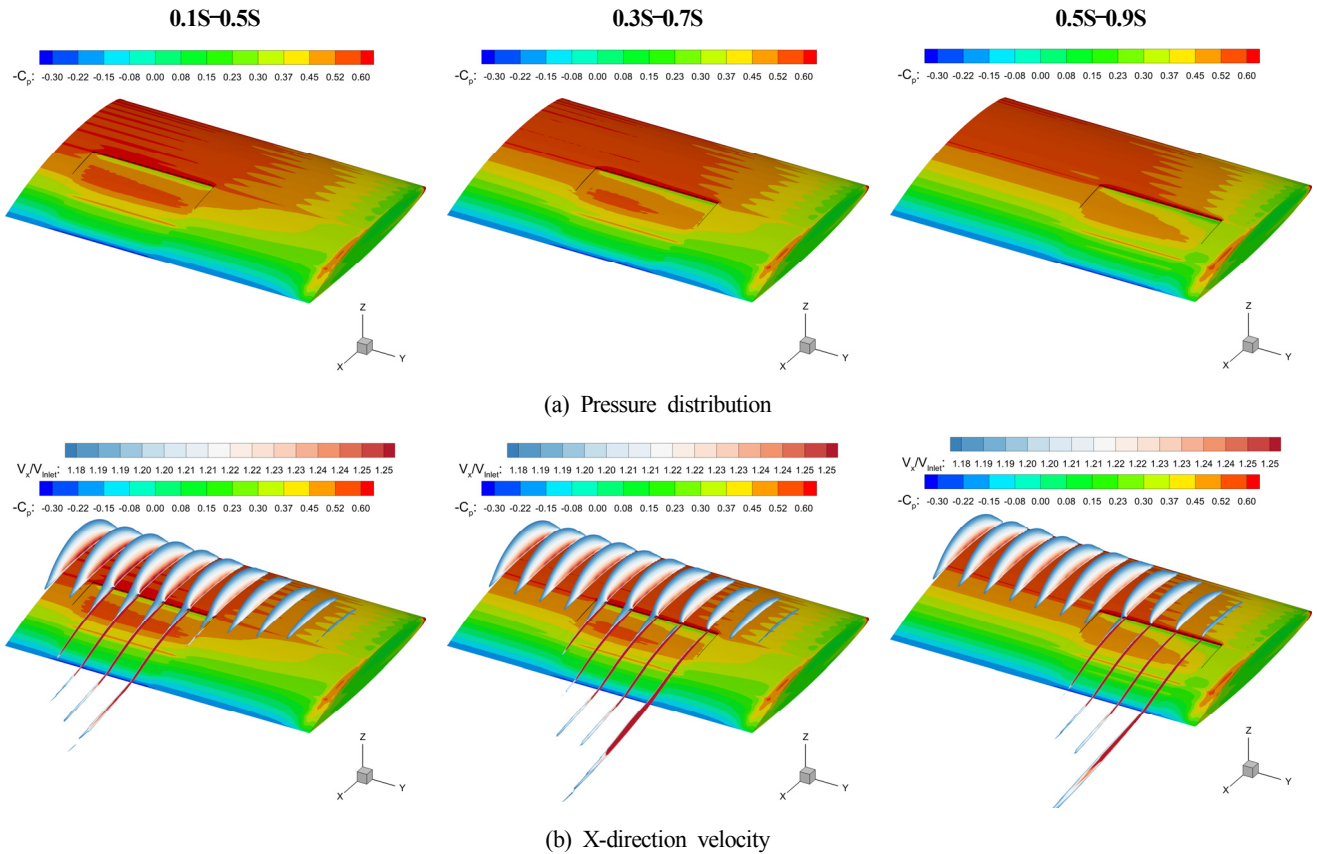


Fig. 22 Flow characteristics around the Coanda hydrofoil with various slit range ($\alpha = 4^\circ$, $C_j = 0.06$) (continuation)

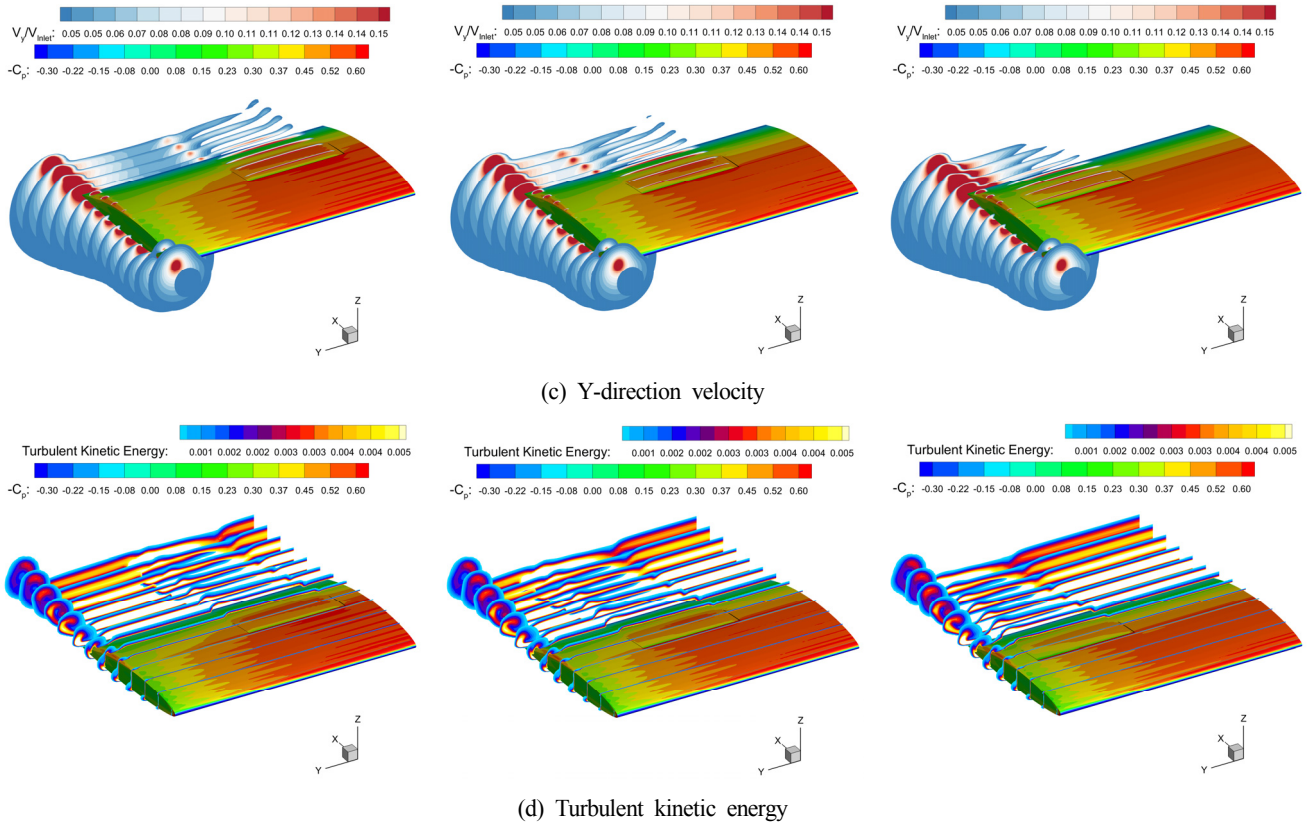


Fig. 22 Flow characteristics around the Coanda hydrofoil with various slit range ($\alpha = 4^\circ$, $C_j = 0.06$)

The lift force decreased overall by approximately 5%–60% in the current case with the half spraying range, as compared to the previous case of spraying 80% in the span direction. As shown in Fig. 21, the drag is extremely similar, with a difference of less than 0.5%, between the slit positions under all conditions, although the lift force shows large differences. When the slit range corresponds to $0.1S$ – $0.5S$, the lift force is at the highest, and as the slit position moves to the side, the lift force tends to decrease. In the case of drag, because the jet spray is identical under all conditions, the propulsion force in the forward direction of the hydrofoil is identical, thereby showing almost no difference in drag. To analyze the cause of the difference in the lift force, Fig. 22 illustrates the flow characteristics at a jet moment coefficient of $C_j = 0.06$.

In Fig. 22(b), as the position of the slit spraying the jet moves to the side, the volume of jet spray changes at the tip of slit, and the jet pushing increases. Furthermore, Figs. 22(c) and (d) show that the flow of the sprayed jet quickly joins the vortex at the side of the hydrofoil. When the slit range is $0.1S$ – $0.5S$, the pressure decrease immediately after the jet spray is the highest because the jet is sprayed at a point relatively far from the vortex at the side of the hydrofoil. Furthermore, considering that the y-direction velocity component increases as the jet spraying slit moves to the side, it is determined that the performance decreases because the sprayed jet is affected by such a vortex. As a result, the performance increases as the sprayed jet is less affected by the vortex generated at the side.

5. Conclusions

Based on a previous study by Eom et al. (2020), to optimize the geometry of jet slit, we conducted a study on the performance variation according to the position and height of the slit and the thickness of the tip where the slit and the top surface of the hydrofoil meet. As the height of slit decreased, the lift force of the hydrofoil increased compared to the drag force. If the thickness of the tip increases, the jet, which has to flow along the hydrofoil, flows along the tip owing to the Coanda effect, thereby increasing the lift and drag performance.

The NACA66 (mod) hydrofoil shows that the best performance is appeared when the slit is positioned at the center of the hydrofoil chord. However, a further study should be conducted to optimize the slit position according to the geometry of the hydrofoil because the pressure distribution is different between hydrofoils.

Afterward, to analyze the 3D effect, a calculation was conducted by opening one side of the hydrofoil in the 2D calculation. When one side is opened, a vortex is generated at the side of the hydrofoil owing to the 3D effect, and for this reason, the fluids flowing into the front part of the hydrofoil are pushed to the span direction, thereby decreasing the lift performance significantly. The vortex has an effect on the sprayed jet. In the results of the analysis conducted by moving the slit position of Coanda hydrofoil, which sprays 40% compared to the span used in the geometry of the Original hydrofoil, the volume of jet spray that joins with the vortex increases as the slit position moves toward the side of the hydrofoil. As a result, the lift performance decreases

because the part that contributes to the circulation of the fluid around the hydrofoil decreases.

Finally, 3D geometries with a taper were studied. Compared to the Original hydrofoil, the hydrofoils having a slope showed a large decrease in vortex at the tip of hydrofoil. In the case of the Original hydrofoil, a large vortex is generated along with the y-direction velocity component, which increases rapidly at the tip of hydrofoil. By contrast, in the 3D geometries with a taper, the fluid is pushed to the span direction because of the y-direction velocity component produced from the front part of the hydrofoil, and as a result, the vortex is decreased at the side. Consequently, the impact of the vortex on the jet spray decreases, thereby increasing the lift and drag performance compared to the cross-sectional area.

Funding

This work was supported by the National Research Foundation of Korea (NRF) grant (No. 2019R1F1A1060883) funded by the Ministry of Science and ICT, Republic of Korea, and the HRD program for Global Advanced Engineer Education Program for Future Ocean Structures (No. P0012646) funded by the Competency Development Program for Industry Specialists of the Korean Ministry of Trade, Industry and Energy, Republic of Korea.

Conflict of interest

No potential conflict of interest relevant to this article was reported.

References

Djojodihardjo, H. (2013). Progress and Development of Coanda Jet and Vortex Cell for Aerodynamic Surface Circulation Control—An Overview. *The SIJ Transactions on Advances in Space Research & Earth Exploration*, 1(1), 32–42. <https://doi.org/10.9756/SIJASREE/V1I12/0102540402>

- Eom, M.J., Paik, K.J., & Lee, J.H. (2020). Numerical Study on the Lift-drag and Cavitation Performances of a Two-dimensional Hydrofoil Using the Coanda Effect. *Journal of Advanced Marine Engineering and Technology*, 44(6), 457–466. <https://doi.org/10.5916/jamet.2020.44.6.457>
- Pfingsten, K.C., & Radespiel, R. (2007). Numerical Simulation of a Wing with a Gapless High-Lift System Using Circulation Control. *New Results in Numerical and Experimental Fluid Mechanics VI*, Springer, Berlin, Heidelberg, 71–79. https://doi.org/10.1007/978-3-540-74460-3_9
- Seo, D.W., Lee, S.J., & Oh, J.K. (2016). Performance Analysis of Stabilizer Fin Applied Coanda System. *Journal of Ocean Engineering and Technology*, 30(1), 18–24. <https://doi.org/10.5574/KSOE.2016.30.1.18>
- Seo, D.W., & Lee, S.H. (2013). A Study to Improve the Lift Performance of a Full Spade Rudder with the Coanda Effect. *Journal of the Society of Naval Architects of Korea*, 50(1), 25–32. <https://doi.org/10.3744/SNAK.2013.50.1.25>
- Yoon, S.H., Jun, D.H., Heo, J.Y., Sung, H.G., & Lee, Y. (2012). Experimental Study of Thrust Vectoring of Supersonic Jet Utilizing Co-flowing Coanda Effects. *Journal of the Korean Society for Aeronautical & Space Sciences*, 40(11), 927–933. <https://doi.org/10.5139/JKSAS.2012.40.11.927>

Author ORCIDs

Author name	ORCID
Eom, Myeong-Jin	0000-0001-7374-7525
Paik, Kwang-Jun	0000-0003-4657-5806
Lee, Ju-Han	0000-0003-3401-0031
Kang, Shin-Min	0000-0003-3638-7465
Kim, Dong-Young	0000-0002-4353-8682

Numerical Study on Taylor Bubble Rising in Pipes

Seung Chul Shin¹, Gang Nam Lee², Kwang Hyo Jung³,
 Hyun Jung Park⁴, Il Ryong Park⁵ and Sung-bu Suh⁵

¹Researcher, Korea Research Institute of Ships and Ocean Engineering (KRISO), Daejeon, Korea

²Post-doctoral researcher, Department of Naval Architecture and Ocean Engineering, Pusan National University, Busan, Korea

³Professor, Department of Naval Architecture and Ocean Engineering, Pusan National University, Busan, Korea

⁴Graduate Student, Department of Naval Architecture and Ocean Engineering, Pusan National University, Busan, Korea

⁵Professor, Department of Naval Architecture and Ocean Engineering, Dong-Eui University, Busan, Korea

KEY WORDS: Slug flow, Multiphase flow, Air injection, Taylor bubble, CFD

ABSTRACT: Slug flow is the most common multi-phase flow encountered in oil and gas industry. In this study, the hydrodynamic features of flow in pipes investigated numerically using computational fluid dynamic (CFD) simulations for the effect of slug flow on the vertical and bent pipeline. The compressible Reynold averaged Navier-Stokes (RANS) equation was used as the governing equation, with the volume of fluid (VOF) method to capture the outline of the bubble in a pipeline. The simulations were tested for the grid and time step convergence, and validated with the experimental and theoretical results for the main hydrodynamic characteristics of the Taylor bubble, i.e., bubble shape, terminal velocity of bubble, and the liquid film velocity. The slug flow was simulated with various air and water injection velocities in the pipeline. The simulations revealed the effect of slug flow as the pressure occurring in the wall of the pipeline. The peak pressure and pressure oscillations were observed, and those magnitudes and trends were compared with the change in air and water injection velocities. The mechanism of the peak pressures was studied in relation with the change in bubble length, and the maximum peak pressures were investigated for the different positions and velocities of the air and water in the pipeline. The pressure oscillations were investigated in comparison with the bubble length in the pipe and the oscillation was provided with the application of damping. The pressures were compared with the case of a bent pipe, and a 1.5 times higher pressures was observed due to the compression of the bubbles at the corner of the bent. These findings can be used as a basic data for further studies and designs on pipeline systems with multi-phase flow.

1. Introduction

Multiphase flow could be encountered in many industrial fields, such as chemical processing, nuclear cooling systems, and oil and gas industries. The oil and gas industry is the most common industry where multiphase flow can occur among them due to the complex processes and oil and gas production, such as drilling, oil and gas transportation from a well to a refinery plant, and separation devices.

The flow patterns/flow regimes can be classified into several types according to the flow rates, the geometry of the system, and the inclination of the pipe in the gas-liquid flow in pipes, such as bubbly flow, slug flow, plug flow, annular flow, and dispersed flow (Brennen, 2005). One of the most common and complex flow regimes is slug flow. Slug flow is identified by the large bullet-shaped bubble occupying more than 60% of the cross-sectional area of the pipe, which is well-known as a Taylor bubble (Davies and Taylor, 1950).

This flow can cause severe internal pipe corrosion, a structural vibration leading to fatigue failure or resonance, and poor reservoir management in oil and gas systems. For a better understanding of slug flow, many experimental studies have been conducted. Among them, the particle image velocimetry (PIV) method is mostly used to measure the flow behavior around the Taylor bubble (Polonsky et al., 1999; Van Hout et al., 2002; Nogueira et al., 2006). Van Hout et al. (2002) investigated the flow field induced by a Taylor bubble rising in a motionless water condition using the PIV method. They measured the average velocity of 100 bubbles and the instantaneous bubble in three different areas. They reported that a rising bubble would not affect the liquid if the liquid was more than 0.5 diameters away from the bubble nose or 12 diameters away from the bubble tail. Nogueira et al. (2006) adopted the PIV method and pulsed shadow technique (PST) to obtain better visualization of the bubble. The velocity field around the bubble and the bubble shape were measured under stagnant and

Received 23 July 2020, revised 26 November 2020, accepted 2 December 2020

Corresponding author Kwang Hyo Jung: +82-51-510-2343, kjung@pusan.ac.kr

© 2021, The Korean Society of Ocean Engineers

This is an open access article distributed under the terms of the creative commons attribution non-commercial license (<http://creativecommons.org/licenses/by-nc/4.0>) which permits unrestricted non-commercial use, distribution, and reproduction in any medium, provided the original work is properly cited.

flowing liquid conditions. The results showed that the bubble shape is strongly dependent on the liquid viscosity.

Although remarkable experimental studies have been conducted to understand slug flow behavior, computation is still necessary to understand the complex nature of slug flow because of the experimental limitations and difficulties. Early numerical studies on slug flow in a vertical pipe revealed computational fluid dynamics (CFD) to be the most effective method to overcome the experimental limitations and study the hydrodynamic characteristics of slug flow in a pipe. Kawaji et al. (1997) reported that the bubble length does not affect the bubble terminal velocity in a stagnant liquid through a vertical pipe using the volume of fluid (VOF) method. Clarke and Issa (1997) proposed a new numerical model that accounts for the small-dispersed bubble behind a Taylor bubble. The model revealed inaccurate results against their assumption. Therefore, they suggested that a future model should use two-fluid model to simulate slug flow with dispersed bubbles properly. Bugg et al. (1998) studied the hydrodynamics characteristics of slug flow in a vertical pipe using VOF. They showed that the results, including bubble shape, bubble rising velocity, liquid film thickness, had good agreement with the experimental data in the literature.

The VOF method is one of the powerful methods that is used widely in this topic (Ndimisa et al., 2005; Taha and Cui, 2006; Zheng and Che, 2007). Among them, Taha and Cui (2006) have published remarkable work. The author discovered that the character of the wake pattern behind the bubble region could be divided by an inverse viscous number, and the change in the liquid viscosity and surface tension results in a change in bubble shape. Later, Kang et al. (2010) discovered that the Archimedes number determines the size of the wake region. Yan and Che (2011) performed a numerical study on the mechanism of slug flow-induced CO₂ corrosion with and without dispersed bubbles. More recently, Massoud et al. (2018) considered dimensionless parameters in the analysis to understand the Taylor bubble rising problem. The correlation, which consists only of the Reynolds and the Froude number, was introduced to calculate the bubble rise velocity.

Despite the significant numerical and experimental studies published on Taylor bubble flow in pipes, they focused mainly on the hydrodynamic features of slug flow; hence, the pressure data induced by slug flow is limited. To investigate the pressure induced by slug flow, a simulation was performed by changing the air injection velocity in the vertical pipe. The effect of the bubble length on the pressure oscillation in the vertical pipe was found, and the peak pressure at different air injection velocities was analyzed. The pressure damping in the pipe was studied using a method to calculate the roll-damping coefficient for the lateral motion of a ship. The bent pipe was studied under the same simulation conditions as the vertical pipe to examine the effects of geometry on the peak pressure in a pipe. In addition, the effects of a change in the air injection velocity on the peak pressure were compared with the effects of a change in the water velocity on the peak pressure.

2. Computational Setup

2.1. Model Geometry

Fig. 1 shows a schematic image of the vertical with the details of two inlets. A 32 mm diameter vertical pipe, 2.5 m in length, with two inlets, one for the water inlet and the other for the air inlet, was used to simulate air-water slug flow in a vertical pipe. Once a certain amount of air was injected, a bubble was self-generated due to the buoyancy induced by the density difference between the water and air. The pressure fluctuations on the wall were monitored using five probes for the simulation time at five different locations (PG1, PG2, PG3, PG4, and PG5). In addition, the same diameter pipeline but bent at 2.5 m was also used to determine the effects of slug flow on a curved pipe wall. Fig. 1(b) presents the bent pipeline geometry. Air was injected through the air inlet at different velocities. Pressure monitors were placed at different positions (PG6, PG7, PG8, and PG9); the solution domain refers to the experiment by Nogueira et al. (2006).

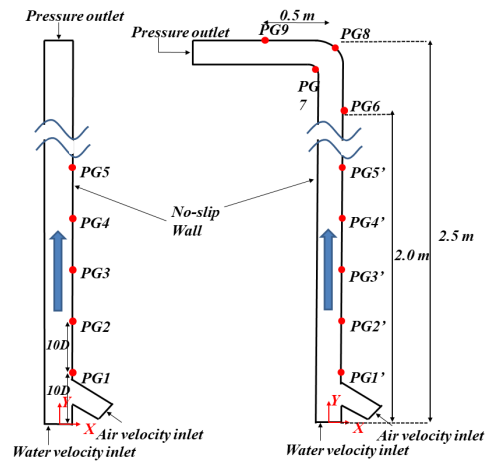


Fig. 1 Schematic image of the computational domain

2.2 Governing Equation

The CFD software Star-CCM+ (CD-Adapco, 2015) was used to simulate the single Taylor bubble rising in the vertical and bent pipe in the co-current condition. In Star-CCM+, the finite volume method (Hirsch, 1988) was considered to discretize the governing equations. As governing equations, continuity Eq. (1) and the Reynolds-averaged Navier-Stokes (RANS) equation (Eq. (2)) are used as follows:

$$\frac{\partial \rho}{\partial t} + \frac{\partial(\rho \bar{u}_i)}{\partial x_i} = 0 \quad (1)$$

$$\rho \bar{u}_j \frac{\partial \bar{u}_i}{\partial x_j} = \rho g_i + \frac{\partial}{\partial x_j} [-\bar{p} \delta_{ij} + \mu (\frac{\partial \bar{u}_i}{\partial x_j} + \frac{\partial \bar{u}_j}{\partial x_i}) - \overline{\rho u_i u_j}] \quad (2)$$

where u_i , ρ , t , x_i , p , μ , and g_i are the fluid velocity, fluid density, time, coordinate, pressure, kinematic viscosity of the fluid, and gravitational force, respectively. The Realizable $k-\epsilon$ model was used to close the RANS equation throughout the study.

To consider the energy convergence and compressibility of air, the energy convergence equation (Eq. (3)) and the ideal gas equation (Eq. (6)) were used in the study.

$$\frac{\partial \rho E}{\partial t} + \frac{\partial(\rho \bar{E} u_i)}{\partial x_i} = - \frac{\partial(\rho \bar{u}_i)}{\partial x_i} + \frac{\partial(\bar{u}_i \tau_{ij})}{\partial x_j} + \rho g_i u_i \quad (3)$$

$$E = e + \frac{1}{2} \bar{u}_i \bar{u}_i \quad (4)$$

$$de = C_v(T) dT \quad (5)$$

$$P = \rho RT \quad (6)$$

where E , P , R , T , e , and C_v are the energy, pressure, gas constant (287 J/kgK in this study), temperature, internal energy, and specific heat at a constant volume (0.717 kJ/kgK in this study)

The Volume of Fluid (VOF) method developed by Hirt and Nichols (1981) was used to track the interface of air and water. The VOF method calculates the volume fraction of the gas and volume fraction of liquid in every computational cell, as shown in Eq. (7).

$$\frac{\partial \alpha_G}{\partial t} + \frac{\partial(\alpha_G u_i)}{\partial x_i} = 0, \quad \alpha_G + \alpha_L = 1 \quad (7)$$

where α_G is the volume fraction of gas and α_L is the volume fraction of the liquid. When the volume fraction of gas is 0 in the cell, it means it is in the liquid phase, where the volume fraction of liquid is 1. As a result, the gas-liquid interface exists in the cell where the volume fraction of gas is between 0 and 1.

2.3 Convergence and Turbulent Model Test

Before examining the effect of slug flow in a pipe using the CFD tool, the grid convergence test was performed about the terminal velocity, which is the constant speed due to the restraining force exerted by the fluid and is one of the main hydrodynamic features of slug flow. The CFD simulations at a liquid velocity of 0.074 m/s, which corresponds to the Reynolds number based on the bubble terminal velocity (Re_{UTB}) of 325 was carried out, and the simulation results were compared with the available experimental data (Nogueira et al., 2006). The coarse and fine meshes were derived by decreasing and increasing the cell numbers per pipe diameter using a refinement factor (r_k) of $\sqrt{2}$ (Böckmann et al., 2014) with a polyhedral mesh. Table 1 provides details of the mesh system. Fig. 2 presents the result of the convergence tests with three different systems, where UTB denotes the bubble terminal velocity. The bubble terminal velocity decreased with increasing number of cells, especially from the coarse mesh to the base mesh system. Grid uncertainty analysis was conducted using the triplets, G_1 , G_2 , and G_3 , with a uniform parameter ratio chosen for $\sqrt{2}$. S1, S1, and S1 are the corresponding solutions of the bubble terminal velocity using the coarse, base, fine mesh grid, respectively. To determine the convergence, the convergence ratio

(R_k), order of accuracy (P_k), and grid uncertainty (U_k) based on the Grid Convergence Index (GCI, Stern et al., 2006; Seo et al., 2016) were obtained using the Eqs. (8)–(10).

$$R_{k,G} = \frac{\epsilon_{k,G23}}{\epsilon_{k,G12}} \quad (8)$$

$$P_k = \frac{\ln(\epsilon_{k,G23}/\epsilon_{k,G12})}{\ln(r_k)} \quad (9)$$

$$U_k = Fs \left| \frac{\epsilon_{k,G12}}{r_k^{p_{k,est}} - 1} \right| \quad (10)$$

where $\epsilon_{k,G12} = S_{k,G1} - S_{k,G2}$, $\epsilon_{k,G23} = S_{k,G2} - S_{k,G3}$ are the differences between coarse-base and base-fine solutions, Fs is a factor of safety (1.25 was used in this study based on the recommendation by Roache (1998)), and $p_{k,est}$ is an estimate of the limiting order of accuracy to 2. When R_k is in the range between 0 and 1, it is called the monotonic convergence.

The grid uncertainty study revealed a monotonic convergence for the bubble terminal velocity with $R_{k,G} = 0.333$ (Table 2). The grid uncertainty ($U_{k,G}$) of 1.540% also verified the monotonic convergence, which is when $U_{k,G} < 5.00\%$. Based on the results of the grid convergence test, the medium mesh structure (G_2) was chosen for further simulations in the study.

Table 1 Grid numbers and the bubble terminal velocity

Case name	Mesh	Grid number	S_k	Time step (s)
G_1	Coarse	850,000	0.345	
G_2	Base	1,800,000	0.330	1.00×10^{-3}
G_3	Fine	4,490,000	0.325	

Table 2 Grid uncertainty analysis results

Parameter	$\epsilon_{k,G12}$	$\epsilon_{k,G23}$	$R_{k,G}$	P_G	$U_{k,G}\%$
U_{TB}	1.500×10^{-2}	5.00×10^{-3}	0.333	3.170	1.540

%* of fine grid mesh value

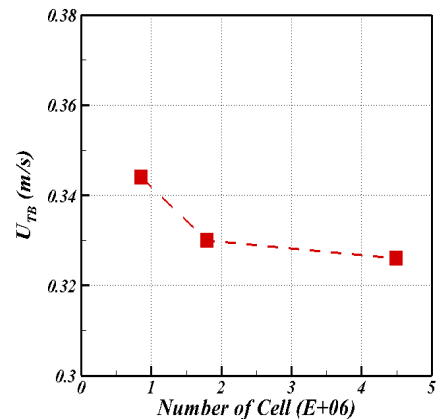


Fig. 2 Grid convergence test for the bubble terminal velocity

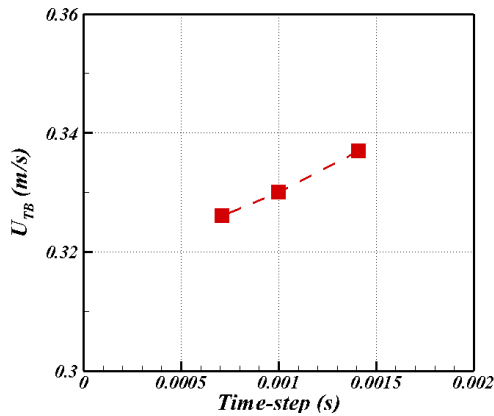
Table 3 Time step and bubble terminal velocity

Case name	Mesh	Time step (s)	U_{TB}	Grid number
T_1	Coarse	1.41×10^{-3}	0.337	
T_2	Base	1.00×10^{-3}	0.330	1,800,000
T_3	Fine	7.07×10^{-4}	0.326	

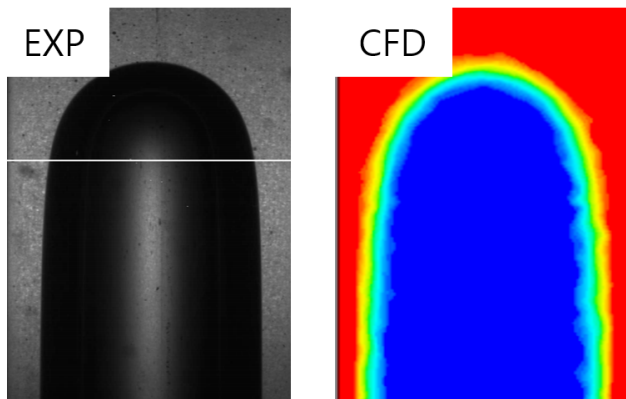
Table 4 Time step uncertainty analysis result

Parameter	$\epsilon_{k,T12}$	$\epsilon_{k,T23}$	$R_{k,T}$	$P_{k,T}$	$U_{k,T}\%$
U_{TB}	7.00×10^{-3}	4.00×10^{-3}	0.571	1.610	1.212

%* of fine grid mesh value


Fig. 3 Time convergence test for the bubble terminal velocity

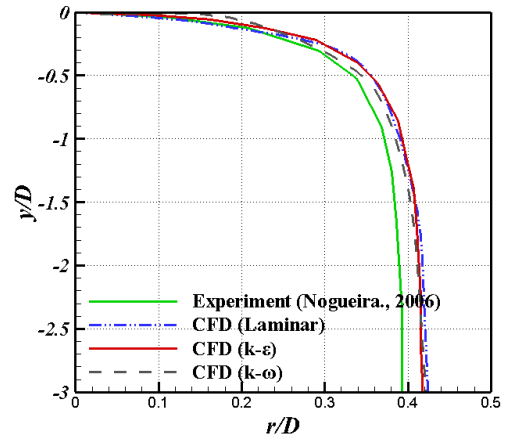
The same procedures were also performed for the time step uncertainty analysis of the simulations. Tables 3 and 4 provide details of the time step uncertainty analysis. The result also shows the monotonic convergence with $R_{k,T} = 0.571$ and time uncertainty with $U_{k,T} = 1.21\%$ (Fig. 3). Both the grid convergence test and time convergence test results were in the monotonic convergence range, and the uncertainty was below 5.00%. Therefore, the base mesh system was chosen, and the time step was set to 1.00×10^{-3} regarding the computational time and accuracy of the result.



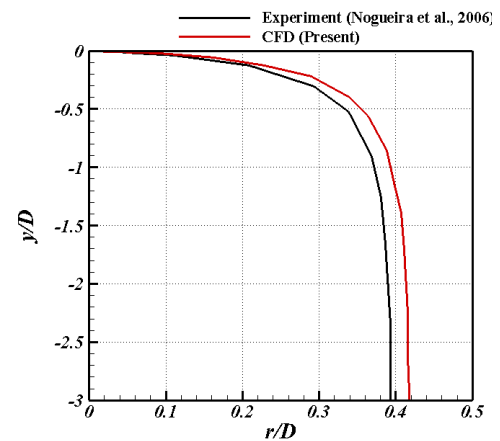
(a) Snapshot

Table 5 Comparison of bubble terminal velocity for various turbulent models

	Experiment (Nogueira et al., 2006)	Laminar	$k-\epsilon$	$k-w$
Velocity (m/s)	0.364	0.292	0.330	0.410
Difference (%)	-	19.7	9.3	12.6


Fig. 4 Comparison of bubble shape for various turbulent models

The flow in the present study was strictly a laminar-liquid and turbulent gas problem (Biberg, 2005). Therefore, the flow characteristics cannot be defined simply by the Reynolds number, such as single-phase flow. To study this type of flow, Naraigh et al. (2011) examined the effects of an interaction between the laminar liquid and turbulent gas in the interface using a physical model. On the other hand, this method is limited in the commercial program Star-CCM+. Therefore, the entire flow region was assumed to be turbulent flow based on fully-developed turbulent gas. Tables 5 and Fig. 4 compare the bubble characteristics in different turbulent models. The Realizable $k-\epsilon$ model showed better agreement than the others. Therefore, the Realizable $k-\epsilon$ was used in this study.



(b) bubble shape

Fig. 5 The experimental and numerical shape of Taylor bubble

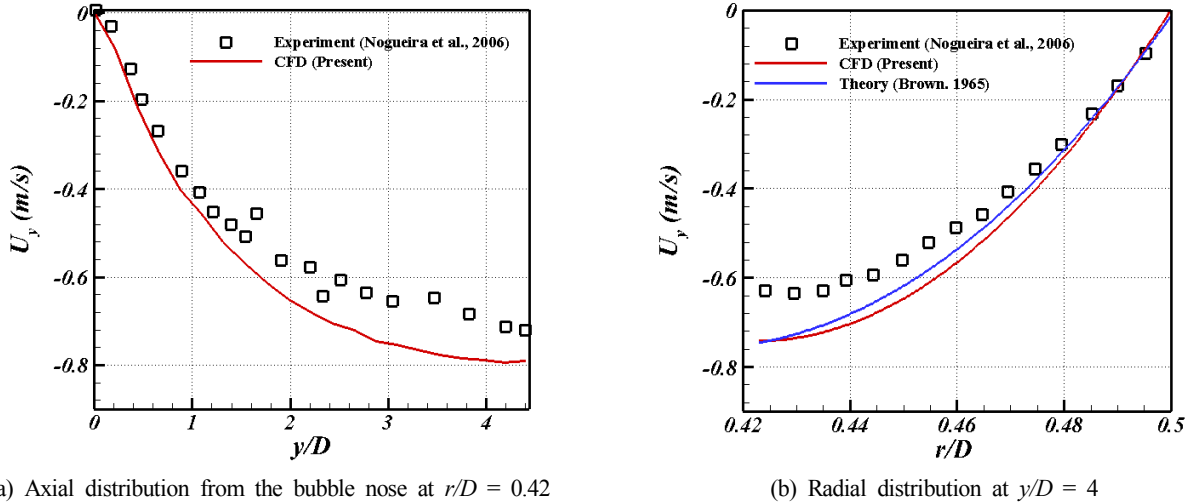


Fig. 6 Experimental and numerical velocity distribution in a fully developed liquid film

2.4 Validation

The simulation was validated by a comparison with the experimental results reported by Nogueira et al. (2006) on a single Taylor bubble rising in co-current flow conditions. The experimental condition corresponds to $Re_{UTB} = 325$, Froud number (Fr_{UTB}) = 0.68, and Eotvos number (E_o) = 167. Fig. 5 compares the simulation and the experimental result of the Taylor bubble shape and liquid film thickness; both are the main hydrodynamic features of the Taylor bubble mentioned by Araújo et al. (2012).

The present simulation agreed well with the bubble shape with a mean difference in the liquid film thickness of 4.11%. The simulation could predict the shape of a bubble with a reasonable liquid film thickness compared to the experimental results.

Fig. 6 shows the axial and radial distribution of the y-direction velocity in the liquid film, comparing the CFD results and experimental results. Fig. 6 presents acceptable matching between the CFD result and experimental result within a 10 % difference. The radial velocity distributions can be compared with the theoretical values suggested by Brown (1965), and the differences were much less than those with the experimental results because the PIV measurements usually have a high level of errors near the bubbles due to the diffraction of its laser sheet.

Furthermore, the bubble terminal velocity of the simulation was compared with the theoretical and experimental results, as shown in Table 6, with the respective deviation. Dumitrescu (1943) suggested a correlation for the bubble terminal velocity, which was developed by Nicklin et al. (1962) as Eqs. (9) and (10).

$$U_0 = 0.351 \sqrt{gD} \quad (11)$$

$$U_{TB} = C_1 U_m + U_0 \quad (12)$$

where g , D , C_1 , and U_m are the gravitational force, diameter,

Table 6 Comparison of the terminal velocity between CFD, theory, and experiment (ρ : 1200.3 kg/m³, μ : 0.043 kg/m·s and Re_{UTB} : 325)

	CFD (Present)	Theory (Nicklin, 1962)	Experiment (Nogueira et al., 2006)
Bubble terminal velocity (m/s)	0.330	0.344	0.364
Difference (%)	-	4.2	10.3

dimensionless coefficient, and mean flow, respectively. The value for the terminal velocity followed the theoretical value and experimental value well. The validation of the present numerical code was conducted around the main hydrodynamic features, such as the bubble shape, bubble terminal velocity, liquid film thickness, and liquid film velocity. All simulations showed good agreement with the experimental data.

2.5 Case Study

In the present study, the first five cases were performed using the vertical pipe by changing the air injection velocity. The liquid velocity and air volume remained constant at 0.074 m/s and 3.06×10^{-4} m³, respectively, which are the same as the experimental data to investigate only the effects of the air injection velocity. The bending pipe was inevitable in the pipeline design for optimal space use under the limited design conditions. Therefore, the vertical pipe and the vertical to horizontal 90° bent pipe were investigated to examine the effects of geometry in the pipe. From Cases 6 to 10, the bent pipe was used to study the effect of geometry under the same conditions as the first five cases. In addition, the simulation considered the laminar, transient, and turbulent regimes by changing the water velocity while keeping the air injection velocity constant to compare the effect of the air injection velocity and the effect of the water velocity. Table 7 provides details of the simulation case.

Table 7 Simulation cases for the bubble rising in a pipe

	Air injection velocity (UA)	Liquid velocity (UL)	Geometry	Re_L	Remark
	(m/s)	(m/s)			
Case 1	0.190		Vertical	66	Laminar
Case 2	0.380		Vertical	66	Laminar
Case 3	0.760	0.074	Vertical	66	Laminar
Case 4	1.520		Vertical	66	Laminar
Case 5	3.040		Vertical	66	Laminar
Case 6	0.190		Bent	66	Laminar
Case 7	0.380		Bent	66	Laminar
Case 8	0.760	0.074	Bent	66	Laminar
Case 9	1.520		Bent	66	Laminar
Case 10	3.040		Bent	66	Laminar
Case 11		0.380	Bent	339	Laminar
Case 12		0.760	Bent	670	Laminar
Case 13		1.520	Bent	1340	Laminar
Case 14	0.380	2.700	Bent	2412	Transition
Case 15		2.900	Bent	2590	Transition
Case 16		3.040	Bent	2714	Transition

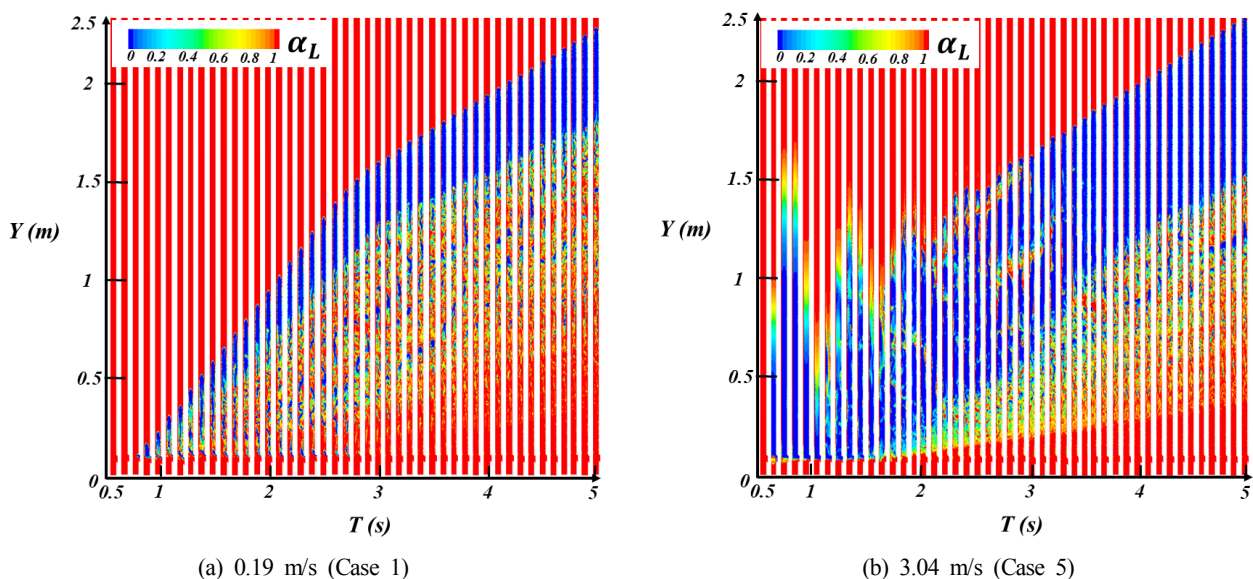
3. Simulation Results

3.1 Slug Flow in a Vertical Pipe

Fig. 7 presents snapshots of the VOF image, which was taken from 0.50 s to 5.00 s with a 0.10 s interval. Cases 1 and 5 were compared to show the difference in bubble behavior at different air injection velocities. The air injection velocity was 0.19 m/s and 3.04 m/s, respectively. In the relatively smaller air injection velocity of 0.19 m/s (Case 1), the air was compressed when the air is started to be injected, and the size of the bubble increased. In Case 5, however, which has a higher air injection velocity of 3.04 m/s, the air fluctuated with the

injection and stabilized. The bubble behavior is described quantitatively as the length of the bubble and is shown in Fig. 8 with the pressure fluctuations at PG2. In Case 1, the bubble length barely changed during the simulation time, and the pressure fluctuations were small. In the Case 5, however, the bubble length initially changed dramatically then stabilized in 2.00 s. A peak pressure occurred at the moment air was first injected, followed by pressure vibrations. Therefore, the air injection velocity affects the bubble length, and it brings a change in pressure fluctuation in the pipe.

Fig. 9 compares the time history of the pressures with various measurement points for cases 1 and 5. The pressures showed the same


Fig. 7 Snapshot of slug flow in a vertical pipe

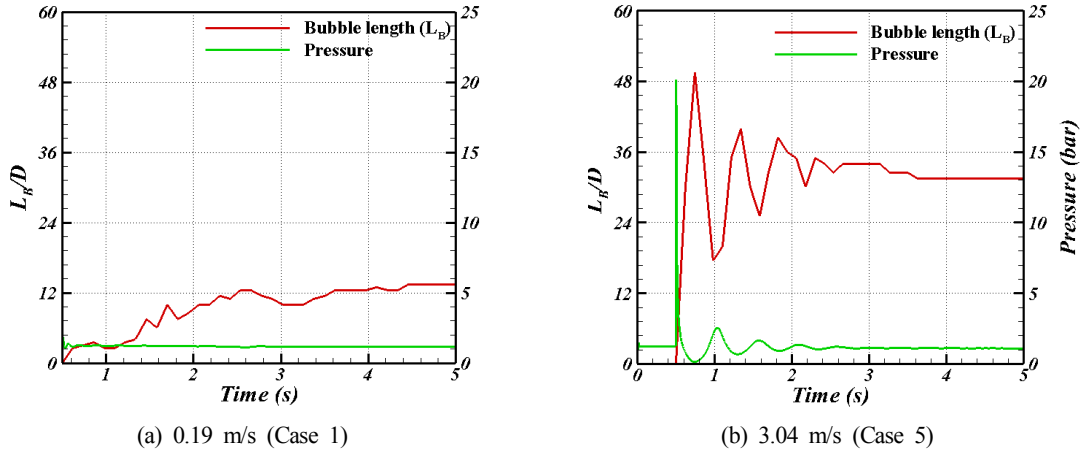


Fig. 8 Bubble length and pressure fluctuation at different air injection velocities

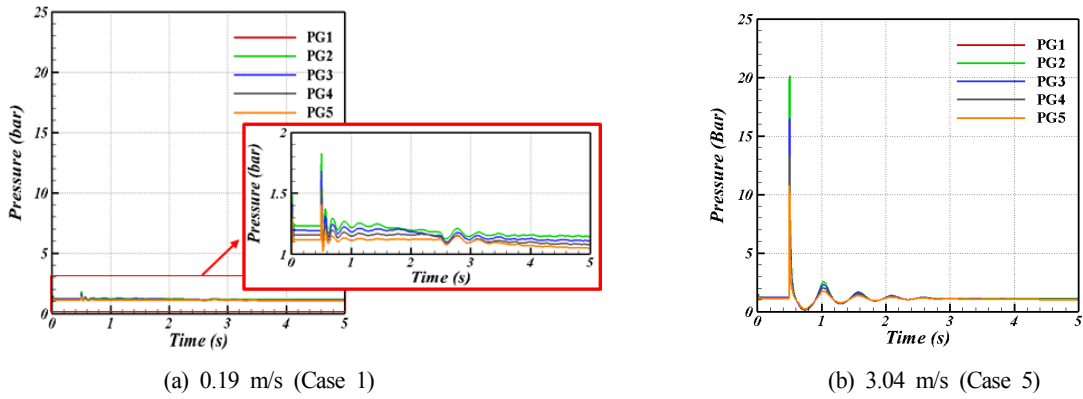


Fig. 9 Comparison of the pressure-time histories for the different measurement positions in Cases 1 and 5

behavior at various measurement positions with those different pressure magnitude. This means that air injection affects the entire region of the pipeline with different injection velocities. Furthermore, a high level of pressure fluctuations was observed in Case 5 because of its high injection velocity. The fluctuations were very small in Case 1, which had the smallest injection velocity.

Fig. 10 presents the results of the peak pressure analysis. The figure shows the change in peak pressure as a function of the air injection velocity and the peak pressure in each location. The peak pressure in the vertical pipe increased linearly with increasing the air injection

velocity (Fig. 10(a)). On the other hand, an opposite trend was observed when the peak pressure was normalized by the air injection velocity. Considering the movement of bubbles (Fig. 7), the peak pressure in the pipe was influenced greatly by the compression of air. When air is injected at a relatively slow flow rate, the air compresses and forms a Taylor bubble and shows a large peak pressure. At a fast flow rate, however, the air is dispersed and shows a small peak pressure, y . Fig. 10(c) shows the dimensionless peak pressure at different locations in each case. The peak pressure increased slightly from PG1 to PG2, and the largest peak pressure is shown in PG2,

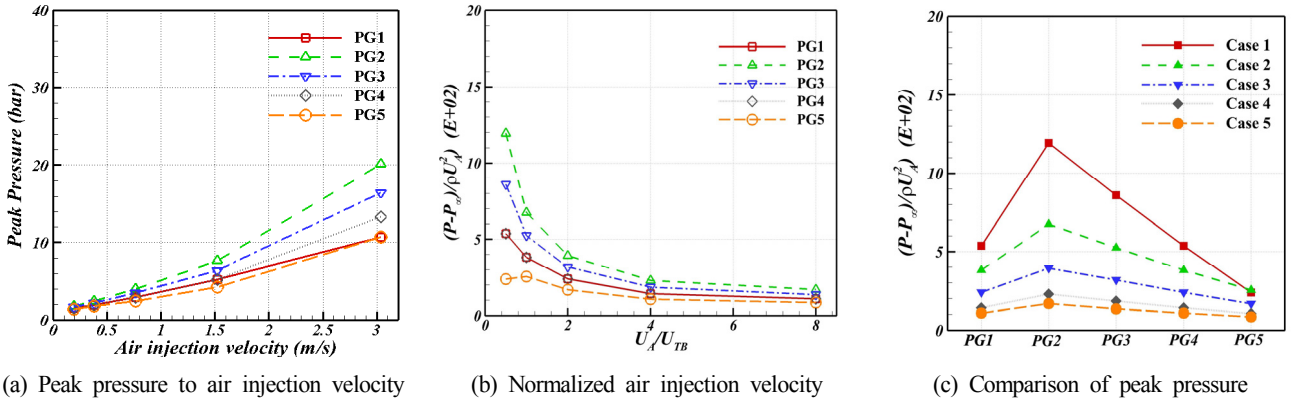


Fig. 10 Peak pressure analysis in a vertical pipe

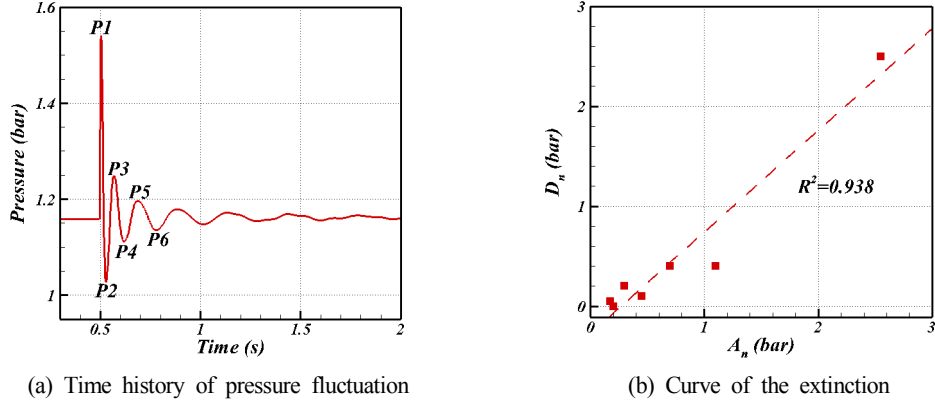


Fig. 11 Example of plotting the extinction curve from the pressure at PG1 in case 1

which decreases gradually from PG2 to PG5 in all cases.

Fig. 11(a) presents the pressure fluctuations at 0.19 m/s of the air injection velocity as a time history. The pressure showed a peak at 0.50 s when air was injected first and decreased with time. The damping was similar to the roll damping for the ship lateral motion. To study this pressure damping, the roll damping coefficient was calculated using Eqs. (13) and (14):

$$A_n = \frac{P_n + P_{n+1}}{2} \tag{13}$$

$$D_n = P_n - P_{n+1} \tag{14}$$

where P_n is the amplitude of the peak pressure, and A_n and D_n are the average and difference of the two successive peak pressure, respectively.

Using Eqs. (13) and (14) with the successive positive peak and negative peak from the pressure data (Fig. 11(a)), the extinction curve was plotted, as shown in Fig. 11(b). At five different locations, the extinction curves were plotted by changing the air injection velocity.

As shown in Fig. 12, the gradient of the extinction curve increased with increasing air injection velocity. This means that the pressure fluctuations at a higher air injection velocity were damped faster than those at a lower air injection velocity. On the other hand, the gradient

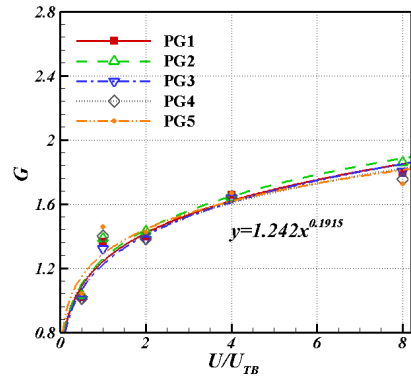
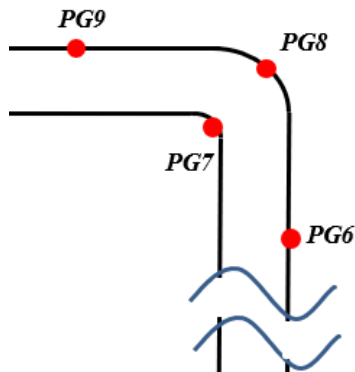


Fig. 12 Gradient of the extinction curve to the air injection velocity for different measurement locations

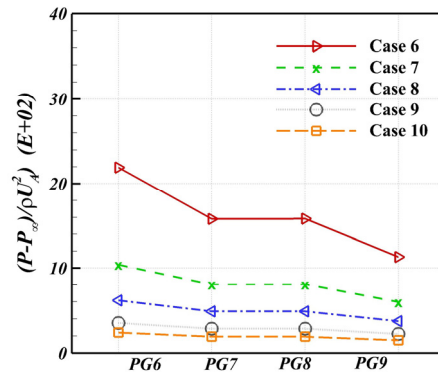
of the extinction curve was unaffected by the location. As described above, the method to calculate the roll-damping coefficient for ship lateral motion was applied to the pressure oscillation induced by the bubble in a pipe. Water appears to play an important role in damping the pressure.

3.2 Slug Flow in a Bent Pipe

As shown in Fig. 13, the peak pressure around the bent area at different air injection velocities was studied. The normalized peak pressure, as the pressure coefficient in the bent pipe, decreased with



(a) Pressure measurement position



(b) Peak pressure

Fig. 13 The peak pressure around the pipe bent

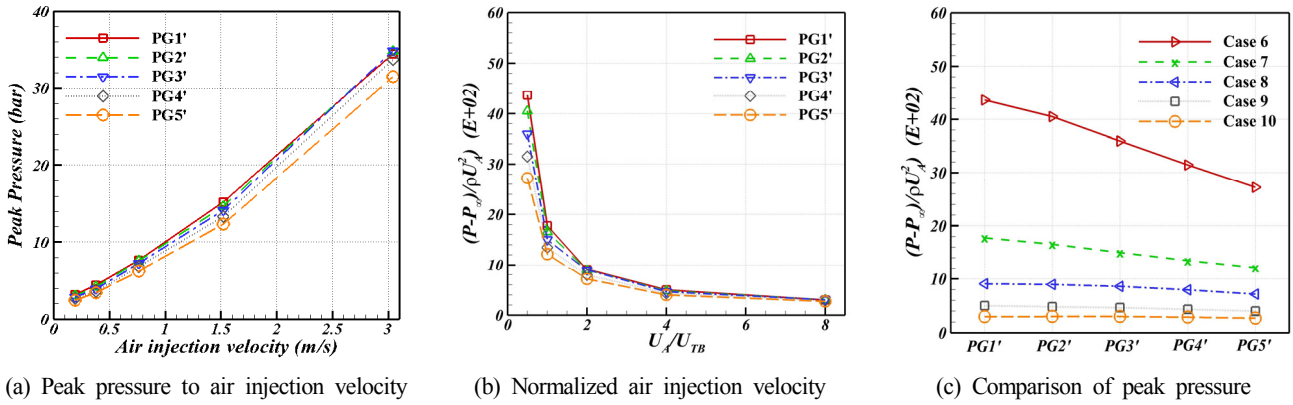


Fig. 14 Peak pressure analysis in the bent pipe

increasing distance from the inlet. This trend weakened as the air injection velocity increased. Although it was expected that the peak pressure difference between PG7 and PG8 was due to the gravitational force, the difference was not noted in terms of the peak pressure. The lack of an apparent difference between PG7 and PG8 might be due to the hydrostatic pressure becoming negligible because of high peak pressure.

The peak pressure analysis in the bent pipe was also conducted and compared with the peak pressure in the vertical pipe. As shown in Fig. 14 (a), the peak pressure in the bent pipe increased with increasing air injection velocity in the same manner of the vertical pipe. Similarly, the peak pressure in the bent pipe was normalized by air injection velocity. The dimensionless peak pressure in the bent pipe decreased more dramatically than that in the vertical pipe as the air injection velocity increased. The largest peak pressure in the bent pipe was 1.5 times higher than that in the vertical pipe. The highest peak pressure in the bent pipe occurred in PG1' and decreased with increasing distance from the inlet to the pressure gauge.

Fig. 15 shows the velocity field of the vertical pipe and bent pipe. When the air was injected, the fluid was stuck at the bend, and instantaneously, a stagnant point that could not be seen in the bent pipe was formed. The velocity was monitored, where the stagnant point was formed in the bent pipe, and the vertical pipe was also monitored at the same location as the one in the bent pipe. Fig. 16 shows the time histories of the velocity at the measurement probe shown in Fig. 15 for Cases 5 and 10. Note that the measurement point for the vertical pipe was 2.4 m away from the inlet and that for the bent pipe was 2.5 m to avoid simulation errors near the pressure outlet. As shown in Fig. 16, the velocity at 0.50 s, when the peak pressure occurs in the vertical pipe, was 4.40 m/s, but the velocity at 0.50 s in the bent pipe was 1.20 m/s. The flow in the bent pipe was slower than that in the vertical pipe, which means that the fluid does not flow properly in the bent pipe. In addition, the velocity in the bent pipe became instantaneously zero when the peak pressure occurred, but there was no point where the velocity became zero in the vertical pipe at 0.50 s. This can explain why the peak pressure in the bent pipe was higher than that in the vertical pipe.

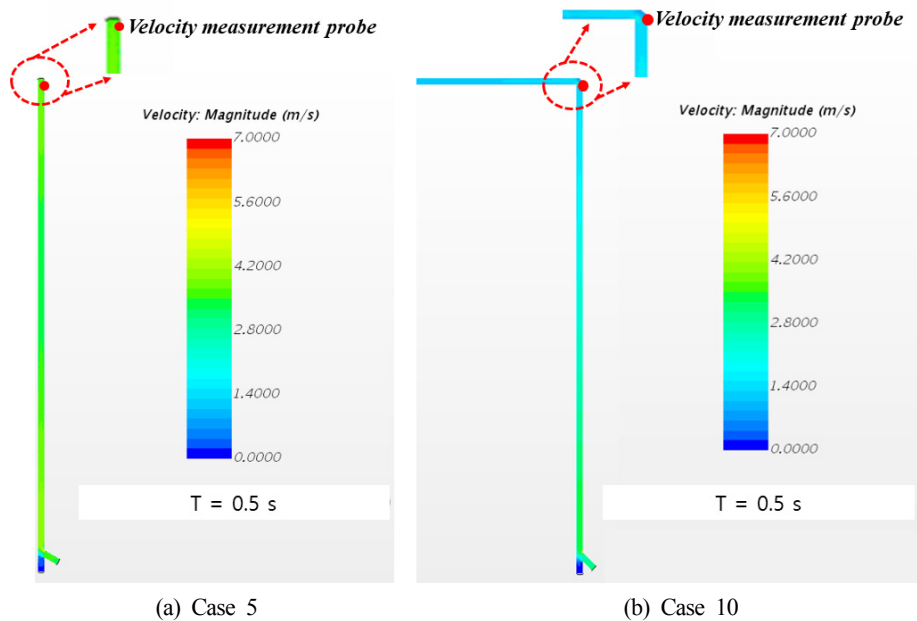


Fig. 15 Velocity field at a 3.04 m/s air injection velocity

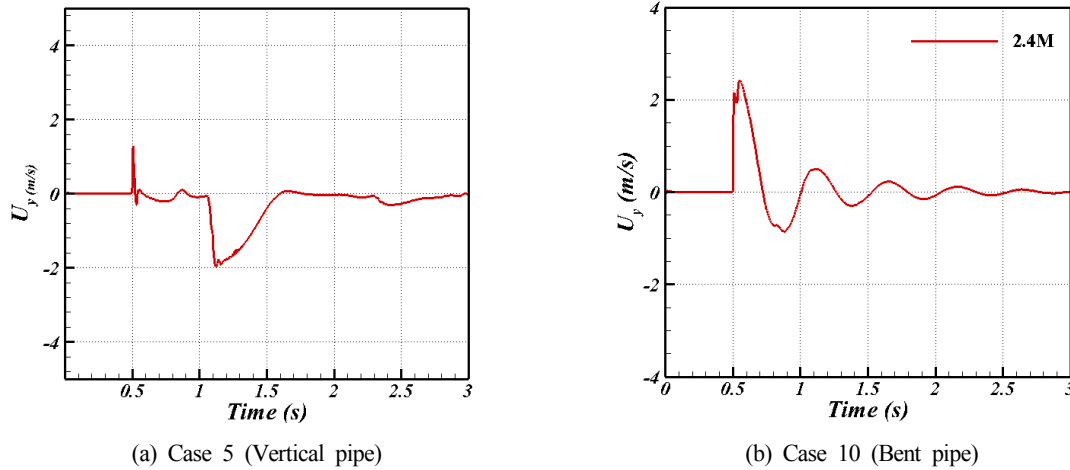


Fig. 16 Time history of the velocity at the measurement probe

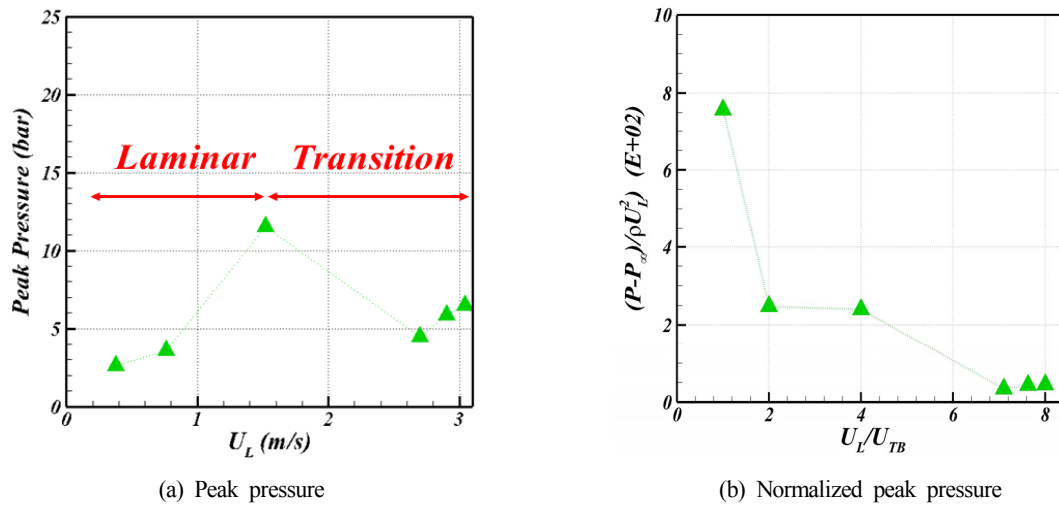


Fig. 17 Comparison of the peak pressures with various water velocity

3.3 Effect of Water Velocity

The effect of the water velocity on the peak pressure in a pipe was investigated by measuring the peak pressure in the bent pipe after changing the water velocity from 0.38 m/s to 3.00 m/s at a fixed air injection. While the peak pressure increased with increasing air injection velocity, the peak pressure increased linearly with increasing water velocity until the water velocity reached to 1.52 m/s, but it decreased after water velocity was more than 1.52 m/s and started to rise slightly at 2.70 m/s and reached the peak pressure, even though the water velocity increased after 3 m/s, as shown in Fig. 17(a). The linear increase region was under the laminar flow. Moreover, the peak pressure of the transient region was irregular, and the region where the peak pressure maintained a certain level was turbulent. When the peak pressure was normalized as the pressure coefficient (Fig. 17(b)), a similar trend was observed for all water flow regimes when the air velocity was changed as the pressure coefficient decreased with increasing water velocity. This means that the compressibility of air is also affected by the water velocity, and its effect is higher when the flow velocity is relatively small.

4. Conclusion

In the present study, the pressures induced by the slug flow in the pipeline were investigated numerically using Star-CCM+. The vertical and bent pipes were considered for various air and water injection velocities. The simulation setups were tested by changing the mesh size and time step based on the GCI method. The simulations were validated with experimental and theoretical data with good agreement for the main hydrodynamic characteristics of a Taylor bubble, i.e., the bubble shape, bubble terminal velocity, and liquid film velocity. The slug flow simulations were conducted by varying the air injection velocity from 0.19 m/s to 3.04 m/s and water velocity from 0.38 to 3.04 to investigate the effects of the bubble on the pressures in the pipeline. The key findings are summarized as follows.

(1) The peak pressures were observed when the air was injected into the pipeline, and pressure oscillations were followed by fluctuations of the bubble length. The pressure oscillations occurred due to the compressibility of air, and the magnitude increased for high air injection velocities. Furthermore, the pressure oscillations showed the

same trend for all the measurement positions because the bubbles affect the entire region of the pipeline.

(2) The peak pressure showed the maximum at the PG2, which was located 20D from the inlet, and it increases with increasing air injection velocity. An opposite trend was shown after normalizing the pressure to the pressure coefficient using the air injection velocity. This means that the peak pressure is strongly affected at lower air injection velocities, because the bubbles can be compressed more at those velocities.

(3) The pressure damping in the vertical pipe was investigated using the method to calculate the roll damping coefficient for the lateral motion of a ship. Damping is stronger at higher air injection velocities, while the distance from the inlet did not affect pressure damping.

(4) When the pipe had a bend, the peak pressure showed a 1.5 times larger magnitude than that in the vertical pipeline in the same air and water injection velocity. The water has a stagnant point at the corner of the bend and causes more air compression in the bent pipe.

(5) The compressibility of the air was also affected by the water velocity, and its effect was higher when the flow velocity was relatively small, showing a similar trend to the air injection velocity. The change in peak pressure with various water velocities was linear when the flow regime was laminar, but it fluctuated when the water velocity increased.

Overall, bends in pipes where slug flow is expected should be minimized in the pipeline design stage because a bent pipe is more vulnerable to slug flow than a vertical one. These findings are based on a simple pipeline geometry, and it can provide useful data for other experimental studies. Nevertheless, further studies on pipeline system design considering slug flow will be needed.

Funding

This study was supported by the R&D Platform Establishment of Eco-Friendly Hydrogen Propulsion Ship Program (No. 20006636), PNU Korea-UK Global Graduate Program in Offshore Engineering (N0001288), and Global Advanced Engineer Education Program for Future Ocean Structures (P0012646) funded by the Ministry of Trade, Industry & Energy (MOTIE, Korea), and the National Research Foundation of Korea (NRF) grant funded by the Ministry of Science and ICT (MSIT, Korea) through GCRC-SOP (No. 2011-0030013).

References

- Araújo, J.D.P., Miranda, J.M., Pinto, A.M.F.R., & Campos, J.B.L.M. (2012). Wide-ranging Survey on the Laminar Flow of individual Taylor Bubbles Rising Through Stagnant Newtonian Liquids. *International Journal of Multiphase Flow*, 43, 131-148. <https://doi.org/10.1016/j.ijmultiphaseflow.2012.03.007>
- Böckmann, A., Pákozdi, C., Kristiansen, T., Jang, H., & Kim, J. (2014). An Experimental and Computational Development of a Benchmark Solution for the Validation of Numerical Wave Tanks. *Proceedings of the ASME 2014 33rd International Conference Ocean, Offshore and Arctic Engineering (Volume 2: CFD and VIV)*, San Francisco, California, USA, V002T08A092. <https://doi.org/10.1115/OMAE2014-24710>
- Biberg, D. (2005). *Mathematical Models for Two-phase Stratified Pipe Flow* (Ph. D Thesis). University of Oslo.
- Brennen, C.E. (2005). *Fundamentals of Multiphase Flow*. Cambridge University Press.
- Brown, R.A.S. (1965). *The Mechanics of Large Gas Bubbles in Tubes: I. Bubble Velocities in Stagnant Liquids*. *The Canadian Journal of Chemical Engineering*, 43(5), 217-223. <https://doi.org/10.1002/cjce.5450430501>
- Bugg, J.D., Mack, K., & Rezkallah, K.S. (1998). A Numerical Model of Taylor Bubbles Rising Through Stagnant Liquids in Vertical Tubes. *International Journal of Multiphase Flow*, 24(2), 271-281. [https://doi.org/10.1016/S0301-9322\(97\)00047-5](https://doi.org/10.1016/S0301-9322(97)00047-5)
- CD-Adapco. (2015). *Star-CCM+ 10.04 User's Manual*.
- Clarke, A., & Issa, R.I. (1997). A Numerical Model of Slug Flow in Vertical Tubes. *Computers & Fluids*, 26(4), 395-415. [https://doi.org/10.1016/S0045-7930\(96\)00016-3](https://doi.org/10.1016/S0045-7930(96)00016-3)
- Davies, R.M., & Taylor, G.I. (1950). *The Mechanics of Large Bubbles Rising Through Extended Liquids and Through Liquids in Tubes*. *Proceedings of the Royal Society of London. Series A. Mathematical and Physical Sciences*, 200(1062), 375-390. <https://doi.org/10.1098/rspa.1950.0023>
- Dumitrescu, D.T. (1943). *Strömung an einer Luftblase im senkrechten Rohr*. *ZAMM-Journal of Applied Mathematics and Mechanics*, 23(3), 139-149. <https://doi.org/10.1002/zamm.19430230303>
- Hirsch, C. (1988). *Numerical Computation of Internal and External Flows (Volume 1: Fundamentals of Numerical Discretization)*. John Wiley and Sons.
- Hirt, C.W., & Nichols, B.D. (1981). Volume of Fluid (VOF) Method for the Dynamics of Free Boundaries. *Journal of Computational Physics*, 39(1), 201-225.
- Kang, C.W., Quan, S., & Lou, J. (2010). Numerical Study of a Taylor Bubble Rising in Stagnant Liquids. *Physical Review E*, 81(6), 066308.
- Kawaji, M., DeJesus, J.M., & Tudose, G. (1997). Investigation of Flow Structures in Vertical Slug Flow. *Nuclear Engineering and Design*, 175(1-2), 37-48. [https://doi.org/10.1016/S0029-5493\(97\)00160-X](https://doi.org/10.1016/S0029-5493(97)00160-X)
- Massoud, E.Z., Xiao, Q., El-Gamal, H.A., & Teamah, M.A. (2018). Numerical Study of an Individual Taylor Bubble Rising Through Stagnant Liquids under Laminar Flow Regime. *Ocean Engineering*, 162, 117-137. <https://doi.org/10.1016/j.oceaneng.2018.04.096>
- Náraigh, L.Ó., Spelt, P.D., Matar, O.K., & Zaki, T.A. (2011). Interfacial Instability in Turbulent Flow over a Liquid Film in a Channel. *International Journal of Multiphase Flow*, 37(7), 812-830. <https://doi.org/10.1016/j.ijmultiphaseflow.2011.02.010>
- Ndinisa, N.V., Wiley, D.E., & Fletcher, D.F. (2005). *Computational Fluid Dynamics Simulations of Taylor Bubbles in Tubular*

- Membranes: Model Validation and Application to Laminar Flow Systems. *Chemical Engineering Research and Design*, 83(1), 40-49. <https://doi.org/10.1205/cherd.03394>
- Nicklin, D.J. (1962). Two-phase Flow in Vertical Tubes. *Transactions of the Institution of Chemical Engineers*, 40(1), 61-68.
- Nogueira, S., Riethmuller, M.L., Campos, J.B.L.M., & Pinto, A.M.F.R. (2006). Flow Patterns in the Wake of a Taylor Bubble Rising through Vertical Columns of Stagnant and Flowing Newtonian Liquids: An experimental Study. *Chemical Engineering Science*, 61(22), 7199-7212. <https://doi.org/10.1016/j.ces.2006.08.002>
- Polonsky, S., Barnea, D., & Shemer, L. (1999). Averaged and Time-dependent Characteristics of the Motion of an Elongated Bubble in a Vertical Pipe. *International Journal of Multiphase Flow*, 25(5), 795-812. [https://doi.org/10.1016/S0301-9322\(98\)00066-4](https://doi.org/10.1016/S0301-9322(98)00066-4)
- Roache, P.J. (1998). *Verification and Validation in Computational Science and Engineering*. Hermosa Publishers: Albuquerque, NM.
- Seo, S., Song, S., & Park, S. (2016). A Study on CFD Uncertainty Analysis and Its Application to Ship Resistance Performance Using Open Source Libraries. *Journal of the Society of Naval Architects of Korea*, 53(4), 329-335. <https://doi.org/10.3744/SNAK.2016.53.4.329>
- Stern, F., Wilson, R., & Shao, J. (2006). Quantitative V&V of CFD Simulations and Certification of CFD Codes. *International Journal for Numerical Methods in Fluids*, 50(11), 1335-1355. <https://doi.org/10.1002/flid.1090>
- Taha, T., & Cui, Z.F. (2006). CFD Modelling of Slug Flow in Vertical Tubes. *Chemical Engineering Science*, 61(2), 676-687. <https://doi.org/10.1016/j.ces.2005.07.022>
- Van Hout, R., Gulitski, A., Barnea, D., & Shemer, L. (2002). Experimental Investigation of the Velocity Field Induced by a Taylor Bubble Rising in Stagnant Water. *International Journal of Multiphase Flow*, 28(4), 579-596. [https://doi.org/10.1016/S0301-9322\(01\)00082-9](https://doi.org/10.1016/S0301-9322(01)00082-9)
- Yan, K., & Che, D. (2011). Hydrodynamic and Mass Transfer Characteristics of Slug Flow in a Vertical Pipe with and without Dispersed Small Bubbles. *International Journal of Multiphase Flow*, 37(4), 299-325. <https://doi.org/10.1016/j.ijmultiphaseflow.2010.11.001>
- Zheng, D., & Che, D. (2007). An Investigation on Near Wall Transport Characteristics in an Adiabatic Upward Gas-liquid Two-phase Slug Flow. *Heat and Mass Transfer*, 43(10), 1019-1036. <https://doi.org/10.1007/s00231-006-0193-8>

Author ORCIDs

Author name	ORCID
Shin, Seung Chul	0000-0002-6275-8090
Lee, Gang Nam	0000-0002-7816-9506
Jung, kwang Hyo	0000-0002-8229-6655
Park, Hyun Jung	0000-0003-1028-9285
Park, Il Ryong	0000-0002-6194-5716
Suh, Sung-Bu	0000-0001-8094-4762

Parameter Study of Boiling Model for CFD Simulation of Multiphase-Thermal Flow in a Pipe

Soh-Myung Chung¹, Yong-Seok Seo², Gyu-Mok Jeon¹, Jae-Won Kim² and Jong-Chun Park³

¹Graduate Student, Department of Naval Architecture and Ocean Engineering, Pusan National University, Busan, Korea

²Under Graduate Student, Department of Naval Architecture and Ocean Engineering, Pusan National University, Busan, Korea

³Professor, Department of Naval Architecture and Ocean Engineering, Pusan National University, Busan, Korea

KEY WORDS: Nucleate boiling, Subcooled boiling, Rohsenow boiling model, Wall boiling model, Computational fluid dynamics (CFD), Multiphase-thermal flow, Pipe flow

ABSTRACT: The demand for eco-friendly energy is expected to increase due to the recently strengthened environmental regulations. In particular, the flow inside the pipe used in a cargo handling system (CHS) or fuel gas supply system (FGSS) of hydrogen transport ships and hydrogen-powered ships exhibits a very complex pattern of multiphase-thermal flow, including the boiling phenomenon and high accuracy analysis is required concerning safety. In this study, a feasibility study applying the boiling model was conducted to analyze the multiphase-thermal flow in the pipe considering the phase change. Two types of boiling models were employed and compared to implement the subcooled boiling phenomenon in nucleate boiling numerically. One was the "Rohsenow boiling model", which is the most commonly used one among the VOF (Volume-of-Fluid) boiling models under the Eulerian-Eulerian framework. The other was the "wall boiling model", which is suitable for nucleate boiling among the Eulerian multiphase models. Moreover, a comparative study was conducted by combining the nucleate site density and bubble departure diameter model that could influence the accuracy of the wall boiling model. A comparison of the Rohsenow boiling and the wall boiling models showed that the wall boiling model relatively well represented the process of bubble formation and development, even though more computation time was consumed. Among the combination of models used in the wall boiling model, the simulation results were affected significantly by the bubble departure diameter model, which had a very close relationship with the grid size. The present results are expected to provide useful information for identifying the characteristics of various parameters of the boiling model used in CFD simulations of multiphase-thermal flow, including phase change and selecting the appropriate parameters.

1. Introduction

In these days, countries around the world have been implementing increasingly stringent environmental regulations on ships. In particular, the International Maritime Organization (IMO) has enforced the regulation to reduce the maximum permitted sulfur content of the exhaust gas emitted from ships from 3.5% to 0.5% since January 1, 2020, and the Maritime Emission Protection Committee (MEPC) agreed to a minimum 50% reduction of the annual greenhouse gas emissions from the total ships by 2050 compared to the level of greenhouse gas emissions in 2008 (Jeong, 2019; Park, 2019; Ji and El-Halwagi, 2020). As a result, alternative energy sources, such as LNG and hydrogen, have begun to attract considerable attention. On the other hand, because LNG-powered ships still emit greenhouse gases (GHG), it is difficult to achieve the MEPC GHG reduction

target, even if all the currently operated vessels are replaced with LNG-powered ships. Therefore, from a long-term perspective, hydrogen-powered ships are attracting increasing attention since hydrogen has similar advantages to LNG. Moreover, hydrogen-powered ships have low noise and vibration, a simple drive system, and no GHG emissions (Lee et al., 2019).

Like LNG, hydrogen needs to be kept in a cryogenic liquid state to maximize its transportation efficiency. Accordingly, it is necessary to develop technologies for a cargo handling system (CHS) and fuel gas supply system (FGSS) by considering insulation and boiling. Hence, methods for accurate analysis of the characteristics of cryogenic liquids are needed to determine the equipment-related specifications of these systems and develop safety standards.

In the analysis of the thermal flow in a pipe through which a cryogenic liquid flows, the physical phenomenon that needs to be

Received 7 December 2020, revised 7 January 2021, accepted 10 January 2021

Corresponding author Jong-Chun Park: +82-51-510-2480, jcpark@pnu.edu

© 2021, The Korean Society of Ocean Engineers

This is an open access article distributed under the terms of the creative commons attribution non-commercial license (<http://creativecommons.org/licenses/by-nc/4.0>) which permits unrestricted non-commercial use, distribution, and reproduction in any medium, provided the original work is properly cited.

considered is 'boiling'. When a cryogenic liquid flows through a pipe, boil-off gas (BOG) or vapor is generated due to the boiling phenomenon caused by heat transfer resulting from the temperature difference between the wall surface and the liquid. An increase in the amount of BOG causes changes pressure in the pipe leading to safety problems. Problems related to BOG generation while transporting cryogenic fluids need to be dealt with urgently before hydrogen-powered ships can be commercialized.

Experimental studies have been carried out to improve the heat transfer performance or investigate the impact of critical heat flux on the industrial equipment and systems in relation to the thermal performance of industrial equipment, such as boilers, nuclear reactors, and cryogenic fluid systems (Krepper et al., 2007). Bartolemei and Chanturiya (1967) proposed relationships between the fluid enthalpy, temperature, and void fraction based on the experimental results. Tolubinsky and Kostanchuck (1970) presented the relationships between the subcooling temperature, bubble departure diameter, and frequency derived from experiments.

In recent years, at the forefront of various engineering design areas, the analysis of fluid flow problems using computational fluid dynamics (CFD) has been gaining attention. Studies to elucidate the process of boiling have been conducted mainly in the field of nuclear engineering. Krepper et al. (2007) performed CFD analysis to compare the experimental values reported by Bartolemei and Chanturiya (1967) with the simulated values. Sontireddy and Hari (2016) compared the Rohsenow boiling model and the wall boiling model with the experiments reported by Bartolemei and Chanturiya. Gu et al. (2017) explained the boiling of subcooled liquids through the combination of several correlation equations using the wall boiling model.

In the present research, one of the experimental cases of Bartolemei and Chanturiya (1967) was implemented using the commercial software, STAR-CCM+ (ver. 15.02.007) to perform a CFD simulation of multiphase-thermal flow considering boiling in the pipes for the transport of cryogenic liquids. Comparative studies of the sensitivity and convergence between different combinations of parameters were performed by varying the coefficients used in the phase change models and grid size.

2. Subcooled Boiling Model

Subcooled boiling occurs when the liquid temperature is lower than the boiling point and the temperature of the wall surface is higher than the boiling point. This refers to a boiling phenomenon, in which bubbles are formed on the heated wall surface, detached from the wall, and absorbed into the liquid. The boiling phenomenon occurs at the initial point of wall boiling when the heat flux is transmitted from the wall, and it is observed in most flows in the pipes. On the other hand, saturated boiling refers to a boiling phenomenon that occurs when most of the liquid reaches the saturation temperature. It occurs when a liquid with the saturation temperature passes over the wall surface that has heat flux. A much larger amount of BOG is generated by saturated

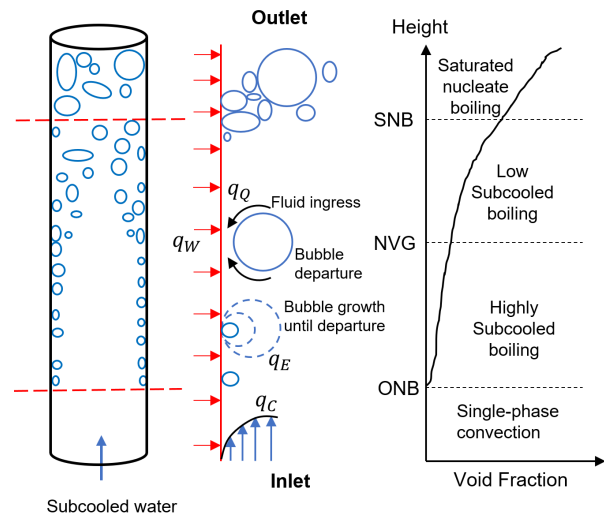


Fig. 1 Schematic diagram of the wall boiling model

boiling than subcooled boiling, so the transportation efficiency is increased if the liquid is set up to maintain a subcooled state when flowing through a pipe.

For example, Fig.1 shows a schematic view of applying the wall boiling model to the experiment reported by Bartolemei and Chanturiya (1967). If subcooled water flows through a pipe and contacts the pipe wall with heat flux, the heat flux is initially used only to increase the temperature of the liquid near the wall. Convection occurs in both the flow near the wall and the flow distant from the wall, resulting in a temperature layer. When the liquid near the wall passes through the onset of nucleate boiling (ONB) stage and reaches the saturation temperature, bubbles are formed in the liquid near the wall. As this vaporization process occurs, boiling occurs gradually. Moreover, as the liquid passes through the net vapor generation (NVG) point, bubbles formed on the wall reach the critical diameter and detach from the wall. Up to this point, some of the liquid detached from the wall is still in a subcooled state, and when the liquid passes through the saturated nucleate boiling (SNB) point, all the liquid in the pipe reaches the saturation temperature.

Approaches of the numerical simulation for multiphase flows using STAR-CCM+ are divided mainly into the volume-of-fluid (VOF) model, the Eulerian mixture model, and the Eulerian multiphase model. Among them, the VOF model calculates the volume fraction of each fluid in the analysis region using a momentum equation for two-phase flow, which are flows of two or more immiscible fluids. This model is applicable to jet flows, bubble flows, and free surface flows. The Eulerian mixture model is similar to the VOF model, but the Eulerian mixture model assumes that the phases can interpenetrate each other. Hence, this model is applied frequently to the problems of pipe flow or mixing flow. Lastly, in the Eulerian multiphase model, it is assumed that the laws of conservation of mass, momentum, and energy are applied to each phase individually with respect to two-phase flows consisting of phases that are treated as interpenetrating continua. Therefore, this model can be applied to several multiphase flow problems that are difficult to deal with using the other two

models, but considerable computation time is needed. In this study, the numerical simulation results of the boiling phenomenon obtained by two different methods, the VOF model and the Eulerian multiphase model, were compared. The two specific models considered in this study were the Rohsenow boiling model among the VOF models and the wall boiling model among the Eulerian multiphase models.

2.1 Rohsenow Boiling Model

The Rohsenow boiling model is a relational expression for a model for nucleate boiling by natural convection and was presented experimentally by Rohsenow (1952). In this model, the heat flux transferred from the wall to the liquid is determined by Eq. (1).

$$q_{bw} = \mu_l h_{lat} \sqrt{\frac{g(\rho_l - \rho_v)}{\sigma}} \left[\frac{C_{pl}(T_w - T_{sat})}{C_{qw} h_{lat} Pr_l^{n_p}} \right]^{3.03} \quad (1)$$

where μ_l is the dynamic viscosity of the liquid phase; h_{lat} is the latent heat of vaporization; g is the gravitational acceleration; ρ_l is the density of the liquid; ρ_v is the density of the vapor; σ is the surface tension coefficient at the liquid-vapor interface; C_{pl} is the specific heat of the liquid phase; T_w is the temperature of the wall; T_{sat} is the saturation temperature; C_{qw} is an empirical coefficient varying with the liquid-surface combination; Pr_l is the Prandtl number of the liquid; n_p is the Prandtl number exponent that depends on the surface-liquid combination.

The vapor mass generation rate, \dot{m}_{ew} , in the region encompassing the total nucleation site was calculated using Eq. (2).

$$\dot{m}_{ew} = \frac{C_{ew} q_{bw}}{h_{lat}} \quad (2)$$

where C_{ew} is the coefficient indicating the degree of contribution of heat flux q_{bw} given by Eq. (1) to vapor bubble formation.

2.2 Wall Boiling Model

The wall boiling model is the nucleate boiling model proposed by Kurul and Podowski (1991), as shown in Fig. 1. The heat flux transferred from the wall to the liquid, q_w , is divided into three components as follows:

$$q_w = q_C + q_E + q_Q \quad (3)$$

where q_C represents convective heat flux, which refers to the contribution of the heat flux transferred from the wall to the convection of the liquid, and is defined by Eq. (4).

$$q_C = h_C (T_w - T_l) (1 - A_b) \quad (4)$$

$$A_b = \min \left(1, K \frac{N_W \pi d_W^2}{4} \right) \quad (5)$$

$$K = 4.8 \exp \left\{ - \frac{J_{a,sub}}{80} \right\} \quad (6)$$

$$J_{a,sub} = \frac{\rho_l C_{pl} \Delta T_{sub}}{\rho_v h_{lat}} \quad (7)$$

where h_C indicates the single-phase heat transfer coefficient; T_l is the average liquid temperature; A_b is a coefficient that depends on the bubble departure diameter and the nucleation site density; K is an empirical constant; N_W is the nucleation site density; d_W is the bubble departure diameter; $J_{a,sub}$ is the subcooled Jacob number; $\Delta T_{sub} = T_{sat} - T_l$ represents the subcooling temperature of the liquid; h_{lat} is the latent heat of evaporation.

q_E indicates the evaporation heat flux. It refers to the contribution of the heat flux transferred from the wall to the boiling of the liquid, and is expressed using Eq. (8).

$$q_E = V_d N_W f \rho_v h_{lat} \quad (8)$$

$$V_d = \frac{\pi d_W^3}{6} \quad (9)$$

$$f = \sqrt{\frac{4}{3} \frac{g(\rho_l - \rho_v)}{d_W \rho_l}} \quad (10)$$

where V_d indicates the volume of vapor bubbles for the bubble departure diameter, and f represents the bubble departure frequency defined by Cole (1960).

Finally, q_Q is the quenching heat flux, which refers to the average heat flux transferred to the liquid when the liquid occupies an empty space immediately after bubble departure, and it is defined using Eq. (11).

$$q_Q = \frac{2k_l}{\sqrt{\pi \lambda_l \tau}} A_b (T_w - T_l) \quad (11)$$

where k_l indicates thermal conductivity; λ_l indicates the diffusivity of the liquid; τ is the periodic time of bubble departure.

In deriving the accurate results from the wall boiling model applied to the analysis of various boiling problems, the most dominant parameters are, N_W , d_W and f . As these parameters vary according to diverse factors, they are generally derived empirically through experiments, and the correlations between these parameters have been studied widely (Kurul, 1990; Alglart, 1993; Alglart and Nylund, 1996; Tu and Yeoh, 2002; Lee et al., 2002; Koncar et al., 2004; Krepper et al., 2007; Chen and Cheng, 2009; Krepper and Rzehak, 2011; Nemitallah et al., 2015; Gu et al., 2017). Previous studies have been confined mostly to selecting the optimal combination of submodels (nucleation site density and bubble departure diameter models), which is suitable only for a specific pressure section of a pipe. Gu et al. (2017) compared five combinations of submodels using ANSYS

Fluent, a commercial analysis program. Compared to ANSYS Fluent, STAR-CCM+ used in this study has limitations in that it does not include the model proposed by Unal (1976) among the bubble departure diameter models. On the other hand, as some combinations were omitted from the comparison in Gu et al. (2017), it was considered necessary to conduct a comparative study using the combinations provided by STAR-CCM+. Therefore, in the present study, an overview of the and models provided by STAR-CCM+ were presented, and a parametric study on the combination of N_W and d_W models and the minimum bubble departure diameter was investigated.

2.2.1 Nucleate site density, N_W

The empirical equation for presented by Lemmert and Chawla (1977) is as follows (LC model):

$$N_W = C^n (T_W - T_{sat})^n \quad (12)$$

where C and n are coefficients determined based on experimental data; they were estimated to be 210 and 1.805, respectively, in Kurul and Podowski (1991).

On the other hand, an empirical equation for N_W proposed by Kocamustafaogullari and Ishii (1983) is as follows (KI model):

$$N_W = \frac{f(\rho^*)}{d_W^2} \left(\frac{4\sigma T_{sat}}{\rho_g h_{lat} d_w \Delta T_e} \right)^{-4.4} \quad (13)$$

$$\Delta T_e = \Delta T_{sup} S \quad (14)$$

$$f(\rho^*) = 2.157 \times 10^{-7} (\rho^*)^{-3.2} (1 + 0.00049\rho^*)^{4.13} \quad (15)$$

$$\rho^* = (\rho_l - \rho_v) / \rho_v \quad (16)$$

where ΔT_e represents the effective superheat, and S is the suppression factor.

2.2.2 Bubble departure diameter, d_W

The general correlation for d_W proposed by Tolubinsky-Kostanchuk (1970) is as follows (TK model):

$$d_W = \min \left(0.0014, 0.006 \exp \left\{ - \frac{\Delta T_{sub}}{45.0} \right\} \right) \quad (17)$$

As shown in Eq. (17), the bubble diameter is limited to 1.4 mm or less in the TK empirical model.

On the other hand, Kocamustafaogullari and Ishii (1983) presented the correlation for d_W as follows (KI model):

$$d_W = 0.0012 (\rho^*)^{0.9} \left[0.0208 \phi \sqrt{\frac{\sigma}{g(\rho_l - \rho_v)}} \right] \quad (18)$$

where ϕ represents the contact angle of bubbles, and ϕ was set to be 80° in Rogers and Li (1994).

3. Numerical Simulation

3.1 Setting Up the Problem of Flow Boiling in a Tube

The accuracy of the boiling model was verified by numerical simulations referring to the experiment conducted by Bartolemei and Chanturiya (1967). As shown in Fig. 2, in the experiment of Bartolemei and Chanturiya (1967), subcooled water with a temperature of 470.63K was induced to flow at a mass flow rate of

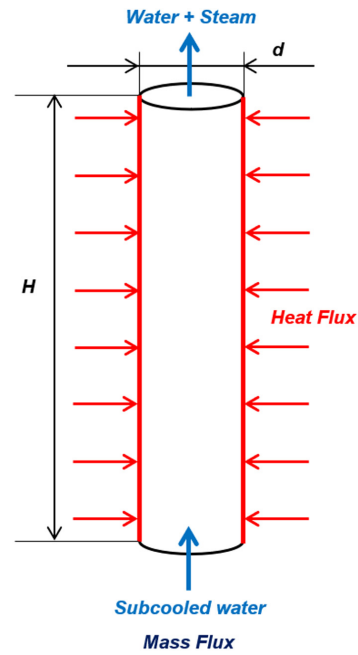


Fig. 2 Definition of the problem of flow boiling in a tube

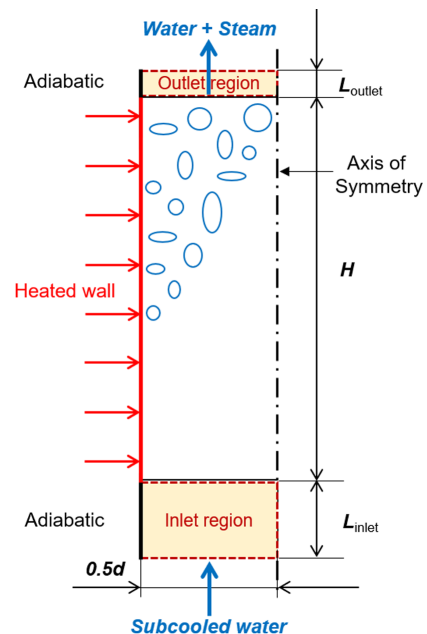


Fig. 3 Simulation conditions of flow boiling in a tube

900kg/m²·s into a vertical tube made of stainless 1Cr18Ni9Ti steel with a height (H) of 2.0m and a diameter (d) of 15.4mm. A constant heat flux of 570 kW/m² was applied to the surrounding wall to induce a phase change of the water into vapor, and the temperature and vapor content according to the flow enthalpy were measured. At this time, the initial pressure inside the tube was set to 45 bar ($= 45 \times 10^5$ Pa).

The conditions and configuration of the numerical simulation were set to be as similar as possible to those of the experiment, as shown in Fig. 3. As reported by Wang and Yao (2016), there were only slight differences between the analysis results of two-dimensional and three-dimensional simulations of multiphase flows in a cylindrical-shaped tube. Hence, two-dimensional simulations were carried out by applying the axis of symmetry to reduce the computation time. At the inlet, the vertical length of the inlet region (L_{inlet}) was set to 0.5m to allow subcooled water to achieve fully developed flow. At the outlet, the vertical length of the outlet region (L_{outlet}) was also set to 0.1m to allow the flow to exit smoothly. Furthermore, by applying axial symmetry, only one wall in Fig. 3 was heated with the heat flux level observed in the experiment. Adiabatic conditions were set for other walls except for the heated section. The simulations were conducted by assuming a steady state based on Sontireddy and Hari's (2016) results, who reported no significant differences in the simulation results between the steady and unsteady states.

3.2 Simulation Results

Regarding the subcooled boiling phenomenon in a boiling tube, the void fraction according to the height was calculated by applying the Rohsenow boiling model and the wall boiling model. The simulations were compared with the experimental results (Bartolemei and Chanturiya, 1967). In the case of the wall boiling model, as summarized in Table 1, the simulation was performed using the combinations of important parameters, such as the nucleation site density and the bubble departure diameter models. After a comparative analysis of the simulated values obtained through simulation, the Kocamustafaogullari-Ishii(KI) model of the nucleation site density

Table 1 Simulation cases with various parameters

Case No.	N_w model	d_w model	Grid size (mm)	Minimum diameter of bubble (mm)
1	LC	TK	0.6	0.1
2	LC	KI	0.6	0.1
3	KI	TK	0.6	0.1
4			1.0	0.1
5			0.8	0.1
6			0.7	0.1
7				10
8				1
9	KI	KI	0.6	0.1
10				0.01
11				0.001
12			0.5	0.1
13			0.4	0.1

model was applied as the final selected condition. Thereafter, for cases to which the KI model was applied for the bubble departure diameter model, after evaluating the grid convergence, research was carried out by varying the minimum diameter of vapor bubbles.

3.2.1 Comparison between different boiling models

Fig. 4 shows the void fraction distribution obtained by applying two different boiling models. In the Rohsenow boiling model, the comparison between simulated and experimental values showed that the initial bubble formation proceeded faster. In the wall boiling model, however, the simulation results from initial bubble formation to the bubble growth process were in relatively good agreement with the experimental values. This difference was because the Rohsenow boiling model does not appropriately reflect the boiling process by forced convection (Domalapally et al., 2012). Boiling by forced convection occurs due to the forced motion of a fluid. Therefore, to consider this phenomenon in future studies, it is necessary to make a comparison by applying the boiling model proposed by Bergles and Rohsenow (1964). On the other hand, a comparison of the void fraction values near the outlet showed that both models yielded void fractions that approximated the experimental values very closely. On the other hand, as summarized in Table 2, a comparison of the total solver elapsed time showed that the wall boiling model took approximately two times longer calculation time than the Rohsenow boiling model. Therefore, the wall boiling model appears to be more suitable for analyzing subcooled boiling problems, including the bubble formation and growth processes near the wall but required two times longer computation time.

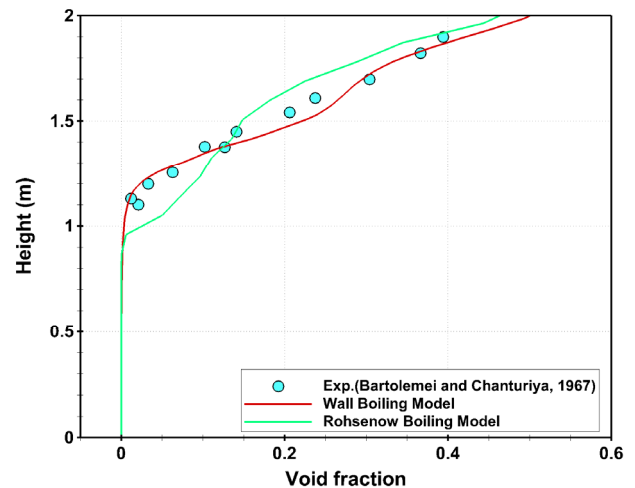


Fig. 4 Comparison of the void fraction distribution through different boiling models

Table 2 Total solver elapsed time for different boiling models

Iterations	Rohsenow boiling model	Wall boiling model
	Total solver elapsed time (s)	
10000	2,086	4,278
20000	4,165	8,669

3.2.2 Comparison of the simulation results by different combinations of nucleation site density and bubble departure diameter models (Cases 1-3 & 9)

For Cases 1-3 and 9 in Table 1, Fig. 5 shows the void fraction distribution according to the height. Comparative analysis is needed because the accuracy of the wall boiling model varies according to the combination of the nucleation site density model and the bubble departure diameter model. An examination of the void fraction distribution obtained by each model combination showed that the changes depending on the bubble departure diameter model were more pronounced than those depending on the nucleation site density model. For this reason, the results obtained by applying the KI model as the bubble departure diameter model were closer to the experimental values. On the other hand, the comparison of Case 2 with case 9 showed that Case 9, in which the KI model was applied as the nucleation site density model, approximated more closely the range of the void fraction distributions measured in the experiment. Based on these results, for the cases where the KI model was applied for both the nucleation site density model and the bubble departure diameter model, the grid convergence test and the sensitivity test were conducted to evaluate the grid convergence and sensitivity according to the minimum bubble diameter. Sections 3.2.3 and 3.2.4 present the methods and results of the grid convergence test and the sensitivity test, respectively.

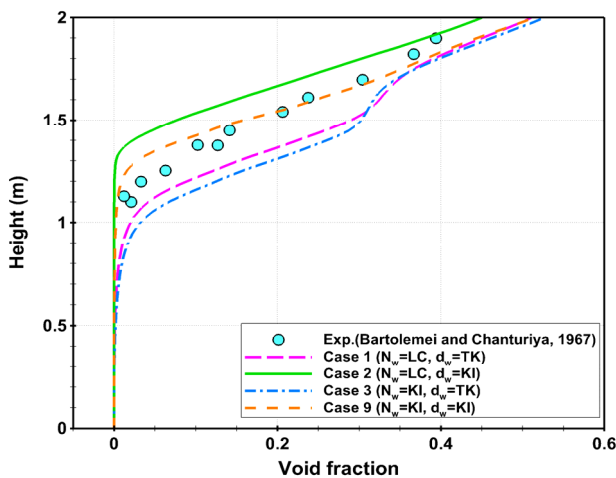


Fig. 5 Comparison of the void fraction distribution with the combinations of several models

3.2.3 Grid convergence test (Cases 4-6, 9, 12 & 13)

Fig. 6 shows the void fraction distribution among the results obtained by the grid convergence test for cases where the KI model was applied in both the nucleation site density model and the bubble departure diameter model. As the grid size became smaller, there was a larger difference between the void fraction distribution in the section of $H=1.1-1.7$ m (the ONB-SNB section), where the initial bubbles started to be generated on the wall, and the results closely approximated the experimental results. At the outlet region, however, there was no significant difference in the void fraction according to the grid system.

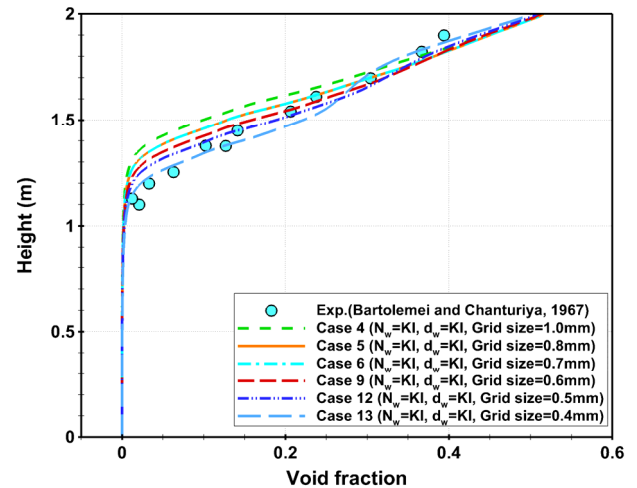


Fig. 6 Distribution of the void fraction with different grid systems

Fig. 7 presents the temperature distribution of the liquid according to the grid system along the central axis of symmetry in the pipe. Looking into the result, the impact of the grid size was found to be mostly insignificant in the overall sections from the inlet region to the onset of nucleate boiling (ONB) section. However, in the net vapor generation-saturated nucleate boiling (NVG-SNB) section ($H \approx 1.3-1.7$ m), where the ratio of vapor in the internal liquid becomes relatively higher, large differences according to the grid size were observed. This is believed to be related to the grid resolution, which indicates the degree of ability to represent the mixture of the generated vapor and liquid numerically. On the other hand, in the SNB section ($H \approx 1.7-2.0$ m), where saturation boiling is dominant, there was a slight difference between the simulated and experimental values regardless of the grid resolution. This disparity was attributed to the increased outlet region for a stable numerical calculation and the constant temperature for the added outlet region. Another cause is believed to be differences due to the combination of the nucleate site density model and bubble departure diameter model. Gu et al. (2017) applied the LC model to the nucleate site density and the KI model to

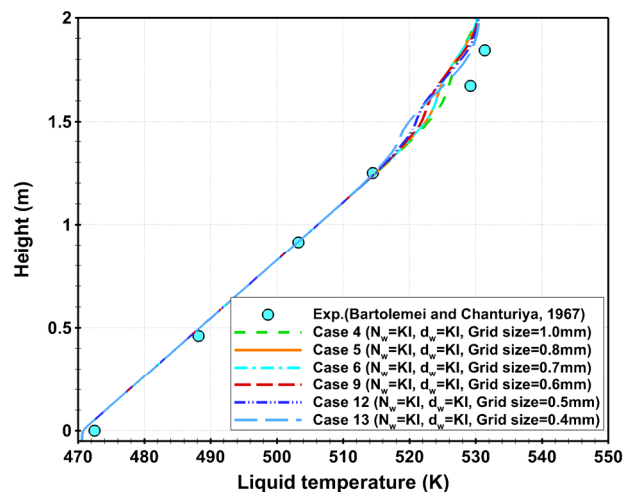


Fig. 7 Distribution of liquid temperature with different grid systems

the bubble departure diameter. They reported that the numerical results for the liquid temperature distribution in the same section ($H \approx 1.7$ – 2.0 m) showed good agreement with the experimental results. On the other hand, a comparison of the void fraction distribution showed large differences. These results suggest that when multiphase-thermal flow in a pipe is simulated, the model combination selected may vary depending on which physical quantities are used as the basis for analysis. Therefore, it is important to apply the optimal boiling model through the combination of submodels and parametric studies.

3.2.4 Relationship between the minimum bubble departure diameter and grid size (Cases 7–11)

Section 3.2.3 showed differences in the growth process of initial bubbles according to the grid size. This section analyzed the relationship between the grid size and the minimum bubble departure diameter. Fig. 8 presents the void fraction distribution obtained by fixing the grid size and varying the minimum diameter of bubbles. The void fraction distribution could be clearly distinguished based on the minimum bubble departure diameter of 1 mm. In Cases 7–11, the grid size is 0.6 mm, and it can be seen that the accuracy of the boiling model may be decreased when the minimum bubble departure diameter is 1 mm or 10 mm, which is larger than the grid size. On the other hand, all the results tended to converge when the minimum bubble departure diameter was smaller than the grid size.

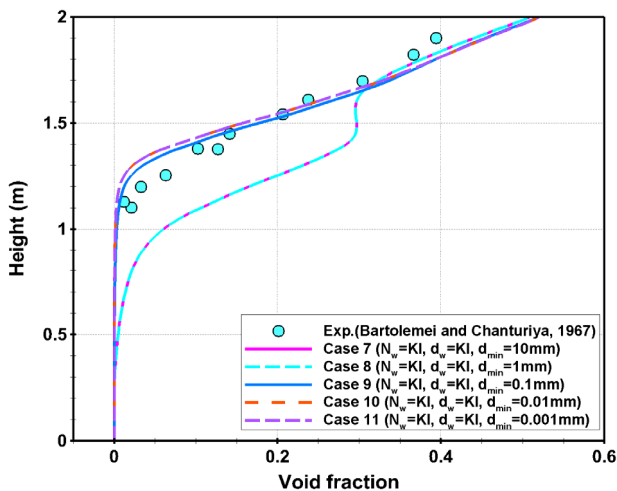


Fig. 8 Comparison of the void fraction distribution by the minimum bubble departure diameter

3.2.5 Results of subcooled boiling (Case 9)

Fig. 9 presents the temperature distribution of the liquid in the pipe and the volume fraction of vapor obtained by numerical simulation for Case 9. The left wall of the tube is heated, and the central axis of symmetry is located on the right. The temperature distribution of the liquid suggests that as subcooled water flows into the heated pipe, the water temperature near the wall increases, and the temperature distribution of the flow in the entire pipe changes with increasing height. In addition, the distribution of the volume fraction of vapor

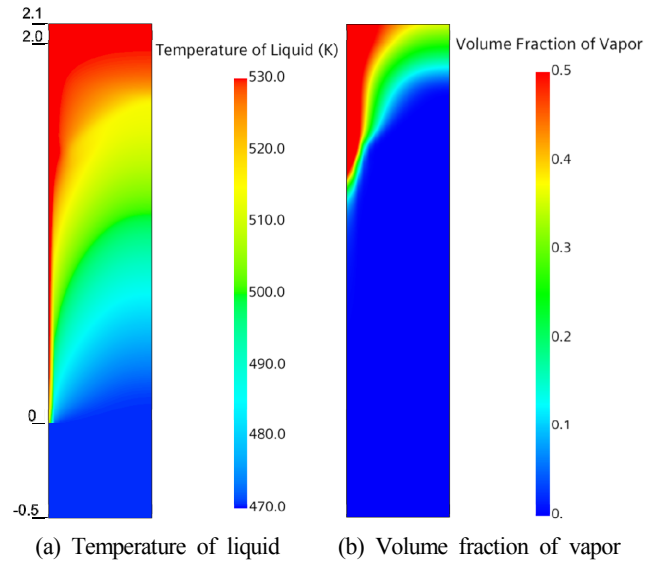


Fig. 9 Distribution of temperature and volume fraction in a vertical section of the tube during flow boiling

shows the mechanism through which as the temperature of the liquid near the wall becomes higher than the saturation temperature; the liquid changes into a vapor, and the liquid and vapor are mixed in the pipe.

4. Conclusion

To simulate multiphase-thermal flow in a pipe, including phase change, the applicability of the VOF model and Eulerian multiphase model, which are numerical models representing the phase change in the Eulerian-Eulerian framework, was verified and investigated. This paper reviewed the major aspects of the heat flux transferred from the wall to the liquid in relation to the Rohsenow boiling model among VOF boiling models and the wall boiling model among Eulerian multiphase models. A comparison of the Rohsenow boiling model and wall boiling model showed that the Rohsenow boiling model does not appropriately represent the initial bubble generation process, but it was closer to the experiment in the case of fully developed flow with a high percentage of vapor. Furthermore, the Rohsenow boiling model required smaller computing power than the wall boiling model. On the other hand, comparative analysis of different combinations of the nucleation site density and bubble departure diameter models used in the wall boiling model showed that the dependence on the bubble departure diameter model was more significant than the dependence on the nucleation site density model. In the grid convergence test for the selected combination of models, the ONB point, which is the location where the initial bubble formation starts at the heated surface, varies according to the grid size. This result highlights the necessity for caution in selecting the grid size. In conclusion, the results of the sensitivity test suggested that the grid size needs to be larger than the minimum bubble departure diameter to establish accurate predictions of the ONB location and a realistic representation of the bubble

development process. The results of this research can be used in analyses to identify the dynamic characteristics of pipes constituting the cargo handling system (CHS) of transport ships handling cryogenic liquefied gases, such as LNG and liquid hydrogen, or pipes comprising the fuel gas supply system (FGSS) of propulsion ships as well as to determine the specifications of related systems. Multiphase-thermal flow analysis in various shaped cryogenic pipes, including insulation, will be performed in a follow-up study. Furthermore, this study will be applied to high accuracy analysis for establishing safety standards for related systems.

Funding

This research was a part of the project titled 'Development of Safety and Control Standards for Hydrogen Ships: Cargo Handling and Fuel Gas Supply Systems', funded by the Ministry of Oceans and Fisheries, Korea.

This work was supported by the National Research Foundation of Korea (NRF) grant funded by the Korean Government (MSIT) (No. 2020R111A3072459)

References

- Alglart, H. (1993). Modeling of Vapour Generation at Wall in Subcooled Boiling Two-phase Flow. In First CFDS International User Conference, Oxford, UK, 183–207.
- Alglart, H., & Nylund, O. (1996). CFD Application to Prediction of Void Distribution in Two-phase Bubbly Flows in Rod Bundles. *Journal of Nuclear Engineering and Design*, 163(1–2), 81–98. [https://doi.org/10.1016/0029-5493\(95\)01160-9](https://doi.org/10.1016/0029-5493(95)01160-9)
- Bartolemei, G.G., & Chanturiya, V.M. (1967). Experimental Study of True Void Fraction When Boiling Subcooled Water in Vertical Tubes. *Journal of Thermal Engineering*, 14(2), 123–128.
- Bergles, A.E., & Rohsenow, W.M. (1964). The Determination of Forced-Convection Surface-Boiling Heat Transfer. *Journal of Heat Transfer*, 86(3), 365–372. <https://doi.org/10.1115/1.3688697>
- Chen, E., Li, Y., & Cheng, X. (2009). CFD Simulation of Upward Subcooled Boiling Flow of Refrigerant -113 Using the Two-fluid Model. *Applied Thermal Engineering*, 29(11–12), 2508–2517. <https://doi.org/10.1016/j.applthermaleng.2008.12.022>
- Cole, R. (1960). A Photographic Study of Pool Boiling in the Region of the Critical Heat Flux. *AIChE Journal*, 6(4), 533–538. <https://doi.org/10.1002/aic.690060405>
- Domalapally, P., Rizzo, E., Richard, L.S., Subba, F., & Zanio, R. (2012). CFD Analysis of Flow Boiling in the ITER First Wall. *Fusion Engineering and Design*, 87(5–6), 556–560. <https://doi.org/10.1016/j.fusengdes.2012.01.024>
- Gu, J., Wang, Q., Wu, Y., Lyu, J., Li, S., & Yao, W. (2017). Modeling of Subcooled Boiling by Extending the RPI Wall Boiling Model to Ultra-high Pressure Conditions. *Applied Thermal Engineering*, 124, 571–584. <https://doi.org/10.1016/j.applthermaleng.2017.06.017>
- Jeong, T.W. (2019). Vessel Greenhouse Gas (GHG) Reduction Strategy Technology and Prospect. KRISO.
- Ji, C., & El-Halwagi, M.M. (2020). A Data-driven Study of IMO Compliant Fuel Emissions with Consideration of Black Carbon Aerosols. *Journal of Ocean Engineering*, 218, 108–241. <https://doi.org/10.1016/j.oceaneng.2020.108241>
- Kocamustafaogullari, G., & Ishii, M. (1983). Interfacial Area and Nucleation Site Density in Boiling Systems. *International Journal of Heat and Mass Transfer*, 26(9), 1377–1387. [https://doi.org/10.1016/S0017-9310\(83\)80069-6](https://doi.org/10.1016/S0017-9310(83)80069-6)
- Koncar, B., Kljenak, I., & Mavko, B. (2004). Modeling of Local Two-phase Flow Parameters in Upward Subcooled Flow Boiling at Low Pressure. *International Journal of Heat and Mass Transfer*, 47(6–7), 1499–1513. <https://doi.org/10.1016/j.ijheatmasstransfer.2003.09.021>
- Krepper, E., Koncar, B., & Egorov, Y. (2007). CFD Modeling of Subcooled Boiling - Concept, Validation and Application to Fuel Assembly Design. *Journal of Nuclear Engineering and Design*, 237(7), 716–731. <https://doi.org/10.1016/j.nucengdes.2006.10.023>
- Krepper, E., & Rzehak, R. (2011). CFD for Subcooled Flow Boiling: Simulation of DEBORA Experiments. *Nuclear Engineering and Design*, 241(9), 3851–3866. <https://doi.org/10.1016/j.nucengdes.2011.07.003>
- Kurul, N. (1990). Multidimensional Effects in Two-phase Flow Including Phase Change (Ph.D. Thesis). Rensselaer Polytechnic Institute.
- Kurul, N., & Podowski, M.Z. (1991). On the Modeling of Multidimensional Effects in Boiling Channels. *Proceedings of the 27th National Heat Transfer Conference*, Minneapolis, Minnesota, 301–314.
- Lee, J.M., Kim, J.H., Kim, S.G., Kim, T.W., & Kim, M.S. (2019). Hydrogen Fuel Cell Ship Overview and Technology Development Trend Introduction. *Journal of the Korean Society of Shipbuilding*, 56, 3–9.
- Lee, T.H., Park, G.C., & Lee, D.J. (2002). Local Flow Characteristics of Subcooled Boiling Flow of Water in a Vertical Concentric Annulus. *International Journal of Multiphase Flow*, 28(8), 1351–1368. [https://doi.org/10.1016/S0301-9322\(02\)00026-5](https://doi.org/10.1016/S0301-9322(02)00026-5)
- Lemmert, M., & Chawla, J.M. (1977). Influence of Flow Velocity on Surface Boiling Heat Transfer Coefficient. *Heat Transfer in Boiling*, 111–116.
- Nemitallah, M.A., Habib, M.A., Mansour, R.B., & Nakla, M.E. (2015). Numerical Predictions of Flow Boiling Characteristics: Current Status, Model Setup and CFD Modeling for Different Non-uniform Heating Profiles. *Applied Thermal Engineering*, 75, 451–460. <https://doi.org/10.1016/j.applthermaleng.2014.09.036>
- Park, H.S. (2019). IMO Aims to Reduce Greenhouse Gas by 40%,

- by 2030. KMI.
- Rogers, J.T., & Li, J.H. (1994). Prediction of the Onset of Significant Void in Flow Boiling of Water. *Journal of Heat Transfer*, 116(4), 1049–1053. <https://doi.org/10.1115/1.2911444>
- Rohsenow, W.M. (1952). A Method of Correlating Heat Transfer Data for Surface Boiling of Liquids. *Transactions of the ASME*, 74, 969.
- Sontireddy, V.R., & Hari, S. (2016). Subcooled Boiling: Validation by Using Different CFD Models. 2016 IEEE 23rd International Conference on High Performance Computing Workshops, 90–99. <https://doi.org/10.1109/HiPCW.2016.021>
- Tolubinsky, V.I., & Kostanchuk, D.M. (1970). Vapour Bubbles Growth Rate and Heat Transfer Intensity at Subcooled Water Boiling. *Heat Transfer 1970, Preprints of Papers Presented at the 4th International Heat Transfer Conference, 5, Paris, France, B2-8*. <https://doi.org/10.1615/IHTC4.250>
- Tu, J.Y., & Yeoh, G.H. (2002). On Numerical Modeling of Low-pressure Subcooled Boiling Flows. *International Journal of Heat and Mass Transfer*, 45(6), 1197–1209. [https://doi.org/10.1016/S0017-9310\(01\)00230-7](https://doi.org/10.1016/S0017-9310(01)00230-7)
- Unal, H.C. (1976). Maximum Bubble Diameter, Maximum Bubble-growth Time and Bubble-growth Rate During the Subcooled Nucleate Flow Boiling of Water up to 17.7 MN/m². *International Journal of Heat and Mass Transfer*, 19(6), 643–649. [https://doi.org/10.1016/0017-9310\(76\)90047-8](https://doi.org/10.1016/0017-9310(76)90047-8)
- Wang, Q., & Yao, W. (2016). Computation and Validation of the Interphase Force Models for Bubbly Flow. *International Journal of Heat and Mass Transfer*, 98, 799–813. <https://doi.org/10.1016/j.ijheatmasstransfer.2016.03.064>

Author ORCIDs

Author name	ORCID
Chung, Soh-Myung	0000-0001-5320-2587
Seo, Yong-Seok	0000-0002-2878-253X
Jeon, Gyu-Mok	0000-0002-6194-8474
Kim, Jae-Won	0000-0002-0190-6942
Park, Jong-Chun	0000-0002-3168-2054

An Experimental Study on the H-Beam Under Fire Load in Open Space

Min Suk Ki¹, Beom Jin Park¹, Kangsu Lee²,
 Byoungjae Park¹, Kyle Fernandez³ and In Sik Nho⁴

¹Senior Researcher, Korea Research Institute of Ships and Ocean Engineering, Daejeon, Korea
²Principle Researcher, Korea Research Institute of Ships and Ocean Engineering, Daejeon, Korea
³Engineer, Southwest Research Institute, San Antonio, USA
⁴Professor, Chungnam National University, Daejeon, Korea

KEY WORDS: Fire experiment, Displacement measurement, Gas temperature measurement, Steel surface temperature measurement, Burner fire

ABSTRACT: To validate the fire safety assessment of structures, many structural experiments under fire load have been conducted. However, most of these experiments were conducted in restricted environments, such as inside a furnace, and experiments were seldom carried out in open space. In this study, an experimental study on H-beams, frequently used as structural reinforcements, was carried out for validating the thermal-structural analysis method under development. A 1.8 MW burner fire was adopted with each end of the H-beam fixed without a mechanical load. Gas temperature, steel surface temperature, and displacements were then measured. During the experiment, gas and steel temperatures were obtained at 9 and 17 points near the H-beam, respectively. In addition, the vertical and horizontal displacements of the H-beam under fire load at 6 points were obtained. Furthermore, it was verified that the stable displacement measurements via the contact and non-contact methods were feasible in harsh environments where flames and smoke were both present.

1. Introduction

The fire safety assessment procedure of ships and offshore structures can be briefly described as a procedure for assessing safety by defining fire loads according to accident scenarios and analyzing their effects on the structure. In general, safety is reviewed via the temperature criteria of the structures under fire loads, and it is assessed in more detail via thermal-structural analysis, which combines fire simulation-heat transfer analysis with structural analysis in the design stage. Therefore, the accuracy of the thermal-structural analysis is crucial for reliable fire safety assessment, and the most applied method for validating the accuracy is to compare with the experimental results. Although fire experiments have been conducted by many researchers to analyze the characteristics of flames and heat transfer of steel members, constructing the temperature-dependent material property data, verifying the fire resistance performance of the structure itself, developing and validating numerical models, including other experiments have been conducted from the perspective of fluids with a primary focus on measuring gas and steel surface temperatures. On the other hand, fire experiments from the perspective of structure, which

measure the displacement of a structure under fire load, were conducted mainly in limited environments such as inside a furnace because it was difficult to measure displacement in a high-temperature environment with a mixture of flames and smoke, as well as controlling the heat of the fire source. In addition, fire experiments conducted in open space have been seldom carried out. The British Steel Corporation (BSC) has summarized standard fire experiment results for structures such as steel beams and columns (Wainman and Kirby, 1988; Wainman et al., 1990). Cong conducted a furnace fire experiment on an I-beam, which is widely used as structural members for offshore structures, under mechanical loads to measure the steel surface temperature and vertical displacement. The vertical displacement was then measured by linear variable differential transformers (LVDTs) installed on top of the specimen exposed to the exterior parts of the furnace (Cong et al., 2005). The results obtained from this experiment have been widely used by other researchers to develop numerical analysis techniques (Kim, 2014; Kim et al., 2017). In addition to steel, fire experiments have also been conducted on sandwich panel structures made of fiber-reinforced plastic (FRP) (Rahm et al., 2017). However, the aforementioned experiments were

Received 4 October 2020, revised 28 December 2020, accepted 31 December 2020

Corresponding author In Sik Nho: +82-42-821-6622, isnho@cnu.ac.kr

© 2021, The Korean Society of Ocean Engineers

This is an open access article distributed under the terms of the creative commons attribution non-commercial license (<http://creativecommons.org/licenses/by-nc/4.0>) which permits unrestricted non-commercial use, distribution, and reproduction in any medium, provided the original work is properly cited.

all conducted inside a furnace. Although the furnace fire experiment has the advantage of a constant temperature maintained inside the furnace, it is limited because technically, it cannot be used to validate the thermal-structural analysis technology for fire safety assessment owing to the fact that it is unnecessary to conduct fire simulation.

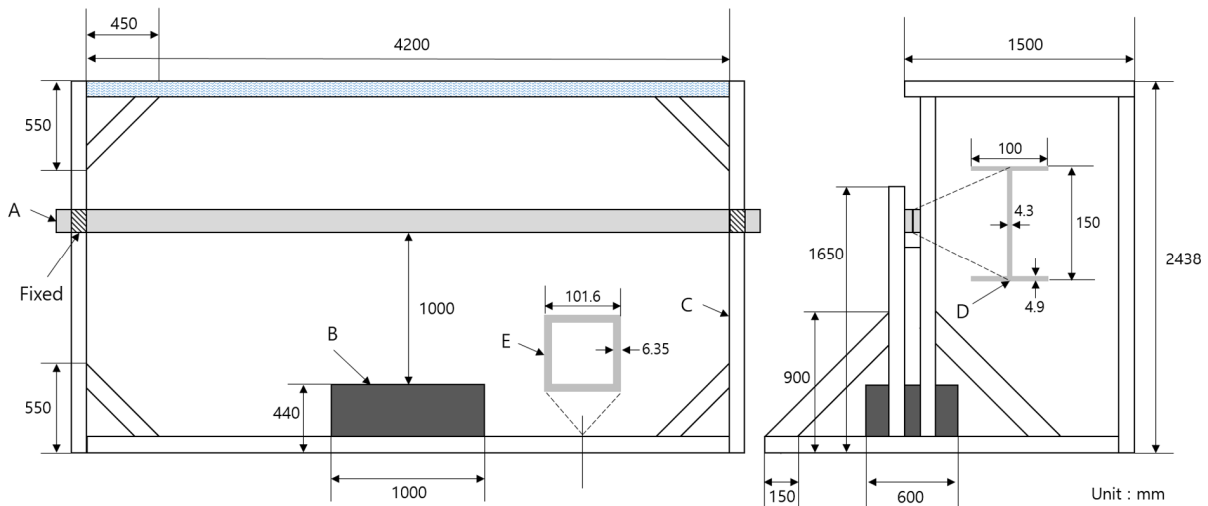
The most widely used method of measuring displacement during fire experiments is using LVDTs. However, LVDTs are difficult to use in high-temperature environment with a mixture of flames and smoke, because they should be installed and used mainly on the non-heated surfaces of the target structure. Efforts are also continuously being made to address this limitation. Choe measured the displacement of a steel beam under local fire load using a specially manufactured potentiometer (Choe et al., 2016), and Hodges evaluated the fire resistance performance of aluminum beams under fire and mechanical loads via thermographic digital image correlation (TDIC) (Hodges et al., 2016). Similarly, studies are being conducted to measure displacement in environments where high-temperature flames and smoke are mixed. The studies on displacement measurement are being conducted towards the application of an insulated extension cable, in the case of adopting contact-type equipment, as well as developing and

verifying a method that adopts imaging equipment when using non-contact equipment.

In this study, a fire experiment was conducted on the H-beam, which is a structural reinforcement that is widely used in ships and offshore structures, to obtain data for validating the thermal-structural analysis technology. A burner fire, which is numerically easy to implement and control was used as the fire source. Consequently, gas temperature, steel surface temperature, and displacement were measured and the results obtained were analyzed. In particular, displacement was determined by measuring the vertical and horizontal displacements using a string potentiometer with extension cable insulated with flexible fire resistant hose, to observe the load path owing to the fire in the time domain.

2. Burner Fire Experiment

Burner fire experiment was conducted at a fire testing facility of the Southwest Research Institute (SwRI), which was established in 1947 and has extensive experience in the field of fire engineering. The size of the fire testing facility is approximately 18 m × 12 m × 12 m, and



(a) Front view



(b) Side view

Fig. 1 Test setup

ventilation openings were installed on the ceiling. The room temperature was 38 °C during the experiment and the experiment was setup as illustrated in Fig. 1.

2.1 Target Structure

An H-beam (A in Fig. 1, ASTM A992, $\sigma_y = 413$ MPa), which is the target structure for the burner fire experiment, was installed on the manufactured support (C in Fig. 1, ASTM A500 grade B, $\sigma_y = 315$ MPa). The designation of the specimen was ASTM W6×4, and its cross-sectional specifications are represented by D in Fig. 1, where the lengths of the specimen and flame exposure were 4,600 and 4,200 mm, respectively. The injected molded specimen was used without alterations to minimize the heat effect from cutting and welding. A part of the support exposed to the flame was insulated using ceramic wool, which is an insulating material; in particular, water was injected into the upper part of the support and circulated to minimize the effect of high temperatures on the support. The cross section of the support is as represented by E in Fig. 1.

2.2 Experimental Conditions

A 1.8 MW burner fire was as the fire source. To implement a uniform fire, a sand diffused propane burner (B in Fig. 1) with dimensions of 600 mm × 1,000 mm × 440 mm was installed at a position 1,000 mm away from the lower center of the specimen. The target heat release rate of 1.8 MW was maintained by providing uniform flow of propane gas to the sand diffused burner verified with a Coriolis mass flow meter, as illustrated in Fig. 2. The target heat release rate was calculated as the product of the fuel flow rate and effective heat of combustion, as expressed in Eq. (1). The total combustion time was 3,600 s.

$$\dot{Q} = \dot{m} \Delta H_{c,eff} \quad (1)$$

where \dot{Q} , \dot{m} , and $\Delta H_{c,eff}$ represent the target heat release rate

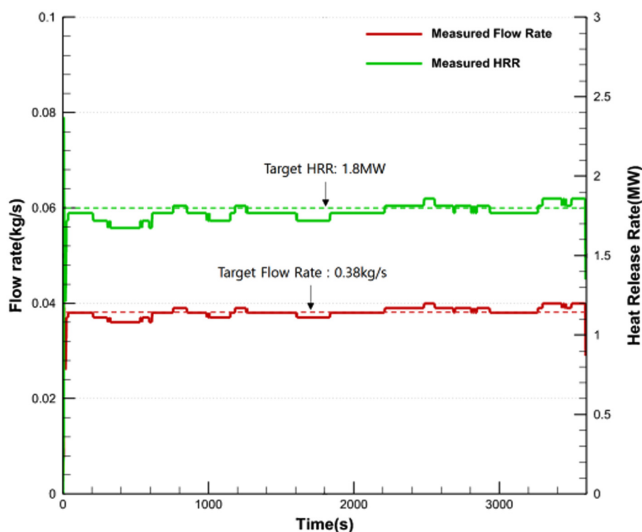


Fig. 2 Measured propane flow rate and calculated heat release rate

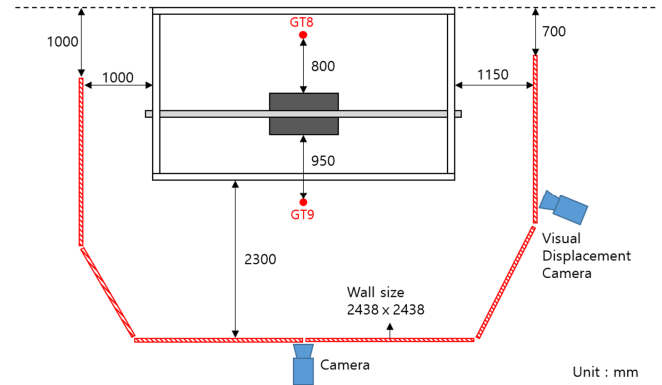


Fig. 3 Location of wind shield walls



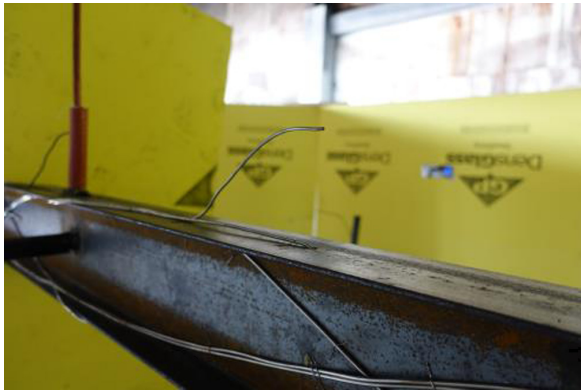
Fig. 4 Fixed end of specimen welded along all edges of both flanges

(MW), target flow rate of fuel (kg/s), and effective heat of combustion (MJ/kg) of the fuel, respectively. In this study, the experiment was conducted by setting the target heat release and target flow rates at 1.8 MW and 0.38 kg/s, respectively, by using 46.5 MJ/kg of propane’s effective heat of combustion.

A significant flame movement was observed when a preliminary experiment was conducted to determine the stability of the burner fire. Therefore, to minimize flame movement and prevent damage to the measurement instrument owing to high temperature, wind shield walls were installed, as shown in Fig. 3. In addition, the experiment was conducted by fixing both ends of the specimen to the support without mechanical load to solely examine the effects of the fire load and boundary conditions triggered by the burner fire. The boundary conditions for fixing both ends of the specimen were implemented via a method that involves welding the contacts by positioning the specimen between the supports and installing an angle, as illustrated in Fig. 4.

2.3 Measured Data

Fig. 5 presents the measurement positions of the gas temperature, steel surface temperature, and displacement in the fire experiment while the actual instruments installed are illustrated in Fig. 6. Figs. 6(a) and (b) show the thermocouples adopted for measuring gas and



(a) Thermocouple for gas temperature measurement



(b) Thermocouple for steel surface temperature measurement



(c) Instrumentation for vertical displacement measurement



(d) Instrumentation for horizontal displacement measurement



(e) Support for horizontal displacement measurement



(f) String potentiometer for displacement measurement

Fig. 6 Measurement instrumentation for fire experiment

Finally, the displacement of the support in the longitudinal direction of the specimen was determined immediately after the experiment using a laser displacement sensor as the support can be deformed by the reaction force of the specimen, which expands in the longitudinal direction owing to the influence of high temperature.

3. Burner Fire Experiment Result

Fig. 7 and Figs. 9–12 presents the time history results obtained from the burner fire experiment for gas temperature, steel surface temperature, vertical displacement, and horizontal displacements and these results were analyzed, respectively.

3.1 Gas Temperature

Fig. 7 presents the measurement results of gas temperature obtained at a position 100 mm away from the upper flange of the specimen in the vertical direction while the gas temperature for each measurement position is presented in Appendix Fig. A1. The highest gas temperature was measured at GT5 (approximately 800°C), which is 500 mm away from the center of the specimen in the longitudinal direction, and this is apparently attributable to the observed flame movement illustrated in Fig. 8. The flame moves from the center of the burner to the left, as shown in Figs. 8(a), (c), (d), and (e), and accordingly, gas temperature was determined to be high at GT2 and GT3 as shown in ①, ③, ④, and ⑤ in Fig. 7, and at GT5 and GT6,

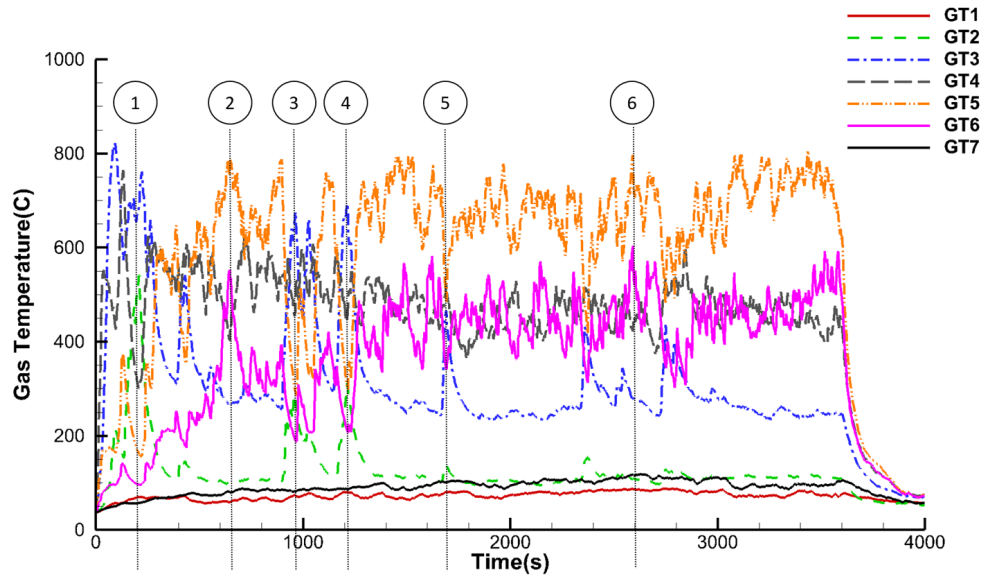


Fig. 7 Gas temperature results of test specimen



(a) 200 s



(b) 650 s



(c) 962 s



(d) 1,210 s



(e) 1,690 s



(f) 2,600 s

Fig. 8 Experimental scene for observing flame movement

which were installed symmetrically around GT4, it was determined to be low.

The opposite case can be observed in Figs. 8(b) and (f), and in ② and ⑥ of Fig. 7. An irregular flame movement was observed although the experiment was conducted in an enclosed space, including wind shields walls. This is presumed to be owing to the air flow that was affected by the asymmetrically installed wind shield walls, as well as the fuel that was not uniformly distributed in the sand flowing into the burner, thereby triggering uneven combustion. The lowest temperature of approximately 80°C was measured at GT1, which was 2,000 mm away from the center of the specimen in the longitudinal direction.

3.2 Steel Surface Temperature

The results of the steel surface temperature of the specimen are divided into upper and lower flanges, as presented in Figs. 9 and 10, and the average and maximum temperatures at each position are as summarized in Table 1. The average temperature is the average of the temperatures measured during the combustion time of 0–3,600 s. In addition, steel surface temperature at each measurement position is presented in Appendix Fig. A2.

In the upper flange case, the highest temperature (average: 610°C, maximum: 734°C) was measured at ST5, which was 500 mm away from the center of the specimen. This result follows the trend of the gas temperature distribution. The longitudinal temperature distribution appeared to be symmetrical around the ST5, and the overlapping temperature histories of ST3 and ST5, which were symmetrical around the burner’s position, indicate a significant influence on the movement of the flame illustrated in Fig. 8.

In the lower flange case, the highest temperature (average: 674°C, maximum: 740°C) was measured at ST15, which was approximately 200 mm away from the center of the specimen, and a high temperature (average: 594°C, maximum: 738°C) was also measured at ST16, which was approximately 700 mm away from the center of the specimen. Similar to the upper flange case, this result follows the gas temperature distribution trend, and it was determined that the temperature

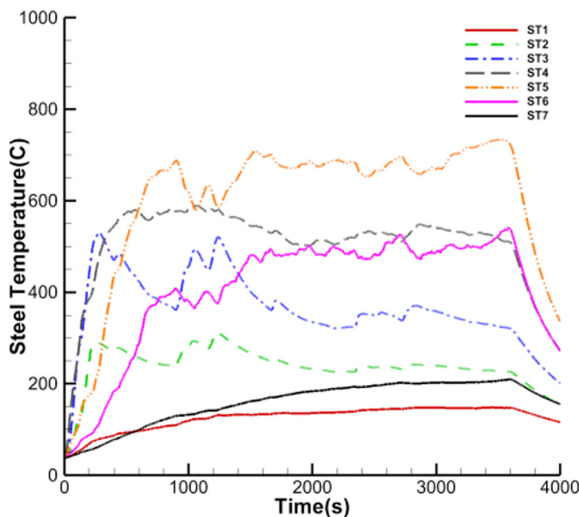


Fig. 9 Steel surface temperature results of upper flange

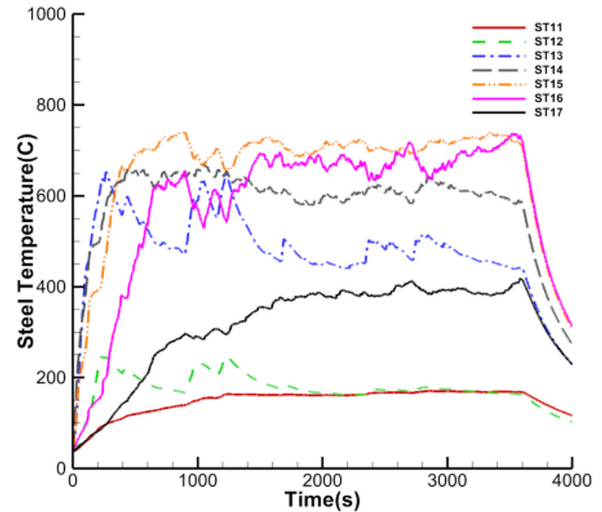


Fig. 10 Steel surface temperature results of lower flange

Table 1 Average and maximum steel surface temperature results of specimen

	ST1	ST2	ST3	ST4	ST5	ST6	ST7
Avg. Temp. (°C)	125	243	377	521	610	410	157
Max. Temp. (°C)	148	313	531	589	734	542	210
	ST11	ST12	ST13	ST14	ST15	ST16	ST17
Avg. Temp. (°C)	149	180	495	602	674	594	318
Max. Temp. (°C)	171	247	653	673	740	738	418

distribution of the lower flange, which is relatively close to the fire source, was more influenced by the flame movement.

In general, lower temperature distribution is exhibited as the distance increases in the longitudinal direction from the position 500 mm to the right from the center of the specimen. However, because the temperature of ST12, located between ST2 and ST3 in the longitudinal direction, was measured lower than ST17, it was determined that the steel surface temperature data were reasonable except the data from this sensor.

3.3 Displacement

The displacement history and deformation shape of the specimen in the vertical and horizontal directions are illustrated together in Figs. 11–13, and the displacement for each the measurement position is presented in Appendix Fig. A3. Visuals Z and Y in the graph represent the vertical and horizontal displacements, respectively, that are measured via video image processing.

Regarding the final displacement in the vertical direction of the specimen at 3,600 s, which occurred at the end of the fire experiment, approximately 9 mm (maximum: 13.8 mm) of deflection was measured at ZD3, which was 500 mm away from the center of the specimen. In contrast, the displacement within approximately 4mm (maximum: 9.6 mm) was measured at ZD2, which is at the center of the specimen while the displacement within approximately 3 mm (maximum: 8.3 mm) was measured at ZD1, which was 500 mm to the

left of the specimen center. These displacements are invisible to the naked eye. A similar trend was observed when comparing the displacement results via video image processing with the displacement results obtained via a string potentiometer. The largest displacement was determined at ZD3, the position at which the steel surface temperature was the highest, and the overall downward behavior in the vertical direction shifted upwards after 150–350 s.

The maximum final displacement in the horizontal direction of the specimen of approximately 20 mm was measured at YD2, at the center of the specimen. Meanwhile, the displacements of 10 and 12 mm were measured at YD1 and YD3, respectively, which were 500 mm away from the center of the specimen in the longitudinal direction. The largest displacement was measured at the center of the specimen. Between YD1 and YD3, a larger displacement measured at YD3, where a relatively higher steel surface temperature was measured. Regarding the behavior of the specimen, deflection (-) to the back was observed before approximately 400 s when the specimen was viewed from the front while forward deflection (+) was observed after 400 seconds. In general, the displacement in the horizontal direction was

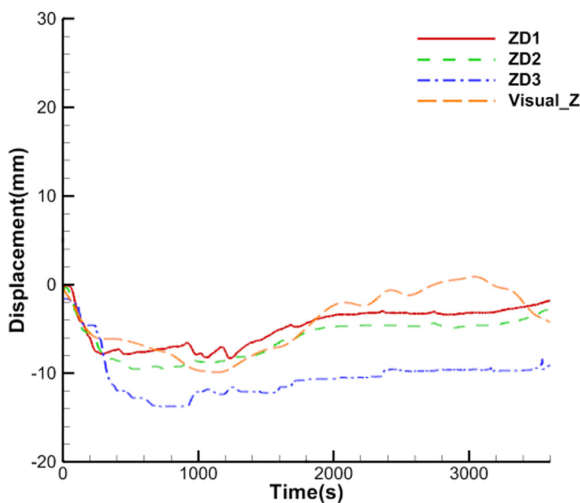


Fig. 11 Vertical displacement results of specimen

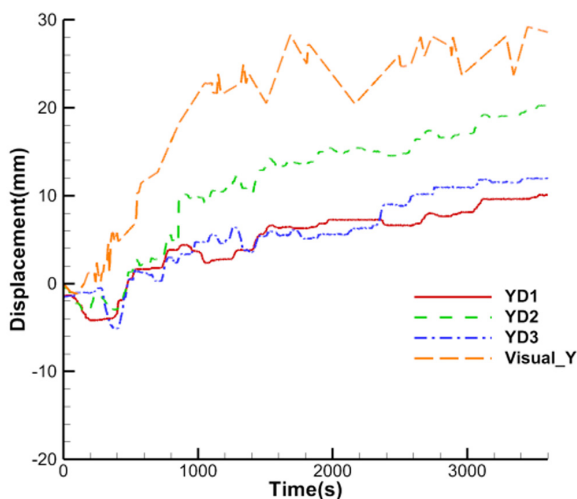


Fig. 12 Horizontal displacement results of specimen



Fig. 13 Deformed shape of specimen

more significant than that in the vertical direction. It is inferred that this phenomenon is owing to the deformation in the horizontal direction with weak stiffness according to the geometric shape of the H-beam cross section because the reaction force, as the displacement of the specimen expanding in the longitudinal direction, is surrounded by the boundary condition of fixed ends, which is similar to the deformation of a beam under a compressive load in the axial direction. In addition, only elastic deformation was observed in the vertical direction, and a permanent deformation of approximately 20 mm was observed in the horizontal direction, when displacement was measured after the fire was extinguished naturally at the end of the experiment, as illustrated in Appendix Fig. A3. Finally, although the horizontal displacement differs significantly more than the vertical displacement when comparing the displacement result via video image processing with the displacement result obtained by the string potentiometer, a similar trend was exhibited overall with video image measurements. The amount of deformation to the support itself, which was determined using a laser displacement sensor immediately after the end of the experiment, was approximately 10 mm.

4. Conclusion

In this study, a fire experiment was conducted on an H-beam, a representative structural reinforcement for offshore structures, to obtain data for validating the thermal-structural analysis technology used in fire safety assessment of offshore structures. Regarding the experimental condition, an experiment was conducted by

implementing the boundary condition of fixed ends without mechanical load to observe the effect of pure thermal load by 1.8 MW burner fire. The gas temperature was measured by positioning the Inconel-sheathed grounded-junction type “K” thermocouple at 7 points, 100 mm away from the upper flange of the specimen, and the steel surface temperature distribution of the specimen in the horizontal and vertical directions was observed by installing the thermocouples equal to the gas temperature at 17 points of the upper flange, web, and lower flange. In addition, the structural behavior of the specimen under the fire load was investigated by measuring vertical and horizontal displacements with a string potentiometer. Furthermore, displacement measurement via video image processing was performed hedge against the failure of the displacement measurement. The experimental results and considerations are summarized as follows:

(1) The gas temperature near the specimen (9 points), steel surface temperature (17 points), vertical displacements, and horizontal displacements of the specimen (6 points) under the fire load were measured during the flame exposure for 3,600 s.

(2) The highest temperature (approximately 800°C) was measured at GT5, which was 500 mm away from the center of the specimen in the longitudinal direction, and the general gas temperature distribution tended to decrease as the distance from the center of GT5 increased in the longitudinal direction.

(3) The highest gas temperature was observed at GT5, which was 500 mm to the right from the center of the specimen, and not at GT4 located in the center of the specimen or closest to the burner because the movement of the flame observed during the experiment was very significant, and the overall steel surface temperature measurement results obtained also followed this trend. The highest steel surface temperature (average: 610°C, maximum: 734°C) was measured at ST5, 500 mm away from the center of the specimen in the upper flange case, and the highest temperature (average: 674°C, maximum: 740°C) was measured at ST15, approximately 200 mm away from the center of the specimen in the lower flange case.

(4) Regarding the maximum final displacement in the vertical direction of the specimen under the fire load, a deflection of approximately 9 mm was measured at ZD3, 500 mm to the right from the center of the specimen, and the maximum final displacement in the horizontal direction was determined to be approximately 20 mm in YD2, which is at the center of the specimen. In general, the displacement in the horizontal direction was more significant than that in the vertical direction, which is inferred to be owing to the deformation in the horizontal direction with weak stiffness according to the geometric shape of the H-beam cross section.

In this study, we obtained the gas temperature, steel surface temperature, and displacement history in the time domain that can be used to verify the thermal-structural analysis technology of ship and offshore structures. In particular, the displacement history in the vertical and horizontal directions of the position directly exposed to

the flame was obtained, and it was determined that the results were similar to that of the displacement measurement via video image processing. Consequently, it was determined that displacement can be stably measured via contact and non-contact methods even in harsh environments where high-temperature flames and smoke are mixed. However, the movement of the flame observed during the experiment was very significant, which significantly influenced the distributions of the gas and steel surface temperatures around the specimen. This phenomenon is inferred to be owing to combining the limitations of the experiment conducted in an open space, rather than in an enclosed space, where the amount of heat can be stably controlled, such as in a furnace, in addition to the uncertainty in the fire experiment as fuel was not evenly distributed in the sand filling the burner despite supplying sufficient fuel for the target heat release rate. In the future, the behaviour of structure under fire load will be analyzed using thermal-structural analysis which reflect flame movement observed in this study, as well as additional experiments to obtain data suitable for this analysis.

Funding

This research was supported by “Development of core technology for evaluating structural damage of hydroelasticity-based offshore structures in consideration of uncertainty (1/5) [PES3490]”, which is a major project in Korea Research Institute of Ships and Ocean Engineering, and we are grateful for the support in form of the research fund.

References

- Choe, L.Y., Ramesh, S., Zhang, C., & Gross, J.L. (2016). The Performance of Structural Steel Beams Subject to a Localized Fire. In 9th International Conference on Structures in Fire, Princeton University, USA, 392-399.
- Cong, S., Liang, S., & Dong, W. (2005). Experimental Investigation of Behavior of Simple Supported Steel Beams Under Fire. *Journal of Southeast University (Natural Science Edition)*, 35, 66-68.
- Hodges, J.L., Rippe, C., Case, S.W., & Lattimer, B.Y. (2016). Thermographic Digital Image Correlation (TDIC) Measurements of Mechanically-Loaded Structures. In 9th International Conference on Structures in Fire, Princeton University, USA, 811-818.
- Kim, J.H. (2014). A New Procedure for Fire Structural Assessment of Offshore Installations (Ph.D. thesis). Pusan National University, Busan, Korea.
- Kim, S.J., Lee, J., Kim, S.H., Seo, J.K., Kim, B.J., Ha, Y.C., ... Sohn, J.M., (2017). Nonlinear Structural Response in Jet Fire in Association with the Interaction Between Fire Loads and Time-variant Geometry and Material Properties. *Ocean Engineering*, 144, 118-134. <https://doi.org/10.1016/j.oceaneng.2017.08.028>

- Rahm, M., Evegren, F., Johnson, E., & Ringsberg, J.W. (2017). Structural fire integrity testing of lightweight multiple core sandwich structures, In *Progress in the Analysis and Design of Marine Structures*, Lisbon, Portugal, pp. 869-876.
- Wainman, D.E., & Kirby, B.R. (1988). *Compendium of UK Standard Fire Test Data: Unprotected Structural Steel – 1*. Rotherham, England: British Steel Corporation (BSC).
- Wainman, D.E., Kirby, B.R., Tomlinson, L.N., Kay, T.R., & Preston, R.R. (1990). *The Behaviour of Unprotected Steel Floor Beams in the Standard Fire Resistance Test – Compendium of Predicted Temperature Profiles*. Rotherham, England: British Steel Corporation (BSC).

Author ORCIDs

Author name	ORCID
Ki, Min Suk	0000-0001-6253-0531
Park, Beom Jin	0000-0001-9729-4313
Lee, Kangsu	0000-0002-9505-6802
Park, Byoungjae	0000-0002-8943-1477
Fernandez, Kyle	0000-0003-2740-354X
Nho, In Sik	0000-0003-1665-4968

Appendix

Appendix A Fire experiment results

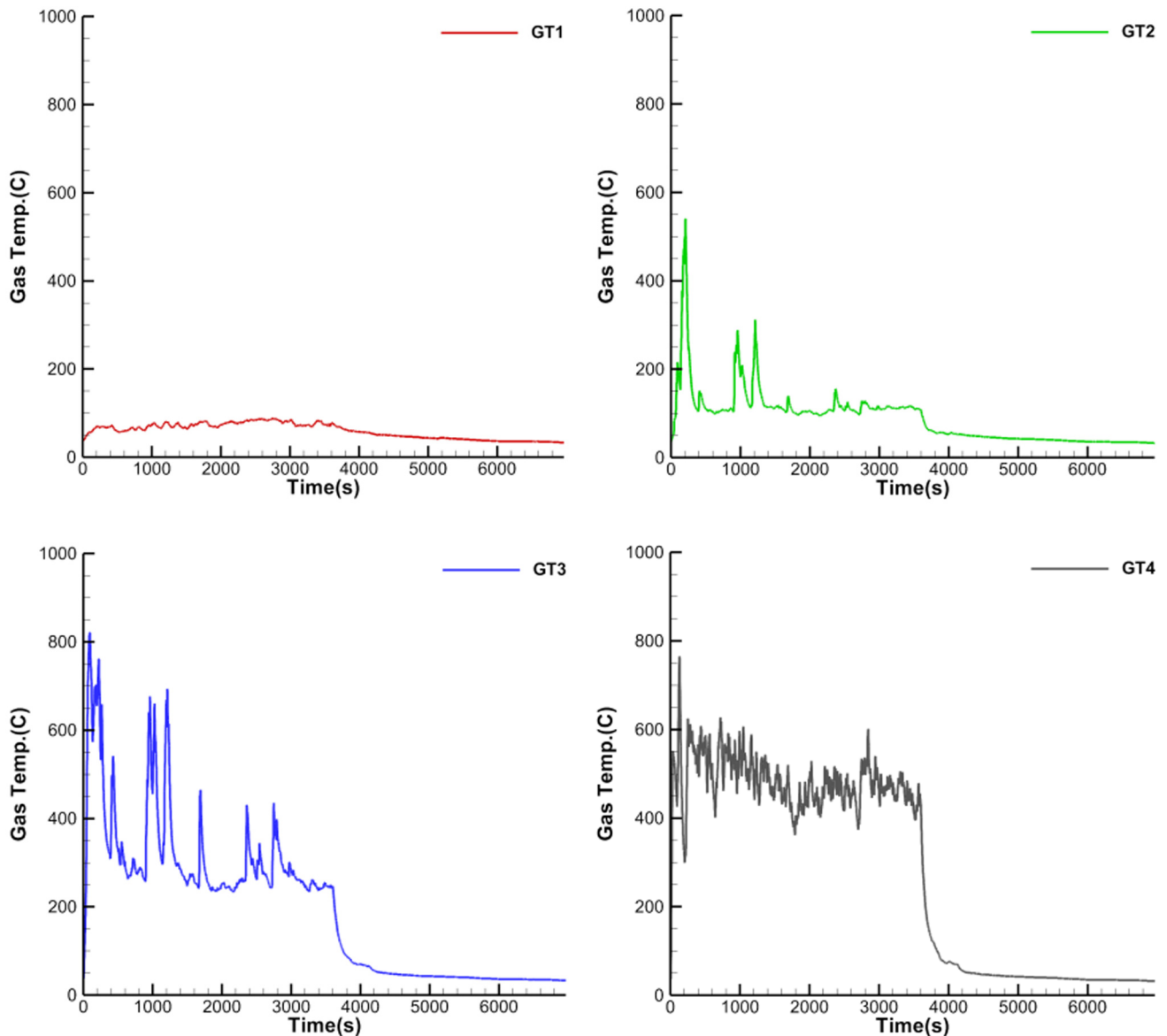


Fig. A1 Test results – gas temperature (continuation)

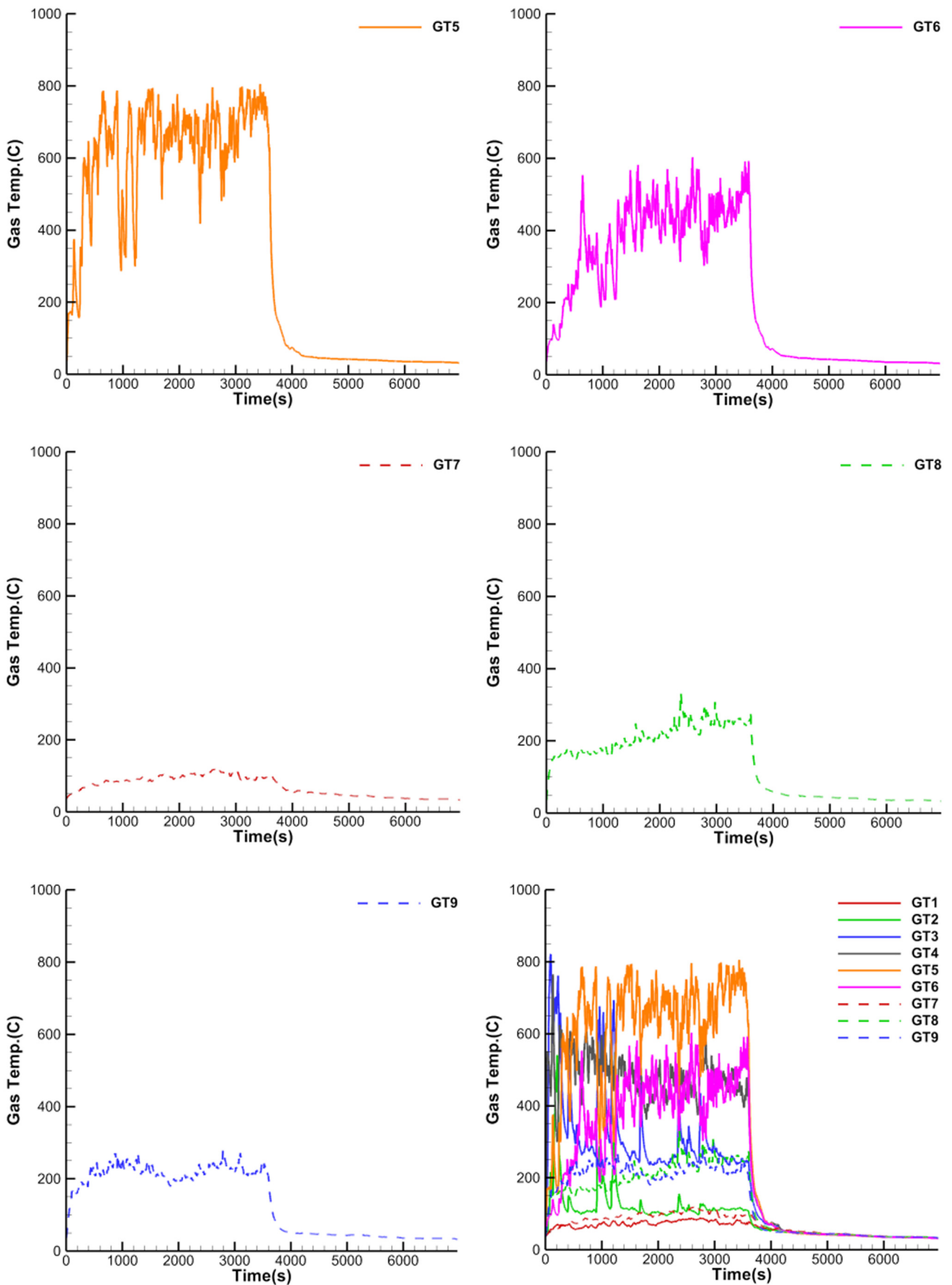


Fig. A1 Test results - gas temperature

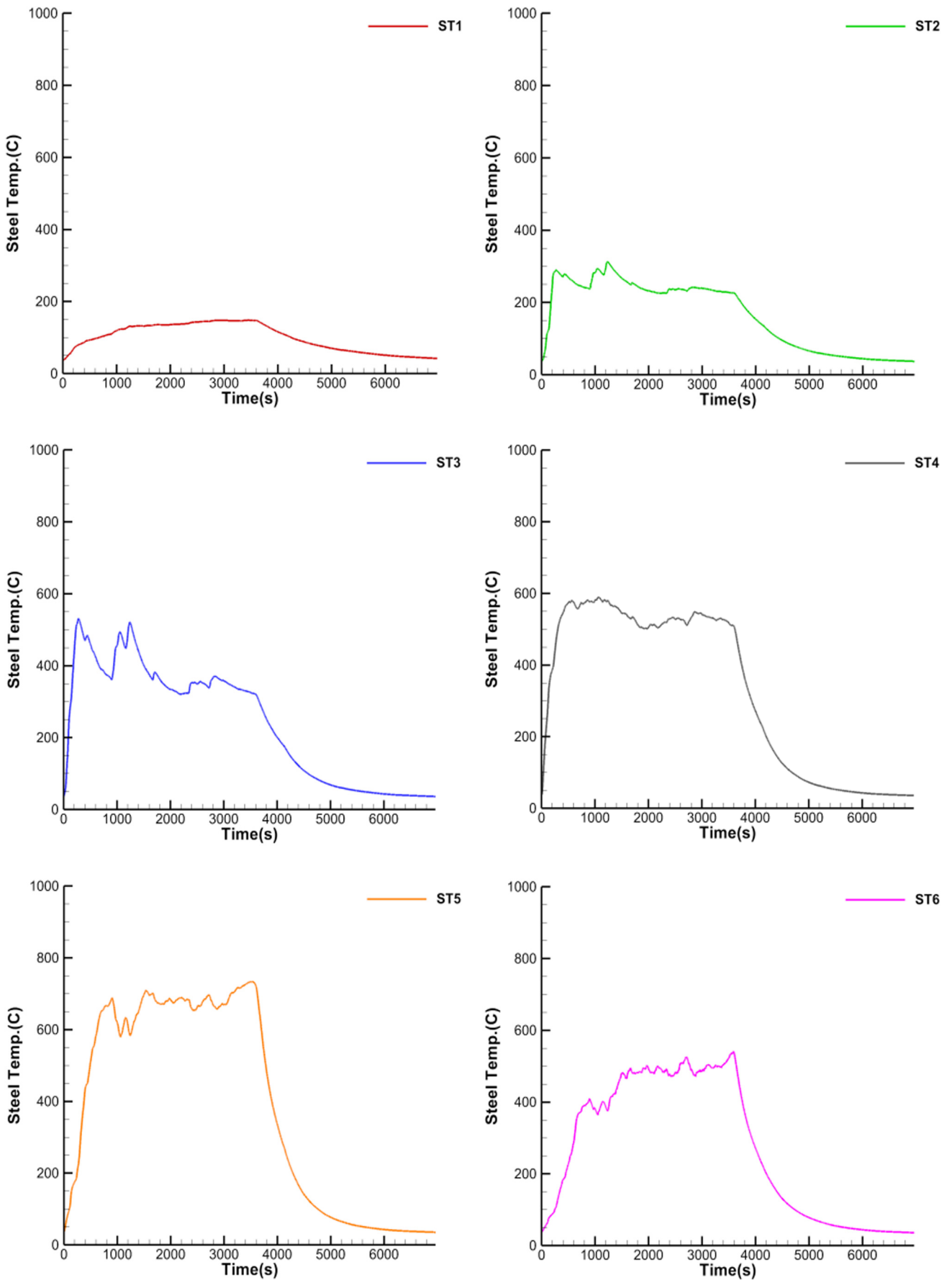


Fig. A2 Test results - steel surface temperature (continuation)

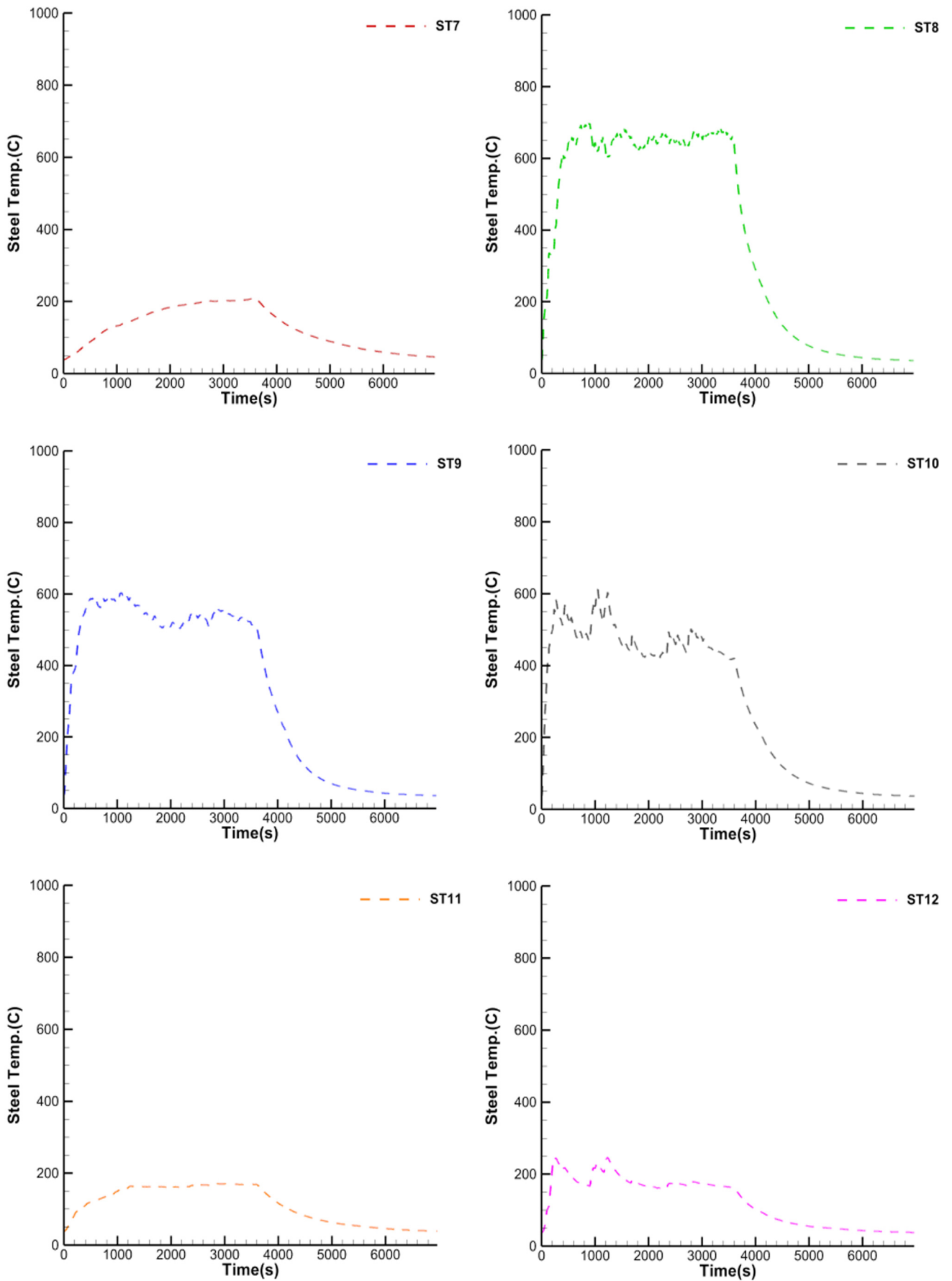


Fig. A2 Test results – steel surface temperature (continuation)

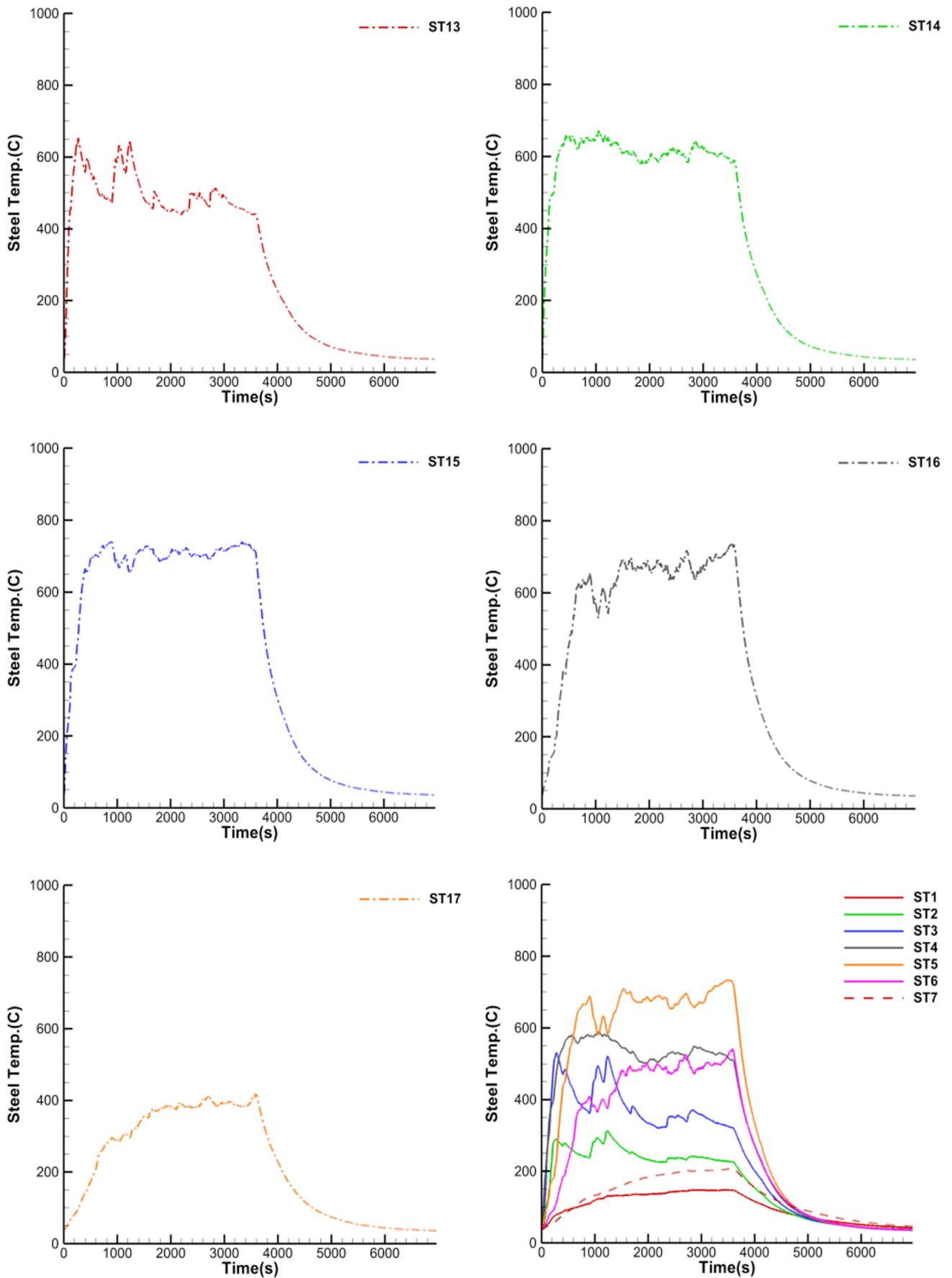


Fig. A2 Test results - steel surface temperature (continuation)

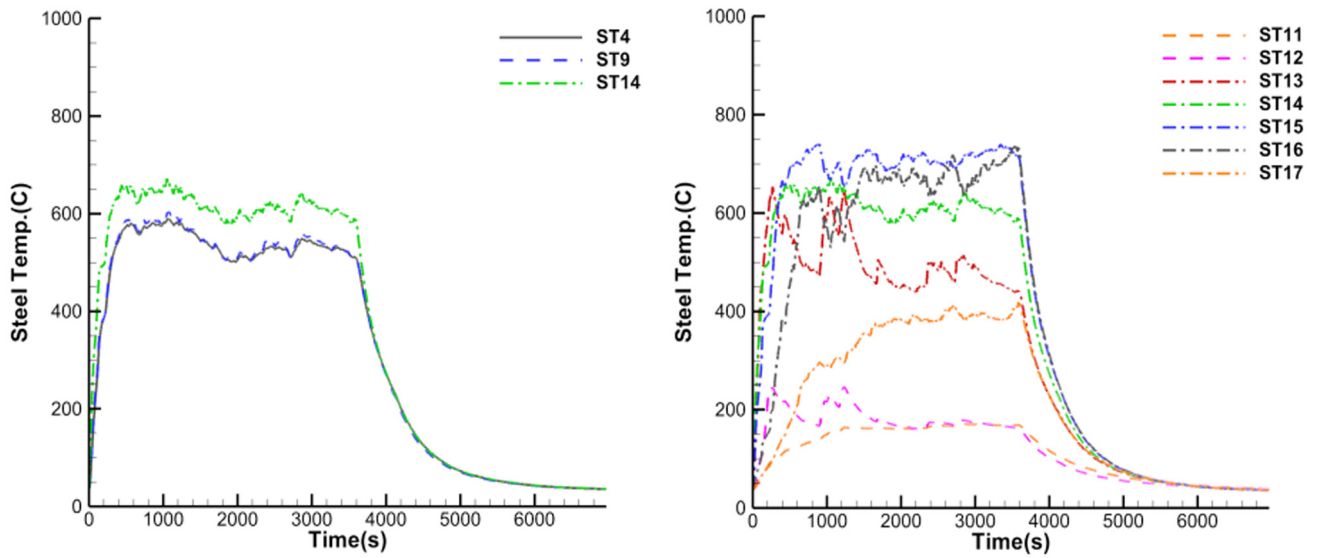


Fig. A2 Test results – steel surface temperature

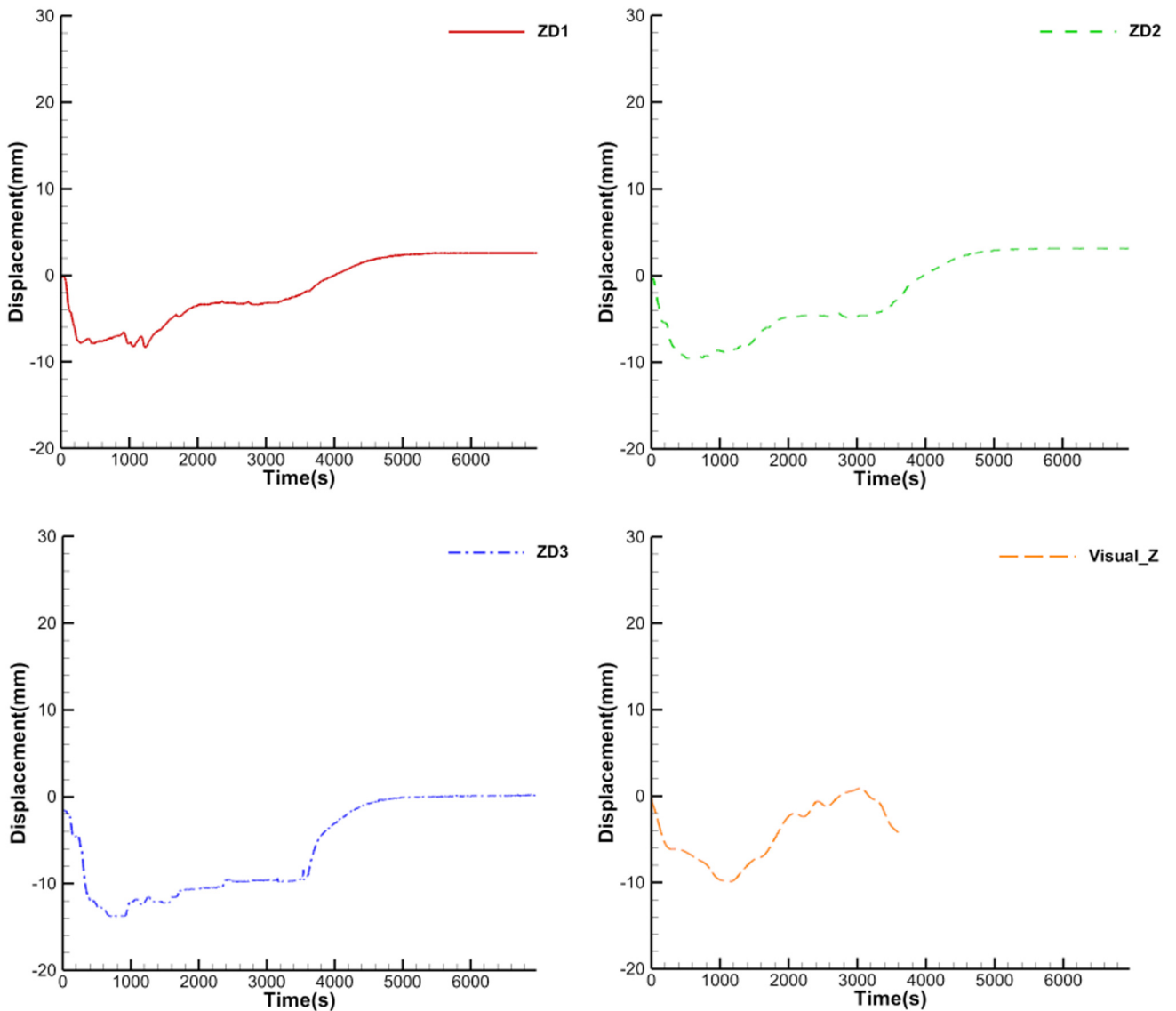


Fig. A3 Test results – displacement (continuation)

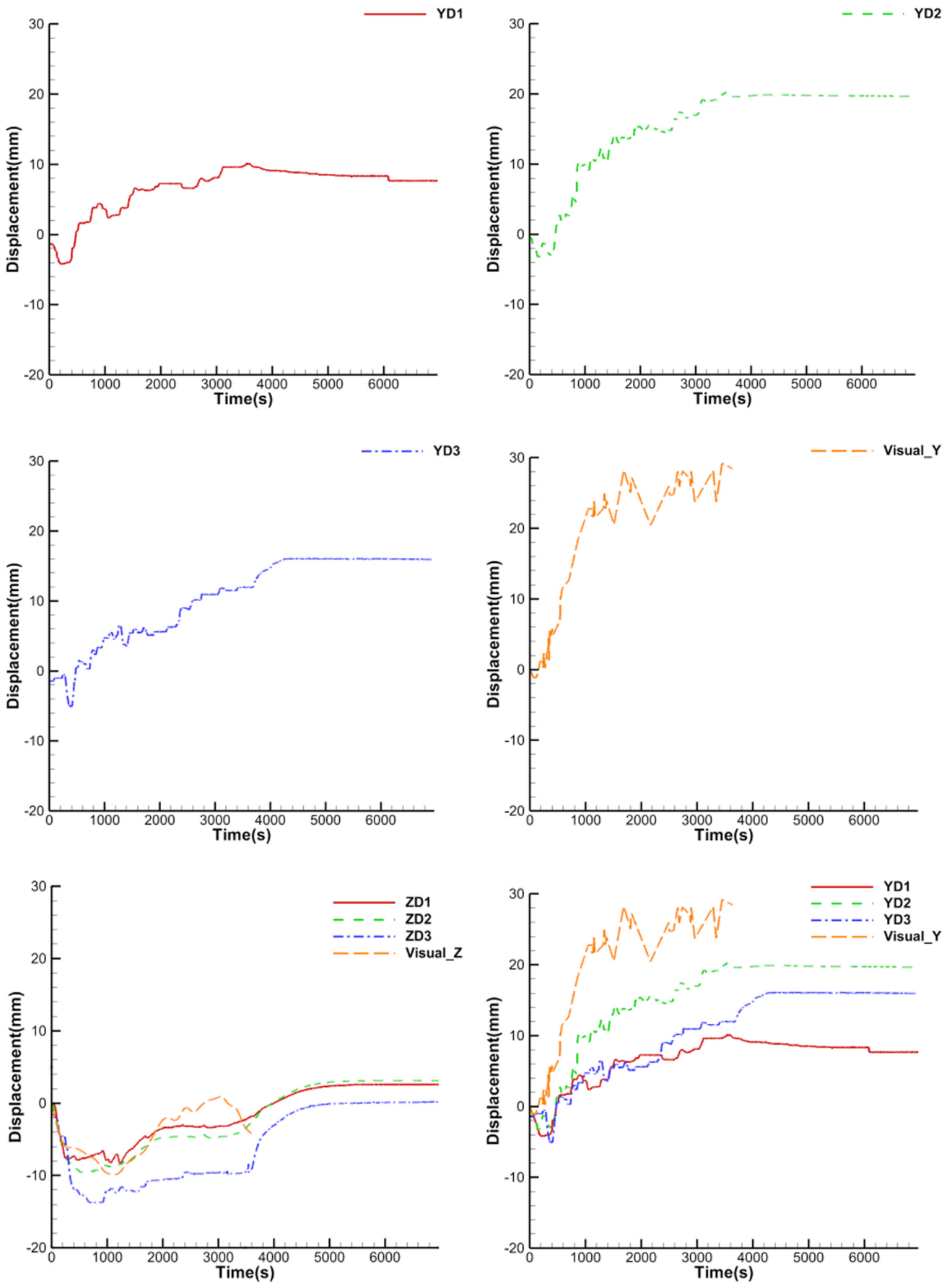


Fig. A3 Test results - displacement

Application of the Artificial Coral Reef as a Coastal Erosion Prevention Method with Numerical-Physical Combined Analysis (Case Study: Cheonjin-Bongpo Beach, Kangwon Province, South Korea)

Sunghoon Hong¹, Yeon Myeong Jeong², Taeyoon Kim¹, Van Men Huynh¹,
 Inho Kim³, Jungmin Nam⁴, Dong Soo Hur⁵, Jooyong Lee⁶ and Soonchul Kwon⁷

¹Graduate Student, Department of Civil and Environmental Engineering, Pusan National University, Busan, Korea

²Research Professor, Institute of Marine Industry, Gyeongsang National University, Tongyeong, Korea

³Professor, Department of Earth and Environmental Engineering, Kangwon National University, Samcheok, Korea

⁴Ph.D Candidate, Department of Earth and Environmental Engineering, Kangwon National University, Samcheok, Korea

⁵Professor, Department of Ocean Civil Engineering, Gyeongsang National University, Tongyeong, Korea

⁶Research Professor, Research Institute of Industrial Technology, Pusan National University, Busan, Korea

⁷Associate Professor, Department of Civil and Environmental Engineering, Pusan National University, Busan, Korea

KEY WORDS: Artificial coral reef, Field observation, SWAN model, 2D Physical model test, Dean's parameter, Surf-scaling parameter

ABSTRACT: Artificial Coral Reefs (ACRs) have been introduced to help solve coastal erosion problems, but their feasibility has not been assessed with field data. This study conducted a feasibility analysis of ACRs on their erosion mitigation effects by performing a case study of Cheonjin-Bongpo beach, South Korea. A numerical-physical combined analysis was carried out using a SWAN model simulation and physical model test with a scale of 1/25 based on field observations of Cheonjin-Bongpo beach. Both Dean's parameter and the surf-scaling parameter were applied to comparative analysis between the absence and presence conditions of the ACR. The results for this combined method indicate that ACR attenuates the wave height significantly (59–71%). Furthermore, ACR helps decrease the mass flux (~50%), undertow (~80%), and maximum wave set up (~61%). The decreases in Dean's parameter (~66%) and the surf-scaling parameter suggest that the wave properties changed from the dissipative type to the reflective type even under high wave conditions. Consequently, an ACR can enhance shoreline stability.

1. Introduction

Coastal erosion is occurring all over the world. For example, the amount of permanent land loss (28,000 km²) is more than double the land area gained (Mentaschi et al., 2018). According to the US Army Corps of Engineers (1984), erosion occurs due to natural and artificial factors. Moreover, severe coastal disasters can result from sea-level rise and high waves (Ams et al., 2017).

To cope with these coastal erosion problems, many researchers have attempted to develop different types of coastal erosion prevention methods. In this regard, artificial coral reefs (ACRs) were introduced by Han Ocean Corp. to help mitigate coastal erosion problems. For example, Hong et al. (2018) analyzed the wave attenuation and erosion mitigation performance using a two-dimensional experiment. Hong et

al. (2020) examined the variation characteristics of the irregular wave propagate over the ACR. The impacts of the new application of the ACR with conventional submerged breakwater, called the hybrid type method, were discussed in a previous study (Kim et al., 2020). On the other hand, there has been no research on real applications. Therefore, this study assessed the feasibility of an ACR as a coastal erosion prevention method.

2. Experimental Methods

Field observation, physical model test, and numerical analysis were performed to investigate the shoreline protection effects of the ACR in a real coast, as shown in Fig. 1. The followings present the analysis methods applied in this study.

Received 12 November 2020, revised 1 December 2020, accepted 1 December 2020

Corresponding author Soonchul Kwon: +82-51-510-7640, sckwon@pusan.ac.kr

© 2021, The Korean Society of Ocean Engineers

This is an open access article distributed under the terms of the creative commons attribution non-commercial license (<http://creativecommons.org/licenses/by-nc/4.0>) which permits unrestricted non-commercial use, distribution, and reproduction in any medium, provided the original work is properly cited.

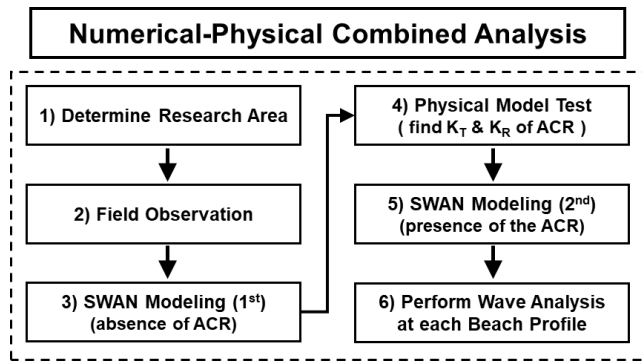


Fig. 1 Flowchart of the research methods

2.1 Research Area: Cheonjin-Bongpo Beach, South Korea

Some beaches that had erosion issues were sampled to determine the research area. Because previous studies of ACRs did not examine the longshore current and drift, beaches with a pocket or spiral shape were preferred. Therefore, Cheonjin-Bongpo beach was used as the research area, which is denoted as ‘GW 12 littoral cell’ in South Korea. Fig. 2 shows the location of the research area.

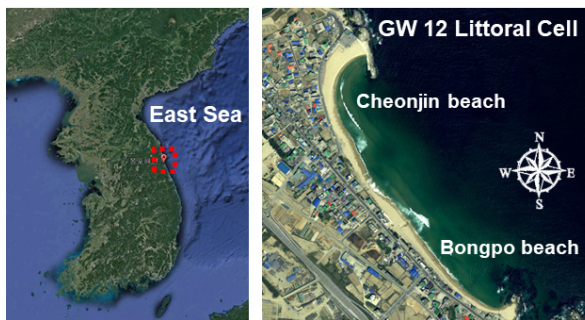


Fig. 2 Location of Cheonjin-Bongpo beach (Google, 2005)

2.2 Field Observation

Field observations were conducted to investigate the characteristics of the research area. During the observation, echo sounder devices (Sonar-tech, AquaRuler 200S; CEE HydroSystem, CEESTAR; and VALEPORT, MIDAS) were used, and the water depth was measured until 25 m. Global Navigation Satellite System (GNSS) devices (Leica, GX1230; Leica, Viva GS16) were used to obtain shoreline data when the wave height was less than 0.7 m. The wave data were acquired using an acoustic wave and current profiler (Nortek AS, AWAC). The median grain size (D_{50}) of the sand particle was determined to be 1.493 mm, and the calculated settling velocity was 16.7 cm/s using the van Rijn(1984)’s equation.

2.3 Application of SWAN Model

SWAN (Simulating waves nearshore) model 3rd generation was developed by Delft University of Technology (Booij et al., 1999), which aims to simulate the deformation of multi-direction irregular waves based on the wave action balance equation. The SWAN model is considered a practical method to predict wave deformation because it can consider wave reflection, diffraction, shoaling, and wave

Table 1 Conditions for SWAN modeling

Item	Contents	Note
Computation Region (m)	1,100 × 500	
The number of the grid cell	550 × 250	
Computational Grid Interval (m)	2	
Wave height (m)	2.54	Winter
Wave period (s)	9.02	Winter
Wave direction (°)	N80.7E	Winter
Wave height (m)	2.19	Summer
Wave period (s)	6.85	Summer
Wave direction (°)	E43.7N	Summer

breaking. Because of these advantageous features, the 3rd generation model (Version 41.31) of SWAN based on the field observation data was used to examine the impacts of an ACR under high wave conditions. In this study, SWAN modeling was conducted with two procedures. At first, the winter wave condition for the absence of an ACR was simulated to find the incident wave height for a physical model test.

After determining both the transmission and reflection coefficient from the physical model test, second SWAN modeling was performed for both winter and summer wave conditions to examine the wave height distributions in the presence of an ACR. During SWAN modeling, the maximum wave ($H_{1/250}$) was used as an incident wave for simulating the high wave condition. Moreover, bathymetry was rotated 45° counter-clockwise to perform easier modeling. Table 1 lists the specific conditions for SWAN modeling. As the SWAN model has been used widely in both the research and business practice field, an additional model verification process was omitted.

2.4 Two-dimensional Physical Model Test and Wave Analysis

The transmission and reflection coefficient values are required as input parameters to simulate the ACR installation conditions in the SWAN model. As there was no prior research explaining the transmission and reflection coefficient according to the ACR design, a physical model test was conducted to find its values. Therefore, it was assumed that the ACR installation locations refer to the designs of a submerged breakwater in the research area from the basic plan for the 2nd coastal maintenance project (Ministry of Ocean and Fisheries, 2014). The incident wave height for the physical model was determined using both cross-sectional and planar designs for the ACR. The wave height values for the incident and transmission are located 10 m away from the ACR offshore side and 20 m away from the onshore side in the points of the prototype scale. In addition, the Froude scale with a ratio of 1 : 25 in the length scale and 1 : 5 in the time scale was applied to the physical model test. A seabed slope of 1/30 was applied because the beach slope of the east sea is generally 1/30. The capacity type of wave gauge (Kenek, CH-608E) and wave probes (Kenek, CHT-30E) were used during the physical model test. Wave calibration processes were conducted at every measuring point

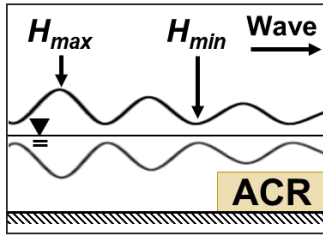


Fig. 3 Scheme of a partial standing wave

to obtain precise and reliable wave data. The transmission coefficient was defined as the ratio of the incident wave height (H_i) to transmitted wave height (H_t), as shown in Eq. (1).

$$K_T = \frac{H_t}{H_i} \quad (1)$$

Healy's formula (Healy, 1953) was applied to calculate the reflection coefficient (K_R), as shown in Eq. (2), which is based on the partial standing wave theory. To apply this equation, both the largest (H_{max}) and smallest (H_{min}) wave height at antinode and node of the partial standing wave, respectively, were used (see Fig. 3).

$$K_R = \frac{H_{max} - H_{min}}{H_{max} + H_{min}} \quad (2)$$

2.5 Wave Analysis with Representative Beach Profiles

Six representative beach profile ($BP1 \sim BP6$) lines, which are the normal direction to the shoreline, were set to investigate the erosion-mitigation effects of the ACR (see Fig. 4). Generally, the trends of the wave height distribution are different between the open inlet and behind the submerged structure. In this regard, the beach profile lines were determined at the open inlet of the ACR ($BP1$, $BP3$, and $BP5$). Moreover, $BP2$, $BP4$, and $BP6$ represent the beach profile lines, which are located behind the ACR structure.

With these beach profiles, the critical wave heights at each water depth condition were calculated based on the McCowan (1894)'s wave breaking parameter (κ), which has a general value of 0.78 (see Eq. (3)).

$$H_b = \kappa \times h_b = 0.78 h_b \quad (3)$$

Subsequently, wave-breaking locations were determined, where the

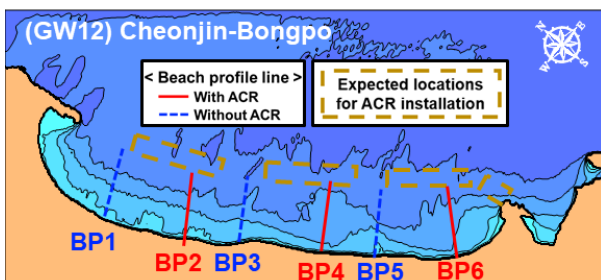


Fig. 4 Beach profile lines (Note that BP means the Beach Profile)

Table 2 Type of beach profile based on the Dean's parameter

Dean's parameter	Type
$3.0 < \Omega$	Dissipative
$1.5 < \Omega < 7.0$	Long-shore bar trough
$1.0 < \Omega < 5.0$	Rhythmic bar & beach
$0.6 < \Omega < 3.0$	Transverse bar & rip
$0.4 < \Omega < 2.5$	Ridge-and runnel and low-tide terrace
$\Omega < 1.0$	Reflective

wave height value given by SWAN modeling is greater than that of the wave breaking parameter cases. The height (H_b) and depth (h_b) of the breaking wave were decided. The slope for the beach profile ($\tan\beta$) was defined as an angle from the wave breaking point to the shoreline.

The Dean's parameter (Ω) introduced by Dean (1977), mass flux (M), undertow (u_b), maximum wave setup ($\bar{\eta}_{max}$), and surf-scaling parameter (ϵ_s), which are relevant factors to elucidate the high wave control performance of the ACR, were computed.

$$\Omega = \frac{H_b}{w_f T} \quad (4)$$

where, H_b , w_f , and T represent the wave height at breaking point, settling velocity of a sand particle, and wave period, respectively.

$$M = \rho \int_{-h}^{\eta} u dz \approx \frac{\rho g}{8} \times \frac{H^2}{\sqrt{gh}} \quad (5)$$

$$u_b = \frac{M}{\rho h} \approx \frac{\sqrt{g}}{8} \frac{H^2}{h^{3/2}} \quad (6)$$

$$\frac{\bar{\eta}_{max}}{H_b} = 0.232 \quad (\text{FEMA, 2015}) \quad (7)$$

$$\epsilon_s = \frac{\pi}{\xi_b^2} \quad (\text{Guza and Inman, 1975}) \quad (8)$$

($\epsilon_s > 33$: dissipative, $33 > \epsilon_s \geq 2.0 \sim 2.5$: intermediate, $\epsilon_s \leq 2.0 \sim 2.5$: high reflective)

$$\xi_b = \frac{\tan\beta}{\sqrt{H_b/L_o}} \quad (\text{Batjjes, 1974}) \quad (9)$$

where, ξ_b and L_o mean the surf similarity parameter and wavelength for deep water, respectively.

3. Numerical-Physical Combined Analysis

3.1 SWAN Modeling for Incident Wave Determination

SWAN modeling was first carried out to determine the incident wave for the physical model test and examine the wave height distribution without an ACR. In this regard, the wave heights in front

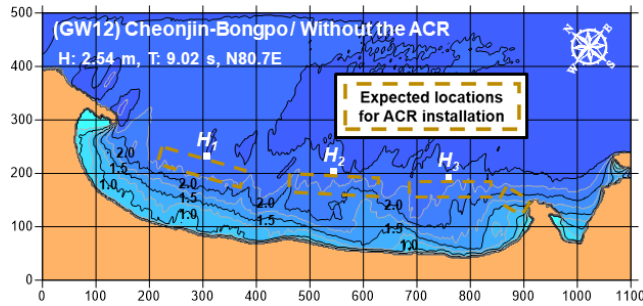


Fig. 5 Wave height distribution (without an ACR)

Table 3 Wave heights

H_1	H_2	H_3	Average
2.48 m	2.35 m	2.38 m	2.40 m

of three ACRs, denoted as H_1 , H_2 , and H_3 , were averaged (see Fig. 5). Consequently, the incident wave was determined to be 2.40 m for performing the physical model test, as shown in Table 3.

3.2 Physical Model Test for Finding K_T and K_R

To determine the relevant transmission and reflection coefficient, the structure geometry and wave condition were designed based on the Froude similarity scales (Table 4). A regular wave was generated until it reproduced the target wave ($H = 9.56$ cm, $T = 1.80$ s) at the incident wave measuring point.

Table 4 Experimental designs with the Froude scale

Contents	Proto type	Model
Crown depth (cm)	50	2
Crown width (m)	40	1.6
Wave height (cm)	240	9.56
Wave period (s)	9.02	1.80

Fig. 6 shows the experimental design for this physical model. The incident and transmitted wave heights were measured at $WP1$ and $WP2$, respectively. Moreover, the wave measurement was conducted from 17.2 m to 23.5 m to determine both the transmission coefficient (K_T) and reflection coefficient (K_R).

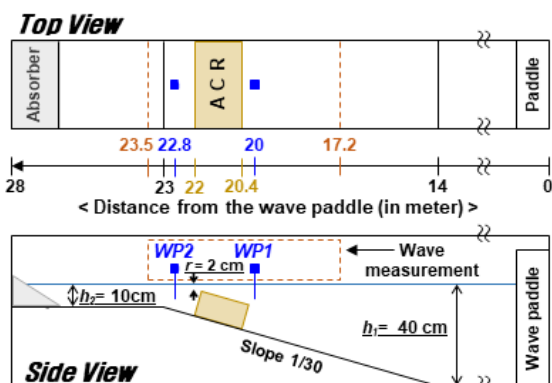


Fig. 6 Experimental design for the physical model test

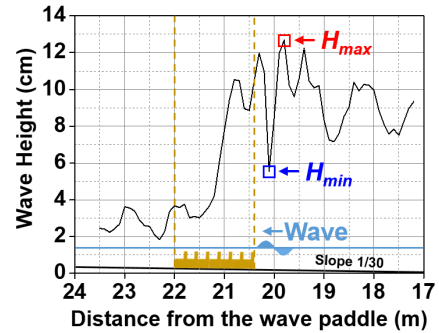


Fig. 7 Results of wave height in the physical model

Fig. 7 shows the results of the wave measurement. The results indicate that remarkable wave attenuation occurred from the ACR. Moreover, a partial standing wave occurred in front of the ACR. In this regard, the calculated transmission coefficient (K_T) was 0.36 based on the H_i (9.44 cm) and H_t (3.40 cm) values. Moreover, the calculated reflection coefficient (K_R) was 0.39. These K_T and K_R values were applied to both the winter and summer wave simulations.

4. Impacts of the ACR Installation on Wave Control

4.1 Trends of Wave Height Reduction and Wave Breaking

The second SWAN modeling was performed to investigate the wave height distribution trends with ACR installation for winter and summer wave conditions. Fig. A1 provides detailed information on the ACR structure. Fig. 8 shows the wave height distribution results in the presence of the ACR for a winter wave.

Table 5 lists the wave height percentile in the presence and absence of an ACR case calculated at each beach profile line. The results of significant wave reduction indicate that ACR installation plays a

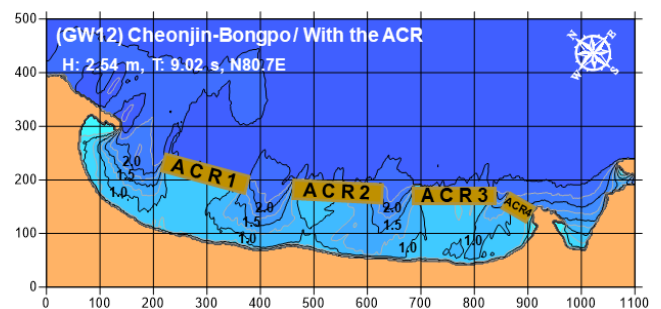


Fig. 8 Wave height distribution (with an ACR)

Table 5 Wave height ratio for each wave profiles

Beach profile	Winter (%)	Summer (%)	Average (%)
BP 1 (Without ACR)	91.9	94.7	93.30
BP 2 (With ACR)	72.6	69.2	70.90
BP 3 (Without ACR)	95.4	96.9	96.15
BP 4 (With ACR)	74.1	66.9	70.50
BP 5 (Without ACR)	81.1	86.8	83.95
BP 6 (With ACR)	60.1	57.8	58.95

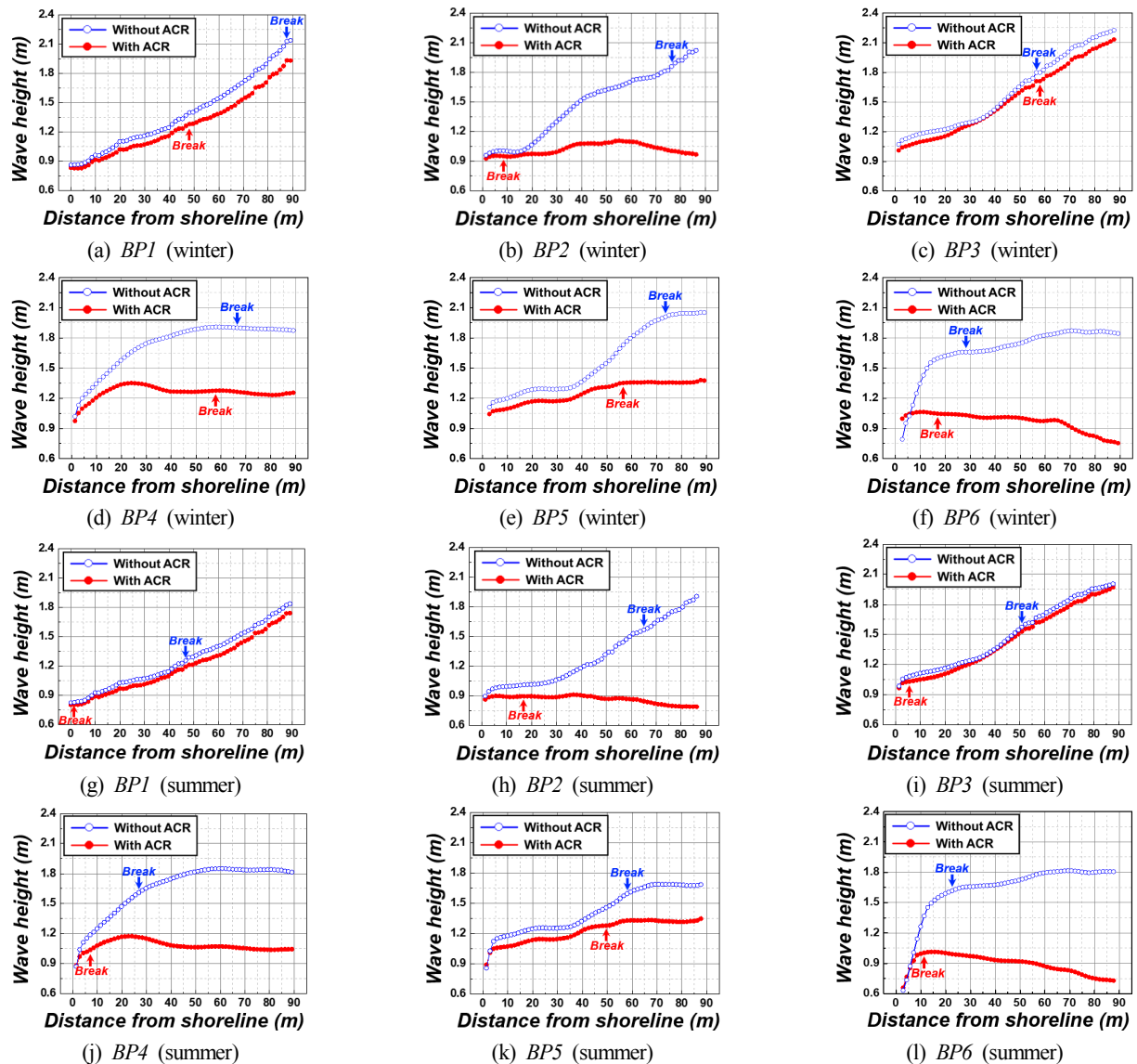


Fig. 9 Wave breaking trends at each beach profile according to ACR installation

crucial role in wave attenuation at the rear side of its structure for both winter and summer cases. Moreover, greater wave height mitigation (58.95~70.90%) occurred in the presence of an ACR, whereas no significant wave reduction occurred without ACR installation (83.95~96.15%).

The wave breaking trends also differed according to the ACR installation. Fig. 9 shows the wave-breaking height and wave-breaking distance from the shoreline. In the case of ACR installation, waves with smaller heights break near the shoreline, whereas relatively larger waves break further from the shoreline. The ACR induced breaking for larger waves in advance, allowing only smaller waves to propagate over the ACR. A significant difference was not observed between the winter and summer high waves, which means that the ACR plays a positive role in terms of wave height reduction.

4.2 Impacts of Wave-induced Nearshore Current

The mass flux (M), undertow (u_b), and maximum wave setup ($\bar{\eta}_{\max}$)

at each beach profile were calculated and compared to investigate the impacts of wave-induced current. Table 6 lists the computed values of M , u_b , and $\bar{\eta}_{\max}$. According to average values for the winter and summer results, smaller mass flux (~50%), undertow (~80%), and

Table 6 Computed values related to the nearshore current

Contents	Absence of the ACR ¹	Presence of the ACR ²	Unit
M (Winter wave)	256.0	129.9	kg/s
M (Summer wave)	220.2	101.0	
u_b (Winter wave)	1.13	0.86	m/s
u_b (Summer wave)	1.04	0.88	
$\bar{\eta}_{\max}$ (Winter wave)	1.22	0.78	m
$\bar{\eta}_{\max}$ (Summer wave)	1.11	0.65	

¹ Average values of BP2, BP4, and BP6 in the Natural beach case

² Average values of BP2, BP4, and BP6 in the ACR installation case

wave set up values (~61%) were observed with ACR installation, highlighting the positive impacts on shoreline stability.

4.3 Application of Morpho-dynamic Parameter for Wave Analysis

As a wave is a key parameter that determines the shape of the shoreline, the Dean's parameter (Ω) and surf-scaling parameter (ϵ_s) were computed to determine the impacts of the waves in terms of shoreline changes (Table 7 and Table 8). Under winter and summer high wave conditions, the Dean's parameter decreased in the ACR cases, which is closer to the reflective wave type compared to the dissipation wave type.

Table 7 Dean's parameter (Ω) for each beach profile

Beach profile	Winter wave		Summer wave	
	Without ACR	With ACR	Without ACR	With ACR
BP 1	1.41	0.84	1.09	0.71
BP 2	1.24	0.63	1.35	0.73
BP 3	1.20	1.14	1.41	0.90
BP 4	1.17	0.90	1.43	0.85
BP 5	1.34	0.90	1.38	1.14
BP 6	1.09	0.70	1.41	0.86
Average	1.24	0.85	1.35	0.87

Table 8 Surf-scaling parameter (ϵ_s) for each beach profile

Beach profile	ϵ_s for Winter wave		
	Without ACR	With ACR	Wave control
BP 1	55.10 (Dissipative)	28.04 (Intermediate)	Improved
BP 2	53.75 (Dissipative)	1.15 (Highly Reflective)	Improved
BP 3	28.41 (Intermediate)	30.58 (Intermediate)	-
BP 4	38.26 (Dissipative)	38.52 (Dissipative)	-
BP 5	41.76 (Dissipative)	37.29 (Dissipative)	Slightly Improved
BP 6	5.10 (Intermediate)	2.32 (Highly Reflective)	Improved
Beach profile	ϵ_s for Summer wave		
	Without ACR	With ACR	Wave control
BP 1	48.04 (Dissipative)	0.25 (Highly Reflective)	Improved
BP 2	73.49 (Dissipative)	1.48 (Highly Reflective)	Improved
BP 3	44.25 (Dissipative)	0.98 (Intermediate)	Improved
BP 4	14.16 (Intermediate)	1.23 (Highly Reflective)	Improved
BP 5	68.43 (Dissipative)	49.71 (Dissipative)	Slightly Improved
BP 6	8.70 (Intermediate)	4.61 (Intermediate)	Slightly Improved

When waves propagate over the ACR, a decrease in surf-scaling parameters usually occurs, particularly in BP2, BP4, and BP6, suggesting that wave-induced erosion can be mitigated. Moreover, the planar design of the ACR suggested in this study appears to be more effective for summer waves (improved in six beach profiles) than winter waves (improved in four beach profiles) in terms of high wave control. Overall, an ACR can mitigate erosion caused by high waves.

5. Conclusions

To investigate the feasibility of an artificial coral reef (ACR) as a coastal erosion prevention method, a case study was conducted by performing field observations and the numerical-physical combined method for Cheonjin-Bongpo Beach in South Korea. The main results of this research can be summarized as follows.

(1) The calculated wave transmission and reflection coefficients of the ACR were 0.36 and 0.39, respectively, based on the 1/25 Froude scale of the physical model test.

(2) Remarkable and greater wave height reduction (58.95~70.90%) occurred in each beach profile with ACR installation, whereas no significant wave height attenuation took place for the absence of ACR cases (83.95~96.15%). In addition, under the ACR installation condition, small waves break near the shoreline, but larger waves break far from the coast.

(3) In the presence of an ACR, the mass flux (M), undertow (u_b), and maximum wave setup ($\bar{\eta}_{max}$) were smaller than in the absence of an ACR. This suggests that an ACR plays a remarkable role in mitigating wave-induced current.

(4) When an ACR was applied to the research area, both the Dean's parameter (Ω) and surf-scaling parameter (ϵ_s) decreased. Therefore, a wave with the dissipative property changed to the reflective or intermediate type, which plays a positive role in erosion mitigation from high waves. In addition, the planar design for the ACR applied in this study showed greater wave control performance than the winter wave condition.

Because of the complicated coastal process and uncertainty of irregular waves, further studies will be needed to verify the feasibility of an ACR and consider more wave conditions. Furthermore, this model should be applied to other research areas.

Funding

This research was a part of the project titled 'Practical Technologies for Coastal Erosion Control and Countermeasure', funded by the Ministry of Oceans and Fisheries, Korea. (20180404)

Acknowledgments

The authors thank Professor Jung Lyul Lee of Sungkyunkwan University for sharing his valuable knowledge and insights that encourage us to conduct this research.

References

- Arns, A., Dangendorf, S., Jensen, J., Talke, S., Bender, J., & Pattiaratchi, C. (2017). Sea-level Rise Induced Amplification of Coastal Protection Design Heights. *Scientific Reports*, 7, 40171. <https://doi.org/10.1038/srep40171>
- Batjies, J.A. (1974). Surf Simiarity. *Coastal Engineering Proceedings*, 1(14), 26. <https://doi.org/10.9753/icce.v14.26>
- Booij, N., Ris, R.C., & Holthuijsen, L.H. (1999). A Third-generation Wave Model for Coastal Regions: 1. Model Description and Validation. *Journal of Geophysical Research*, 104(C4), 7649-7666. <https://doi.org/10.1029/98JC02622>
- Dean, R.G. (1977). Equilibrium Beach Profiles: U.S. Atlantic and Gulf Coasts, Department of Civil Engineering. Ocean Engineering Report 12, University of Delaware, Newark, Delaware.
- Federal Emergency Management Agency (FEMA). (2015). Guidance for Flood Risk Analysis and Mapping. Coastal Wave Setup, Guidance Document, 44.
- Google. (2005). Google Earth Pro. Downloaded March, 2020 from https://www.google.com/intl/ko_ALL/earth/versions/#download-pro
- Guza, R.T., & Inman D.L. (1975). Edge Waves and Beach Cusps. *Journal of Geophysical Research*, 80(21), 2997-3012. <https://doi.org/10.1029/JC080i021p02997>
- Healy, J.J. (1953). Wave Damping Effect of Beaches. *Proceedings: Minnesota International Hydraulic Convention*, Minnesota, United States, 213-220.
- Hong, S., Kim, T., Choi, Y., Kim, J., Kwon, Y., Lee, S., ... , Kwon, S. (2018). Study on Wave Reduction and Beach Sand Capture Performance of Artificial Coral Reefs for In-situ Application. *Journal of Ocean Engineering and Technology*, 32(6), 485-491. <https://doi.org/10.26748/KSOE.2018.32.6.485>
- Hong, S., Kim, T., Kim, J., & Lee, J. (2020). Variation Characteristics of Irregular Waves Passing over the Artificial Coral Reef. *Proceedings of International Conference on Aquatic Science & Technology*, Busan, Korea, 69.
- Kim, T., Baek, S., Kwon, Y., Lee J., Cha, S.M., & Kwon, S. (2020). Improved Coastal Erosion Prevention using a Hybrid Method with an Artificial Coral Reef: Large-scale 3D Hydraulic Experiment. *Water*, 12(10), 1-16. <https://doi.org/10.3390/w12102801>
- McCowan, J. (1894). On the Highest Wave of Permanent Type. *The London, Edingburgh, and Dublin Philosophical Magazine and Journal of Science*, 5(38), 351-358. <https://doi.org/10.1080/14786449408620643>
- Mentaschi, L., Vousdoukas, M.I., Pkekl, J.F., Voukouvalas, E., & Feyen, L. (2018). Global Long-term Observations of Coastal Erosion and Accretion. *Scientific Reports*, 8, 12876. <https://doi.org/10.1038/s41598-018-30904-w>
- Ministry of Oceans and Fisheries. (2014). Basic Plan for 2nd Coastal Maintenance Project (2010-2019). Retrieved from <http://www.mof.go.kr/article/view.do?articleKey=20592&boardKey=2¤tPageNo=1>
- US Army Corps of Engineers. (1984). *Shoreline Protection Manual I* (4th ed.). Washington DC, USA
- Van Rijn, L.C. (1984). Sediment Transport, Part II: Suspended Load Transport. *Journal of Hydraulic Engineering*, 110(11), 1613-1641. [https://doi.org/10.1061/\(ASCE\)0733-9429\(1984\)110:11\(1613\)](https://doi.org/10.1061/(ASCE)0733-9429(1984)110:11(1613))

Appendix

Fig. A1 Dimensions and formation of the ACR structure.

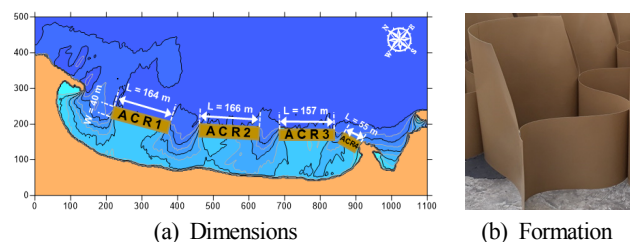


Fig. A1 Detail information of the ACR structure

Author ORCIDs

Author name	ORCID
Hong, Sunghoon	0000-0003-1952-7622
Jeong, Yeon Myeong	0000-0003-3349-1427
Kim, Taeyoon	0000-0002-5060-5302
Huynh, Van Men	0000-0001-8878-584X
Kim, Inho	0000-0003-3466-588X
Nam, Jungmin	0000-0002-8950-6897
Hur, Dong Soo	0000-0003-4627-7593
Lee, Jooyong	0000-0003-0130-1676
Kwon, Soonchul	0000-0003-3764-331X

Analysis of Wave Transmission Characteristics on the TTP Submerged Breakwater Using a Parabolic-Type Linear Wave Deformation Model

Jin-Hwan Jeong¹, Jin-Hoon Kim² and Jung-Lyul Lee³

¹Graduate student, School of Civil, Architecture and Environmental System Engineering, Sungkyunkwan University, Suwon, Republic of Korea

²Researcher, Department of Earth and Environmental Engineering, Kangwon National University, Samcheok, Republic of Korea

³Professor, Graduate School of Water Resource, Sungkyunkwan University, Suwon, Republic of Korea

KEY WORDS: Submerged breakwater, Wave transmission coefficient, Error function, Field observation, Wave deformation model

ABSTRACT: Owing to the advantages of assuring the best views and seawater exchange, submerged breakwaters have been widely installed along the eastern coast of Korea in recent years. It significantly contributes to promoting the advancement of shorelines by partially inhibiting incident wave energy. Observations were carried out by a pressure-type wave gauge in the Bongpo Beach to evaluate the coefficients of wave transmission via a submerged breakwater, and the results obtained were compared with those of existing conventional equations on the transmission coefficient derived from hydraulic experiments. After reviewing the existing equations, we proposed a transmission coefficient equation in terms of an error function. Although it exhibited robust relationships with the crest height and breaking coefficient, deviations from the observed data were evident and considered to be triggered by the difference in the incident wave climate. Therefore, in this study, we conducted a numerical experiment to verify the influence of wave period on the coefficients of wave transmission, in which we adopted a parabolic-type mild-slope equation model. Consequently, the deviation from calculated results appears to practically cover all deviation range in the observed data. The wave period and direction of the incident wave increased, the transmission coefficient decreased, and the wave direction was determined to demonstrate a relatively significant influence on the transmission coefficient. It was inferred that this numerical study is expected to be used practically in evaluating the design achievement of the submerged breakwater, which is adopted as a countermeasure to coastal beach erosion.

1. Introduction

To prevent coastal erosion, several beach and costal structures are actively being developed and constructed. These structures include submerged breakwaters, which are structures that protect beaches by breaking waves that enter from the open sea, thus suppressing wave energy. Submerged breakwaters are mainly used to reduce erosion damage caused by the incursion of high waves, as well as to protect and nourish the sand. Unlike detached breakwaters, submerged breakwaters are installed underwater; therefore they can preserve sea views and minimize environmental pollutants by promoting seawater exchange. However, despite these advantages, the shoreline alteration and coastal erosion prevention functions of submerged breakwaters remain quite unclear, and there have been cases of erosion behind submerged breakwaters (Ranasinghe and Turner, 2006). Therefore, calculating the transmission coefficients of submerged breakwaters is vital to improve the control capacity of wave energy, which is the inherent function of submerged breakwaters.

Several studies have been conducted on analyzing the transmission characteristics of submerged breakwaters according to their shapes and materials. Seelig (1980), Ahrens (1987), Van der Meer and Daemen (1994), and other researchers have conducted hydraulic experiments and proposed empirical equations to determine the reflection and transmission coefficients of submerged breakwaters in single-incident wave conditions. Takayama et al. (1985) proposed the empirical equation of a transmission coefficient based on hydraulic experiments conducted on a tetrapod (TTP) wave-dissipating block body in irregular wave conditions. To analyze transmission characteristics according to the breakwater's width, Seabrook and Hall (1998) conducted hydraulic experiments on submerged breakwaters that adopt rubble mounds as their body material. Ahrens (1987) and Van der Meer and Daemen (1994) inferred that the empirical equation of the transmission coefficient determined by Seabrook and Hall (1998) differed from that of their hydraulic experiment results when the width of the submerged breakwater was large, and they proposed a novel empirical equation for the transmission coefficient. Later, Van

Received 12 November 2020, revised 1 December 2020, accepted 2 December 2020

Corresponding author Jung-Lyul Lee: +82-31-290-7540, jllee6359@hanmail.net

© 2021, The Korean Society of Ocean Engineers

This is an open access article distributed under the terms of the creative commons attribution non-commercial license (<http://creativecommons.org/licenses/by-nc/4.0>) which permits unrestricted non-commercial use, distribution, and reproduction in any medium, provided the original work is properly cited.

der Meer et al. (2005) concluded that most empirical equations of transmission coefficients are based on limited data. Therefore, they developed a hydraulic experiment database containing 2,337 experiments conducted on several types of submerged breakwaters. On this backdrop, existing transmission-coefficient empirical equations were compared and a novel empirical equation for the transmission coefficient was proposed.

The aforementioned studies on the characteristics of submerged breakwater transmission mainly proposed empirical equations based on the results of hydraulic model experiments, and such equations are limited in recreating actual coastal environments. Furthermore, unlike western countries that adopt breakwaters with high crest heights and rubble mound bodies, South Korea mainly employs TTP-body submerged breakwaters, which possess a low crest height for more effective wave control. Consequently, the practical applications of the aforementioned empirical equations are limited. Therefore, to analyze the transmission characteristics of submerged breakwaters, this study observed waves at the front and back of the submerged breakwater in the Kangwon-do Bongpo Beach during Typhoon Krosa, which directly affected the eastern coast of Korea on August 16, 2019. Hence, this study presents a suitable transmission coefficient empirical equation for Korean coasts, which is compared to existing empirical equations (Takayama et al., 1985; d'Angremond et al., 1996). To compensate for the inability of the pressure-type wave gauge to identify wave-direction information, this study adopted a wave-deformation numerical model to analyze the influence of incident wave direction on the transmission coefficient. The applied wave model was implemented using a wave deformation model (WADEM) that performs numerical analysis using the alternating direction implicit (ADI) technique, presented by Lee (1994), on the parabolic mild-slope equation of Radder (1979).

2. Transmission Characteristics Analysis of Submerged Breakwater via Wave Observations

2.1 Analysis of Transmission Coefficient Empirical Equation

Takayama et al. (1985) proposed a transmission-coefficient empirical equation via hydraulic experiments conducted on a TTP wave-dissipating block body in irregular wave conditions, as expressed below:

$$K_t = -0.92 \left(\frac{B}{L_o} \right) + 0.42 \left(\frac{R_c}{H_o'} \right) + 3.80 \left(\frac{H_o'}{L_o} \right) + 0.51 \quad (1)$$

where, B , L_o , R_c , and H_o' represent the crest width of the submerged breakwater, deep-water wavelength, crest height, and equivalent deep-water wave height, respectively.

Van der Meer and Daemen (1994) harnessed the diameter of the rubble mounds to analyze the wave transmission coefficient according to the breakwater crest height, and based on the results obtained from hydraulic experiments, they proposed the following transmission

coefficient empirical equation:

$$K_t = a \frac{R_c}{D_{n50}} + b \quad (2)$$

Van der Meer and Daemen (1994) verified that when the ratio of the incident wave height H_i to the rubble mound diameter D_{n50} is less than one ($H_i/D_{n50} < 1$), the transmission coefficient K_t is dispersed. In addition, a is defined using H_i and D_{n50} while b is defined using the waveform wave steepness S , B , H_i , and D_{n50} , as expressed in Eqs. (3) and (4), respectively.

$$a = 0.031 \frac{H_i}{D_{n50}} - 0.024 \quad (3)$$

$$b = -5.42S + 0.0323 \frac{H_i}{D_{n50}} - 0.017 \left(\frac{B}{D_{n50}} \right)^{1.84} + 0.51 \quad (4)$$

d'Angremond et al. (1996) stated that breaking the shapes of waves affects the transmission coefficient. They noted that the effect of breaking waves was omitted from the transmission coefficient empirical equation of Van der Meer and Daemen's (1994); therefore, they presented a modified equation that can be applied to both impermeable structures and rubble mound breakwaters.

$$K_t = -0.4 \frac{R_c}{H_i} + 0.64 \left(\frac{B}{H_i} \right)^{-0.31} (1 - e^{-0.5\xi}) \quad (5)$$

ξ , the surf-similarity parameter (Battjes, 1974), is an index that determines the shape of the breaking waves, as expressed in Eq. (6).

$$\xi = \frac{\tan\beta}{\sqrt{\frac{H_o}{L_o}}} \quad (6)$$

where β and H_o represent the inclination angle of the beach cross section at the breaker zone and deep-water wave height, respectively.

It should be noted that the recreation range of the transmission coefficient presented by the transmission coefficient empirical equation of Van der Meer and Daemen (1994) is limited to a K_t range of 0.75–0.075, whereas that of d'Angremond et al. (1996) is limited to a K_t range of 0.8–0.075. Furthermore, based on the study conducted by Van der Meer et al. (2005), the aforementioned equations were compared to the transmission coefficients observed at actual beaches, and the results showed that the reproducibility of the equations decreased as the ratio of the crest width to the incident wave height (B/H_i) increased. In particular, it was determined that the equation presented by d'Angremond et al. (1996) tends to overestimate the transmission coefficient at $B/H_i > 8$ when the crest width is larger.

Seabrook and Hall (1998) conducted 2D and 3D hydraulic experiments and inferred that the results of the aforementioned

transmission coefficient empirical equations produce inaccurate results with an increase in the crest width of the rubble mound of submerged breakwaters. Consequently, they proposed the following transmission coefficient empirical equation, which exhibits high reproducibility even for very wide submerged breakwaters:

$$K_t = 1 - \left(e^{-0.65 \left(\frac{R_c}{H_i} \right) - 1.09 \left(\frac{H_i}{B} \right)} + 0.047 \left(\frac{BR_c}{LD_{n50}} \right) - 0.067 \left(\frac{R_c H_i}{BD_{n50}} \right) \right) \quad (7)$$

where L is the incident wavelength. However, the empirical equation of the transmission coefficient presented by Seabrook and Hall (1998) can properly recreate results of 2D hydraulic experiments but it cannot recreate that of a 3D hydraulic experiment. Additionally, outside the range expressed in Eqs. (8) and (9), where the crest width B of the submerged breakwater was excessively large or small, the reproducibility of the equation was poor.

$$0 \leq \frac{BR_c}{LD_{n50}} \leq 7.08 \quad (8)$$

$$0 \leq \frac{R_c H_i}{BD_{n50}} \leq 2.14 \quad (9)$$

Van der Meer et al. (2005) collated results obtained from the hydraulic experiments conducted by Seabrook and Hall (1998), including those of other researchers, and assembled more than 2,300 data to analyze the characteristics of transmission coefficient according to rubble mound protection. In addition, they compared the data with existing empirical equations presented by Van der Meer and Daemen (1994), d'Angremont et al. (1996), etc., then they proposed a transmission-coefficient empirical equation based on the B/H_i range. At $B/H_i < 8$, the equation presented by d'Angremont et al. (1996) exhibits high reproducibility, when Eq. (4) was applied. At $B/H_i > 12$ they adopted an empirical equation with high reproducibility, as expressed in Eq. (10). However, at $8 < B/H_i < 12$, they performed linear interpolation.

$$K_t = -0.35 \frac{R_c}{H_i} + 0.51 \left(\frac{B}{H_i} \right)^{-0.65} (1 - e^{-0.41\xi}) \quad (10)$$

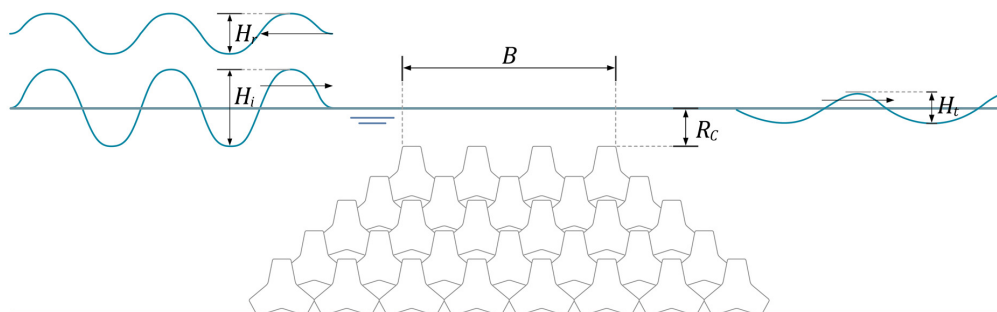


Fig. 1 Definition sketch of crest height R_c , incident wave height H_i , reflected wave height H_r , and transmitted wave height H_t

The submerged breakwaters constructed in South Korea are mainly large-scale TTP rather than rubble mounds, as illustrated in Fig. 1. They are very wide submerged breakwaters with low crest heights of approximately 40 m used to increase the wave reducing effect. Consequently, errors can occur when applying the aforementioned transmission coefficient empirical equations of submerged breakwater to Korean structures. Therefore, this study adopted wave data that were observed in the front of and back of a submerged breakwater at the Bongpo Beach on the eastern coast of Korea to propose a transmission coefficient empirical equation of submerged breakwater with high reproducibility in the submerged breakwater environments of Korea.

2.2 Wave Observations Before and After Submerged Breakwater

Wave observations were conducted to analyze the transmission characteristics of the submerged breakwaters installed in the coastal areas of South Korea. The wave observations were carried out at Bongpo Beach, located in Kangwon-do Goseong-gun, from the 6th to 21st of August, 2019, during Krosa, the 10th typhoon of the season, which directly affected Korea's eastern coast. The length, crest width, and crest height dimensions of the Bongpo Beach submerged breakwater are 150, 40, and 0.5 m, respectively. Three submerged breakwater segments were supposed to be built at 80 m intervals, and 110 m from the shoreline. Section 1 of the submerged breakwater, which is installed at the southern part of Bongpo Beach, has a length, crest width, and crest height of 40, 20, and 0.5 m, respectively. The bodies of the submerged breakwaters at the Bongpo Beach are all TTP 12.5t grade with porosity of 50%. Regarding the wave observations, pressure type wave gages (WTG-256) were installed in the front and back of the submerged breakwater located at the center of the Bongpo Beach, as shown in Fig. 2.

The wave heights at both sides were observed at 10-min intervals to obtain wave observations, as shown in Fig. 3. WTG-256 is a pressure type wave gage that measures wave height and period of time series data installed on the sea floor however, it cannot measure the wave direction. If the water is significantly deep, the accuracy of the measured water pressure may decrease. Therefore, it is recommended that the WTG-256 should only be used in shallow seas with depths of 30 m or less. In short-period wave conditions, WTG-256 tends to underestimate wave height (US Army Corps of Engineers, 1984). In

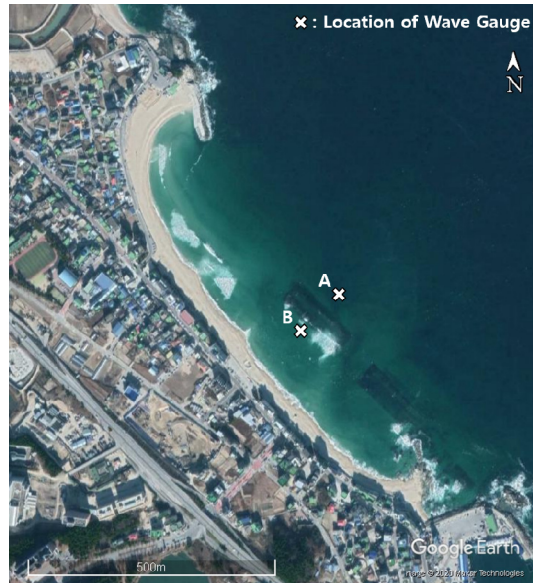


Fig. 2 Location of wave gauges at Bongpo beach

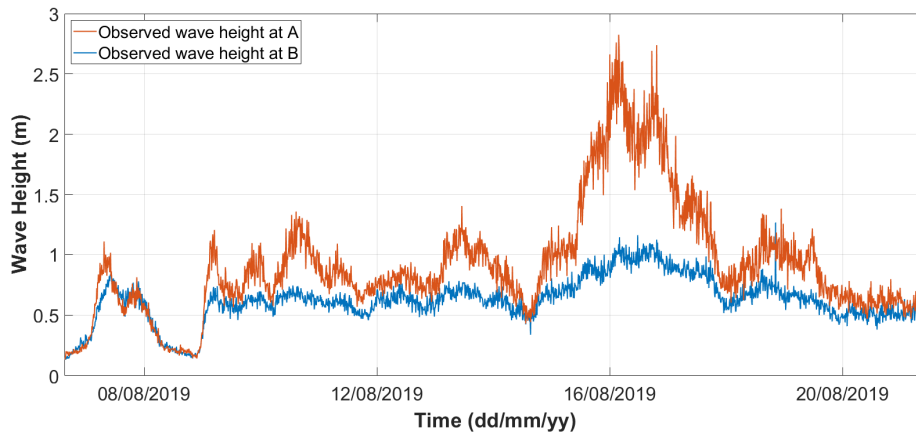


Fig. 3 Time series observed at both sides of submerged breakwater at Bongpo beach

the results obtained from wave observation, the transmission coefficient when Krosa hit on August 16, 2019 remarkably decreased, which means that the design goal of controlling high waves effectively was optimally achieved.

2.3 Analysis of Submerged Breakwater Transmission Coefficient via Wave Observations

This study analyzed transmission characteristics according to incident wave height using the wave data obtained before and after the Bongpo Beach submerged breakwater. In the analysis results of the observation data, it is evident that waves were controlled by breaking mainly at the crest height. Additionally, via the effective crest height R_c and the breaking coefficient γ , changes in the transmission wave height owing to the incident wave height can be easily expressed as the error function below. Here, the effective crest height refers to the crest height, as well as the effects of evaporation, permeability, etc., caused by the porosity of the submerged breakwater porosity.

$$H_t = \gamma R_c \operatorname{erf} \left(\frac{H_i}{R_c} \right) \quad (11)$$

Therefore, the following transmission coefficient empirical equation can be obtained from Eq. (11).

$$K_t = \frac{\gamma R_c \operatorname{erf} \left(\frac{H_i}{R_c} \right)}{H_i} \quad (12)$$

Fig. 4 presents the results obtained from comparing Eqs. (11) and (12) with the wave data observed at the coast. It can be observed that the empirical equations of the transmission coefficient exhibit high reproducibility. Here, 0.78 was taken as the breaking coefficient γ . Based on the observed values presented in Fig. 4, transmission cases where the coefficient K_t was greater than one, owing to reflected waves, were considered to be attributable to reflected waves. The data obtained from the observation of location A were considered to be the incident wave height H_i , which ignores the effect of reflected waves. When the crest heights, 0.5 and 1.0 m, specified in the design diagram of the Bongpo Beach's submerged breakwater, are used in Eqs. (11) and (12), the results diverge from the observed values, as indicated by

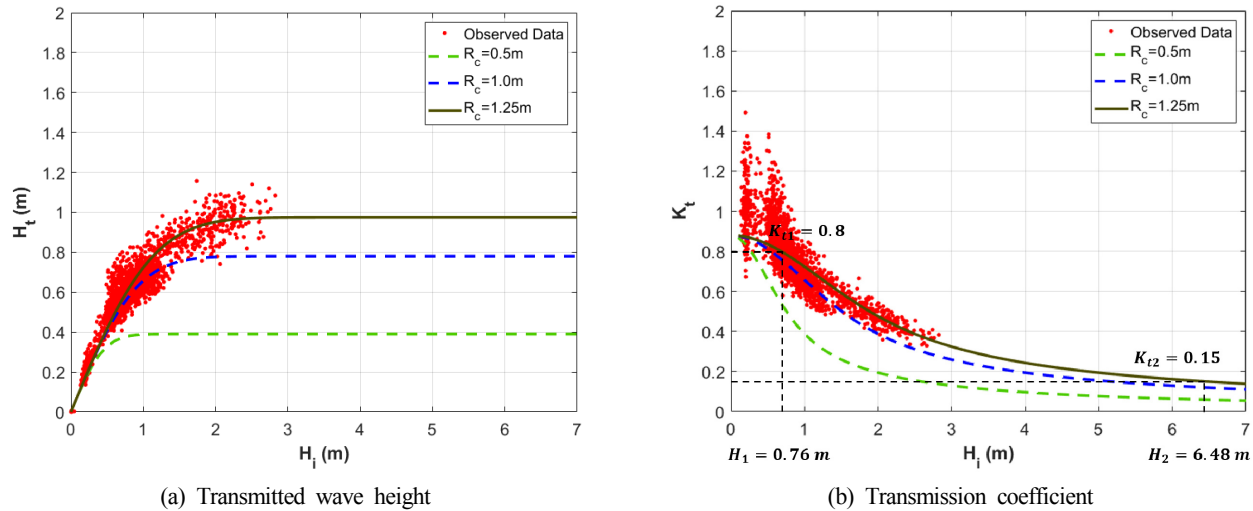


Fig. 4 Comparison between observed wave data and results obtained by Eqs. (11) and (12)

the dotted lines in Fig. 4. However, when 1.25 m is used, the results correspond optimally with the observed values, as illustrated by the solid line. This indicates that the effective crest height of the Bongpo Beach is R_c . Therefore, using Eq. (12), the transmission coefficient of the submerged breakwater is estimated to be 0.8 when the incident wave height is equal to Bongpo Beach's average wave height of 0.76 m, and the transmission coefficient is estimated to be 0.15 at a 30-year wave height of 6.48 m.

Fig. 5 presents the results obtained from comparing the transmission-coefficient empirical equation proposed in this study with those of Takayama et al. (1985) and d'Angremond et al. (1996). Here, the gradient of the submerged breakwater installed at Bongpo Beach is 3:4, and $\tan\beta = 3/4$ is adopted while wave period T is set at 7 s. In the comparison results, when $H_i > 2$ m, the equations proposed by Takayama et al. (1985) and d'Angremond et al. (1996) both converge in the $0.2 < K_t < 0.4$ range as the incident wave height increases, similar to the observed data case. However, at a small wave height of

$H_i > 2$ m, a tendency to underestimate the transmission coefficient was observed.

3. Transmission Coefficient Analysis of Submerged Breakwater via Numerical Modeling

The data observed by the pressure-type wave gauge do not include information on wave direction. Therefore, a wave deformation numerical model was used to analyze the effects of wave direction, as well as the wave height and period. This study examined the effects of the direction angles of incident wave, 0° , 10° , and 20° , on the transmission coefficient. For the wave model, this study adopted 2D WADEM, which employs a parabolic mild-slope equation.

3.1 Wave Deformation Numerical Model

The wave deformation phenomena modeled by WADEM include shoaling, refraction, diffraction, and reflection. Excluding non-linearity, most of the phenomena were recreated by the model using the mild-slope equation (Lee and Lee, 2006). The wave model that was used to analyze the transmission characteristics of the submerged breakwater was the WADEM numerical model, which performs numerical analysis on linear and hyperbolic mild-slope equations using the ADI technique introduced by Lee (1994). This model consists of the parabolic equation presented by Radder (1979), which can be used in large areas, and the hyperbolic wave model of Madsen and Larsen (1987), which excels at modeling harbor tranquility after harbor construction. This study adopted Eq. (13) as the governing equation, and it employed a parabolic wave model that provides accurate results on the shoaling, refraction, and wave crossing phenomena in a large area, with significantly stable numerical calculations.

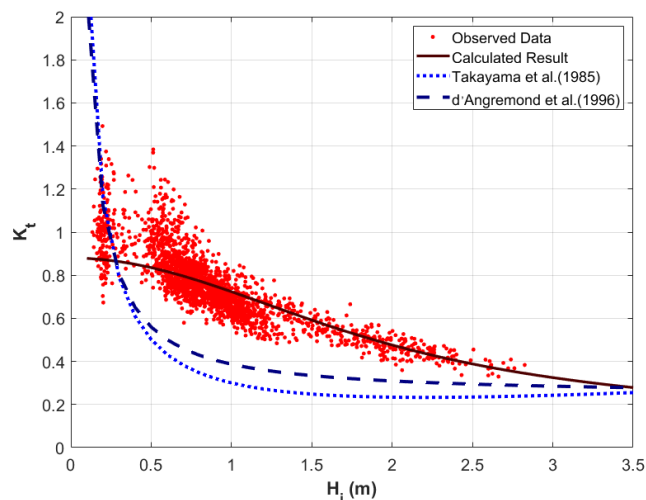


Fig. 5 Comparison between existing formulas and novel formula presented in this study

$$2ik_o \frac{\partial A}{\partial x} + (k_c^2 - k_o^2)A + \frac{\partial^2 A}{\partial y^2} = 0 \quad (13)$$

Here, $k_c^2 = k^2 + \nabla^2(CC_y)^{0.5}/(CC_y)^{0.5}$ and the numerical analysis are performed by the implicit method using a tridiagonal matrix. Boundary processing was carried out by Lee (1998). In this model, the energy attenuation caused by breaking waves was considered by the breaking wave formula, expressed in Eq. (14).

$$H_b = \gamma h_b \tag{14}$$

where the subscript b represents the breaking wave location.

3.2 WADEM Application Results

The numerical model used to analyze the transmission characteristics of the submerged breakwater created a regular grid, $\Delta x = \Delta y = 2$ m, in a 400×400 m area, and submerged breakwater with a width, length, and depth of 40, 200, and 4 m, respectively. Fig. 6(a) presents a contour line of bathymetry at Bongpo Beach where the wave observations were conducted. Fig. 6(b) illustrates the water depth that was created for the numerical model.

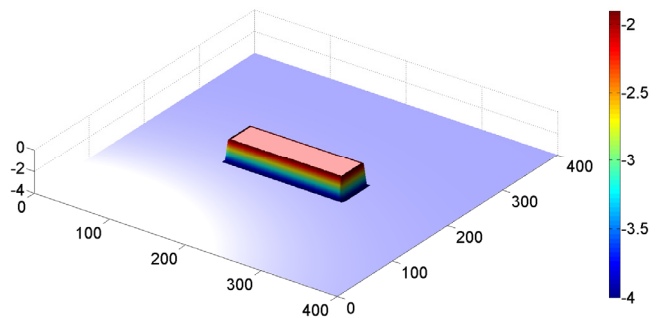
WADEM was utilized to analyze the transmission characteristics of three submerged breakwaters with crest heights of 1.5, 1.7, and 1.9 m, respectively, according to wave height, as presented in Table 1. Fig. 7

Table 1 Test conditions adopted in this study

Crest height (m)	Incident wave height (m)	Wave period (s)	Wave angle (°)
1.5	0.25	7, 9, 11	0, 10, 20
	0.50		
	0.75		
	1.00		
	1.50		
	3.00		
	0.25		
1.7	0.50	7, 9, 11	0, 10, 20
	0.75		
	1.00		
	1.50		
	3.00		
	0.25		
	0.50		
1.9	0.75	7, 9, 11	0, 10, 20
	1.00		
	1.50		
	3.00		

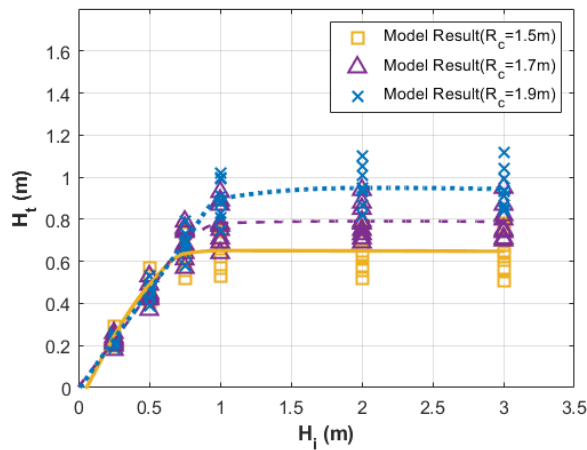


(a) Contour line of bathymetry at Bongpo beach

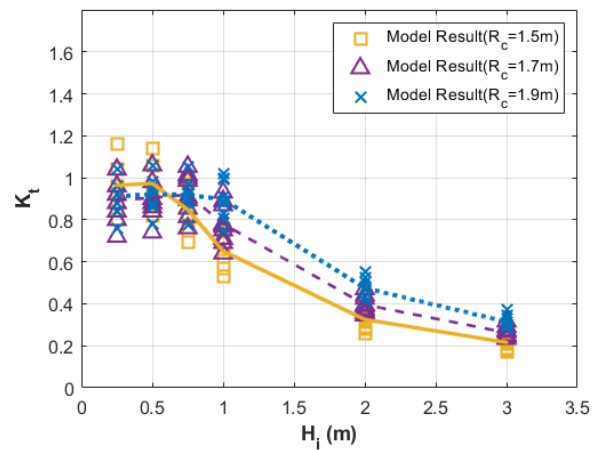


(b) Water depth for wave model

Fig. 6 Water depth at Bongpo beach and for wave model



(a) Transmitted wave height



(b) Transmission coefficient

Fig. 7 Transmission characteristics at crest height R_c via numerical model

presents the results of the numerically modeled transmission wave heights for six incident wave heights from 0.25 to 3 m at wave periods of 7, 9, and 11 s, as well as wave directions of 0°, 10°, and 20°. Here, a wave direction of 0° indicates a wave approaching perpendicularly to the submerged breakwater. Additionally, the wave direction was altered in a clockwise direction. As shown in Fig. 7, at the same incident wave height, the transmitted wave height decreased with the crest height. This indicates that wave control was effectively achieved by a low crest height.

3.3 Transmission Characteristics Analysis of Submerged Breakwater via Numerical Modeling

The three crest height cases modeled in Fig. 7 were compared to the field observation data and Eqs. (11) and (12). As can be observed in Fig. 8, the results show that the characteristics observed in the field were best reflected at a crest height of 1.9 m. Here, the breakwater used in the wave model had a porosity of 0%, whereas TPP, which was adopted as the body of the submerged breakwater installed on the

coast, conventionally exhibits a porosity of around 50%, and the results of hydraulic experiment agreed well with this value (Shin et al., 2008). Shin et al. (2008) performed hydraulic experiments that confirmed that the transmission coefficient of breakwater increases with its porosity. This means that submerged breakwaters with low porosity exhibit superior wave dissipating effects. Therefore, it is inferred that the transmission coefficient results of the numerical model's wave height are greater than those of the observed data owing to the difference in submerged breakwater porosity.

Fig. 9 presents the results of the numerical model for the transmission coefficient according to the wave period and direction when the crest height was 1.9 m. It can be observed that the transmission coefficient appeared to decrease as the wave period and incident wave direction angle increased. It can also be observed that the transmission coefficient exerts a greater effect on the wave period, and the wave control effect of the submerged breakwater is greater when the wave approaches the submerged breakwater perpendicularly compared to when it approaches obliquely.

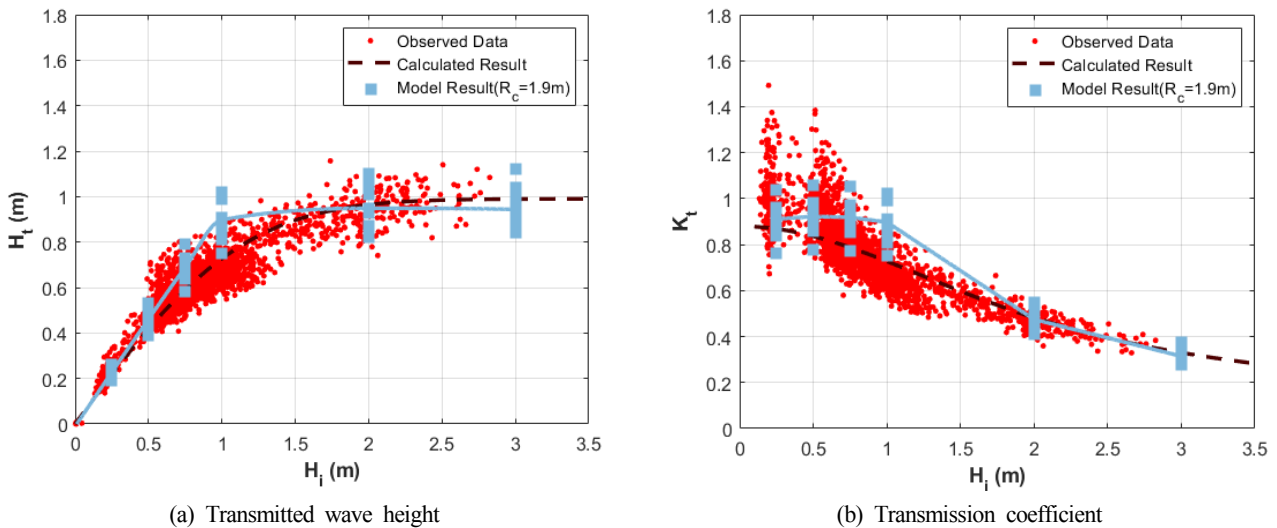


Fig. 8 Comparison of observed data, calculated, and numerical model results ($R_c = 1.9$ m)

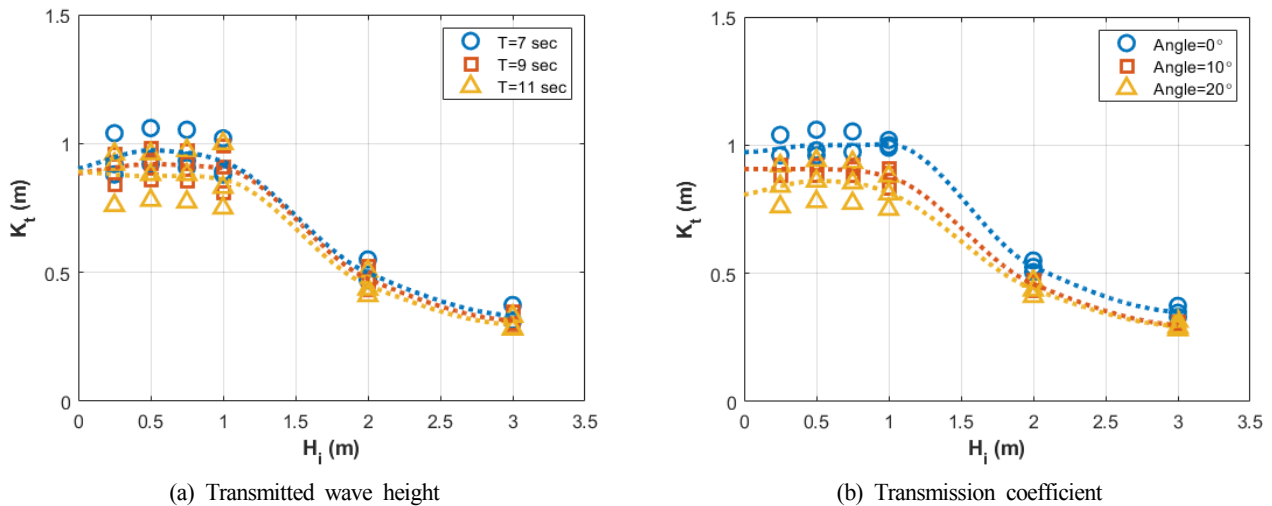


Fig. 9 Influence of wave period and wave angle on wave transmission coefficient via numerical model

4. Conclusion

In South Korea, submerged breakwater construction is often used to reduce the energy of incident waves and minimize damage to the landscape, and the transmission coefficient of a submerged breakwater plays a major role in determining the performance of the breakwater. However, research on analyzing the transmission characteristics of submerged breakwaters in South Korea has been insufficient, where the submerged breakwaters usually have low crest heights and large crest widths, and TTP is utilized as the submerged breakwater body. Consequently, it is unavoidable to adopt foreign empirical equations for transmission coefficients of submerged breakwater which leads to inaccurate analysis results when calculating the transmission coefficients. Therefore, this study has proposed an empirical equation for a transmission coefficient that implements wave data observed at actual coastal areas. Additionally, this study has adopted WADEM to analyze the effect of wave direction and compensate for the limitations of the observation data.

When Typhoon Krosa hit in August 2019, two pressure-type wave gages were installed to conduct wave observations at both sides of a submerged breakwater at Bongpo Beach in Kangwon-do Goseong-gun, where coastal improvement projects are currently taking place. Based on these observations, this study has proposed Eq. (12), an empirical equation with high reproducibility for the transmission coefficient of wave height. This equation was analyzed and compared with the empirical equations of transmission coefficient proposed by Takayama et al. (1985) and d'Angremond et al. (1996). The analysis results demonstrate that the existing equations of transmission coefficient converge on a wave height transmission coefficient range of 0.2–0.4 when the incident wave height is 2 m or greater, similar to that of the observed wave data. However, at an incident wave height of 2 m or less, the equations diverged significantly from the observed wave data. It is inferred that this divergence occurs because of the construction environment in South Korea, where highly porous TTP is preferred to rubble mounds, and low crest heights are used for effective wave control.

The observed data did not include information on wave direction, and 2D WADEM was adopted to analyze the wave period and direction effects. The analysis results showed that the transmission coefficient decreased as the wave period and direction increased, and the wave direction exerted a relatively significant effect on the transmission coefficient. In addition, it was inferred that the transmission coefficient results of the numerical model diverged from the observed data owing to the porosity of the submerged breakwater, and it was concluded that the transmission coefficient of the submerged breakwater increases with its porosity. Therefore, it will be necessary to perform further research to analyze the influence of porosity on the wave height transmission coefficient according to the shape and body of the submerged breakwater.

Funding

This study was conducted with the support of the Korea Institute of Marine Science and Technology Promotion through a 2020 grant from the Ministry of Maritime Affairs and Fisheries (20180404 Coastal Erosion Management and Response Technology Commercialization).

References

- Ahrens, J.P. (1987). Characteristics of Reef Breakwaters (CERC-87-17). US Army Corps of Engineers.
- Battjes, J.A. (1974). Surf Similarity. *Coastal Engineering Proceedings*, 1(14), 466-480. <http://doi.org/10.9753/icce.v14.26>
- d'Angremond, K., Van der Meer, J.W., & De Jong, R.J. (1996). Wave Transmission at Low-Crested Structures. *Proceedings of 25th International Conference on Coastal Engineering, ASCE*, 3305-3318. <https://doi.org/10.1061/9780784402429.187>
- Lee, J.L. (1994). Quasi-3D Wave-induced Circulation Model. *Journal of The Korean Society of Coastal and Ocean Engineers*, 6(4), 459-471.
- Lee, J.L. (1998). A High-accuracy Approach for Modeling Flow-dominated Transport. *Transactions on Ecology and the Environment*, 18, 277-286.
- Lee, J.L., & Lee, D.H. (2006). Introduction of WADEM (Wave DEformation Model) Operated with GUI. *Proceedings of Fall Conference of Korean Society for Marine Environment & Energy*, 155-162.
- Madsen, P.A. & Larsen, J. (1987). An Efficient Finite-difference Approach to the Mild-slope Equation. *Coastal Engineering*, 11(4), 329-351. [https://doi.org/10.1016/0378-3839\(87\)90032-9](https://doi.org/10.1016/0378-3839(87)90032-9)
- Radder, A.C. (1979). On the Parabolic Equation Method for Water-wave Propagation. *Journal of Fluid Mechanics*, 95(1), 159-176.
- Ranasinghe, R., & Turner, I.L. (2006). Shoreline Response to Submerged Structures. *Coastal Engineering*, 53(1), 63-79. <https://doi.org/10.1016/j.coastaleng.2005.08.003>
- Seabrook, S.R., & Hall, K.R. (1998). Wave Transmission at Submerged Rubble Mound Breakwaters. *Proceeding of 26th International Conference on Coastal Engineering, Copenhagen, Denmark, 2000-2013*. <https://doi.org/10.1061/9780784404119.150>
- Seelig, W.N. (1980). Estimation of Wave Transmission Coefficients for Overtopping of Impermeable Breakwaters. *CERC Coastal Engineering Technical Aid*, 80(7).
- Shin, M.S., Lee, H.J., & Park, K.Y. (2008). An Experimental Study on Wave Decrease Effect by Porosity in Submerged Breakwater. *Proceeding of Conference of Korean Society of Civil Engineers*, 1136-1145.
- Takayama, T., Nagai, K., & Sekiguchi, T. (1985). Irregular Wave Experiments on Wave Dissipation Function of Submerged Breakwater with Wide Crown. *Proceedings of 32th Japanese Conference on Coastal Engineering, JSCE*, 32, 545-549.

- US Army Corps of Engineers. (1984). Shore Protection Manual (4th Ed.). Washington D.C, 1-337.
- Van der Meer, J.W., Briganti, R., Zanuttigh, B., & Wang, B. (2005). Wave Transmission and Reflection at Low-crested Structures: Design Formulae, Oblique Wave Attack and Spectral Change. *Coastal Engineering*, 52(10-11), 915-929. <https://doi.org/10.1016/j.coastaleng.2005.09.005>
- Van der Meer, J.W., & Daemen, I.F.R. (1994). Stability and Wave Transmission at Low Crested Rubble Mound Structures. *Jornal of Waterway, Port Coastal and Ocean Engineering*, 120(1), 1-19. [https://doi.org/10.1061/\(ASCE\)0733-950X\(1994\)120:1\(1\)](https://doi.org/10.1061/(ASCE)0733-950X(1994)120:1(1))

Author ORCIDs

Author name	ORCID
Jeong, Jin-Hwan	0000-0001-9736-1168
Kim, Jin-Hoon	0000-0001-6061-5267
Lee, Jung-Lyul	0000-0001-9410-9725

Fundamental Research for Video-Integrated Collision Prediction and Fall Detection System to Support Navigation Safety of Vessels

Bae-Sung Kim¹, Yun-Tae Woo², Yung-Ho Yu³ and Hun-Gyu Hwang¹

¹Senior Researcher, Ocean ICT & Advanced Materials Technology Research Division, RIMS, Busan, Korea

²Researcher, Ocean ICT & Advanced Materials Technology Research Division, RIMS, Busan, Korea

³Technical Director, Research Institute of Ocean and Ship ICT Convergence, MEIPA, Busan, Korea

KEY WORDS: Navigation safety, Video-integrated, Collision prediction, Fall detection, Automatic identification system

ABSTRACT: Marine accidents caused by ships have brought about economic and social losses as well as human casualties. Most of these accidents are caused by small and medium-sized ships and are due to their poor conditions and insufficient equipment compared with larger vessels. Measures are quickly needed to improve the conditions. This paper discusses a video-integrated collision prediction and fall detection system to support the safe navigation of small- and medium-sized ships. The system predicts the collision of ships and detects falls by crew members using the CCTV, displays the analyzed integrated information using automatic identification system (AIS) messages, and provides alerts for the risks identified. The design consists of an object recognition algorithm, interface module, integrated display module, collision prediction and fall detection module, and an alarm management module. For the basic research, we implemented a deep learning algorithm to recognize the ship and crew from images, and an interface module to manage messages from AIS. To verify the implemented algorithm, we conducted tests using 120 images. Object recognition performance is calculated as mAP by comparing the pre-defined object with the object recognized through the algorithms. As results, the object recognition performance of the ship and the crew were approximately 50.44 mAP and 46.76 mAP each. The interface module showed that messages from the installed AIS were accurately converted according to the international standard. Therefore, we implemented an object recognition algorithm and interface module in the designed collision prediction and fall detection system and validated their usability with testing.

1. Introduction

South Korea has a large ocean area, complex coastlines, and many small and large islands. Because of these geographic characteristics, ships are widely used as a method of commercial transportation (Kim et al., 2020). Maritime accidents that occur during the navigation of such vessels result in a high number of human casualties and substantial property damage. If oil is spilled from the vessel, the environment also becomes polluted, leading to greater societal loss. The current management system and follow-up measures for preventing such accidents are limited, and the actual effect of these measures has been insignificant. As a result, the frequency of maritime accidents greatly varies each year. In addition, the activity boundary of fishing boats and the demand for tourism in island regions have risen, resulting in an increased risk of accidents. Moreover, the country is highly dependent on marine transport, yet it is not possible to transport

goods by land during the import and export process due to the geographical environments. Hence, most goods are transported by maritime vessels. As a result, maritime traffic and congestion are rising rapidly. Meanwhile, small and medium-sized ships, such as fishing boats and coastal passenger vessels, make up a large proportion of the registered vessels in South Korea, and many maritime accidents are caused by these ships (Jung, 2013; Park et al., 2018). Most ship accidents are caused by marine navigational mistakes, such as lack of vigilance, violation of navigation laws, and failure to comply with work safety regulations. Even a large proportion of human casualties are attributed to overboard accidents caused by loss of footing or carelessness. To prevent maritime accidents caused by human factors, such as ships colliding or running aground and overboard falls, it is necessary to adopt a system that promptly recognizes and predicts risk factors by linking the navigation communication equipment with CCTV (Closed-circuit television) camera images and alerting

Received 27 November 2020, revised 21 January 2021, accepted 21 January 2021

Corresponding author Hun-Gyu Hwang: +82-51-974-5572, hghwang@rims.re.kr

It is noted that this paper is revised edition based on proceedings of KIICE 2020 in Gyeongju.

© 2021, The Korean Society of Ocean Engineers

This is an open access article distributed under the terms of the creative commons attribution non-commercial license (<http://creativecommons.org/licenses/by-nc/4.0>) which permits unrestricted non-commercial use, distribution, and reproduction in any medium, provided the original work is properly cited.

navigators with warnings based on the situation and the safety information related to the sea route.

Therefore, to enhance the safety and navigational reliability of small and medium-sized vessels, this paper presents a fundamental study of a video-integrated collision prediction and fall detection system that combines data from an automatic identification system (AIS), which is essential navigation communication equipment for ships, with images from a CCTV camera. Section 2 of this paper analyzes the background and needs, including related studies conducted in South Korea and overseas. Section 3 describes the composition of the system being developed and the design of each component. Section 4 discusses the implementation of the algorithm and interface modules, and Section 5 deals with the content related to testing and performance verification. Section 6 concludes the paper with the conclusion and suggestions for future studies.

2. Background and Literature Review

2.1 Background and Needs

According to statistics, a total of 2,971 maritime accidents occurred in 2019. Although both major and minor causes played a role in the maritime accidents, human mistakes accounted for approximately 80% of the accidents (MOF, 2020). These human mistakes can be attributed to a variety of factors, such as the behavior, habits, and mindset of operators, the internal and external environment, customary practices and the culture of the organization, and relationships with co-workers (Kim et al., 2011). It is difficult to accurately identify and eliminate complicated human errors, and the conventional methods of re-education and training have limitations. Furthermore, more than 84% of the accidents were caused by small and medium-sized ships. This is because, in comparison with large vessels, these ships are relatively vulnerable to the marine environment, their navigators are older, they have inadequate communication equipments for navigation, or they have insufficient information. For overboard accidents, a timely response in rescuing people who have fallen overboard is important. However, man overboard (MOB) equipment operates after a person falls overboard, so it cannot prevent or predict such accidents.

2.2 Literature Reviews

Domestic studies that utilize images to aid maritime safety include the development of an algorithm that uses computer vision to measure maritime traffic and to confirm collision with marine structures; the implementation of an augmented reality-based image analysis module that visualizes the navigation information to enable the navigator to simultaneously check both outside of the ship's bridge and the navigation information; the development of a camera-AIS-linked active monitoring and approach alarm system to protect marine buoys; and the study of a search and rescue method using cameras and drones for overboard accidents (Joo et al., 2011; Lee et al., 2013; Kim and Jeong, 2017; Hwang et al., 2018). However, the objectives of these

studies were to prevent other ships from approaching the vessel and to help in incidents of maritime distress. Hence, their systems performed different functions than the system developed in this study. Moreover, these systems were not integrated with the equipment installed on the vessel, so they had to be operated separately. Because the number of pieces of equipment used in navigation is thus increased, more burden is placed on the navigator.

In other countries, research on automated maritime surveillance using CCTV cameras is actively ongoing to cope with increased maritime traffic. One study was conducted to develop a system to track vessels and provide visualized information using the identification information obtained by combining the data collected by the vessel traffic service (VTS) system with CCTV images (Bloisi et al., 2011; Bloisi et al., 2016; Xiao et al., 2018). Because the systems developed in these studies operated on land, they mainly supported control activities and could not recognize or respond to dangerous situations on the vessel.

Therefore, the system developed in this study recognizes vessels in the CCTV camera images using artificial intelligence and displays the vessel's information in an integrated manner by linking with the navigation communication equipment. In addition, because it recognizes people, the system can detect an overboard fall, which could occur while the crew members are working. It also provides the navigator with warnings in each phase to raise awareness in response to dangerous situations such as collision and drowning.

3. Design of the System

3.1 Automatic Identification System (AIS)

When the vessel is navigating, it uses various types of navigation communication equipment to identify maritime traffic conditions and consider them in operation and navigation plans to prevent maritime accidents. A radar emits electromagnetic waves out to sea, and then it receives, analyzes, and displays the signals reflected from the surface of objects. Because radars are expensive, they are installed and operated predominantly in large vessels. However, their reception sensitivity is degraded under inclement weather conditions or when the waves are high. Furthermore, radars can only check for the existence of other ships. They cannot identify other information, such as the name and type of the ship and its cargo, without installing additional equipment. Radars have a disadvantage in that it is difficult to detect a target behind a bend or an obstacle. To remedy such issues, the International Maritime Organization (IMO) recommends installing AIS on vessels.

The AIS is a piece of navigation communication equipment used to exchange a vessel's information with another vessel, as well as between vessel and land. According to the status or demand of the vessel, it can transmit wireless data over the VHF (Very high frequency) frequency band. The AIS also provides maritime mobile service identities (MMSI), static information (the IMO identification number, name of the vessel, vessel specifications, etc.), and dynamic



Fig. 1 AIS Receiver used by the proposed system

information (navigation status, speed, location, and course of the vessel). Using the AIS, the VTS center manages the passage of vessels and supports vessels when they navigate coastal waters. Fig. 1 shows the AIS receiver installed for this study.

3.2 Composition of the System

As shown in Fig. 2, the video-integrated collision prediction and alarm system, which combines the AIS with CCTV camera images, consists of the following six components.

(1) The ship recognition algorithm obtains images of the visual scene in front of the ship from a camera facing the ship's bow. Using artificial intelligence, the ship recognition algorithm recognizes other vessels in these images, such as large, medium, and small ships and fishing boats, that could be a risk factor during navigation.

(2) The crew recognition algorithm obtains images of the visual scene behind the ship using a camera facing the ship's stern. Using artificial intelligence, the crew recognition algorithm recognizes the crew in these images to identify human accidents due to falls that could occur the carelessness of people onboard the ship. The term crew means people who are operating or navigating the ship or performing desk jobs. However, everyone onboard the ship, including the crew members, passengers, and people living on the islands, is exposed to the risk of overboard falls. Therefore, in this study, the term crew is used to refer to everyone onboard the ship.

(3) The interface module analyzes the AIS data received in the IEC 61162-1/2(NMEA 0183) sentence format. Based on the analysis, the interface module converts and processes the location of the host ship and the static and dynamic information about other vessels.

(4) If the ship recognition algorithm recognizes another vessel, and that vessel's location matches the location processed by the interface

module, the integrated display module displays the name, speed, and location of that vessel in text format on the camera image layer. For any vessel that was recognized as a marine obstacle but whose accurate location information could not be acquired because the AIS was not installed, only the distance between that vessel and the host ship is displayed.

(5) The collision prediction and fall detection module calculates the distance between the marine obstacle recognized by the ship recognition module and the interface module. It also calculates the location of the predicted collision. In addition, this module monitors dangerous situations, such as when a crew member who is recognized is approaching a set boundary or falls over the guardrail.

(6) The alarm management module receives the data analyzed by the collision prediction and fall detection module and triggers the navigator alarm according to the set risk stages.

4. Implementation of the Algorithm and Interface Module

Prior to developing an overall video-integrated collision prediction and fall detection system to support the navigation safety of small and medium-sized ships, we implemented the ship and crew recognition algorithm and the AIS data interface module.

4.1 Implementation of the Ship and Crew Recognition Algorithm

Past studies on object recognition identified an object by evaluating the features of the object. Afterward, the object was divided into a grid. The feature information was constructed for each area, and machine learning was used for object recognition. However, convolutional neural network (CNN)-based deep learning has emerged, which shows performance superior to previous methods. Hence, the object recognition rate has improved (Lee et al., 2018). Therefore, an algorithm was implemented to recognize ships and crew in the images obtained based on a deep learning model appropriate for real-time image recognition. The you only look once (YOLO) v2, which is widely used in related fields, was used as the deep learning model. This method sections the input image into a grid and finds the object to be recognized in each cell. The network structure diagram for this method is shown in Fig. 3.

The 2014 COCO dataset (COCO, 2014) includes a variety of images, such as vessels, people, cars, and animals. It also includes the coordinates, width, and height information of the objects. The

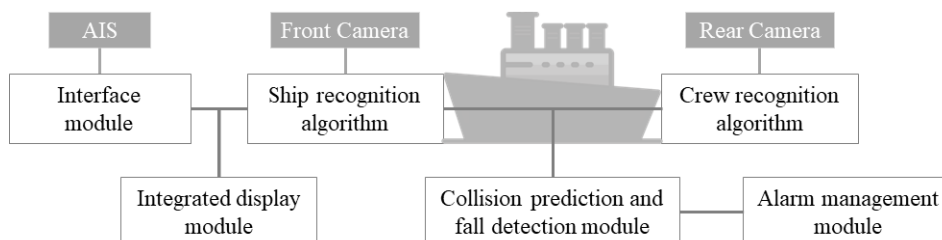


Fig. 2 Conceptual diagram of the designed system

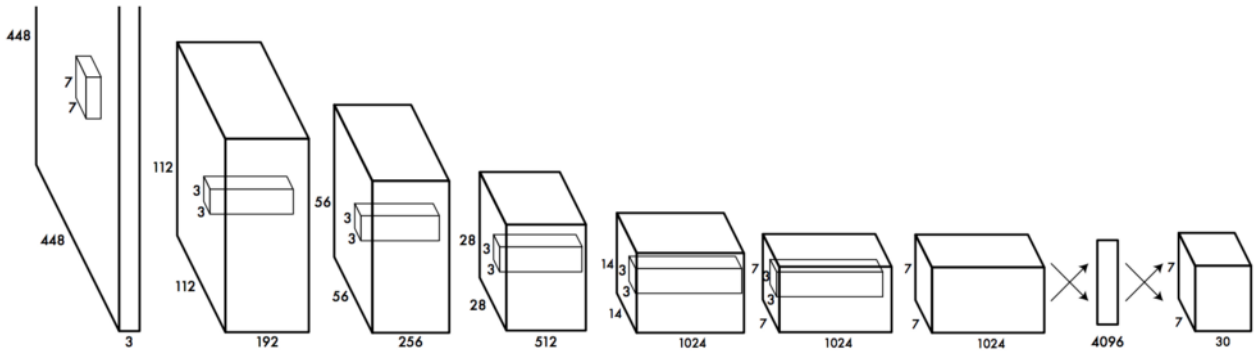


Fig. 3 YOLOv2 network structure (Redmon et al., 2016)

2014 COCO dataset was selected as the learning data, and approximately 82,000 images were used in training. Based on the observation that the input images were in color, arbitrary lighting was added to adjust the brightness. The images were preprocessed by adjusting the brightness to improve the performance and effects of the deep learning model during the learning process. The algorithm was developed as a C++ library to make it easy to expand it to application software and apply it to an operating system. NVIDIA CUDA was used to process the images at high speed.

4.2 Implementation of the Interface Module

The AIS interface software module is needed to map and display the information about the ship shown on the CCTV camera image. Out of a total of 27 messages (number 1 through number 27), message number 5 contains static and navigation-related data for Class A equipment. Message numbers 1 through 3 are the dynamic and location reporting data of Class A equipment. The AIS interface software module was implemented to convert and process these messages. Here, Class B equipment is used by small vessels in South Korea. However, fishing boats make up a large proportion of these vessels. Instead of Class B equipment, fishing boats use the vessel pass (V-Pass) equipment, which automatically reports the location of the vessel to the VTS center and transmits a distress signal if the ship is tilted beyond a certain angle. However, for security reasons, the permission and agreement of the Korean Coast Guard are required

before V-Pass data can be collected, analyzed, and used. Therefore, the V-Pass data are excluded from this study.

The functions of the interface module, such as a serial communication port and speed settings, that store the text related to the received data, remove the list, and exit this interface module are shown on the upper left corner of the screen. The list of the received AIS raw data is shown on the bottom left corner of the screen. The interface module was implemented to show compressed messages on the right side after they are converted and processed according to the IEC 61162-1/2 (NMEA 0183) international standard. Fig. 4 shows the implemented interface module.

5. Component Testing and Performance Verification

A test program was developed to evaluate the performance of the ship and crew recognition algorithm. The test program places a blue border around the object deemed to be the pre-defined object in the input image using the object’s coordinates. The program also places a red border around the object recognized using the algorithm and prints and saves the screen. Moreover, the program was implemented to calculate and display the mean average precision (mAP) for the object recognition performance, which is used as a performance indicator in object detection related application fields, to represent the object recognition performance quantitatively. First, 120 images were collected from an Internet portal to test the recognition of ships. Fig. 5 shows some of the results obtained by inputting the collected images into the test program.

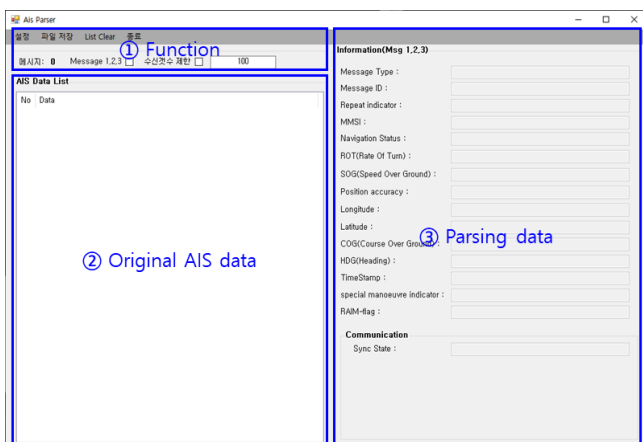


Fig. 4 GUI of the interface module

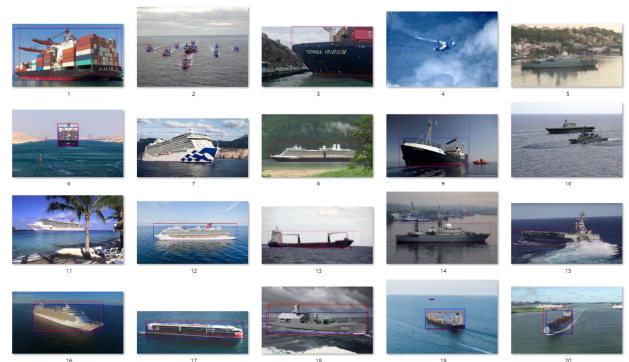


Fig. 5 Test result image sets for ship recognition

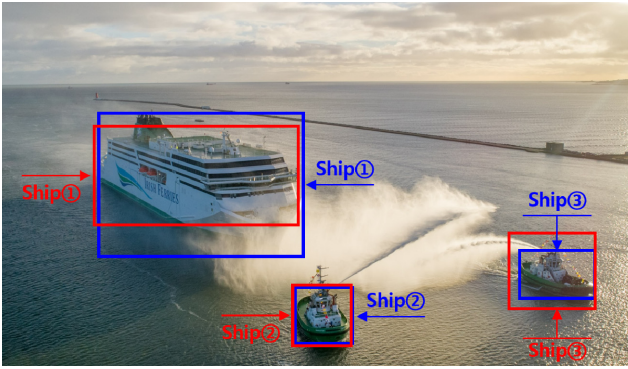


Fig. 6 Test result for the ship recognition

```

Sorting by probability...
Calculate Precision Recall...
recall = 0, precision = 1
recall = 0.1, precision = 0.972973
recall = 0.2, precision = 0.959184
recall = 0.3, precision = 0.909091
recall = 0.4, precision = 0.859813
recall = 0.5, precision = 0.847458
recall = 0.6, precision = 0
recall = 0.7, precision = 0
recall = 0.8, precision = 0
recall = 0.9, precision = 0
recall = 1, precision = 0
Interpolation Precision...
Calculate Average Precision...
Average Precision = 0.504411

mAP = 50.4411%
    
```

Fig. 7 mAP for ship recognition

In the result image shown in Fig. 6, there are three vessels in the picture. It is evident that the blue border area was defined by the ships, and the red border area was based on the algorithm overlap, and there is not much difference between them. Also, the implemented algorithm showed a ship recognition performance of 50.44 mAP, and Fig. 7 shows this result.

The evaluation data were collected to test crew recognition using the same method. The data were input into the program, and tests were performed. Fig. 8 shows some of the test results on 120 evaluation images collected for the crew recognition, and Fig. 9 shows one of the resulting images. In Fig. 9, there are three people in the picture. However, the result marked by the algorithm shows one additional border area in addition to the three border areas overlapping the defined areas. The analysis revealed that the algorithm misidentified the guardrail of the yacht as a person. To improve the recognition accuracy, pictures of people taken from various angles must be obtained, and further learning is required. The crew recognition performance of the implemented algorithm is 46.76 mAP, and this result is shown in Fig. 10.

The AIS was installed to test the interface module. The compressed information for the interface and the message numbers for the data received via the AIS were converted and processed, as shown in Fig.

11. The tenth item in the list of the received AIS raw data is message number 1. It indicates that a vessel with MMSI number 352689000 is navigating using an engine. This vessel is moving at a speed of approx. 8.0 km/h with a heading of 89° at a longitude of 128°49'30.2"E and a latitude of 35°04'20.4"N. The same raw data were input into the AIS message decoder available online. A comparison of the two results confirmed that the interface module processed the message accurately (Thomas, n.d.).



Fig. 8 Test result image sets for crew recognition

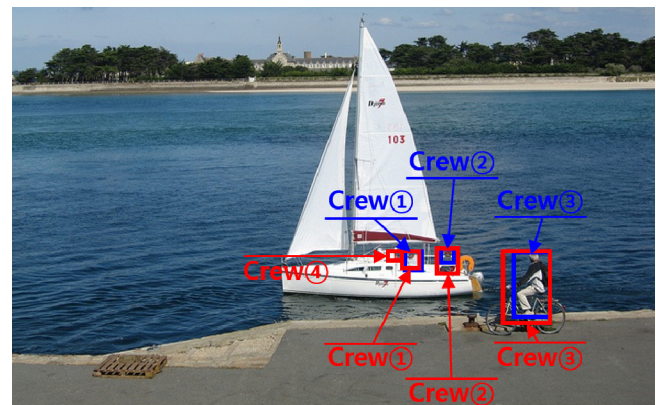


Fig. 9 Test result for the crew recognition

```

Sorting by probability...
Calculate Precision Recall...
recall = 0, precision = 1
recall = 0.1, precision = 0.882979
recall = 0.2, precision = 0.841398
recall = 0.3, precision = 0.818868
recall = 0.4, precision = 0.815172
recall = 0.5, precision = 0.785558
recall = 0.6, precision = 0
recall = 0.7, precision = 0
recall = 0.8, precision = 0
recall = 0.9, precision = 0
recall = 1, precision = 0
Interpolation Precision...
Calculate Average Precision...
Average Precision = 0.467634

mAP = 46.7634%
    
```

Fig. 10 mAP for the crew recognition

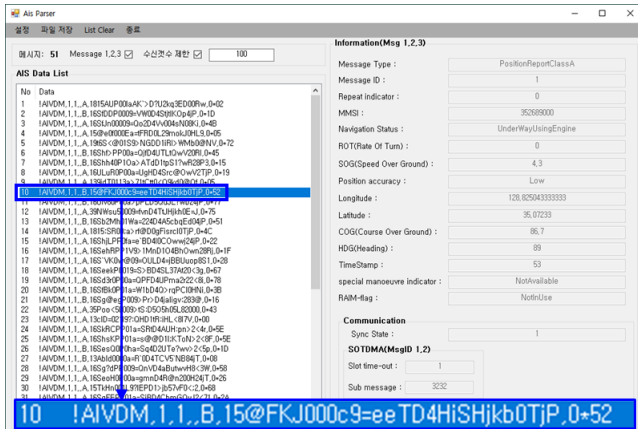


Fig. 11 Test result for the implemented interface module

6. Conclusion and Future Studies

This paper described a fundamental study on a video-integrated collision prediction and fall detection system to support small and medium-sized vessels in navigating safely. Based on artificial intelligence, this system recognizes ships and the crew in the images obtained from a CCTV camera installed on the vessel, predicts collision, and detects an overboard fall. Furthermore, the system converts the static and dynamic data for a vessel collected via the AIS and displays the images and information in an integrated manner. The system also alerts the navigator with warnings in each phase according to the analysis result of dangerous situations. The system components were designed, and the ship and crew recognition algorithm and the interface module were implemented and tested. The result showed a ship recognition performance of 50.44 mAP and a crew recognition performance of 46.76 mAP. The interface module was tested by verifying whether the message received through the installed AIS is converted and processed according to international standards.

We are currently developing the collision prediction and fall detection module to predict accidents involving the ships and crew recognized in the images. We are also researching an overlay technique specialized for maritime cameras to display information in an integrated manner. Furthermore, we are improving the algorithm's object recognition accuracy. We plan to complete the development of the designed video-integrated collision prediction and fall detection system in the future. We also plan to verify the performance and function of the system in the maritime environment using a real vessel to ensure that the system is useful.

Funding

This research was financially supported by the Ministry of Trade, Industry and Energy (MOTIE) and Korea Institute for Advancement of Technology (KIAT) through the National Innovation Cluster R&D program (P0006893, A Development of Predictive Maintenance System for Core Facilities in Maneuvering Vessel), and this research was financially supported by the Ministry of Trade, Industry and

Energy (MOTIE) and Korea Institute for Advancement of Technology (KIAT) through the Encouragement Program for The Industries of Economic Cooperation Region (Grant Number : P0008664).

References

- Bloisi, D., Iocchi, L., Fiorini, M., & Graziano, G. (2011). Automatic Maritime Surveillance with Visual Target Detection. Proceedings of International Defense and Homeland Security Simulation Workshop, Rome, Italy, 141–145.
- Bloisi, D., Previtali, F., Pennisi, A., Nardi, D., & Fiorini, M. (2016). Enhancing Automatic Maritime Surveillance Systems with Visual Information. *IEEE Transactions on Intelligent Transportation Systems*, 18(4), 824–833. <https://doi.org/10.1109/TITS.2016.2591321>
- Common Objects in COntext (COCO). (2014). 2014 Train images. Retrieved August 2020 from <http://images.cocodataset.org/zips/train2014.zip>
- Hwang, H.G., Kim, B.S., Kim, H.W., Kang, Y.S., & Kim, D.H. (2018). A Development of Active Monitoring and Approach Alarm System for Marine Buoy Protection and Ship Accident Prevention Based on Trail Cameras and AIS. *Journal of Korea Institute of Information and Communication Engineering*, 22(7), 1021–1029. <https://doi.org/10.6109/jkiice.2018.22.7.1021>
- Joo, K.S., Jeong, J.S., Kim, C.S., & Jeong, J.Y. (2011). The Vessels Traffic Measurement and Real-time Track Assessment using Computer Vision. *Journal of Korean Society of Marine Environment & Safety*, 17(2), 131–136. <https://doi.org/10.7837/kosomes.2011.17.2.131>
- Jung, C.H. (2013). A Study on the Requirement to the Fishing Vessel for Reducing the Collision Accidents. *Journal of Korean Society of Marine Environment and Safety*, 20(1), 18–25. <https://doi.org/10.7837/kosomes.2014.20.1.018>
- Kim, B.S., Hwang, H.G., Woo, Y.T., Yoo, J.Y., & Kim, T.S. (2020). A Conceptual Design of Video-complex Collision Risk Prevention and Alarm System for Safety Navigation of Small and Medium Ships. *Proceeding of the Korea Institute of Information and Communication Engineering*, Gyeongju, Korea, 522–524.
- Kim, H.T., Na, S., & Ha, W.H. (2011). A Case Study of Marine Accident Investigation and Analysis with Focus on Human Error. *Journal of Ergonomics Society of Korea*, 30(1), 137–150. <https://doi.org/10.5143/JESK.2011.30.1.137>
- Kim, S.R., & Jeong, J.S. (2017). A Study on Search and Rescue Method in Manoverboard Using Drone. *Journal of Korean Institute of Intelligent Systems*, 27(3), 236–240. <https://doi.org/10.5391/JKIIS.2017.27.3.236>
- Lee, J.M., Lee, K.H., & Kim, D.S. (2013). Image Analysis Module for AR-based Navigation Information Display. *Journal of Ocean Engineering and Technology*, 27(3), 22–28. <https://doi.org/10.5574/KSOE.2013.27.3.022>
- Lee, J.S., Lee, S.K., Kim, D.W., Hong, S.J., & Yang, S.I. (2018).

- Trends on Object Detection Techniques Based on Deep Learning. *Journal of Electronics and Telecommunications Trends*, 33(4), 23–32.
- Ministry of Oceans and Fisheries (MOF). (2020). Marine Accident Statistics. Retrieved March 2020 from <https://www.kmst.go.kr/kmst/statistics/annualReport/selectAnnualReportList.do>
- Park, T.G., Kim, S.J., Chu, Y.S., Kim, T.S., Ryu, K.J., & Lee, Y.W. (2018). Reduction Plan of Marine Casualty for Small Fishing Vessels. *Journal of Korean Society of Fisheries and Ocean Technology*, 54(2), 173–180. <https://doi.org/10.3796/KSFOT.2018.54.2.173>
- Redmon, J., Divvala, S., Girshick, R., & Farhadi A. (2016). You Only Look Once: Unified, Real-Time Object Detection. *Proceedings of IEEE Conference on Computer Vision and Pattern Recognition, Las Vegas, USA*, 779–788. <https://doi.org/10.1109/CVPR.2016.91>
- Thomas B.S. (n.d.). Online AIS Message Decoder. Retrieved August 2020 from <http://ais.tbsalling.dk/decode#>
- Xiao, L., Xu, M., & Hu, Z. (2018). Real-time Inland CCTV Ship Tracking. *Mathematical Problems in Engineering*, 2018, 1205210. <https://doi.org/10.1155/2018/1205210>

Author ORCIDs

Author name	ORCID
Kim, Bae-Sung	0000-0001-6504-3712
Woo, Yun-Tae	0000-0003-4753-3931
Yu, Yung-Ho	0000-0001-8305-268X
Hwang, Hun-Gyu	0000-0001-7119-0719

Instructions for Authors

General information

To submit a manuscript to the Journal of Ocean Engineering and Technology (JOET), it is advised to first carefully read the aims and the scope section of this journal, as it provides information on the editorial policy and the category of papers it accepts. Unlike many regular journals, JOET usually has no lag in acceptance of a manuscript and its publication. Authors that find a match with the aims and the scope of JOET are encouraged to submit as we publish works from all over the world. JOET adheres completely to guidelines and best practices published by professional organizations, including Principles of Transparency and Best Practice in Scholarly Publishing (joint statement by COPE, DOAJ, WAME, and OASPA (<http://doaj.org/bestpractice>) if otherwise not described below. As such, JOET would like to keep the principles and policies of those professional organizations during editing and the publication process.

Research and publication ethics

Details on publication ethics are found in <http://joet.org/authors/ethics.php>. For the policies on research and publication ethics not stated in the Instructions, Guidelines on Good Publication (<http://publicationethics.org/>) can be applied.

Requirement for membership

One of the authors who submits a paper or papers should be member of the Korean Society of Ocean Engineers (KSOE), except a case that editorial board provides special admission of submission.

Publication type

Article types include scholarly monographs (original research articles), technical articles (technical reports and data), and review articles. The paper should have not been submitted to other academic journal. When part or whole of a manuscript was already published to conference papers, research reports, and dissertations, then the corresponding author should note it clearly in the manuscript.

Copyright

After published to JOET, the copyright of manuscripts should belong to KSOE. A transfer of copyright (publishing agreement) form can be found in submission website (<http://www.joet.org>).

Manuscript submission

Manuscript should be submitted through the on-line submission website (<http://www.joet.org>). The date that manuscript was received through on-line website is the official date of receipt. Other correspondences can be sent by an email to the Editor in Chief or secretariat. The manuscript must be accompanied by a signed statement that it has been neither published nor currently submitted for publication elsewhere. The manuscript should be written in English or Korean. Ensure that online submission are in a standard word processing format. Corresponding author must write the manuscript using the JOET template provided in Hangul or MS Word format. Ensure that graphics are high-resolution.

Be sure all necessary files have been uploaded/ attached.

Authors' checklist

Please refer to "Authors' Checklist" for details.

Article structure

Manuscript must be edited in the following order: (1) Title, (2) Authors' names and affiliations, (3) Keywords, (4) Abstract, (5) Nomenclature (optional), (6) Introduction, (7) Main body (analyses, tests, results, and discussions), (8) Conclusions, (9) Conflict of interest (optional), (10) Funding (optional), (11) Acknowledgements (optional), (12) References, (13) Appendices (optional), (14) Author's ORCIDs.

Abstract

A concise and factual abstract is required. The abstract should state briefly the background, purpose and methods of the research, the principal results and conclusions. An abstract should be written in around 300 words. References are not cited in abstract whenever possible. Also, non-standard or uncommon abbreviations should be avoided, but if essential they must be defined at their first mention in the abstract itself.

Keywords

Immediately after the abstract, provide a maximum of 5 or 6 keywords.

Unit

Use the international system units(SI). If other units are mentioned, please give their equivalent in SI.

Equations

All mathematical equations should be clearly printed/typed using well accepted explanation. Superscripts and subscripts should be typed clearly above or below the base line. Equation numbers should be given in Arabic numerals enclosed in parentheses on the right-hand margin.

Tables

Tables should be numbered consecutively with Arabic numerals. Each table should be fully titled. All tables should be referred to in the texts.

Figures

Figures should be numbered consecutively with Arabic numerals. Each figure should be fully titled. All figures should be referred to in the texts. All the illustrations should be of high quality meeting with the publishing requirement with legible symbols and legends.

Conflict of interest

It should be disclosed here according to the statement in the Research and publication ethics regardless of existence of conflict of interest. If the authors have nothing to disclose, please state: "No potential

conflict of interest relevant to this article was reported.”

Funding

Funding to the research should be provided here. Providing a FundRef ID is recommended including the name of the funding agency, country and if available, the number of the grant provided by the funding agency. If the funding agency does not have a FundRef ID, please ask that agency to contact the FundRef registry (e-mail: fundref.registry@crossref.org). Additional detailed policy of FundRef description is available from <http://www.crossref.org/fundref/>. Example of a funding description is as follows: The study is supported by the Inha University research fund (FundRef ID: 10.13039/501100002632), and the Korea Health Personnel Licensing Examination Institute research fund (FundRef ID: 10.13039/501100003647).

Acknowledgments

Any persons that contributed to the study or the manuscript, but not meeting the requirements of an authorship could be placed here. For mentioning any persons or any organizations in this section, there should be a written permission from them.

References in text

References in texts follow the APA style. Authors can also see how references appear in manuscript text through the ‘Template’.

Reference list

Reference list follows the APA style. Authors can see how references should be given in reference section through the ‘Template’.

Appendices

The appendix is an optional section that can contain details and data supplemental to the main text. If there is more than an appendix, they should be identified as A, B, C, etc. Formulae and equations in appendices should be given separate numbering: Eq. (A1), Eq. (A2), etc.; in a subsequent appendix, Eq. (B1) and so on. Similarly for tables and figures: Table A1; Fig. A1, etc.

ORCID (Open Researcher and Contributor ID)

All authors are recommended to provide an ORCID. To obtain an ORCID, authors should register in the ORCID web site: <http://orcid.org>. Registration is free to every researcher in the world. Example of ORCID description is as follows:

Joonmo Chung: <https://orcid.org/0000-0003-1407-9031>

Peer review and publication process

The peer review process can be broadly summarized into three groups: author process, review process, and publishing process for accepted submissions. General scheme is presented in Figure 1.

Check-in process for review

If the manuscript does not fit the aims and scope of the Journal or does not adhere to the Instructions to Authors, it may be rejected immediately after receipt and without a review. Before reviewing, all submitted manuscripts are inspected by Similarity Check powered by iThenticate (<https://www.crossref.org/services/similarity-check/>), a plagiarism-screening tool. If a too high degree of similarity score is found, the Editorial Board will do a more profound content screening.

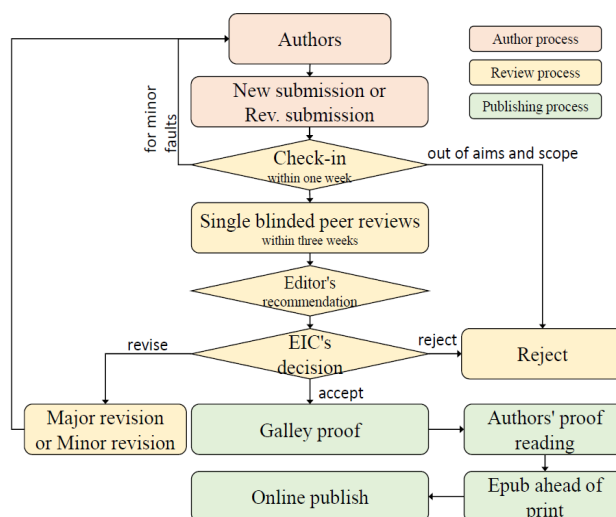


Figure 1 Flow chart of the peer review and publication process of JOET

The criterion for similarity rate for further screening is usually 15%; however, rather than the similarity rate, the Editorial Board focuses on cases where specific sentences or phrases are similar. The settings for Similarity Check screening are as follows: It excludes quotes, bibliography, small matches of 6 words, small sources of 1%, and the Methods section.

Number of reviewers

Reviewers will be selected from the list of reviewers. Manuscripts are then peer reviewed by at least 2 experts in the corresponding field, usually by 2.

Peer review process and the author response to the reviewer comments
JOET adopts single blind review, which means that the authors do not know the identity of the reviews. All papers, including those invited by the Editor, are subject to peer review.

The review period is 4 weeks. Usually the first decision is made within a week after completion of the review. The Editorial Board's decision after the review will be one of followings: Accept, Minor revision, Major revision, or Rejection. The Editorial Board may request the authors to revise the manuscript according to the reviewers' comments. If there are any requests for revision of the manuscript by the reviewers, the authors should do their best to revise the manuscript. If the reviewer's opinion is not acceptable or is believed to misinterpret the data, the author should reasonably indicate that. After revising the manuscript, the author should upload the revised files with a separate response sheet to each item of the reviewer's commentary. The author's revisions should be completed within 3 months after the request. If it is not received by the due date, the Editorial Board will notify the author. To extend the revision period beyond 3 months, the author should negotiate that with the Editorial Board. The manuscript review process can be provided for up two rounds. If the authors wish further review, the Editorial Board may consider it. The Editorial Board will make a final decision on the approval of the submitted manuscript for publication and can request any further corrections, revisions, and deletions of the article text if necessary. Statistical editing is also performed if the data requires professional statistical review by a statistician.

Processing after acceptance

If the manuscript is finally accepted, the galley proof will be sent to the corresponding author after professional manuscript editing and English proofreading. Proofreading should be performed for any misspellings or errors by the authors. Proofreading manuscript for publication is provided to the corresponding author, and the corresponding author must review the proofreading manuscript. Corresponding authors are responsible for the content of the proofreading manuscript and any errors. After final proofreading, the manuscript may appear at the journal homepage as an article in press with a unique DOI number for rapid communication. All published articles will be replaced by the replacement XML file and a final PDF.

Feedback after publication

If the authors or readers find any errors, or contents that should be revised, it can be requested from the Editorial Board. The Editorial Board may consider erratum, corrigendum or a retraction. If there are any revisions to the article, there will be a CrossMark description to announce the final draft. If there is a reader's opinion on the published article with the form of Letter to the editor, it will be forwarded to the authors. The authors can reply to the reader's letter. Letter to the editor and the author's reply may be also published.

How the journal handle complaints and appeals

The policy of JOET is primarily aimed at protecting the authors, reviewers, editors, and the publisher of the journal. If not described below, the process of handling complaints and appeals follows the guidelines of the Committee of Publication Ethics available from: <https://publicationethics.org/appeals>

- Who complains or makes an appeal?

Submitters, authors, reviewers, and readers may register complaints and appeals in a variety of cases as follows: falsification, fabrication, plagiarism, duplicate publication, authorship dispute, conflict of interest, ethical treatment of animals, informed consent, bias or unfair/inappropriate competitive acts, copyright, stolen data, defamation, and legal problem. If any individuals or institutions want to inform the cases, they can send a letter via the contact page on

our website: <https://www.joet.org/about/contact.php>. For the complaints or appeals, concrete data with answers to all factual questions (who, when, where, what, how, why) should be provided.

- Who is responsible to resolve and handle complaints and appeals?

The Editorial Board or Editorial Office is responsible for them. A legal consultant or ethics editor may be able to help with the decision making.

- What may be the consequence of remedy?

It depends on the type or degree of misconduct. The consequence of resolution will follow the guidelines of the Committee of Publication Ethics (COPE).

Article processing charge

Payment due

Article processing charge (APC) covers the range of publishing services JOET provides. This includes provision of online tools for editors and authors, article production and hosting, and customer services. Upon editorial acceptance of an article for the regular review service and upon submission of an article for the fast review service, the corresponding author will be notified that payment is due.

APC

The APC up to 6 pages is ₩200,000 (or \$200) and ₩550,000 (or \$550) for the for the regular and fast review services, respectively. An extra APC of \$50 per page is charged for papers longer than 6 pages. No taxes are included in this charge. For the fast review service, an advance fee of ₩250,000 (\$250) should be paid on submission.

Payment methods

Credit card payment can be made online using a secure payment form as soon as the manuscript has been editorially accepted. We will we send a receipt by email once payment has been processed. Please note that payment by credit card carries a surcharge of 10% of the total APC.

Invoice payment is due within 7 days of the manuscript receiving editorial acceptance. Receipts are available on request.

Title of Article

Firstname Lastname¹, Firstname Lastname² and Firstname Lastname³

¹Professor, Department of OO, OO School, OO University, Busan, Korea

²Graduate Student, Department of OO, OO University, Seoul, Korea

³Senior Researcher, Department of OO, OO Engineering, Corp., Seoul, Korea

KEY WORDS: Lumped mass line model, Explicit method, Steel lazy wave riser (Immediately after the abstract, provide a maximum of 5 or 6 keywords.)

ABSTRACT: A concise and factual abstract is required. The abstract should state briefly the background, purpose and methods of the research, the principal results and conclusions. An abstract should be written in around 300 words. References are not cited in abstract whenever possible. Also, non-standard or uncommon abbreviations should be avoided, but if essential they must be defined at their first mention in the abstract itself.

Nomenclature (Optional)

$ITOC$	Increment of total operating cost (\$/yr)
LHV	Lower heating value (kJ/kg)
P_w	Power (kW)
T	Temperature (K)
V	Volume (m ³)
ρ	Density (kg/m ³)

1. Introduction

The introduction should briefly place the study in a broad context and highlight why it is important. It should define the purpose of the work and its significance. The current state of the research field should be reviewed carefully and key publications cited. Please highlight controversial and diverging hypotheses when necessary. Finally, briefly mention the main aim of the work and highlight the principal conclusions. As far as possible, please keep the introduction comprehensible to scientists outside your particular field of research.

2. General Information for Authors

2.1 Research and Publication Ethics

Authorship should be limited to those who have made a significant contribution to the conception, design, execution, or interpretation of the reported study. All those who have made significant contributions should be listed as co-authors. Where there are others who have participated in certain substantive aspects of the research project, they should be acknowledged or listed as contributors.

The corresponding author should ensure that all appropriate co-authors and no inappropriate co-authors are included on the paper, and that all co-authors have seen and approved the final version of the paper and have agreed to its submission for publication.

Details on publication ethics are found in the journal's website (<http://joet.org/authors/ethics.php>). For the policies on research and publication

Received 00 February 2100, revised 00 October 2100, accepted 00 October 2100

Corresponding author Firstname Lastname: +82-51-759-0656, e-mail@e-mail.com

It is a recommended paper from the proceedings of 2019 spring symposium of the Korea Marine Robot Technology (KMRTS).

© 2100, The Korean Society of Ocean Engineers

This is an open access article distributed under the terms of the creative commons attribution non-commercial license (<http://creativecommons.org/licenses/by-nc/4.0>) which permits unrestricted non-commercial use, distribution, and reproduction in any medium, provided the original work is properly cited.

ethics not stated in the Instructions, Guidelines on Good Publication (<http://publicationethics.org/>) can be applied.

2.2 Requirement for Membership

One of the authors who submits a paper or papers should be member of The Korea Society of Ocean Engineers (KSOE), except a case that editorial board provides special admission of submission.

2.3 Publication Type

Article types include scholarly monographs (original research articles), technical articles (technical reports and data), and review articles. The paper should have not been submitted to other academic journal. When part or whole of a manuscript was already published to conference papers, research reports, and dissertations, then the corresponding author should note it clearly in the manuscript.

Example: It is noted that this paper is revised edition based on proceedings of KAOST 2100 in Jeju.

2.4 Copyright

After published to JOET, the copyright of manuscripts should belong to KSOE. A transfer of copyright (publishing agreement) form can be found in submission website (<http://www.joet.org>).

2.5 Manuscript Submission

Manuscript should be submitted through the on-line submission website (<http://www.joet.org>). The date that manuscript was received through on-line website is the official date of receipt. Other correspondences can be sent by an email to the Editor in Chief or secretariat. The manuscript must be accompanied by a signed statement that it has been neither published nor currently submitted for publication elsewhere. The manuscript should be written in English or Korean. Ensure that online submission are in a standard word processing format. Corresponding author must write the manuscript using the JOET template provided in Hangul or MS Word format. Ensure that graphics are high-resolution. Be sure all necessary files have been uploaded/ attached.

2.5.1 Author's checklist

Author's checklist and Transfer of copyright can be found in submission homepage (<http://www.joet.org>).

3. Manuscript

Manuscript must be edited in the following order: (1) Title, (2) Authors' names and affiliations, (3) Keywords, (4) Abstract, (5) Nomenclature (optional), (6) Introduction, (7) Main body (analyses, tests, results, and discussions), (8) Conclusions, (9) Conflict of interest (optional), (10) Funding (optional), (11) Acknowledgements (optional), (12) References, (13) Appendices (optional), (14) Author's ORCID.

3.1 Unit

Use the international system units(SI). If other units are mentioned, please give their equivalent in SI.

3.2 Equations

All mathematical equations should be clearly printed/typed using well accepted explanation. Superscripts and subscripts should be typed clearly above or below the base line. Equation numbers should be given in Arabic numerals enclosed in parentheses on the right-hand margin. The parameters used in equation must be defined. They should be cited in the text as, for example, Eq. (1), or Eqs. (1)–(3).

$$G_{GEV}(x; \mu, \sigma, \xi) = \begin{cases} \exp[-(1 + \xi(x - \mu)/\sigma)^{-1/\xi}] & \xi \neq 0 \\ \exp[-\exp(-(x - \mu)/\sigma)] & \xi = 0 \end{cases} \quad (1)$$

in which μ , σ , and ξ represent the location ("Shift" in figures), scale, and shape parameters, respectively.

3.3 Tables

Tables should be numbered consecutively with Arabic numerals. Each table should be typed on a separate sheet of paper and be fully titled. All tables should be referred to in the texts.

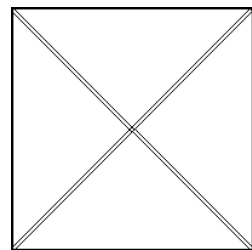
Table 1 Tables should be placed in the main text near to the first time they are cited

Item	Buoyancy riser
Segment length ¹⁾ (m)	370
Outer diameter (m)	1.137
Inner diameter (m)	0.406
Dry weight (kg/m)	697
Bending rigidity (N·m ²)	1.66E8
Axial stiffness (N)	7.098E9
Inner flow density (kg·m ³)	881
Seabed stiffness (N/m/m ²)	6,000

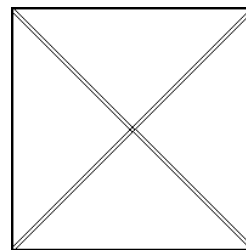
¹⁾Tables may have a footer.

3.4 Figures

Figures should be numbered consecutively with Arabic numerals. Each figure should be fully titled. All the illustrations should be of high quality meeting with the publishing requirement with legible symbols and legends. All figures should be referred to in the texts. They should be referred to in the text as, for example, Fig. 1, or Figs. 1–3.



(a) Description of what is contained in the first panel



(b) Description of what is contained in the second panel

Fig. 1 Schemes follow the same formatting. If there are multiple panels, they should be listed as: (a) Description of what is contained in the first panel; (b) Description of what is contained in the second panel. Figures should be placed in the main text near to the first time they are cited

3.5 How to Describe the References in Main Texts

All references should be listed at the end of the manuscripts, arranged in order of Alphabet. References in texts follow the American Psychological Association (APA) style. The exemplary form of listed references is as follows:

Single author: (Kim, 1998) or Kim (1998)

Two authors: (Kim and Lee, 2000) or Kim and Lee (2000)

Three or more authors: (Kim et al., 1997) or Kim et al. (1997)

Two or more papers: (Lee, 1995a; Lee, 1995b; Ryu et al., 1998)

Year unknown: (Kim, n.d.) or Kim (n.d.)

4. Results

This section may be divided by subheadings. It should provide a concise and precise description of the experimental results, their interpretation as well as the experimental conclusions that can be drawn. Tables and figures are recommended to present the results more rapidly and easily. Do not duplicate the content of a table or a figure with in the Results section. Briefly describe the core results related to the conclusion in the text when data are provided in tables or in figures. Supplementary results can be placed in the Appendix.

5. Discussion

Authors should discuss the results and how they can be interpreted in perspective of previous studies and of the working hypotheses. The findings and their implications should be discussed in the broadest context possible. Future research directions may also be highlighted

6. Conclusions

This section can be added to the manuscript.

Conflict of Interest (Optional)

It should be disclosed here according to the statement in the Research and publication ethics regardless of existence of conflict of interest. If the authors have nothing to disclose, please state: “No potential conflict of interest relevant to this article was reported.”

Funding (Optional)

Please add: “This research was funded by Name of Funder, grant number XXX” and “The OOO was funded by XXX”. Check carefully that the details given are accurate and use the standard spelling of funding agency names at <https://search.crossref.org/funding>

Acknowledgments (Optional)

In this section you can acknowledge any support given which is not covered by the author contribution or funding sections. This may include administrative and technical support, or donations in kind (e.g., materials used for experiments). For mentioning any persons or any organizations in this section, there should be a written permission from them.

References

- Journal name should not be abbreviated.
- A private report with limited access or download availability can not be a reference.
- Include the digital object identifier DOI or URL for all references where available.
- Reference list follows the American Psychological Association (APA) style.

Referring to journal publications:

Author, A.A., Author, B.B., & Author, C.C. (Year). Title of Article. Journal Title, vol(no), pp-pp. <https://doi.org/xx.xxxx/xxxxxx>

Author, A.A., Author, B.B., Author, C.C. (accepted; in press). Title of Article. Title of Periodical. Retrieved from <http://xx.xxx/x.pdf>

Lee, T.K., Kim, T.W., Rim, C.W., & Kim, S.C. (2013). A Study on Calculation of Local Ice Pressures for ARAON Based on Data Measured at Arctic Sea. Journal of Ocean Engineering and Technology, 27(5), 88–92. <https://doi.org/10.5574/KSOE.2013.27.5.088>

Lee, T.K., Kim, T.W., Rim, C.W., & Kim, S.C. (accepted; in press). A Study on Calculation of Local Ice Pressures for ARAON Based on Data Measured at Arctic Sea. Journal of Ocean Engineering and Technology, Retrieved from <http://xxx.xxx/xxx.pdf>

Referring to conference proceedings:

Author, A.A., Author, B.B., & Author, C.C. (Year). Title of Article. Proceeding Title, City, Country, pp-pp. <https://doi.org/xx.xxxx>

Aoki, S., Liu, H., & Sawaragi, T. (1994). Wave Transformation and Wave Forces on Submerged Vertical Membrane. Proceedings of International Symposium Waves - Physical and Numerical Modeling, Vancouver, Canada, 1287–1296.

Tsukamoto, C.L., Lee, W., Yuh, J., Choi, S.K., & Lorentz, J. (1997). Comparison Study on Advanced Thruster Control of Underwater Robots. Proceedings of International Conference on Robotics and Automation, 1845–1850. <https://doi.org/110.1109/ROBOT.1997.619056>

Referring to books:

Author, A.A. (Year). Title of Book (xx ed.). Location: Publisher.

Strunk, W., & White, E.B. (2000). The Elements of Style (4th ed.). New York, USA: Longman.

Schlichting, H. (1968). Boundary Layer Theory (6th ed.). New York, USA: McGraw-Hill.

Referring to theses or dissertations:

Author, A.A. (Year). Title of Doctoral Dissertation or Master’s thesis (Doctoral Dissertation or Master’s thesis). Name of Institution, City, Country.

Giovanni, I. (1998). Modelling and Identification of Underwater Robotic Systems (Ph.D. Thesis). University of Genova, Genova, Italy.

Referring to technical reports, rules, or guidelines:

Author, A.A. (Year). Title of report (Reprot No. xxx), Location: Publisher.

Likhomanov, V. (2010). Full-Scale Ice Trials of the Korean Research Icebreaker ARAON. Daejeon, Korea: Arctic and Antarctic Research Institute (AARI).

ABS. (2011). Guide for Ice Loads Monitoring Systems. Houston, USA: American Bureau of Shipping.

Lloyd's Register. (2011). FDA ICE Fatigue Induced by Ice Loading, ShipRight Design and construction - Fatigue Design Assesment. London, United Kingdom: Lloyd's Register.

Larson, M., & Kraus, N.C. (1989). SBEACH: Numerical Model for Simulating Storm-Induced Beach Change - Report 1 Empirical Foundation and Model Development (Technicla Report CERC-89-9). Coastal Engineering research center Vicksburg Ms.

Referring to patents:

Righsholder, A.A. (Year). Title of Patent. Patent number, Patent office with country.

Dawoo Shipbulding & Maringe Engineering (DSME). (2013). Distance Length Standardization Method for Preventing Interference at the time of Uploading Cell Guide of Container Ship. Unexamined Patent Publication 1020130044635, Korean Interllectual Property Office.

Referring to websites:

Righsholder, A.A. (Year). Title of webpage. Retrieved Month Year from <http://xxxx>

International Association of Classification Societies (IACS). (2010a). Common Structural Rules for Bulk Carriers. Retrieved July 2010 from <http://www.iacs-data.org.uk>

US Congressional Hearing. (2009). Strategic Importance of the Arctic in Us Policy. Retrieved June 2019 from <https://fas.org/irp/arctic.pdf>

Dawoo Shipbulding & Maringe Engineering (DSME). (2013). Distance Length Standardization Method for Preventing Interference at the time of Uploading Cell Guide of Container Ship. Retrieved June 2019 from <https://patentimages.storage./pdfs/792.pdf>

Referring to software:

Righsholder, A.A. (Year). Title of Software. Downloaded Month Year from <http://xxxx>

Standard

Organization. (Year). Title of the standard in italics [Translated title – if applicable] (Standard No.). Retrieved from <https://...>

International Organization for Standardization. (2005). Industrial sewing machines: Safety requirements for sewing machines, units and systems (ISO Standard No. 10821). Retrieved from <http://www.standard.no/no/Nettbutikk/produktkatalogen/Produktpresentasjon/?ProductID=113554>

Translation

Author, A. A. (Year of publication). Title of work: Capital letter also for subtitle (T. Translator, Trans.). Location: Publisher. (Original work published YEAR). DOI

Ura, T., & Takakawa, S. (2015). All about Submersibles (W.S. Kim, D.S. Kim, Y.H. Choi, C.H. Park, J.S. Park, P.M. Lee, H.S. Jung, Trans.). Korea: CIR. (Original Work Published in 1994, Japan: Seizan-Shoten Publishing)

in text: (Ura and Takakawa, 1994/2015)

Referring to some exceptional cases:

- when authors are missing, institution can replace authors

National Oceanic and Atmospheric Administration (NOAA). (2015). Deep-ocean Assessment and Reporting of Tsunamis (DART). Retrieved December 2019 from <https://nctr.pmel.noaa.gov/Dart/>

- when dates or years are missing, it is replaced with "n.d."

National Oceanic and Atmospheric Administration (NOAA). (n.d.). Deep-ocean Assessment and Reporting of Tsunamis (DART).

- when more then seven authors, first 6 authors ... last author.

Yeu, T., Choi, H.T., Lee, Y., Chae, J., Lee, Y., Kim, S.S., ... Lee, T.H. (2019). Development of Robot Platform for Autonomous Underwater Intervention. Journal of Ocean Engineering and Technology, 33(2), 168-177. <https://doi.org/10.26748/KSOE>. 2019.021

Appendix (Optional)

The appendix is an optional section that can contain details and data supplemental to the main text. For example, explanations of experimental details that would disrupt the flow of the main text, but nonetheless remain crucial to understanding and reproducing the research shown; figures of replicates for experiments of which representative data is shown in the main text can be added here if brief, or as Supplementary data. Mathematical proofs of results not central to the paper can be added as an appendix.

All appendix sections must be cited in the main text. In the appendixes, Figures, Tables, etc. should be labeled starting with 'A', e.g., Fig. A1, Fig. A2, etc.

Examples:

<https://doi.org/10.26748/KSOE.2019.022>

<https://doi.org/10.26748/KSOE.2018.4.32.2.095>

Author ORCIDs

All authors are recommended to provide an ORCID. To obtain an ORCID, authors should register in the ORCID web site: <http://orcid.org>. Registration is free to every researcher in the world. Example of ORCID description is as follows:

Author name	ORCID
So, Hee	0000-0000-000-00X
Park, Hye-Il	0000-0000-000-00X
Yoo, All	0000-0000-000-00X
Jung, Jewelry	0000-0000-000-00X

Authors' Checklist

The following list will be useful during the final checking of a manuscript prior to sending it to the journal for review. Please submit this checklist to the KSOE when you submit your article.

< Checklist for manuscript preparation >

- I checked my manuscript has been 'spell-checked' and 'grammar-checked'.
- One author has been designated as the corresponding author with contact details such as
 - E-mail address
 - Phone numbers
- I checked abstract 1) stated briefly the purpose of the research, the principal results and major conclusions, 2) was written in around 300 words, and 3) did not contain references (but if essential, then cite the author(s) and year(s)).
- I provided 5 or 6 keywords.
- I checked color figures were clearly marked as being intended for color reproduction on the Web and in print, or to be reproduced in color on the Web and in black-and-white in print.
- I checked all table and figure numbered consecutively in accordance with their appearance in the text.
- I checked abbreviations were defined at their first mention there and used with consistency throughout the article.
- I checked all references mentioned in the Reference list were cited in the text, and vice versa according to the APA style.
- I checked I used the international system units (SI) or SI-equivalent engineering units.

< Authorship checklist >

JOET considers individuals who meet all of the following criteria to be authors:

- Made a significant intellectual contribution to the theoretical development, system or experimental design, prototype development, and/or the analysis and interpretation of data associated with the work contained in the article.
- Contributed to drafting the article or reviewing and/or revising it for intellectual content.
- Approved the final version of the article as accepted for publication, including references.

< Checklist for publication ethics >

- I checked the work described has not been published previously (except in the form of an abstract or as a part of a published lecture or academic thesis).
- I checked when the work described has been published previously in other proceedings without copyright, it has clearly noted in the text.
- I checked permission has been obtained for use of copyrighted material from other sources including the Web.
- I have processed Plagiarism Prevention Check through reliable web sites such as www.kci.go.kr, <http://www.ithenticate.com/>, or <https://www.copykiller.org/> for my submission.
- I agree that final decision for my final manuscript can be changed according to results of Plagiarism Prevention Check by JOET administrator.
- I checked one author at least is member of the Korean Society of Ocean Engineers.
- I agreed all policies related to 'Research and Publication Ethics'
- I agreed to transfer copyright to the publisher as part of a journal publishing agreement and this article will not be published elsewhere including electronically in the same form, in English or in any other language, without the written consent of the copyright-holder.
- I made a payment for reviewing of the manuscript, and I will make a payment for publication on acceptance of the article.
- I have read and agree to the terms of Authors' Checklist.

Title of article :

Date of submission : DD/MM/YYYY

Corresponding author :

signature

Email address :

※ E-mail this with your signature to ksoehj@ksoe.or.kr

Publishing Agreement

ARTICLE DETAILS

Title of article :
Corresponding author :
E-mail address :
DOI : <https://doi.org/10.26748/KSOE.2XXX.XXX>

YOUR STATUS

I am one author signing on behalf of all co-authors of the manuscript.

ASSIGNMENT OF COPYRIGHT

I hereby assign to the Korean Society of Ocean Engineers, the copyright in the manuscript identified above and any tables, illustrations or other material submitted for publication as part of the manuscript (the "Article"). This assignment of rights means that I have granted to Korean Society of Ocean Engineers the exclusive right to publish and reproduce the Article, or any part of the Article, in print, electronic and all other media (whether now known or later developed), in any form, in all languages, throughout the world, for the full term of copyright, and the right to license others to do the same, effective when the Article is accepted for publication. This includes the right to enforce the rights granted hereunder against third parties.

SCHOLARLY COMMUNICATION RIGHTS

I understand that no rights in patents, trademarks or other intellectual property rights are transferred to the Journal owner. As the author of the Article, I understand that I shall have: (i) the same rights to reuse the Article as those allowed to third party users of the Article under the CC-BY-NC License, as well as (ii) the right to use the Article in a subsequent compilation of my works or to extend the Article to book length form, to include the Article in a thesis or

dissertation, or otherwise to use or re-use portions or excerpts in other works, for both commercial and non-commercial purposes. Except for such uses, I understand that the assignment of copyright to the Journal owner gives the Journal owner the exclusive right to make or sub-license commercial use.

USER RIGHTS

The publisher will apply the Creative Commons Attribution-Noncommercial Works 4.0 International License (CC-BY-NC) to the Article where it publishes the Article in the journal on its online platforms on an Open Access basis.

The CC-BY-NC license allows users to copy and distribute the Article, provided this is not done for commercial purposes and further does not permit distribution of the Article if it is changed or edited in any way, and provided the user gives appropriate credit (with a link to the formal publication through the relevant DOI), provides a link to the license, and that the licensor is not represented as endorsing the use made of the work. The full details of the license are available at <http://creativecommons.org/licenses/by-nc/4.0/legalcode>.

REVERSION OF RIGHTS

Articles may sometimes be accepted for publication but later rejected in the publication process, even in some cases after public posting in "Articles in Press" form, in which case all rights will revert to the author.

I have read and agree to the terms of the Journal Publishing Agreement.

Corresponding author:

name

signature

※ E-mail this with your signature to ksoehj@ksoe.or.kr (Papers will not be published unless this form is signed and returned)

Research and Publication Ethics

Journal of Ocean Engineering and Technology (JOET) adheres to the guidelines published by professional organizations, including Committee on Publication Ethics (COPE; <https://publicationethics.org/>)

1. Authorship

JOET considers individuals who meet all of the following criteria to be authors:

- 1) Made a significant intellectual contribution to the theoretical development, system or experimental design, prototype development, and/or the analysis and interpretation of data associated with the work contained in the article.
- 2) Contributed to drafting the article or reviewing and/or revising it for intellectual content.
- 3) Approved the final version of the article as accepted for publication, including references.

Contributors who do not meet all of the above criteria may be included in the Acknowledgment section of the article. Omitting an author who contributed to your article or including a person who did not fulfill all of the above requirements is considered a breach of publishing ethics.

Correction of authorship after publication: JOET does not correct authorship after publication unless a mistake has been made by the editorial staff.

2. Originality and Duplicate Publication

All submitted manuscripts should be original and should not be in consideration by other scientific journals for publication. Any part of the accepted manuscript should not be duplicated in any other scientific journal without permission of the Editorial Board, although the figures and tables can be used freely if the original source is verified according to the Creative Commons Attribution License (CC BY-NC). It is mandatory for all authors to resolve any copyright issues when citing a figure or table from other journal that is not open access.

3. Conflict-of-Interest Statement

Conflict of interest exists when an author or the author's institution, reviewer, or editor has financial or personal relationships that inappropriately influence or bias his or her actions. Such relationships are also known as dual commitments, competing interests, or competing loyalties. These relationships vary from being negligible to having a great potential for influencing judgment. Not all relationships represent true conflict of interest. On the other hand, the potential for conflict of interest can exist regardless of whether an individual believes that the relationship affects his or her scientific judgment. Financial relationships such as employment, consultancies, stock ownership, honoraria, and paid expert testimony are the most easily identifiable conflicts of interest and the most likely to undermine the credibility of the journal, the authors, or of the science itself. Conflicts can occur for other reasons as well, such as personal relationships, academic competition, and intellectual passion. If there are any conflicts of interest, authors should disclose them in the manuscript. The conflicts of interest may occur during the research process as well; however, it is important to provide disclosure. If there is a disclosure, editors, reviewers, and reader can approach the manuscript after understanding the situation and the background of the completed research.

4. Management Procedures for the Research and Publication Misconduct

When JOET faces suspected cases of research and publication misconduct such as a redundant (duplicate) publication, plagiarism, fabricated data, changes in authorship, undisclosed conflicts of interest, an ethical problem discovered with the submitted manuscript, a reviewer who has appropriated an author's idea or data, complaints against editors, and other issues, the resolving process will follow the flowchart provided by the Committee on Publication Ethics (<http://publicationethics.org/resources/flowcharts>). The Editorial Board of JOET will discuss the suspected cases and reach a decision. JOET will not hesitate to publish

errata, corrigenda, clarifications, retractions, and apologies when needed.

5. Editorial Responsibilities

The Editorial Board will continuously work to monitor and safeguard publication ethics: guidelines for retracting articles; maintenance of the integrity of the academic record; preclusion of business needs from compromising intellectual and ethical standards; publishing corrections, clarifications, retractions, and apologies when needed; and excluding plagiarism and fraudulent data. The editors maintain the following responsibilities: responsibility and authority to reject and accept articles; avoiding any conflict of interest with respect to articles they reject or accept; promoting publication of corrections or retractions when errors are found; and preservation of the anonymity of reviewers.

6. Hazards and human or animal subjects

If the work involves chemicals, procedures or equipment that have any unusual hazards inherent in their use, the author must clearly identify these in the manuscript. If the work involves the use of animal or human subjects, the author should ensure that the manuscript contains a statement that all procedures were performed in compliance with relevant laws and institutional guidelines and that the appropriate institutional committee(s) has approved them. Authors should include a statement in the manuscript that informed consent was obtained for experimentation with human subjects. The privacy rights of human subjects must always be observed.

Ensure correct use of the terms sex (when reporting biological factors) and gender (identity, psychosocial or cultural factors), and, unless inappropriate, report the sex and/or gender of study participants, the sex of animals or cells, and describe the methods used to determine sex and gender. If the study was done involving an exclusive population, for example in only one sex, authors should justify why, except in obvious cases. Authors should define how they determined race or ethnicity and justify their relevance.

7. Secondary publication

It is possible to republish manuscripts if the manuscripts satisfy the conditions of secondary publication. These are:

- The authors have received approval from the Editorial Board of both journals (the editor concerned with the secondary publication must have access to the primary version).
- The priority for the primary publication is respected by a publication interval negotiated by editors of both journals and the authors.
- The paper for secondary publication is intended for a different group of readers
- The secondary version faithfully reflects the data and interpretations of the primary version.
- The secondary version informs readers, peers, and documenting agencies that the paper has been published in whole or in part elsewhere, for example, with a note that might read, "This article is based on a study first reported in the [journal title, with full reference]"
- The title of the secondary publication should indicate that it is a secondary publication (complete or abridged republication or translation) of a primary publication.

8. Complaints and Appeals

The process of handling complaints and appeals follows the guidelines of the COPE available from: <https://publicationethics.org/appeals>

9. Post-publication discussions and corrections

The post-publication discussion is available through letter to editor. If any readers have a concern on any articles published, they can submit letter to editor on the articles. If there found any errors or mistakes in the article, it can be corrected through errata, corrigenda, or retraction.



The Korean Society of Ocean Engineers